SEABED DYNAMICS AND BREAKING WAVES

A Dissertation

Presented to the Faculty of the Graduate School

of Cornell University

in Partial Fulfillment of the Requirements for the Degree of

Doctor of Philosophy

by

Yongsung Park

August 2009

SEABED DYNAMICS AND BREAKING WAVES

Yongsung Park, Ph.D.

Cornell University 2009

The dynamics of the sea bottom boundary and the free surface breaking in the coastal areas have been studied. For each of the studied topics, theoretical analysis is supported by careful laboratory experiments as well as numerical simulations.

In the first part, the dynamics of the bottom boundary with various rheological properties has been examined within the framework of the boundary layer theory. Experimental measurements on the laminar boundary layer flows under a long wave clearly proved the validity of the theory. In particular, a flow reversal was observed during the deceleration phase of the long wave, which agreed with the theoretical prediction very well. Then the theory was extended to describe wave-induced flows inside a viscous mud. Two sets of experiments were conducted, one in the wave tank and the other in the U-tube to investigate the role of the mud-layer thickness compared to the boundary-layer thickness of the mud. Again excellent agreement between the theory and the experiment was achieved. Then the U-tube, which was specially built for the current research, enabled the study of the oscillatory flows of a non-Newtonian fluid. Experimental results showed that the generalized Newtonian constitutive relations, in which the shear stress is assumed to be some function of the rate of shear strain only, are not appropriate in describing unsteady flows of the yield-stress material. More relevant rheological properties were directly calculated from the velocity data and the resulting analytical solutions matched the experimental

data very well.

Aiming to identify the origins and the development paths of the mean quasi-steady flow characteristics in surf zone, laboratory experiments on a train of almost identical solitary waves breaking on a 1:20 sloping beach were carried out and the preliminary results are reported for the first time. Up to two successive waves were generated with the stroke length of the current wave maker. Particle Image Velocimetry technique with fluorescent seeding particles and an optical filter to exclude scattered laser light from broken free surface and air bubbles was employed and the flow field in the surf zone was obtained. By varying the time separation between the wave crests, the interactions were examined in terms of the Froude number and the reflected waves. Further experiments with more waves are needed before reaching any conclusion. In response to this research, a new wave maker has been installed in the DeFrees Hydraulics Laboratory at Cornell University. More results will follow in the near future.

BIOGRAPHICAL SKETCH

The author was born in Seoul, Republic of Korea, in October 10, 1976. In 1999, he graduated top in the Department of Civil Engineering at Seoul National University, where he also earned the Master's Degree two years later. Since August 2004, he has been studying fluid mechanics in the School of Civil & Environmental Engineering at Cornell University. He is very much interested in theoretical analysis of fluid mechanics problems and experimental verifications. Very often he gets unexpected results from his experiments and that is when the research becomes more interesting and perhaps more useful.

To Jungeun

ACKNOWLEDGEMENTS

I thank my parents for their infinite love and trust in their son. I owe everything that I have ever achieved to you. I also thank my parents-in-law for their equally great love and for entrusting their beloved daughter to me. Supports and cheers from my brother Yongil and my sister-in-law Jueun are much appreciated.

I would like to deeply thank my advisor, Professor Philip Liu. His endless curiosity, enthusiasm and the most insightful questions (about everything) have been my source of inspiration. Whenever I have questions or problems (either academic or personal), he has always been there with the right answers.

I wish to sincerely thank the Special Committee members: Professors Stephen Pope, James Jenkins and Todd Cowen for their crucial help in improving the quality of the dissertation. I also thank them very much for their belief in me. Special thanks go to Professor Rand who acted as the proxy for Professor Jenkins for the defense.

I am very happy that I have given many opportunities as a teaching assistant for Professors Liu, Shoemaker and Cowen. Working with such great teachers with different styles has been invaluable experience. Also I thank Professor Brutsaert for hiring me as a grader in my first semester at Cornell.

I thank Professor Claude Cohen for his interest and great help with the experiments on the yield-stress fluid. Also I wish to thank Professor Archer and Mr. Qi for helping to use their rheometer.

Many people have helped me during the last five years of my staying at Cornell. Liao, In Mei, Evan and P.J. taught me how to use the laboratory facilities and instruments. Jack, Tim and Paul taught me how to use the tools in the machine shop and helped me to build experimental apparatus. Very special thanks go to Sergiy for preventing the flooding which I was responsible for. I

enjoyed working with Javier and Juan when they were visiting Cornell. Special thanks go to the REU students (Steve, Brandon and Scott) for working in the lab with me. I also thank former and current members of EFMH (Tso-Ren, Vince, Russ, Laurent, Qinghai, Xiaoming, Weihua, Allie, Seth, Rafael, I-Chi, C.P., Jorge, Ammar, Themistoklis and Blair) for their friendship and encouragement. When I was going through difficult times, encouragements from Barbara, Pete and Sister Donna were very helpful.

Finally, I thank Jungeun for her love, support and patience. I must acknowledge that most of the experiments in Chapter 5 were carried out with her help.

TABLE OF CONTENTS

LIST OF TABLES

LIST OF FIGURES

CHAPTER 1

INTRODUCTION

1.1 Motivation of the study

More than 20% of the world's population live within 100 km of a coast and within 100 m above sealevel, where the average population densities are nearly three times higher than the global average population density (Small & Nicholls, 2003). In the United States, coastal counties (for the definition, see Crossett *et al.*, 2004) constitute only 17% of the total land area excluding Alaska, but account for 53% of the national population (Crossett *et al.*, 2004). Coastal areas are vulnerable to natural disasters such as tsunamis and storm surges and the damage is often intensified due to human-induced environmental degradation (e.g. Adger *et al.*, 2005). For example, the 2004 Indian Ocean Tsunami caused more than 250,000 casualties (e.g. Liu *et al.*, 2005) and the 2005 Hurricane Katrina took death toll of more than 1,800 not to mention the infrastructure damage that amounts to 80 billion USD (Knabb, Rhome & Brown, 2005). Moreover, it is very likely that coastal areas will be exposed to increasing risks in coming decades due to climate change and sea level rise (Nicholls *et al.*, 2007). In this context, the role of engineers in protecting the coastal areas is of great importance.

On the other hand, global climate change due to anthropogenic greenhouse gases and corresponding human efforts to develop renewable energy sources to replace fossil fuels require rapid technological innovations. Among the portfolio of potential renewable energy sources are ocean energies converted from tides and waves. The global wave energy resource is estimated to be of the same order of magnitude as world electricity consumption (Barstow *et al.*, 2008),

hence wave energy could contribute significantly in reducing greenhouse gas emissions.

Both in protecting coastal areas and in harnessing ocean energies, of fundamental importance is understanding of wave propagation in the near-shore region and its interaction with natural geographies or man-made structures. However, there are still many steps to take before we fully understand the physical processes. The linear wave theory ceases to be valid as waves enter coatal region from deep ocean and the effects of the bottom boundary become significant. Seabed is characterized by complex geometry and sophisticated rheology of its constituent materials, which renders interactions between wave and seabed extremely difficult to comprehend. Furthermore, increasing nonlinearity often culminates in wave breaking, which is followed by substantially enhanced level of turbulence, entrained air bubbles and transport of sediments.

Therefore, motivated by the importance of deeper understanding of coastal processes and by the aforementioned challenges in doing so, dynamics of bottom boundaries of various rheologies and free surface breaking of long waves are studied in this dissertation. In the following two sections, detailed objectives and the outline of the study will be described, respectively.

1.2 Objectives and scope of the study

Ocean waves are bounded by the free surface and the bottom boundary, and it is the objective of this research to study dynamics of both the upper and the lower boundaries of long waves. For each of the studied topics, which will be detailed in the next section, theoretical analysis is supported by careful labora-

tory experiments. When unexpected experimental results are obtained, efforts are made to further develop the theoretical models.

First in considering the bottom boundary, it is immediately recognized that both bottom topography and constitutive relation of the seabed material are important. However, only the latter is of interest here as the former, often in realtion to reflection, refraction and diffraction, has been extensively studied (e.g. Mei, 1983). In dealing with wave-induced flows inside or near the flat seabed, furthermore, the boundary layer approach has been employed as the theoretical framework, with the pressure gradient due to the water surface motion being the only forcing of the boundary layer flow. While it is acknowledged that free-stream flow as well as boundary layer flow is often turbulent and thus the shear stress at the water–seabed interface can be the dominant forcing, those are left for future works. Rather thorough experimental, and sometimes numerical, verifications of the simpler cases have been emphasized in this research believing that the effort will serve as the starting point toward deeper understanding of the fundamental physics. Whenever available, however, the connection with or possible extension to turbulent flows will be addressed.

Wave breaking is the main driving force in the surf-zone hydrodynamics as well as sediment transport in the coastal area, but the three-dimensional flow structure and the rapid aeration have hindered full understanding of its physics. Traditionally, mean flow fields of periodic incident waves have been mainly studied, while some researchers have studied breaking of a solitary wave to isolate a single run-up–run-down process. In both approaches, interactions between successively breaking waves are obscure or absent, and it is the other half of the present research to investigate the interactions using a train of solitary

waves breaking on a sloping beach. It also reflects the fact that tsunami usually comes as a group of waves. As there is no established theoretical framework available, this part of the research is mainly observational and experimental.

1.3 Overview of the dissertation

Overall, this dissertation can be divided into two parts: (i) flows inside or near the bottom boundary are discussed in Chapters 2 to 4, while (ii) Chapter 5 is devoted to experimental studies on breaking solitary waves on a plane beach.

1.3.1 Wave-induced flows inside or near the bottom boundary

As the backbone of the first part of the research, laminar boundary layer flow under a transient, long wave is studied in Chapter 2. The boundary-layer equation derived by Liu & Orfila (2004) is solved numerically and excellent agreement with the experiment is shown. Most importantly, the flow reversal during the deceleration phase is observed, which results in significant phase difference (opposite directions) between the depth-averaged velocity and the bottom shear stress. A possible extension to the turbulent boundary layer is also discussed. Parts of this work have been published in Liu, Park & Cowen (2007) and in Liu & Park (2008).

Propagating waves can be significantly dissipated by a soft deformable seabed (Gade, 1958). According to the rheological properties, researchers have modeled it as viscous, viscoplastic, viscoelastic or elastic material with increasing sediment concentration (Winterwerp & van Kesteren, 2004). Here con-

sidered are a viscous muddy seabed in Chapter 3 and an extension to non-Newtonian mud in the following chapter.

For the viscous mud case, essentially the same approach as used in Chapter 2 can be applied by replacing the bottom boundary layer of a viscous fluid with the mud layer underlying the inviscid fluid. One immediate consequence of this replacement is that the boundary-layer thickness can be comparable to the thickness of the mud layer itself. In the usual boundary layer formulation such as the one in Chapter 2, on the other hand, the boundary layer occupies only a small fraction compared to the depth of the whole fluid. If the vertical coordinate is scaled with the boundary-layer thickness, therefore, the upper boundary is formally placed at infinity. This is not the case for the mud layer with very high viscosity. Even with the same scaling, the mud layer can have a finite thickness. Consequently the thickness of the mud bed with respect to that of its own boundary layer characterizes mud flow regimes. Again good agreement between the theory and the laboratory experiment is obtained and parts of this work have been published in Park, Liu & Clark (2008).

The seemingly straightforward extension to non-Newtonian, particularly viscoplastic, mud turns out to be an extremely challenging task. Viscoplastic material, often called yield-stress fluid, remains as a rigid solid as long as the applied shear stress is less than a threshold (yield stress), while it can flow like a viscous fluid otherwise. This constitutive relation implicitly assumes that the process is reversible: the fluidized material returns to solid state once the shear stress falls below the yield stress. However experimental results using a material that faithfully follows a typical yield-stress model are found characteristically different from those of numerical simulations using the same con-

stitutive equation. Here it is argued that the deformability or the elasticity of the unyielded material can play a significant role under dynamic forcing. Also the solid–fluid transition may be virtually irreversible depending on the microscopic structure of the material. Taking these dynamic behaviors into account, more relevant rheological properties are derived from the flow field measurement, and the resulting analytical solution shows much improved agreement with the experiments.

1.3.2 A train of solitary waves breaking on a plane beach

Aiming to identify origins and development paths of the mean quasi-steady flow characteristics in surf zone, laboratory experiments on a train of almost identical solitary waves breaking on a sloping beach were carried out and reported for the first time. Up to two successive waves could be generated with the stroke length of the current wave maker. Particle Image Velocimetry technique with fluorescent seeding particles and an optical filter to exclude scattered laser light from broken surface and air bubbles is employed and the flow field in the surf zone is obtained. The vast amount of data are effectively summarized in terms of the time-varying Froude number based on the depth-averaged velocity and the total water depth. By varying the time separation between the wave crests, the interactions are examined in terms of the Froude number and the reflected waves. However, important information such as void fraction and turbulence could not be measured and the number of waves that could be generated are limited. Consequently, this research is by no means complete. Instead, the focus is on identification of fundamental questions and a new research direction through careful observations of the available data.

CHAPTER 2

BOUNDARY LAYER FLOWS UNDER TRANSIENT LONG WAVES

2.1 Introduction

In studying ocean wave propagation in the near-shore region particularly from the viewpoints of disaster mitigations and of coastal sediment managements, the shear stress at the bottom plays the key role. Specifically, viscous damping due to the bottom friction is one of the main mechanisms of wave amplitude attenuation over a long distance compared to the wavelength, and it is also the shear stress that links coastal hydrodyamic models to sediment transport models. However the length scale of bottom boundary layer is typically much smaller than the size of the flow domain of interest, which poses major challenges in measuring and/or calculating the bed shear stress accurately.

For practical reasons, bed shear stress τ_b' has often been modeled as some function of inviscid free-stream velocity outside the boundary layer in the direction parallel to the bottom, say U'. In the quadratic form, for example,

$$\tau_b' = \frac{1}{2} C_f \rho_w' |U'| U', \tag{2.1}$$

in which ρ_w' denotes the density of water and C_f the bottom friction coefficient (see e.g. Mei, 1983). Although the friction coefficient is known to be a function of bottom surface condition and Reynolds number (Cox, Kobayahi & Okayasu, 1996), a constant value is often assigned in calculating the bed shear stress under waves (Barnes *et al.*, 2009).

One consequence of using (2.1) with a constant fricition coefficient is that the bed shear stress is always in-phase with the free-stream velocity. However it is

well-known that a phase lag exists between them. To illustrate, let us consider a laminar boundary layer flow under a small-amplitude sinusoidal wave with the frequency ω'. The free-stream velocity can be expressed as

$$U'(x', t') = U_0'(x')\ \mathrm{e}^{\mathrm{i}\omega' t'}, \tag{2.2}$$

in which t' is the time coordinate. Note that only the real part of the complex expression in (2.2) is of interest. Neglecting the nonlinear term, the horizontal component of the momentum equation reads

$$\frac{\partial u'}{\partial t'} = -\frac{1}{\rho_w'}\frac{\partial p'}{\partial x'} + \nu_w'\frac{\partial^2 u'}{\partial z'^2}, \tag{2.3}$$

where p' denotes the pressure and ν_w' the kinematic viscosity of water. Outside the boundary layer, viscous effects are negligible, that is

$$-\frac{1}{\rho_w'}\frac{\partial p'}{\partial x'} = \frac{\partial U'}{\partial t'}. \tag{2.4}$$

Therefore, the pressure gradient term in (2.3) can be expressed in terms of the given free-stream velocity, and the analytical solution for (2.3) can be easily found with the appropriate boundary conditions. If the depth of water h' is much larger than the boundary-layer thickness δ', where

$$\delta' = \sqrt{\frac{2\nu_w'}{\omega'}} \tag{2.5}$$

is the Stokes boundary-layer thickness, the analytical solution for (2.3) reduces to (Mei, 1983)

$$u' = U_0'\left[1 - \mathrm{e}^{-(1+\mathrm{i})z'/\delta'}\right]\mathrm{e}^{\mathrm{i}\omega' t'}. \tag{2.6}$$

Note that the no-slip condition at the bottom ($z' = 0$) has been applied. Then the bed shear stress can be obtained as

$$\tau_b' = \sqrt{2}\frac{\rho_w'\nu_w' U_0'}{\delta'}\,\mathrm{e}^{\mathrm{i}(\omega' t' + \pi/4)}. \tag{2.7}$$

Comparing (2.7) with (2.2), the bed shear stress is out of phase with the free-stream velocity by $\pi/4$. It is remarked here that phase lags have also been observed in the turbulent oscillatory boundary layer (e.g. Jensen, Sumer & Fredsøe, 1989), albeit smaller than that in the laminar case.

In the near-shore region, effects of nonlinearity and dispersion become significant, hence the linear wave theory becomes no longer valid. Keulegan (1948) considered, for the first time, the viscous damping of a solitary wave that is weakly nonlinear and weakly dispersive. He first solved the linearized boundary layer equation (2.3) under a general transient wave, then used Boussinesq's solution of the solitary wave as the inviscid free-stream velocity:

$$U'(x',t') = U_0' \operatorname{sech}^2\left[\sqrt{\frac{3H'}{4h'^3}}(x' - C't')\right], \tag{2.8}$$

where H' is the wave height, $C' = \sqrt{g'(h' + H')}$ the phase speed and g' the gravitational acceleration. Note that the corresponding wave profile $\zeta'(x',t')$ is given as

$$\zeta'(x',t') = H' \operatorname{sech}^2\left[\sqrt{\frac{3H'}{4h'^3}}(x' - C't')\right]. \tag{2.9}$$

Though Keulegan (1948) did not specifically mention the bed shear stress, he calculated the vertical gradient of the horizontal velocity at the bottom which, interestingly, changed its sign during the deceleration phase of the solitary wave when observed at a fixed position. The quadratic friction law (2.1) with a constant friction coefficient cannot adequately describe this significant phase lag. Recently, Liu & Orfila (2004) applied a more rigorous perturbation approach and obtained a fully nonlinear boundary-layer equation that can be systematically extended to higher orders of accuracy. Notice that the linearized leading-order momentum equation of Liu & Orfila (2004) is essentially the same as (2.3). On the other hand, corresponding experimental data is scarce. To the author's best

knowledge, only Ippen, & Mitchell (1957) measured time histories of bed shear stress under solitary waves using a shear plate. Though the accuracy of their data is questionable, it was clearly observed that the bed shear stress changes sign as the solitary wave passes the measurement area.

In this chapter, the structure of the boundary layer under long wave will be studied in detail especially using the boundary layer equation by Liu & Orfila (2004), which will be discussed in the next section. Then the laboratory measurements of the fluid particle velocity inside and above the boundary layer under solitary wave will be presented in §2.3. The agreement between the theoretical solution and the experimental data is very good and the nonlinear terms in the boundary layer equation make no significant difference even with large nonlinearity of the wave as long as the wavelength is long enough. Another important observation is that the solution of the boundary layer equation is valid for different kinds of wave loading in shallow water. To demonstrate this point, cases of two successively generated solitary waves and of cnoidal wave will be considered in §2.4. Finally concluding remarks and future research are presented in the last section of this chapter.

2.2 Theoretical background

Consider a long wave with the surface displacement $\zeta'(x', t')$ propagating in a constant water depth h'. The long wave is characterized by the wave amplitude a', the characteristic wavelength l' and the time-scale $l'/\sqrt{g'h'}$. The following

dimensionless variables are then defined:

$$\left.\begin{aligned} x = x'/l', \quad z = z'/h', \quad t = t'\sqrt{g'h'}/l', \quad \zeta = \zeta'/a', \\ p = p'/\rho'_w g' a', \quad u = u'/\epsilon\sqrt{g'h'}, \quad w = w'\mu/\epsilon\sqrt{g'h'}. \end{aligned}\right\} \tag{2.10}$$

Two dimensionless parameters have been introduced in the above equations:

$$\epsilon = a'/h', \quad \mu = h'/l'. \tag{2.11}$$

Note that, throughout this dissertation, variables without prime ($'$) denote dimensionless quantities and vice versa.

The flow motions associated with long wave can be considered as essentially irrotational except in the boundary layers adjacent to the free surface, $z = 1 + \epsilon\zeta$, and the bottom, $z = 0$. Inside these boundary layers, the fluid viscosity plays a role of generating and diffusing vorticity into the flow domain. Therefore, rotational velocity components must be added inside the boundary layers. Since the no-slip boundary condition on the bottom is required, the leading-order horizontal rotational velocity component inside the bottom boundary layer must be the same as that of the irrotational velocity, i.e. $O(1)$. On the other hand, the stress-free conditions are applied at the free surface and the leading-order horizontal rotational velocity component inside the free surface boundary layer is weaker, i.e. $O(\alpha)$ (Mei & Liu, 1973), where

$$\alpha^2 = \frac{\nu'_w}{l'\sqrt{g'h'}}, \tag{2.12}$$

can be viewed as the inverse of a Reynolds number. Accordingly, only the bottom boundary layer flow will be discussed in this chapter.

2.2.1 Formulation

Liu & Orfila (2004) introduced the following perturbation expansions for the

velocity field in the bottom boundary layer:

$$u = U(x,z,t) + u_0^r(x,z,t) + \alpha u_1^r(x,z,t) + \cdots, \tag{2.13}$$

$$w = W(x,z,t) + \alpha\mu w_1^r(x,z,t) + \cdots. \tag{2.14}$$

Note that U and W are the inviscid free-stream velocity components and are assumed known, while the superscript r denotes the rotational velocity components. The perturbation expansions are accurate up to $O(\alpha)$. Since the ratio of the boundary-layer thickness and the length-scale is of $O(\alpha)$, here introduced is the stretched coordinate

$$\eta = \frac{z}{\alpha/\mu}. \tag{2.15}$$

The leading-order continuity equation and the horizontal momentum equation for the rotational velocity in the bottom boundary layer becomes

$$\frac{\partial u_0^r}{\partial x} + \frac{\partial w_1^r}{\partial \eta} = 0, \tag{2.16}$$

$$\frac{\partial u_0^r}{\partial t} + \epsilon\left[u_0^r\frac{\partial u_0^r}{\partial x} + w_1^r\frac{\partial u_0^r}{\partial \eta}\right] = \frac{\partial^2 u_0^r}{\partial \eta^2}. \tag{2.17}$$

Note that the leading-order dynamic pressure gradient across the boundary layer is $\partial p/\partial\eta = O(\alpha\mu)$.

The no-slip and no-flux boundary conditions on the bottom require that the rotational velocity satisfies the following boundary conditions:

$$u_0^r = -U, \quad w_1^r = -W/(\alpha\mu), \quad \eta = 0. \tag{2.18}$$

At the outer edge of the boundary layer, $\eta \to \infty$, the horizontal rotational velocity components vanish,

$$u_0^r,\ w_1^r \to 0, \quad \eta \to \infty. \tag{2.19}$$

2.2.2 Linearized bounday layer solution

If the nonlinear convective acceleration terms in (2.17) can be neglected, the analytical solution for a general transient wave loading is readily available (see Liu & Orfila, 2004):

$$u_0^r(x,\eta,t) = -\frac{\eta}{\sqrt{4\pi}}\int_0^t \frac{U(x,z=0,s)}{\sqrt{(t-s)^3}}\,\mathrm{e}^{-\eta^2/4(t-s)}\,\mathrm{d}s. \tag{2.20}$$

Note that the irrotational velocity has been assumed to be zero initially. From the continuity equation (2.16), the vertical rotational velocity component can be obtained by integration,

$$w_1^r(x,\eta,t) = -\int_\eta^\infty \int_0^t \frac{\eta^*}{\sqrt{4\pi}}\frac{\partial U(x,z=0,s)/\partial x}{\sqrt{(t-s)^3}}\,\mathrm{e}^{-\eta^{*2}/4(t-s)}\,\mathrm{d}s\,\mathrm{d}\eta^*. \tag{2.21}$$

Also the leading-order bed shear stress can be found by differentiating (2.20):

$$\tau_b \equiv \left.\frac{\partial u_0^r}{\partial \eta}\right|_{\eta=0} = \frac{1}{\sqrt{\pi}}\int_0^t \frac{\partial U(x,z=0,s)/\partial s}{\sqrt{t-s}}\,\mathrm{d}s. \tag{2.22}$$

2.2.3 Nonlinear boundary layer solution

If the nonlinear inertia term is not negligible, the full boundary layer equation (2.17) must be solved numerically. Anticipating the next section in which laboratory experiments on solitary waves are presented, only the waves of permanent form are considered here. First, a moving coordinate is introduced:

$$\xi = Ct - x, \tag{2.23}$$

where C is the dimensionless phase speed. Note that for a fixed location, say $x = 0$, ξ acts like time. From the continuity equation (2.16), then,

$$w_1^r = -\int_\eta^\infty \frac{\partial u_0^r}{\partial \xi}\,\mathrm{d}\eta^*. \tag{2.24}$$

Substituting (2.24) into (2.17),

$$C\frac{\partial u_0^r}{\partial \xi} + \epsilon\left[-u_0^r\frac{\partial u_0^r}{\partial \xi} - \left(\int_\eta^\infty \frac{\partial u_0^r}{\partial \xi}\,\mathrm{d}\eta^*\right)\frac{\partial u_0^r}{\partial \eta}\right] = \frac{\partial^2 u_0^r}{\partial \eta^2}. \tag{2.25}$$

One could try to solve the above differential-integral equation for u_0^r. Alternatively (2.25) can be further simplified by approximating the integrand of the integral by the leading-order term, that is,

$$\frac{\partial u_0^r}{\partial \xi} = \frac{1}{C}\frac{\partial^2 u_0^r}{\partial \eta^2} + O(\epsilon). \tag{2.26}$$

Thus, the approximate nonlinear boundary layer equation can be obtained as

$$(C - \epsilon u_0^r)\frac{\partial u_0^r}{\partial \xi} + \frac{\epsilon}{C}\left(\frac{\partial u_0^r}{\partial \eta}\right)^2 = \frac{\partial^2 u_0^r}{\partial \eta^2} + O(\epsilon^2). \tag{2.27}$$

The boundary conditions are

$$u_0^r = -U, \quad \eta = 0; \qquad u_0^r \to 0, \quad \eta \to \infty. \tag{2.28}$$

The approximate nonlinear boundary layer equation (2.27) is solved numerically by an iterative scheme, in which the nonlinear terms are calculated based on the results from the previous iteration, that is at $(n+1)^{th}$ iteration:

$$\left[\frac{\partial^2 u_0^r}{\partial \eta^2} - C\frac{\partial u_0^r}{\partial \xi}\right]_{n+1} \approx \left[-\epsilon u_0^r\frac{\partial u_0^r}{\partial \xi} + \frac{\epsilon}{C}\left(\frac{\partial u_0^r}{\partial \eta}\right)^2\right]_n. \tag{2.29}$$

Meanwhile the linear operator is discretized by the Crank–Nicolson method. Denoting $u_0^r(j\Delta\xi, k\Delta\eta) = u_{j,k}$, where $\Delta\xi$ and $\Delta\eta$ are the respective step sizes in ξ and in η coordinates, the discretization of (2.29) at $(n+1)^{th}$ iteration is written as

$$\begin{aligned}\theta\frac{u_{j+1,k+1} - 2u_{j+1,k} + u_{j+1,k-1}}{(\Delta\eta)^2} &+ (1-\theta)\frac{u_{j,k+1} - 2u_{j,k} + u_{j,k-1}}{(\Delta\eta)^2} \\ &- C\frac{u_{j+1,k} - u_{j,k}}{\Delta\xi} = R_n,\end{aligned} \tag{2.30}$$

where, R_n is the nonlinear terms calculated from the results of the previous iteration:

$$R_n = \left\{-\epsilon u_{j,k}\frac{u_{j+1,k} - u_{j,k}}{\Delta\xi} + \frac{\epsilon}{C}\left[\theta\frac{u_{j+1,k+1} - u_{j+1,k-1}}{2\Delta\eta} + (1-\theta)\frac{u_{j,k+1} - u_{j,k-1}}{2\Delta\eta}\right]^2\right\}_n. \tag{2.31}$$

Here θ is chosen to be 0.5. Using the linear solution (2.20) as an initial guess, the iteration continues until the maximum relative error between the current and the previous iteration results is smaller than 10^{-6}.

2.3 Laboratory experiments on the laminar boundary layer flows under solitary waves

To validate the theories presented in the previous section, a set of laboratory experiments measuring the boundary layer velocities under solitary waves was carried out in the DeFrees Hydraulics Laboratory at Cornell University. Before discussing the experimental results, first analytical solutions for solitary waves are reviewed.

2.3.1 Analytical solutions for solitary waves

When the viscous effect is completely ignored, analytical solutions describing a solitary wave are available. For example, Grimshaw (1971) presented the solution for the free surface diplacement up to $O\left(\epsilon^2\right)$ as follows:

$$\zeta = s^2 - \frac{3}{4}\epsilon s^2 q^2 + \epsilon^2\left(\frac{5}{8}s^2q^2 - \frac{101}{80}s^4q^2\right), \tag{2.32}$$

where,

$$s = \operatorname{sech}\left[\frac{B}{\mu}(x - Ct)\right], \tag{2.33}$$

$$q = \tanh\left[\frac{B}{\mu}(x - Ct)\right], \tag{2.34}$$

$$B = \sqrt{\frac{3\epsilon}{4}}\left(1 - \frac{5}{8}\epsilon + \frac{71}{128}\epsilon^2\right), \tag{2.35}$$

$$C = \sqrt{1 + \epsilon - \frac{1}{20}\epsilon^2 - \frac{3}{70}\epsilon^3}. \tag{2.36}$$

The corresponding horizontal and vertical velocity can be expressed as

$$\begin{aligned} u(x,z,t) = U &= s^2 - \epsilon\left[-\frac{1}{4}s^2 + s^4 + z^2\left(\frac{3}{2}s^2 - \frac{9}{4}s^4\right)\right] \\ &- \epsilon^2\left[\frac{19}{40}s^2 + \frac{1}{5}s^4 - \frac{6}{5}s^6 + z^2\left(-\frac{3}{2}s^2 - \frac{15}{4}s^4 + \frac{15}{2}s^6\right)\right. \\ &+ \left. z^4\left(-\frac{3}{8}s^2 + \frac{45}{16}s^4 - \frac{45}{16}s^6\right)\right], \end{aligned} \tag{2.37}$$

$$\begin{aligned} w(x,z,t) = W &= \sqrt{\frac{3\mu^2}{\epsilon}}zq\left\{\epsilon s^2 - \epsilon^2\left[\frac{3}{8}s^2 + 2s^4 + z^2\left(\frac{1}{2}s^2 - \frac{3}{2}s^4\right)\right]\right. \\ &+ \epsilon^3\left[-\frac{49}{640}s^2 - \frac{17}{20}s^4 - \frac{18}{5}s^6 + z^2\left(-\frac{13}{16}s^2 - \frac{25}{16}s^4 + \frac{15}{2}s^6\right)\right. \\ &+ \left.\left. z^4\left(-\frac{3}{40}s^2 + \frac{9}{8}s^4 - \frac{27}{16}s^6\right)\right]\right\}. \end{aligned} \tag{2.38}$$

Notice that the leading-order $O(1)$ solutions of Grimshaw's formulae are equivalent to Boussinesq's solutions for solitary waves (2.8 & 2.9).

2.3.2 Generation of solitary waves in the laboratory

The water particle velocity under a long wave propagating in a constant depth is essentially uniform in the entire water column up to the first order except near boundaries. Based on this observation, Goring (1979) developed a long-wave generation theory by approximately matching the velocity of the wave maker paddle with the water particle velocity under the wave. Denoting the trajectory of the paddle as $X'_p(t')$ and the depth-averaged velocity $\overline{u'}(x',t')$, one can solve for X'_p the following nonlinear differential equation:

$$\frac{\mathrm{d}X'_p}{\mathrm{d}t'} = \overline{u'}\left(X'_p, t'\right), \tag{2.39}$$

in which $\overline{u'}(x', t')$, or equivalently, the free surface profile $\zeta'(x', t')$ is given for the desired wave form such as a solitary wave. In figure 2.1, the wave maker trajectory to generate a solitary wave with the nonlinearity $\epsilon = H'/h' = 0.2$ in the water depth $h' = 10$ cm is plotted. Note that Boussinesq's solution (2.8) was used in solving (2.39) and the wave profile was truncated at the both locations where the surface displacement is 1.0% of the wave height. In practice, the waves generated in the wave tank were about 20% smaller in wave heights than desired. To generate a solitary wave with $\epsilon = 0.2$, therefore, the trajectory for $\epsilon = 0.25$ had to be used.

2.3.3 Experimental set-up

The experiments were conducted in a wave tank (32 m long, 0.6 m wide, and 0.9 m deep), which is equipped with a piston-type wave maker. The tank has glass sidewalls and a painted steel bottom. One section of the tank is equipped with a clear extruded acrylic bottom allowing the delivery of laser light from below.

Three different solitary waves have been studied by changing the wave heights ($H' = 0.8$, 2.0 and 3.0 cm), while the water depth was kept constant, $h' = 10$ cm. The characteristics of the waves generated in the experiments are summarized in table 2.1. In the table, the wavelength l' and the wave period T' are defined as

$$l' = 2\sqrt{\frac{4h'^3}{3H'}}\,\mathrm{sech}^{-1}(0.1) \tag{2.40}$$

and

$$T' = \frac{l'}{\sqrt{g'(h' + H')}}, \tag{2.41}$$

respectively. Note that for solitary waves $a' = H'$ in (2.10) and the Reynolds

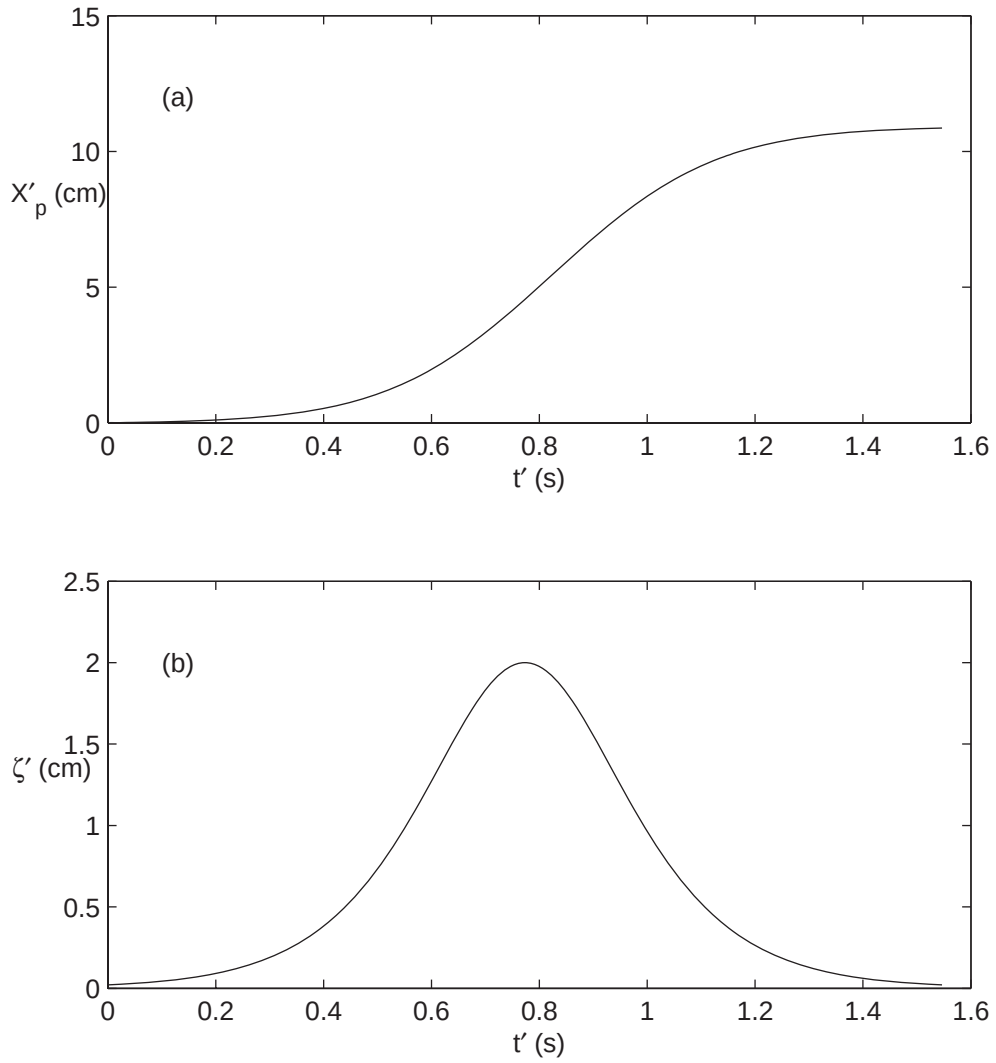

Figure 2.1: The trajectory of the wave maker paddle (*a*) to generate a solitary wave (*b*) given as (2.9).

Table 2.1: Characteristics of solitary waves used in the experiments.

Case No.	H' (cm)	l' (m)	T' (s)	ϵ	μ	α	Re
B1	0.8	2.29	2.20	0.08	0.0437	0.0006	2.59×10^3
B2	2.0	1.52	1.37	0.2	0.0658	0.0008	1.02×10^4
B3	3.0	1.23	1.05	0.3	0.0813	0.0009	1.88×10^4

number Re is defined as (Sumer *et al.*, 2008)

$$Re = \frac{U_0'^2}{\nu' \left(3g'H'/4h'^2\right)^{1/2}}. \tag{2.42}$$

The critical Reynolds number for the laminar–turbulent transition is $Re_c = 5{\times}10^5$ (Sumer *et al.*, 2008), thus all the cases in table 2.1 remain well within the laminar range.

Three acoustic wave gages (Banner Engineering S18U) and an acoustic Doppler velocimeter (ADV, Nortek Vectrino with Plus Firmware) were used along with particle image velocimetry (PIV) system. The PIV system is used primarily to measure the velocity field in the bottom boundary layer in the region with the acrylic bottom and the laser light sheet was delivered vertically through the bed. The locations of measurements are shown in figure 2.2.

Figure 2.3 shows the surface profiles measured at wave gage B sampled at 100 Hz (above the center of the PIV measurement region) for all the cases in table 2.1. Grimshaw's higher-order solution (2.32) is also plotted in the same figure. The agreement between the theoretical results and experimental data is reasonably good. Notice that the theoretical solutions in dimensionless form (2.32) for the three different ϵ values are very close to one another.

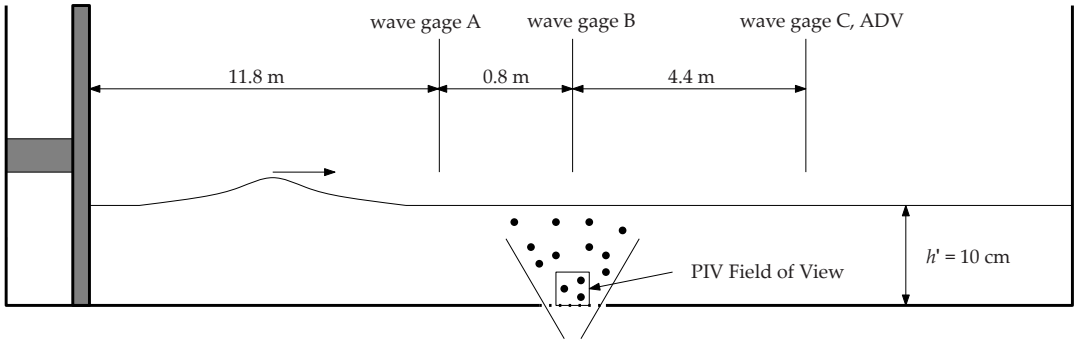

Figure 2.2: Experimental set-up (not to scale).

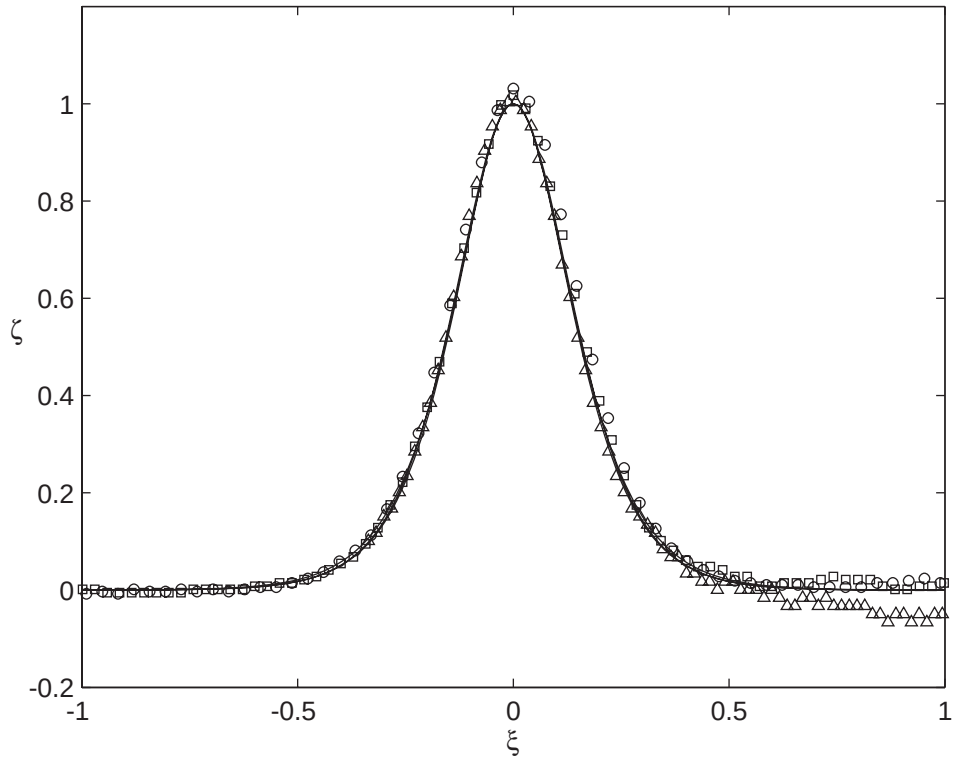

Figure 2.3: Theoretical and experimental dimensionless water surface profiles: ——, Grimshaw's solution (2.32); ∘, wavegage data for the case B1; △, B2; □, B3.

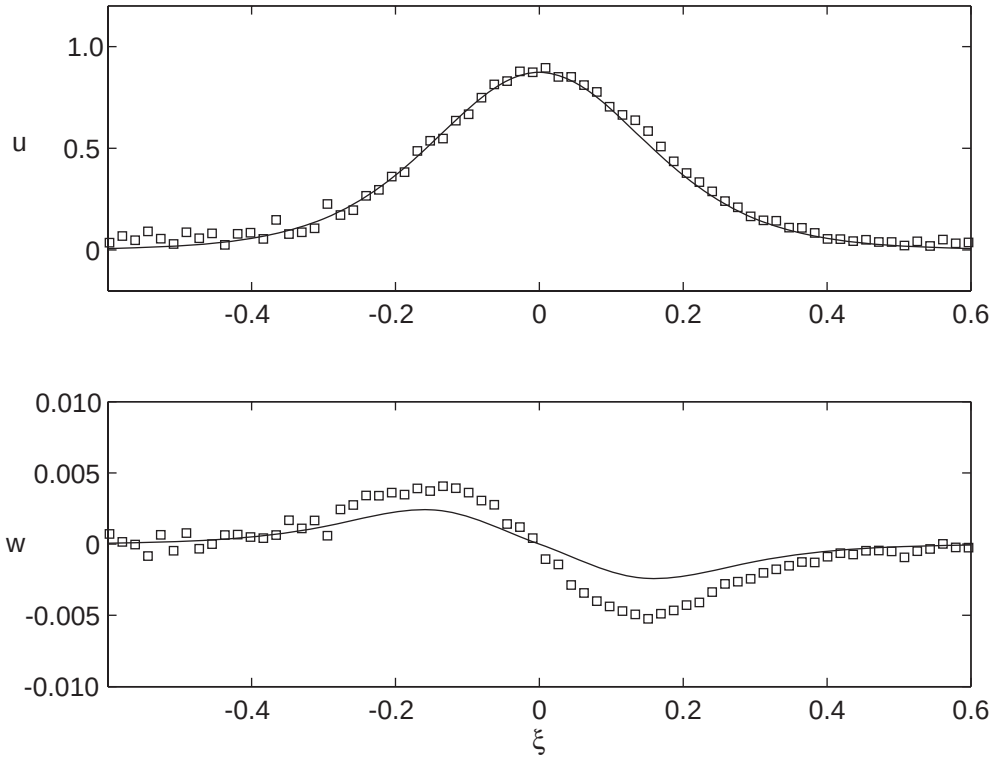

Figure 2.4: Theoretical and experimental dimensionless water particle velocities in the inviscid region: ——, Grimshaw's solution; □, ADV data for the case B2.

As indicated in figure 2.2, ADV data were also collected 4.4 m downstream from the PIV measurement location and 2 cm above the bottom. The sampling frequency is 40 Hz and measurement volume is a circular cylinder with 6 mm diameter and 7 mm height. The experimental data for the horizontal velocity component agree very well with the theoretical solution (2.37) (see figure 2.4). On the other hand, discrepancies between the experimental data for the vertical velocity and the theoretical result (2.38) are visible. However, the expected trend is clearly captured by the ADV data and the amplitudes agree to within the uncertainty of the measurement (5 mm $\sec^{-1}$). Close examination of the vertical rotational velocity component (2.21) reveals that its contribution to the total

vertical velocity (2.14) at the ADV measurement location is too small to explain the discrepancies shown in figure 2.4. Similar good agreement is also observed for the other two cases.

2.3.4 PIV analysis procedure

The primary objective of the experiments was to measure the velocity field inside the bottom boundary layer under the solitary wave. The resolution of the measurements must be sufficient that the bed shear stress can be accurately calculated.

The flow was seeded with hollow glass spheres (Potters Industries Spheriçel 110P8; specific gravity $\gamma \approx 1.1$) and the field of view (FOV) of the image area was illuminated with a Spectra Physics PIV400-30 Nd:YAG laser system (300 mJ pulse^{-1}, 60 Hz dual head system). By passing the laser beam through a cylindrical lens, a light sheet was formed, which was delivered from below the tank bottom to avoid disturbances from the free surface. The FOV was set parallel to the sidewalls and slightly off the tank centerline to increase image magnification (and thereby decreased the size of the FOV). The FOV was 15 cm from the nearest sidewall and the effects of the sidewall boundary layer are not significant. For all of the experimental cases, the image acquisition system was triggered to capture image pairs for subsequent cross-correlation analysis with 2.00 ms time delay. Images were collected with an SMD 1M60-20 camera (12 bits pixel^{-1}, 60 Hz, 1024×1024 pixel) at 30 Hz, yielding a velocity field rate of 15 Hz. A cylindrical lens (TSI) with focal length $f = -50.0$ mm was used and the square FOV had side length 20 mm. A more detailed description of the PIV

Table 2.2: Optimal and measured PIV parameters.

Parameter	Optimal values	Experiments
Particle diameter (pixels)	2.0 - 4.0	2.0 - 4.0
Dynamic range (counts)	> 50	> 200
Seeding density (per 32 by 32 sub-window)	> 10	> 10
Out-of-plane fraction	< 0.15	-
Displacement gradient	< 3	-

technique can be found in Cowen & Monismith (1997) and Cowen *et al.* (2003).

Following Cowen & Monismith (1997), the images were preprocessed by removing the global minimum value across the image sets (180 images per experiment). This significantly reduces the effects of glare at the bed and allows excellent displacement measurements right up to the bed. For the sub-pixel displacement estimator, a three-point Gaussian estimator was used, and the result did not show peak-locking. In addition, Cowen & Monismith (1997) suggested optimal values for several parameters so as to obtain high-quality PIV data; these criteria were met in the current experiments as seen in table 2.2, in which *dynamic range* is defined by the difference in mean maximum particle light intensity and the mean background light intensity. Though the out-of-plane fraction is not estimated here, its effect should be negligible considering the geometry of the flow of interest.

While the time delay between the images of a pair was set at 2.00 ms to minimize the effects of shear, it was recognized that shear still would be a significant issue in the boundary layer. Further, since the goal is to make highly accurate

measurements to allow the direct determination of the gradient, a rectangular interrogation subwindow with long dimension in the horizontal was utilized (128×8 pixel with 75% overlap) which yielded 29 subwindows in the horizontal, 487 in the vertical (0.6 mm horizontal and 0.04 mm vertical resolution). This allows long displacements in the horizontal to be resolved while minimizing the negative impacts on the correlation due to vertical gradients.

Spurious vectors were flagged using an adaptive Gaussian window filter where all returned velocities at a given elevation above the bed are assumed to be homogeneous. The procedure is as follows. First, based on the sample size (initially, $N = 29$ in each row), statistics are calculated to set a threshold, beyond which vectors are removed. Then statistics are recalculated until there is convergence. This filter rejected 20% of the returned data. However, more than 11,000 data points remain. No attempt is made to smooth or interpolate the original data at this point.

Typical PIV results are shown in figure 2.5, in which velocity vectors under the wave crest ($\xi \approx 0$) and those during flow reversal are plotted. Note that the PIV data was plotted only at every other measurement position in the vertical direction. One can observe that the horizontal motion dominates the flow and that the velocity appears to be homogeneous in the horizontal direction within the scale of the FOV. Indeed, the standard deviation is less than 1% of the mean velocity at a given vertical location. In the following discussions, hence, the PIV data are averaged along the wave propagation direction within the FOV.

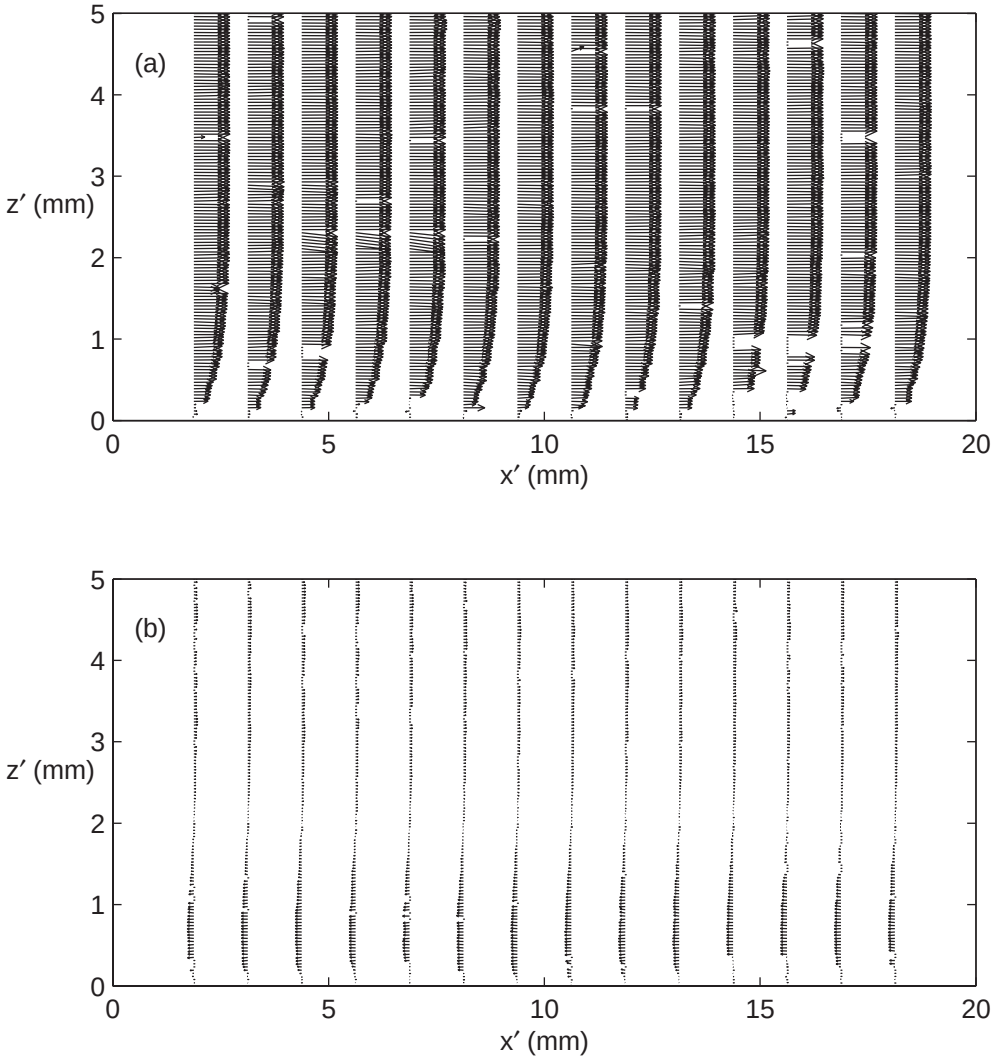

Figure 2.5: Typical results of the PIV analysis for the case B2. (*a*) $\xi = -0.01$ for which $U' \approx 0.17$ m sec^{-1}; (*b*) $\xi = 0.37$ for which $U' \approx 0.02$ m sec^{-1}. Note that only an eighth of the total velocity vectors are shown.

Table 2.3: 95% uncertainty interval of the PIV velocity measurements for the case B1 (numbers in $\mathrm{mm\,sec^{-1}}$).

		u'	Bias	Random	Total	Total (%)
$\xi = -0.21$	$\eta = 0.5$	23.03	±0.58	±0.62	±0.85	±3.68
	$\eta = 1.0$	28.23	±0.71	±0.36	±0.79	±2.81
	$\eta = 2.0$	29.14	±0.73	±0.21	±0.76	±2.60
$\xi = 0.03$	$\eta = 0.5$	47.58	±1.19	±0.57	±1.32	±2.77
	$\eta = 1.0$	63.64	±1.59	±0.34	±1.63	±2.56
	$\eta = 2.0$	72.90	±1.82	±0.67	±1.94	±2.67
$\xi = 0.33$	$\eta = 0.5$	-12.71	±0.32	±0.87	±0.93	±7.32
	$\eta = 1.0$	-9.82	±0.25	±0.33	±0.41	±4.23
	$\eta = 2.0$	1.62	±0.04	±0.50	±0.50	±31.15
$\xi = 0.66$	$\eta = 0.5$	-9.01	±0.23	±0.33	±0.40	±4.41
	$\eta = 1.0$	-10.92	±0.27	±0.47	±0.54	±4.98
	$\eta = 2.0$	-8.43	±0.21	±0.56	±0.60	±7.10

2.3.5 Uncertainty analysis for the PIV velocity measurements

Uncertainty in the PIV measurements consists of bias and random errors (Cowen, 1996). The former is mainly related to the optical calibration of the PIV system, which is accurate within 0.5 mm. This gives a worst case bias error of ±2.5% in u. To estimate the random errors, the bootstrap percentile technique (Efron & Tibshirani, 1993) was used and the 95% confidence interval of the horizontally averaged velocity at each temporal location and vertical location was determined. Note that each data set was resampled 2000 times in the analysis, and the 95% confidence interval was taken directly from the 50th and

Table 2.4: 95% uncertainty interval of the PIV velocity measurements for the case B2 (numbers in $\mathrm{mm\,sec^{-1}}$).

		u'	Bias	Random	Total	Total (%)
$\xi = -0.20$	$\eta = 0.5$	62.65	±1.57	±1.02	±1.87	±2.99
	$\eta = 1.0$	72.91	±1.82	±0.86	±2.02	±2.77
	$\eta = 2.0$	78.47	±1.96	±1.90	±2.73	±3.48
$\xi = -0.01$	$\eta = 0.5$	121.28	±3.03	±1.40	±3.34	±2.76
	$\eta = 1.0$	156.33	±3.91	±0.46	±3.94	±2.52
	$\eta = 2.0$	174.33	±4.36	±0.34	±4.37	±2.51
$\xi = 0.37$	$\eta = 0.5$	-30.32	±0.76	±0.57	±0.95	±3.12
	$\eta = 1.0$	-19.78	±0.49	±0.47	±0.68	±3.46
	$\eta = 2.0$	8.39	±0.21	±0.44	±0.49	±5.87
$\xi = 0.70$	$\eta = 0.5$	-17.81	±0.45	±0.82	±0.94	±5.26
	$\eta = 1.0$	-21.53	±0.54	±0.36	±0.65	±3.01
	$\eta = 2.0$	-11.69	±0.29	±0.15	±0.33	±2.82

1950th ordered bootstrap generated mean statistics.

Typical results for each of the experimental cases are listed in tables 2.3–2.5. In general, the uncertainty during the deceleration phase of the solitary wave ($\xi > 0$) is higher than that of the acceleration phase ($\xi < 0$). Also, for $\xi < 0$, higher uncertainty is observed near the bottom. For $\xi \approx 0.3$, very high relative errors are seen outside the boundary layer ($\eta = 2.0$) in tables 2.3 & 2.5, but that is because the velocity is close to 0.

Table 2.5: 95% uncertainty interval of the PIV velocity measurements for the case B3 (numbers in $\mathrm{mm\,sec^{-1}}$).

		u'	Bias	Random	Total	Total (%)
$\xi = -0.22$	$\eta = 0.5$	91.48	±2.29	±2.20	±3.17	±3.47
	$\eta = 1.0$	103.63	±2.59	±1.35	±2.92	±2.82
	$\eta = 2.0$	107.77	±2.69	±3.28	±4.25	±3.94
$\xi = 0.03$	$\eta = 0.5$	154.87	±3.87	±2.16	±4.43	±2.86
	$\eta = 1.0$	213.50	±5.34	±1.39	±5.52	±2.58
	$\eta = 2.0$	234.98	±5.87	±1.50	±6.06	±2.58
$\xi = 0.39$	$\eta = 0.5$	-41.40	±1.04	±0.58	±1.19	±2.87
	$\eta = 1.0$	-22.30	±0.56	±0.63	±0.84	±3.77
	$\eta = 2.0$	-0.90	±0.02	±0.82	±0.82	±91.41
$\xi = 0.70$	$\eta = 0.5$	-27.14	±0.68	±1.02	±1.23	±4.53
	$\eta = 1.0$	-32.57	±0.81	±0.50	±0.95	±2.93
	$\eta = 2.0$	-27.63	±0.69	±0.70	±0.99	±3.57

2.3.6 Experimental measurements and theoretical results

The vertical profiles of the horizontal velocity inside the boundary layer are shown in figures 2.6–2.8 respectively for each experimental case.

It is remarkable that the difference between the linear boundary layer solutions and the nonlinear solutions is very small. Indeed the wavelength is orders-of-magnitude larger than the water depth, so the flow is almost uniform in the horizontal direction within the length-scale. In other words, the nonlinear inertia terms are very small even with high nonlinearity under the experimental

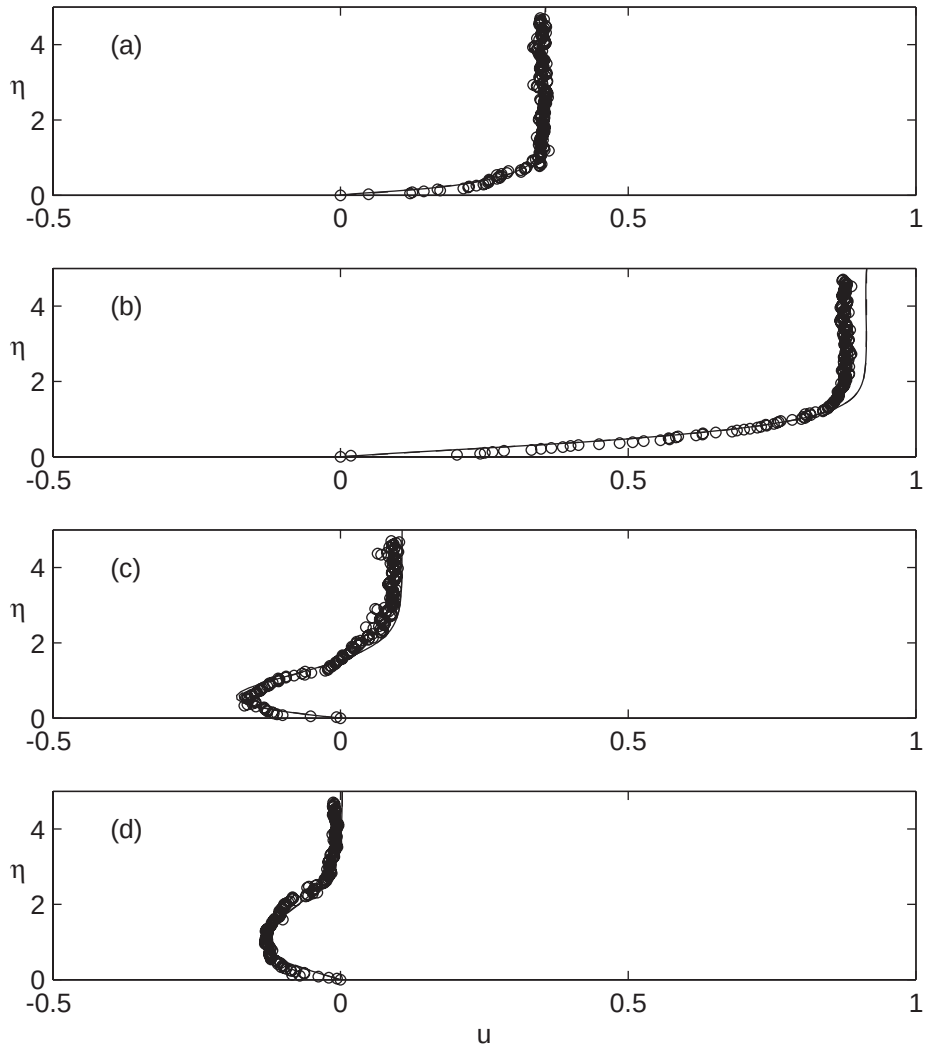

Figure 2.6: Vertical profiles of the dimensionless horizontal velocity for the case B1: ——, the numerical solution of the nonlinear boundary layer equation; – – – – –, the analytical solution of the linear boundary layer equation; ∘, PIV data. (*a*) $\xi = -0.21$; (*b*) $\xi = 0.03$; (*c*) $\xi = 0.33$; (*d*) $\xi = 0.66$.

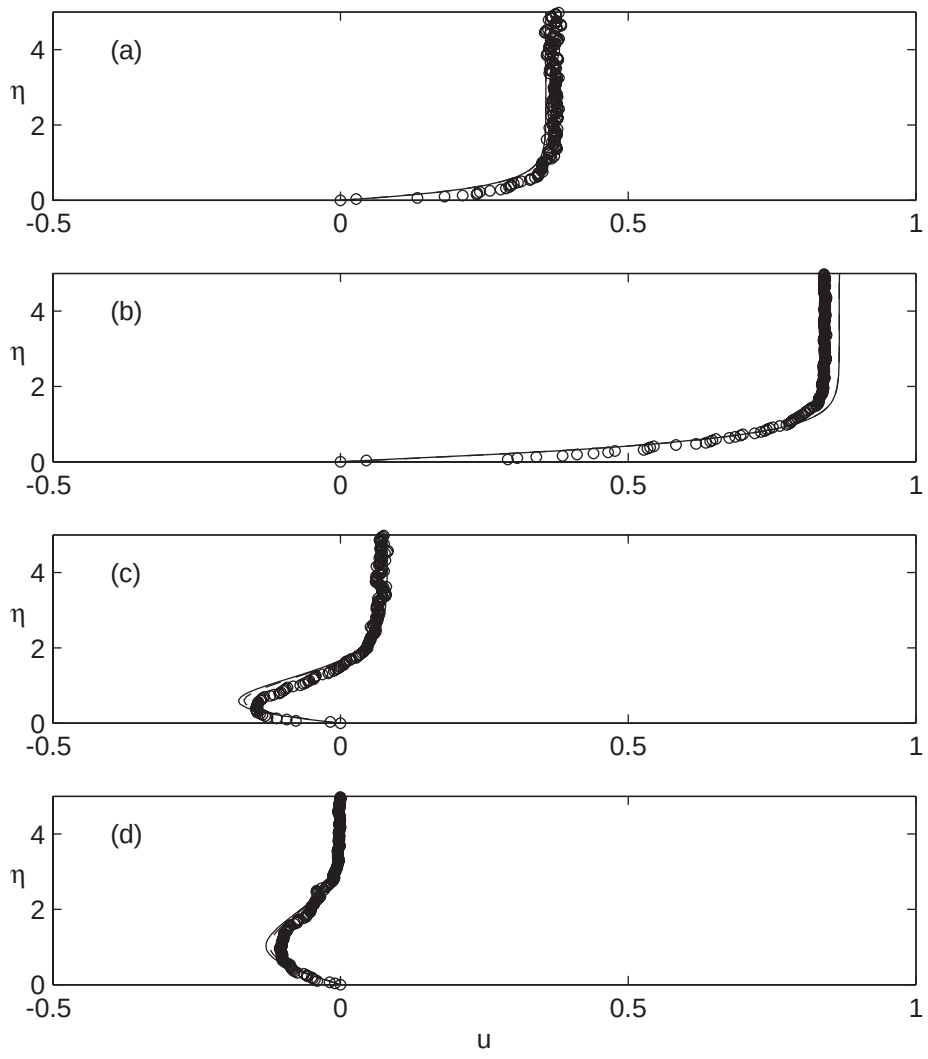

Figure 2.7: Vertical profiles of the dimensionless horizontal velocity for the case B2: ——, the numerical solution of the nonlinear boundary layer equation; − − − − −, the analytical solution of the linear boundary layer equation; ∘, PIV data. (*a*) $\xi = -0.20$; (*b*) $\xi = -0.01$; (*c*) $\xi = 0.37$; (*d*) $\xi = 0.70$.

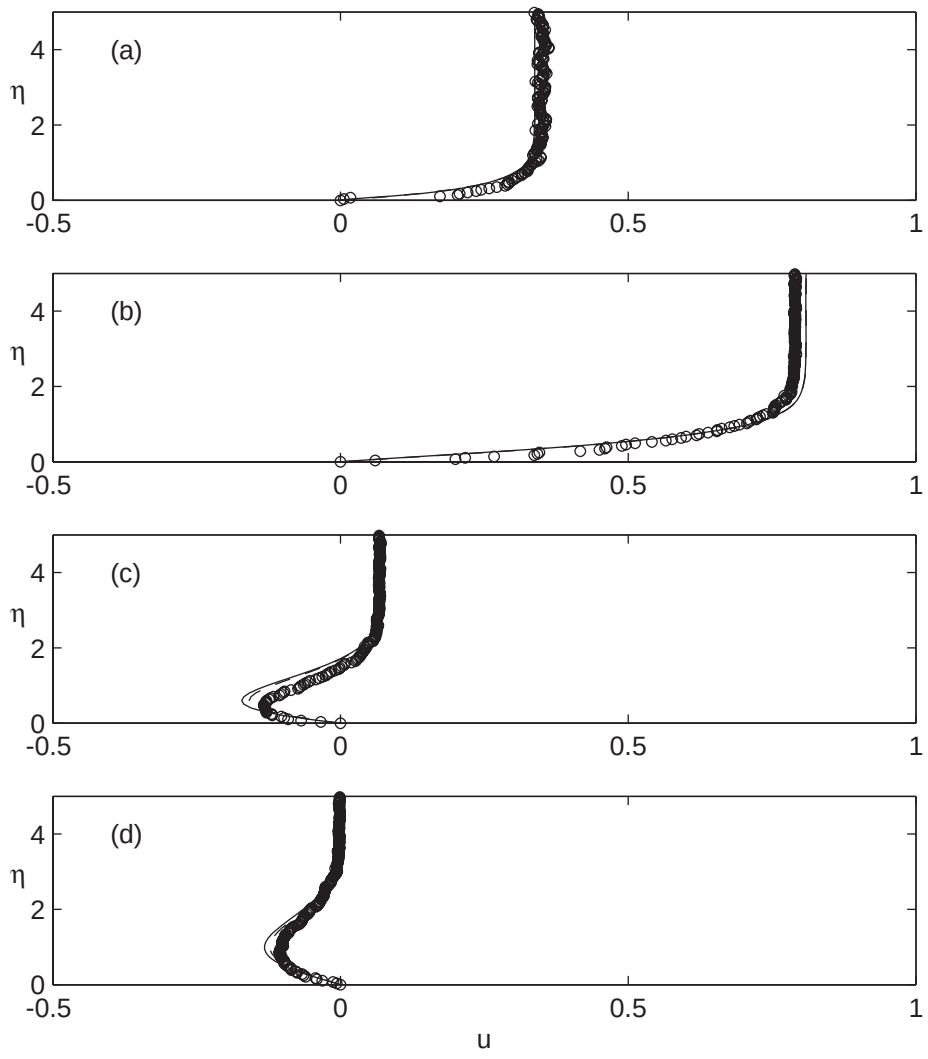

Figure 2.8: Vertical profiles of the dimensionless horizontal velocity for the case B3: ——, the numerical solution of the nonlinear boundary layer equation; – – – – –, the analytical solution of the linear boundary layer equation; ∘, PIV data. (*a*) $\xi = -0.22$; (*b*) $\xi = 0.03$; (*c*) $\xi = 0.39$; (*d*) $\xi = 0.70$.

conditions. To observe effects of nonlinearity, one would need at least an order-of-magnitude larger water depth.

In the first two panels (*a* & *b*) in each of figures 2.6–2.8, the flow at the outer edge of the boundary layer is accelerating and reaches the maximum value under the wave crest. During the accelerating phase the horizontal velocities inside the boundary layer are moving in the same direction as wave propagation. On the other hand, as the wave crest passes the measurement location, the last two panels of each figure (*c* & *d*), the velocity starts to decrease. The horizontal velocity inside the boundary layer reverses its direction starting from the bottom in response to the unfavorable pressure gradient and diffuses upward into the entire boundary layer. Overall, the agreement between the theoretical prediction and the experimental measurement is very good.

In figures 2.9–2.11 the time histories of the horizontal velocity at different vertical locations are shown. The flow reversal inside the boundary layer during the deceleration phase is clearly demonstrated for all the experimental cases. Note that the flow reversal always occurs earlier near the bottom. Also, closer to the bottom, the positive velocities are smaller. Again general agreement of the experimental data with the theoretical solution is observed for all the experimental cases.

As mentioned before, one of the most significant consequences of the flow reversal, caused by flow deceleration, is that the bed shear stress changes direction. In other words, the bed shear stress has the opposite sign to the free-stream velocity, defined as the horizontal velocity at the outer edge of the boundary layer. The theoretical predictions are compared with estimates from PIV data near the bottom (see figures 2.12–2.14). The experimental results are obtained

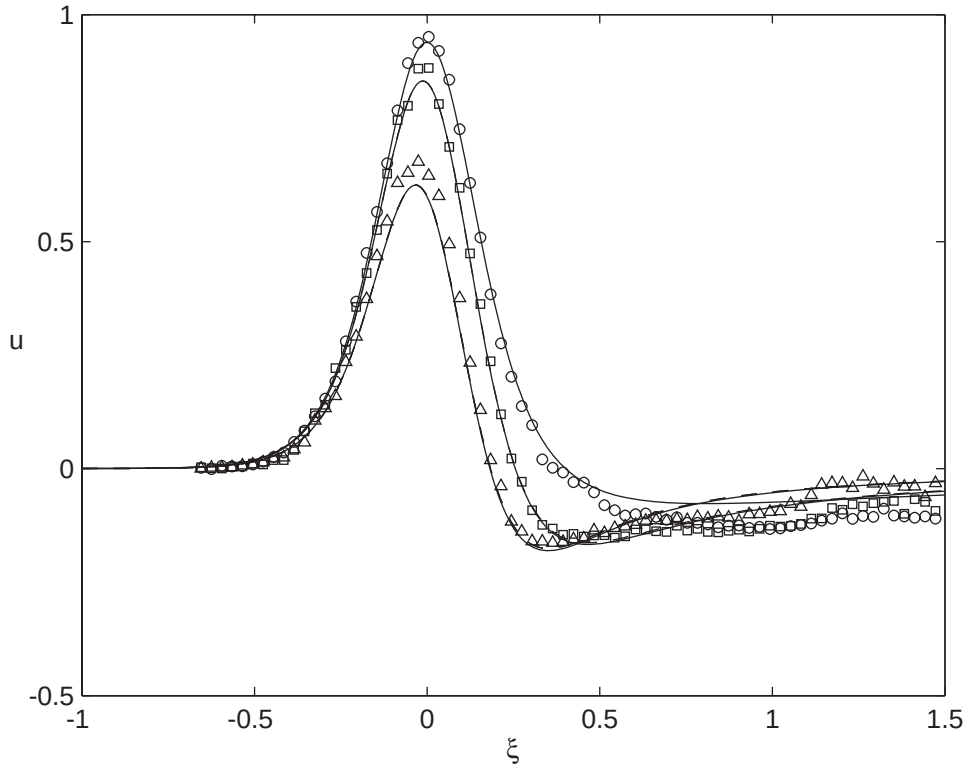

Figure 2.9: Time histories of the dimensionless horizontal velocity for the case B1: ——, the numerical solution of the nonlinear boundary layer equation; − − − − −, the analytical solution of the linear boundary layer equation; △, PIV data at $\eta = 0.5$; □, PIV data at $\eta = 1.0$; ∘, PIV data at $\eta = 2.0$.

by least-square fitting a straight line through eight data points (within 0.3 mm) above the bed. As may be seen in figure 2.5, where the velocity vectors are plotted only at every other measurement position in the vertical direction, the resolution of the PIV data is high enough to accurately estimate the gradient of horizontal velocity near the bottom. Generally good agreement of the experimental data with the theoretical solutions is observed.

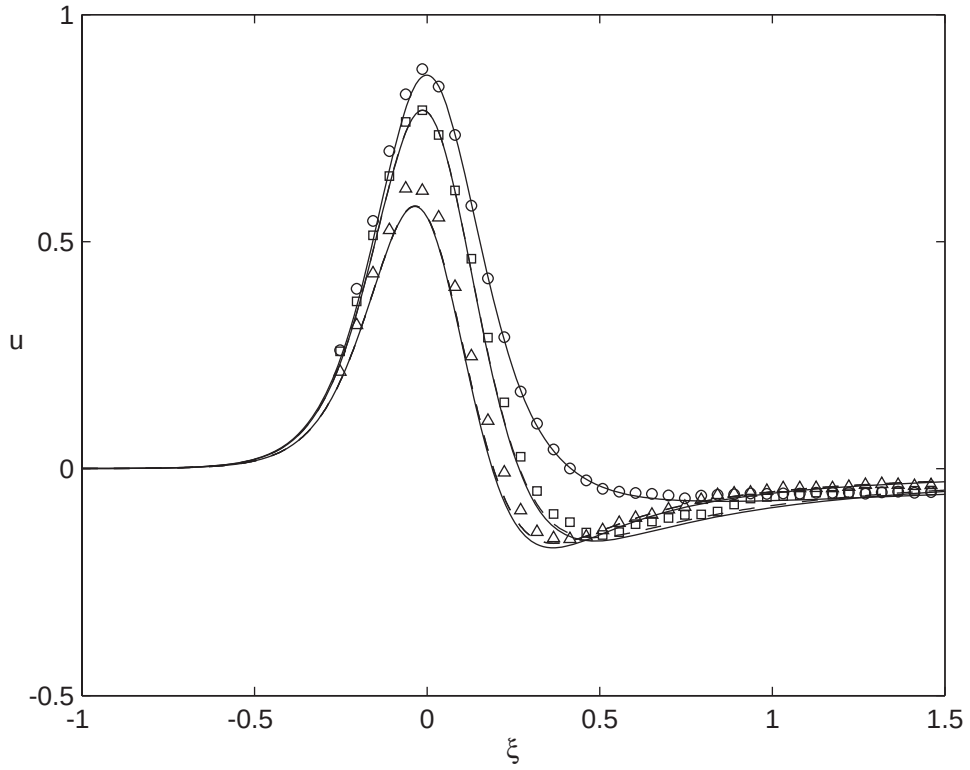

Figure 2.10: Time histories of the dimensionless horizontal velocity for the case B2: ——, the numerical solution of the nonlinear boundary layer equation; – – – – –, the analytical solution of the linear boundary layer equation; △, PIV data at $\eta = 0.5$; □, PIV data at $\eta = 1.0$; ∘, PIV data at $\eta = 2.0$.

2.3.7 Mass transport inside the boundary layer

With the identification of the reverse flow within the boundary layer, a natural question arises regarding the resultant net displacement profile of water parcels. The displacement of water parcels can be expressed as an integral equation:

$$x(t) = x_0 + \int_{t_0}^{t} u(x(s), s)\ \mathrm{d}s, \tag{2.43}$$

where all quantities are appropriately non-dimensionalized. Assuming that the vertical velocity component is negligible, net displacements at four differ-

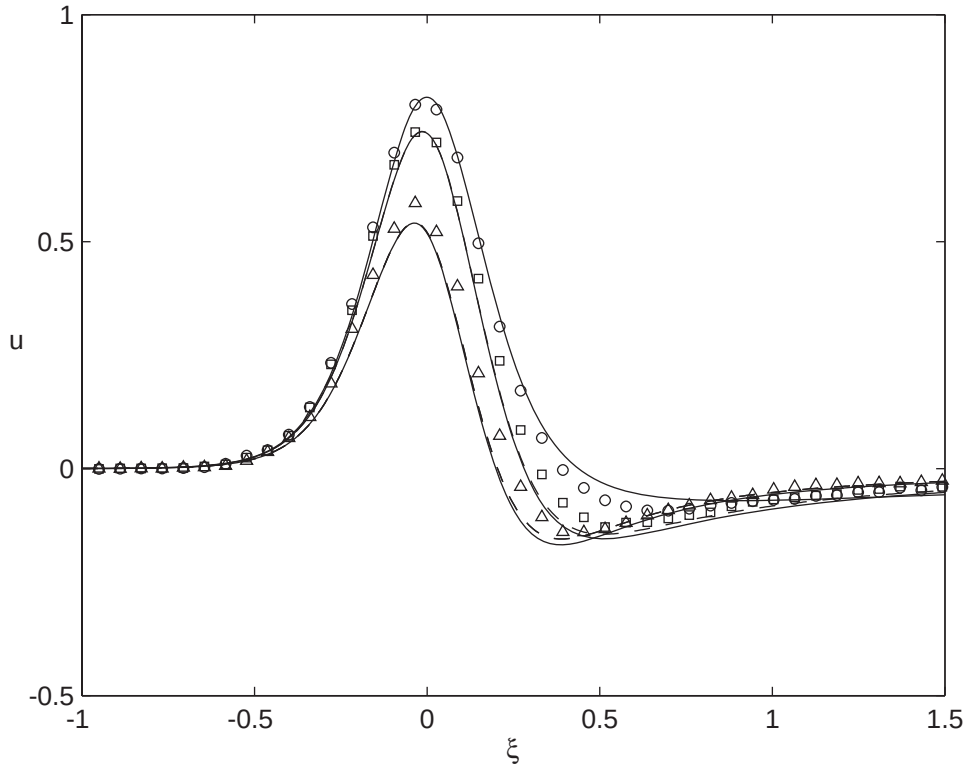

Figure 2.11: Time histories of the dimensionless horizontal velocity for the case B3: ——, the numerical solution of the nonlinear boundary layer equation; – – – – –, the analytical solution of the linear boundary layer equation; △, PIV data at $\eta = 0.5$; □, PIV data at $\eta = 1.0$; ○, PIV data at $\eta = 2.0$.

ent vertical positions have been calculated using the fourth-order Runge–Kutta method.

For example the results for the case B2 are ploted in figure 2.15, in which the net displacements are always positive. That is, even though the reverse flow occurs, it is not strong enough to cause a net negative displacement at any elevation within the boundary layer.

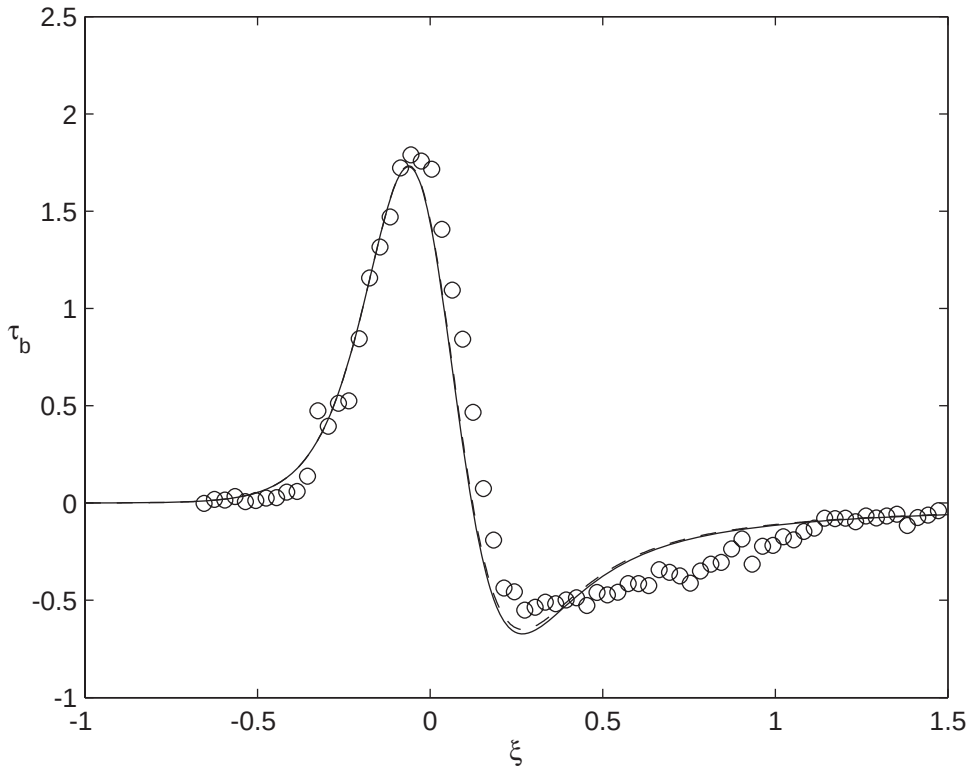

Figure 2.12: Time history of the dimensionless bed shear stress for the case B1: ——, the numerical solution of the nonlinear boundary layer equation; − − − − −, the analytical solution of the linear boundary layer equation; ◯, PIV data.

2.4 Laminar boundary layer flows of general long waves

So far it has been experimentally shown that the solution of (2.17) together with the boundary conditions (2.18 & 2.19) accurately describes the structure of the boundary layer under a solitary wave. In principle, the theoretical results are also valid for any other kind of wave loading in shallow water. In this section, two cases will be considered: (i) two successively generated solitary waves, and (ii) periodic cnoidal waves.

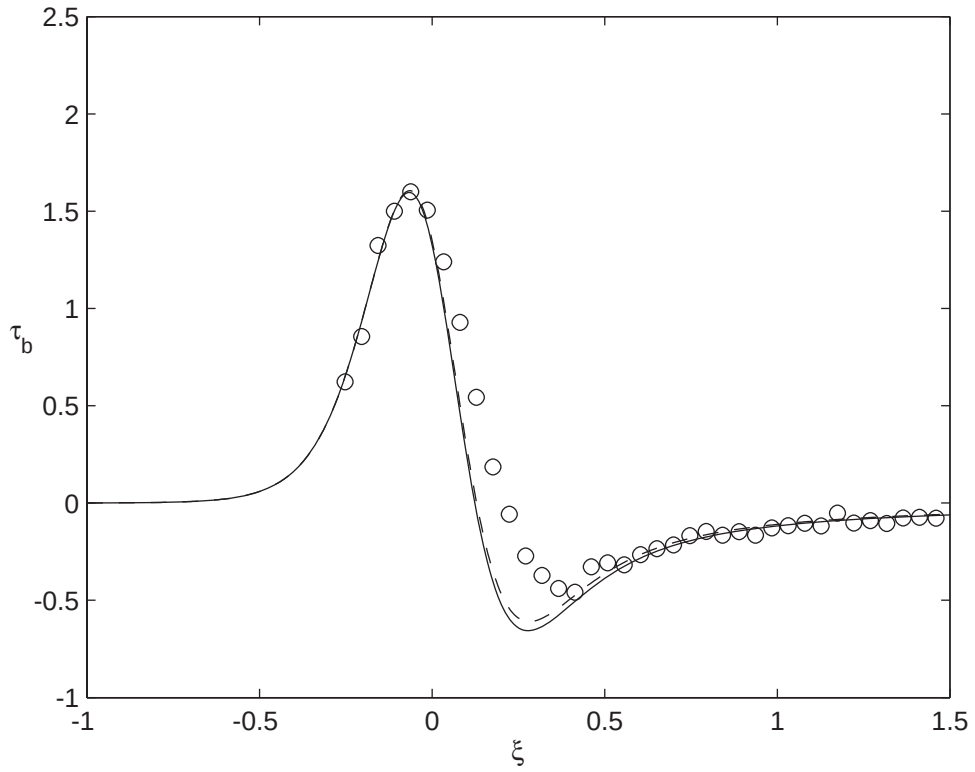

Figure 2.13: Time history of the dimensionless bed shear stress for the case B2: ——, the numerical solution of the nonlinear boundary layer equation; − − − − −, the analytical solution of the linear boundary layer equation; ◯, PIV data.

2.4.1 A train of two successive solitary waves

During the course of experiments discussed in the previous section, an additional measurement was made by generating the two almost identical solitary waves.

The trajectory of the wave maker paddle to generate a train of solitary waves can be approximated by an array of the identical trajectories for a single solitary wave such as the one in figure 2.1(a). Time separation between the crests can be adjusted by pausing the wave maker for a desired period of time between each

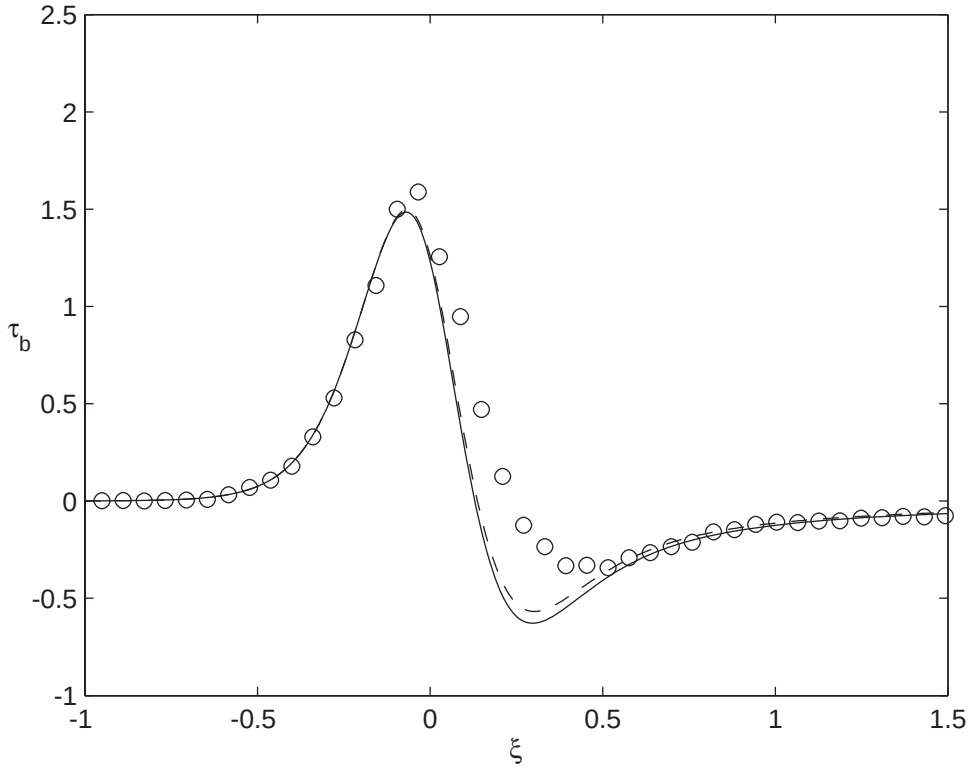

Figure 2.14: Time history of the dimensionless bed shear stress for the case B3: ——, the numerical solution of the nonlinear boundary layer equation; – – – – –, the analytical solution of the linear boundary layer equation; ◯, PIV data.

trajectory. Without pausing, the minimum separation would be the same as the wave period. The process may be repeated to generate more solitary waves in the train. In practice, however, the maximum number of waves is limited by the stroke length of the wave maker paddle.

The paddle trajectory for the experimental case is plotted in figure 2.16. Since each wave resembles the one used in the case B2 (see table 2.1), the result is normalized in the same way as the case B2 in the following discussion.

In figure 2.17, the free-stream velocity is compared with the sum of the two

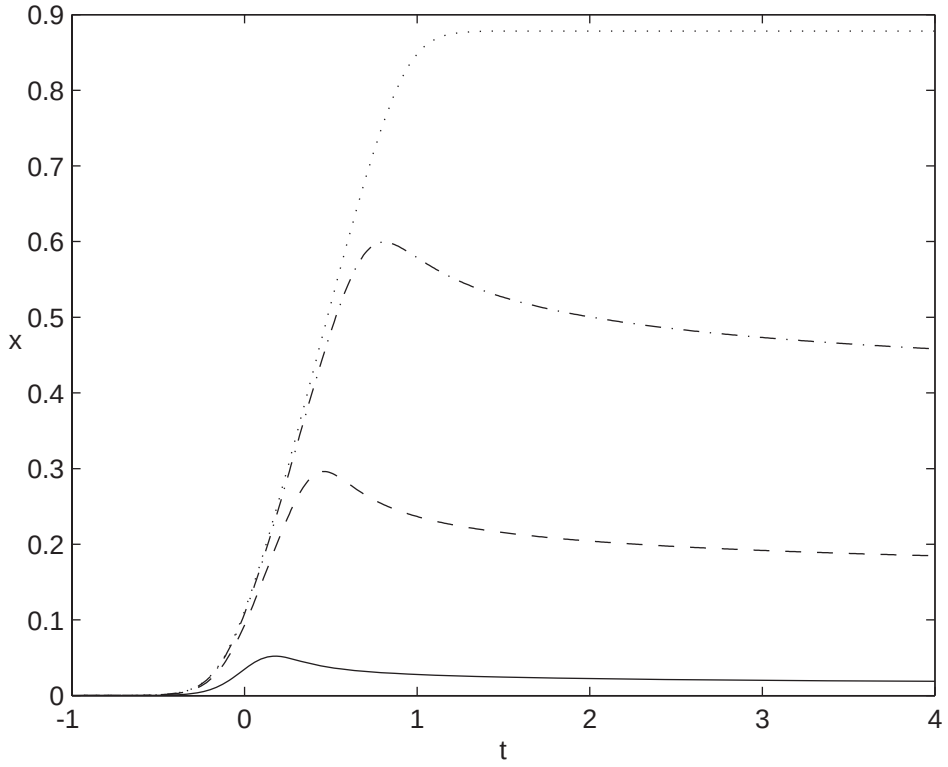

Figure 2.15: Net horizontal displacements of particles initially located at four different vertical positions for the case B2. ——, $\eta = 0.1$; – – – – –, $\eta = 0.5$; —·—, $\eta = 1.0$; · · · · ·, $\eta = 10.0$.

identical solitary wave solutions (2.37), one of which is centered at $\xi = 0$ and the other at $\xi = 1$. Though the second wave is slightly smaller, the agreement between the experimental measurement and the theoretical solution is good.

Then the theoretical solution is substituted to (2.22) to calculate the bed shear stress. Note that the solution of the linearized boundary layer equation is used in view of the results in the previsous section where the difference between the linear and the nonlinear solutions was negligible. Figure 2.18 shows the result. Again the agreement is encouraging.

It appears, however, that the theory overpredicts the bed shear stress dur-

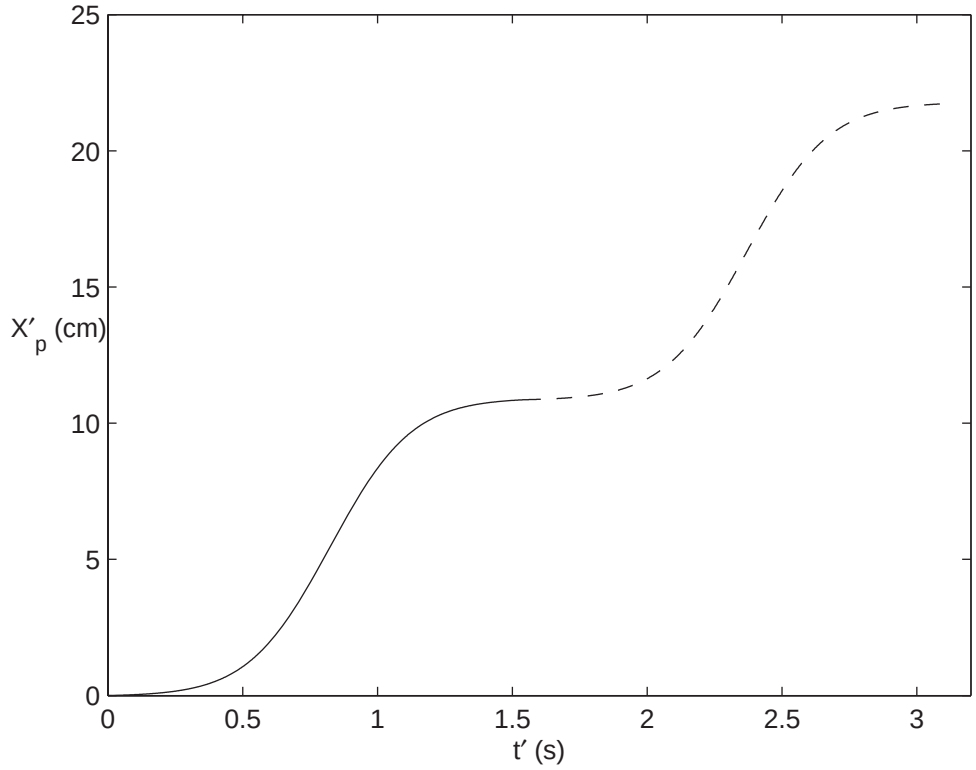

Figure 2.16: The trajectory of the wave maker paddle to generate two successive solitary waves with the minimum time separation between the crests ($\epsilon = 0.2$ in $h' = 10$ cm): ——, paddle trajectory for the first wave; −−−−−, paddle trajectory for the second wave.

ing the deceleration phase. Similar observation can also be made in cases with single solitary wave (figures 2.12–2.14). In general, experimental uncertainty is amplified when the gradient is to be calculated. Furthermore, especially in the beginning of the flow reversal, the linear curve-fitting of multiple data points can result in underestimated shear stress. Indeed the coefficient of determination (R-square value) drops below 0.5 for $\xi \approx 0.25$ and $\xi \approx 1.25$, while it is close to 1 otherwise. For clarification, experimental data with even more accuracy or direct measurement of shear stress may be required.

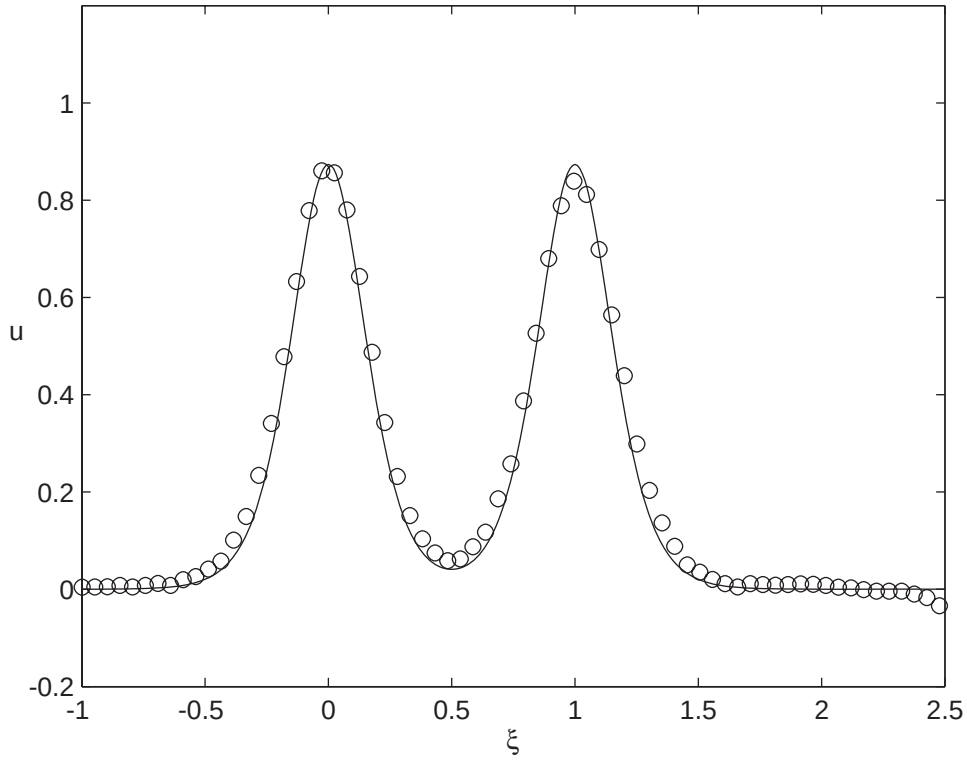

Figure 2.17: Time history of the dimensionless free-stream velocity (2 cm above the bottom) for the case of two successively generated solitary waves: ——, the sum of the two solitary wave solutions (2.37), one at $\xi = 0$ and the other at $\xi = 1$; ◯, PIV data.

2.4.2 Cnoidal waves

The cnoidal wave is the periodic solution to the KdV equation that is weakly nonlinear and weakly dispersive (e.g. Miles, 1981). More description on this wave will be given in §3.2.5 and here the focus is on the shear stress measurement under the flow similar to a cnoidal wave.

Sana *et al.* (2006) measured boundary layer flows under asymmetric cnoidal-like wave forcing in an oscillating tunnel. In this set-up, the horizontal velocity is indeed uniform except near both ends of the horizontal section of the tunnel,

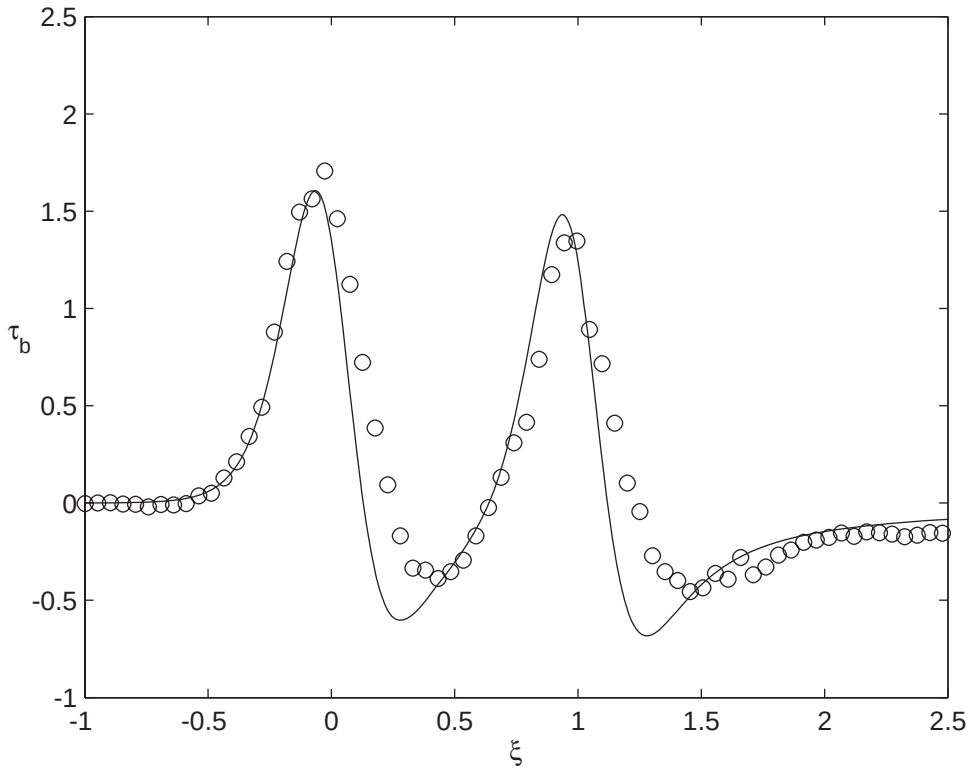

Figure 2.18: Time history of the dimensionless bed shear stress for the case of two successively generated solitary waves: ——, the analytical solution of the linear boundary layer equation; ◯, PIV data.

thus the linearized boundary layer equation becomes exact. For the case 2 in their experiment, Sana *et al.* (2006) provided the velocity at the axis of symmetry of the tunnel as well as the bed shear stress as a function of time. Here, the experimental data are compared with the theoretical solution (2.22).

The free-stream velocity is approximated by a Fourier series truncated after 15 terms (see figure 2.19). In figure 2.20, the experimental measurements of the shear stress are compared with the theoretical solution using the curve-fitted expression of the free-stream velocity. The agreement between the analytical solution and the experimental data is excellent.

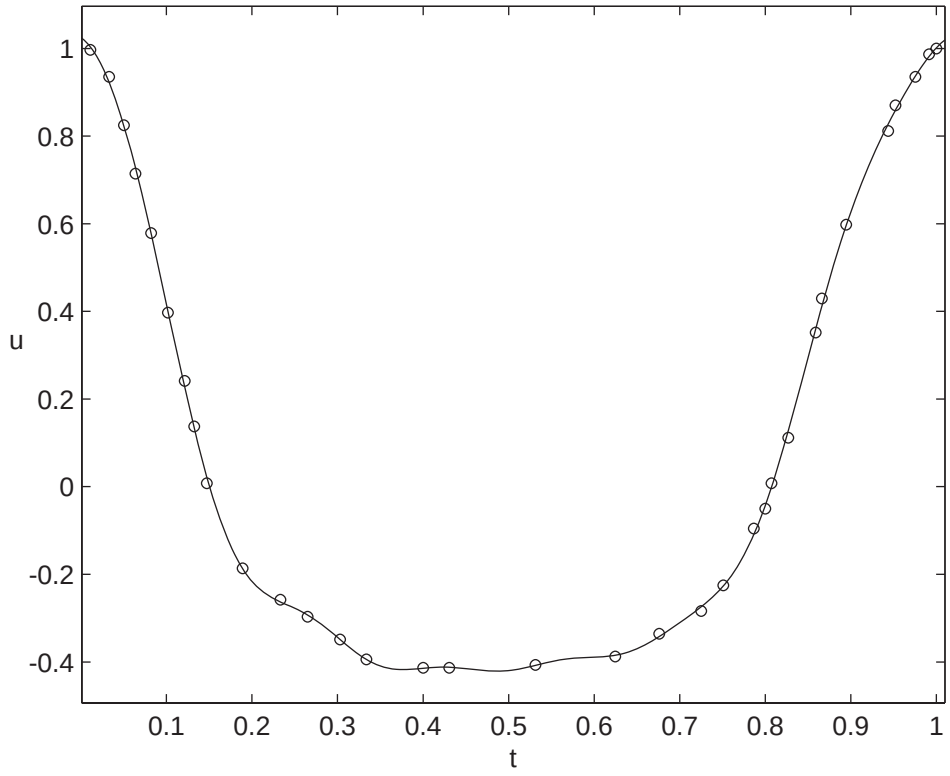

Figure 2.19: Time history of the phase-averaged dimensionless free-stream velocity of a cnoidal-like wave: ∘, measured data by Sana *et al.* (2006); ——, the least-square fitted curve using a Fourier series truncated after 15 terms.

2.5 Concluding remarks

In this chapter, the laminar bottom boundary layer flows under long waves have been examined both theoretically and experimentally. Most importantly, the horizontal velocity inside the boundary layer is not always in phase with the free-stream velocity and a flow reversal starts at the bed as the flow at the outer edge of the boundary layer begins to decelerate. Consequently, the bed shear stress also changes direction. Due to the long horizontal length-scale, the velocities under the long waves are practically uniform in the horizontal direction,

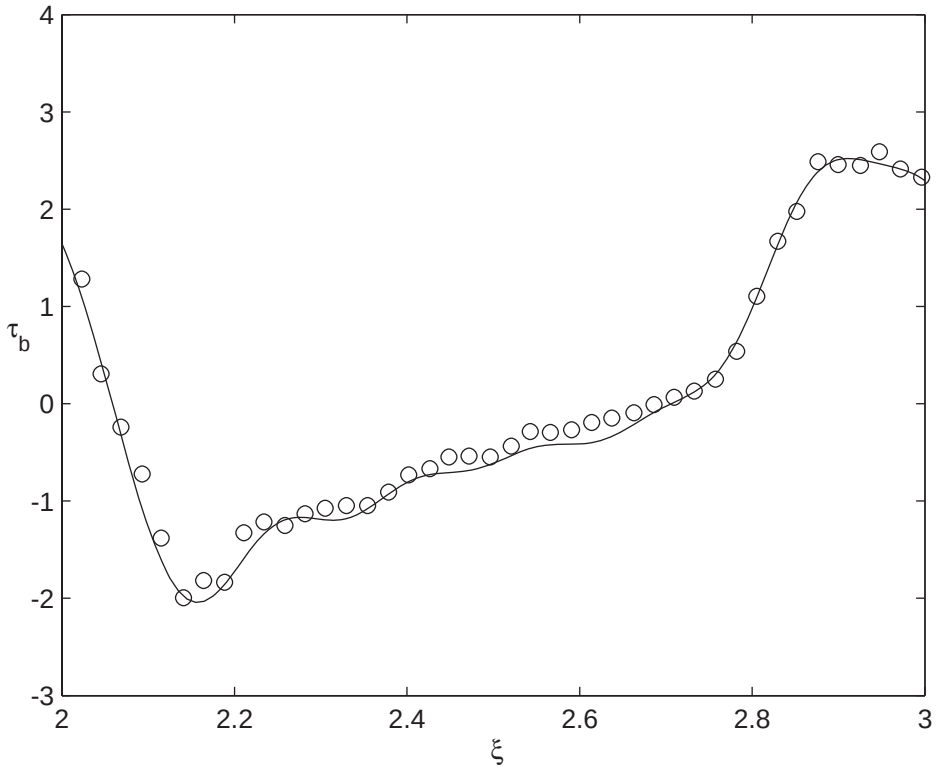

Figure 2.20: Time history of the dimensionless bed shear stress under a cnoidal-like wave forcing: ——, the analytical solution of the linear boundary layer equation; ◯, experimental data by Sana *et al.* (2006).

thus the nonlinear convective acceleration term in the momentum conservation equation seems to be negligible even with a large nonlinearity for the cases considered herein.

While this work provides the first measurements of detailed velocity fields inside the laminar boundary layer under solitary waves, more theoretical and experimental researches on turbulent boundary layer are needed.

Assuming that the eddy viscosity for a fully developed turbulent boundary layer flow is a power function of the elevation from the bed, Liu (2006)

derived approximate analytical solution for the turbulent flow velocities under long waves. In particular, Prandtl's power-law formulas (Prandtl, 1952) are used, which are valid for steady turbulent boundary layers up to Reynolds number 10^5 with negligible pressure gradients. Certainly, flows of interest here are neither steady nor pressure-gradient-free. Though Liu (2006) did not mention how Prandtl's theory for a steady-state boundary layer can be applied to unsteady flows, earlier Patel (1977) showed that the mean flow and turbulent intensity distributions are quite insensitive to the free-stream oscillations in his measurements with traveling waves. Moreover Jensen, Sumer & Fredsøe (1989) also observed log-law regions in oscillatory turbulent boundary layers, which were in good agreement with the corresponding steady boundary layer flows. Furthermore, Liu (2006) showed that his model can explain the decrease of the phase lag in the turbulent boundary layer. Thus there is a possibility that Liu (2006)'s approximate solutions can capture some important physics in spite of the assumptions employed.

Liu & Park (2008) compared the analytical solutions of Liu (2006) with experimental measurements by Sana *et al.* (2006) which is reproduced in figure 2.21. The vertical coordinate in figure 2.21 has been normalized by the boundary layer thickness based on the 'effective viscosity' that requires the use of the friction velocity. Since the friction velocity depends on the free-stream velocity, Liu (2006) assigned a constant to simplify his analysis. In figure 2.21, the friction velocity has been chosen by trial-and-error to be 2% of the maximum free-stream velocity. In other words, the effective viscosity can be viewed as a fitting parameter characterizing the turbulent boundary layer flows. Therefore, rigorous experimental investigations are needed to assign either a single number or a functional relationship to the parameter.

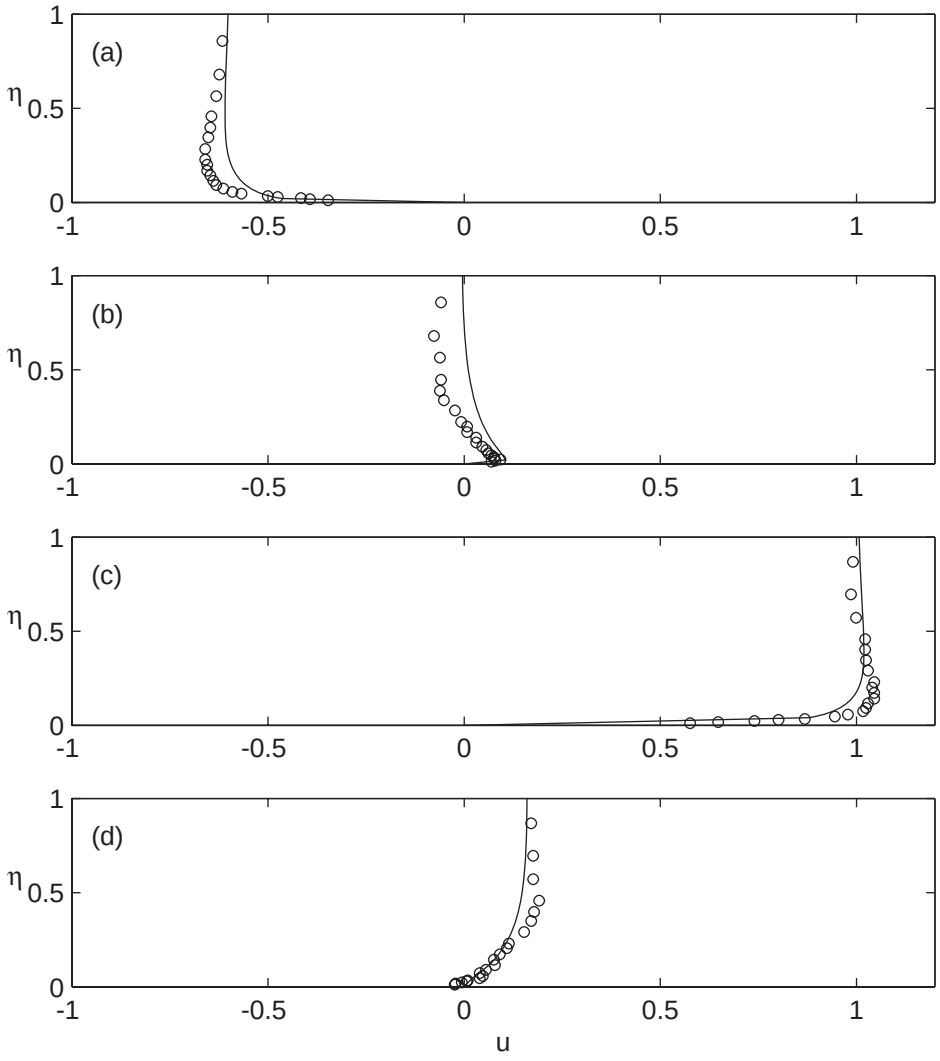

Figure 2.21: Vertical profiles of the dimensionless horizontal velocity inside and above the turbulent boundary layer under cnoidal-like wave: ——, the theoretical results; ∘ measurements by Sana *et al.* (2006). (*a*) $\xi = 2.5$; (*b*) $\xi = 2.8$; (*c*) $\xi = 3.0$; (*d*) $\xi = 3.2$, where wave crests are located at $\xi = 0,\ \pm 1,\ \pm 2,\ \cdots$.

CHAPTER 3

VISCOUS FLOWS IN A MUDDY SEABED

3.1 Introduction

The interactions of propagating water surface waves and seabed sediments, typically in forms of percolation or wave-induced seabed deformation, can result in wave energy attenuation. For the case of soft muddy seabed, in particular, effects of the internal friction are at times so pronounced that waves can be almost completely dissipated within a few wavelengths. For example, the ocean water above the Mud Hole off the coast of Louisiana usually remains calm even during severe storms and therefore the local fishing boats often use it as an emergency harbor (Gade, 1958). Also, mud banks formed during the monsoon season on the southwest coast of India exhibit similar wave-dissipative characteristics and are very important in protecting the beach and in trapping the sediments (Mini-rani & Kurup, 2007). In this and the next chapters, soft deformable seabeds made of cohesive sediments are studied.

Rheological properties of muddy seabed strongly depend on a number of factors such as the physical and chemical composition of constituent materials, concentration and the sea state (see e.g. McAnally *et al.*, 2007*a*,*b*). In addition, muds are most likely to be density-stratified as they are mainly formed as mixture of water and cohesive sediments that naturally sort themselves according to their specific gravities (Winterwerp & van Kesteren, 2004). On one end of the mud rheology spectrum is the elastic solid owing to the internal microscopic structure, while on the other end is the viscous fluid with much higher viscosity than that of water (Gade, 1958). Depending on the geographical location,

time and depth, therefore, the characteristics of muds vary widely. Apparently no single model is known to describe the entire spectrum of the mud rheology. Rather, different models have been applied to different situations, namely elastic (Foda, 1989; Wen & Liu, 1995), viscous (Gade, 1958; Dalrymple & Liu, 1978; Liu & Chan, 2007) or viscoelastic (MacPherson, 1980; Jain & Mehta, 2009) to name a few. The focus in this chapter is on the viscous muddy seabed. It will be shown that approaches and results presented in the previous chapter can be extended to the viscous fluid-mud problem with slight modification.

Gade (1958) studied the damping of water surface waves over a Newtonian fluid-mud within the framework of the linear wave theory. The water was assumed inviscid and only the shallow water wave was considered. It was shown that the thickness of the mud layer normalized by the Stokes boundary layer thickness ($\overline{d}$ as defined in §3.2) based on the mud viscosity is an important parameter that characterizes the rate of wave damping and the associated seabed dynamics. Interestingly, the damping rate achieves the maximum for $\overline{d} \approx 1.2$. Later Dalrymple & Liu (1978) extended the theory by removing the limitation on water depth and including the viscosity of water. They also confirmed the critical role of $\overline{d}$ in seabed dynamics and observed the maximum wave attenuation rate for $\overline{d} \sim O(1)$.

More recently, Liu & Chan (2007) derived a set of Boussinesq-type equations for transient long waves with the effects of a viscous muddy seabed. In their derivation, three major assumptions were made: (i) the mud bed is characterized as a viscous fluid and its viscosity is several orders-of-magnitude higher than that of the water; (ii) the thickness of the mud bed is much less than the characteristic wavelength; and (iii) the displacement of the water–mud interface

is negligible. Notice that the aforementioned assumptions result in the governing equation for the wave-induced flow in the mud layer that is essentially the same as the one used in the previous chapter. One might think that the bottom boundary layer of a viscous fluid, i.e. water in Chapter 2, is now replaced with the mud layer with much higer viscosity and sharp interface. Though Liu & Chan (2007) did not mention, the earlier studies by Gade (1958) and Dalrymple & Liu (1978) suggested that the ratio of the mud layer thickness to its own boundary layer thickness would play an important role also in this context of the weakly nonlinear wave theory. In this chapter, that will be confirmed theoretically and experimentally.

In the next section, the governing equations as well as the boundary conditions will be derived adpating the aforementioned assumptions of Liu & Chan (2007). The analytical solution is available for the linearized equation as shown by Liu & Chan (2007), which will be compared with the numerical solution of the approximate nonlinear equation dervied in this study. In addition, effects of the nonlinearity and those of the mud layer thickness will be investigated in detail. Then, two kinds of experiments have been carried out to validate the theory. The first set of experiments, in which the mud layer thickness is less than its own boundary layer thickness, will be presented in §3.3, while results with the opposite conditions will be examined in §3.4. Finally the concluding remarks will be made in §3.5.

3.2 Theoretical background

As in §2.2, the surface displacement of a long wave is denoted as $\zeta'(x', t')$. The long wave propagates in a constant water depth h' over a viscous mud bed of thickness d'. The same scaling arguments listed in (2.10) as well as the two dimensionless parameters, ϵ and μ defined in (2.11), are also used here. Additionally the velocity components inside the mud bed (u'_m, w'_m) are introduced, which are normalized as follows:

$$u_m = u'_m/\epsilon\sqrt{g'h'}, \quad w_m = w'_m/\alpha\epsilon\sqrt{g'h'}, \tag{3.1}$$

where α is re-defined using the kinematic viscosity of the mud ν'_m:

$$\alpha^2 = \frac{\nu'_m}{l'\sqrt{g'h'}}. \tag{3.2}$$

Notice that, in terms of the stretched vertical coordinate η as defined in (2.15), the undisturbed mud layer occupies the range of $-d \le \eta \le 0$, where

$$d = d'\left(\frac{\sqrt{g'h'}}{\nu'_m l'}\right)^{1/2} \tag{3.3}$$

represents the ratio of the mud bed thickness and the long-wave-induced boundary layer thickness in the mud bed. For an oscillatory flow, a similar quantity can be defined:

$$\overline{d} = \frac{d'}{\delta'_m}, \tag{3.4}$$

where the Stokes boundary-layer thickness of the viscous mud has been defined as

$$\delta'_m = \sqrt{\frac{2\nu'_m}{\omega'}}. \tag{3.5}$$

Comparing (3.3) with (3.4), one can see that

$$d = \overline{d}/\sqrt{\pi}. \tag{3.6}$$

3.2.1 Formulation

If one considers the situation in which the viscosity of the mud is several orders-of-magnitude larger than that of the water, flow motions in the water associated with the long wave can be regarded as inviscid. Assuming that the inviscid water particle velocity components (U, W) are given, the continuity and the horizontal momentum equations in the mud layer can be written as

$$\frac{\partial u_m}{\partial x} + \frac{\partial w_m}{\partial \eta} = 0, \tag{3.7}$$

$$\frac{\partial u_m}{\partial t} + \epsilon\left(u_m \frac{\partial u_m}{\partial x} + w_m \frac{\partial u_m}{\partial \eta}\right) = -\frac{1}{\gamma}\frac{\partial p}{\partial x} + \alpha^2 \frac{\partial^2 u_m}{\partial x^2} + \frac{\partial^2 u_m}{\partial \eta^2}, \tag{3.8}$$

where, $\gamma = \rho'_m/\rho'_w$ is the specific gravity of the mud. The no-slip and the no-flux boundary conditions along the bottom are imposed, i.e.

$$u_m = 0, \quad w_m = 0, \quad \eta = -d. \tag{3.9}$$

Along the water–mud interface, the pressure is continuous. In addition, the tangential stress vanishes since the water is being assumed inviscid and the vertical velocity is continuous, that is

$$\frac{\partial u_m}{\partial \eta} = 0, \quad w_m = W/\alpha\mu, \quad \eta = 0. \tag{3.10}$$

Note that the upper boundary condition given in (3.10) is applied at a fixed position, $\eta = 0$, assuming interface displacement is negligible. This assumption will be justified when the measured and the predicted interfacial displacements are discussed in §3.3.4.

3.2.2 Analytical solutions for the linearized mud layer equation

Liu & Chan (2007) further assumed that the mud bed thickness is small enough that the pressure is essentially uniform in the vertical direction within the layer. Then the horizontal gradient of the dynamic pressure in (3.8) is approximated by the inviscid water particle acceleration along the water–mud interface:

$$\frac{\partial p}{\partial x} = -\frac{\partial u_b}{\partial t}, \tag{3.11}$$

where

$$u_b = U(x, z = 0, t). \tag{3.12}$$

Note that the horizontal mud velocity at the interface $u_m\,(x, z = 0, t)$ is not necessarily the same as u_b. Indeed by (3.11), the problem at hand reduces to the usual boundary layer approach as used in Chapter 2. It is remarked here that the assumption could still be applicable as long as the vertical velocity component and the interfacial displacement are negligible even with a much thicker mud layer.

Keeping only the leading-order terms in (3.8), Liu & Chan (2007) presented the analytical solution for the mud velocity as follows:

$$\begin{aligned} u_m(x, \eta, t) = \frac{1}{\gamma}\Bigg\{ u_b - \int_0^t \frac{\partial u_b}{\partial s}\,\mathrm{erfc}\left[\frac{\eta + d}{\sqrt{4(t-s)}}\right] \mathrm{d}s \\ - \sum_{n=1}^{\infty} (-1)^n \int_0^t \frac{\partial u_b}{\partial s}\left[-\mathrm{erfc}\left(\frac{-\eta + (2n-1)d}{\sqrt{4(t-s)}}\right) + \mathrm{erfc}\left(\frac{\eta + (2n+1)d}{\sqrt{4(t-s)}}\right)\right] \mathrm{d}s \Bigg\}, \end{aligned} \tag{3.13}$$

in which the complementary error fuction is defined as

$$\mathrm{erfc}\,(x) = 1 - \mathrm{erf}\,(x) = \frac{2}{\sqrt{\pi}} \int_x^{\infty} \mathrm{e}^{-u^2}\,\mathrm{d}u. \tag{3.14}$$

The vertical velocity component w_m can be found from the continuity equation (3.17), and here only the solution at $\eta = 0$ is presented, since it is needed in

estimating the interfacial displacement later in §3.3.4:

$$\begin{aligned} w_m(x,0,t) &= -\frac{d}{\gamma}\frac{\partial u_b}{\partial x} + \frac{1}{\gamma}\int_0^t \frac{\partial^2 u_b}{\partial s \partial x} \\ &\times \left\{ \sqrt{\frac{4(t-s)}{\pi}}\left[1 - \exp\left(\frac{-d^2}{4(t-s)}\right)\right] + d\ \mathrm{erfc}\left(\frac{d}{4(t-s)}\right)\right\} \mathrm{d}s \\ &- \frac{1}{\gamma}\sum_{n=1}^{\infty}(-1)^n \int_0^t \frac{\partial^2 u_b}{\partial s \partial x}\left\{ \sqrt{\frac{4(t-s)}{\pi}}\left[-3\exp\left(-\frac{(2nd)^2}{4(t-s)}\right)\right.\right. \\ &+ \sum_{m=-1}^{1}\exp\left(-\frac{((2n+m)d)^2}{4(t-s)}\right)\Bigg] + d\left[2n\ \mathrm{erfc}\left(\frac{2nd}{\sqrt{4(t-s)}}\right)\right. \\ &+ \left.\left.\sum_{m=-1}^{1}(-1)^m(2n-m)\ \mathrm{erfc}\left(\frac{(2n-m)d}{\sqrt{4(t-s)}}\right)\right]\right\} \mathrm{d}s. \end{aligned} \tag{3.15}$$

Finally, one can calculate the nondimensional shear stress along the bottom of the mud bed τ_{mb} by differentiating u_m with respect to η at $\eta = -d$:

$$\tau_{mb}(x,t) = \frac{1}{\gamma\sqrt{\pi}}\int_0^t \frac{\partial u_b}{\partial s}\frac{1}{\sqrt{t-s}}\left[1 + 2\sum_{n=1}^{\infty}(-1)^n \exp\left(-\frac{(nd)^2}{t-s}\right)\right] \mathrm{d}s. \tag{3.16}$$

Notice that the terms of the infinite series in the analytical solutions (3.13, 3.15 & 3.16) are due to the finite domain and become insignificant with $d >> 1$.

3.2.3 Approximate nonlinear mud layer equation

If the nonlinear inertia term cannot be neglected, the full governing equations (3.7 & 3.8) must be solved. First, notice that α^2 is two orders-of-magnitude smaller than ϵ in all of the experimental cases (see tables 3.1), thus the second term in the right-hand side of (3.8) is omitted. This simplification is consistent with Liu & Orfila (2004), as they assumed $O(\alpha) \sim O\left(\epsilon^2\right)$ and here only the terms up to $O(\epsilon)$ need to be retained.

From the continuity equation (3.7),

$$w_m = -\int_{-d}^{\eta}\frac{\partial u_m}{\partial x}\,\mathrm{d}\eta^*. \tag{3.17}$$

Introducing the moving coordinate $\xi = Ct - x$ and using (3.17), the horizontal momentum equation (3.8) becomes

$$C\frac{\partial u_m}{\partial \xi} + \epsilon\left[-u_m\frac{\partial u_m}{\partial \xi} + \left(\int_{-d}^{\eta}\frac{\partial u_m}{\partial \xi}\,\mathrm{d}\eta^*\right)\frac{\partial u_m}{\partial \eta}\right] = \frac{1}{\gamma}\frac{\partial p}{\partial \xi} + \frac{\partial^2 u_m}{\partial \eta^2}. \tag{3.18}$$

The integrand of the integral in (3.18) can be approximated by the linearized equation, i.e.

$$C\frac{\partial u_m}{\partial \xi} = \frac{1}{\gamma}\frac{\partial p}{\partial \xi} + \frac{\partial^2 u_m}{\partial \eta^2} + O(\epsilon). \tag{3.19}$$

Substituting (3.19) into (3.18), we have

$$C\frac{\partial u_m}{\partial \xi} - \epsilon u_m\frac{\partial u_m}{\partial \xi} + \frac{\epsilon}{C}\left[\int_{-d}^{\eta}\left(\frac{1}{\gamma}\frac{\partial p}{\partial \xi} + \frac{\partial^2 u_m}{\partial \eta^2}\right)\mathrm{d}\eta^*\right]\frac{\partial u_m}{\partial \eta} = \frac{1}{\gamma}\frac{\partial p}{\partial \xi} + \frac{\partial^2 u_m}{\partial \eta^2}, \tag{3.20}$$

where $O\left(\epsilon^2\right)$ terms have been omitted.

It is reminded here that the horizontal pressure gradient is assumed to be independent of the vertical coordinate, hence one can carry out the integration in the equation above as follows:

$$\int_{d}^{\eta}\left(\frac{1}{\gamma}\frac{\partial p}{\partial \xi} + \frac{\partial^2 u_m}{\partial \eta^2}\right)\mathrm{d}\eta^* = \frac{1}{\gamma}\left(\eta + d\right)\frac{\partial p}{\partial \xi} + \frac{\partial u_m}{\partial \eta} - \tau_{mb}. \tag{3.21}$$

Though the gradient of shear stress in the mud layer may not necessarily vanish, the water is being assumed inviscid which results in a virtually uniform velocity profile along the depth. At the water–mud interface, therefore, the momentum equation for the horizontal water particle velocity u_b can be written as

$$C\frac{\partial u_b}{\partial \xi} - \epsilon u_b\frac{\partial u_b}{\partial \xi} = \frac{\partial p}{\partial \xi}. \tag{3.22}$$

Hence, the horizontal pressure gradient $\partial p/\partial \xi$ can be expressed in terms of u_b.

By substituting (3.21) and (3.22) into (3.20), finally the approximate nonlinear mud layer equation up to $O(\epsilon)$ reduces to

$$\begin{aligned} C\frac{\partial u_m}{\partial \xi} \;-\; & \frac{\partial^2 u_m}{\partial \eta^2} + \epsilon\left[\frac{1}{\gamma}\left(\eta + d\right)\frac{\partial u_b}{\partial \xi} - \frac{\tau_{mb}}{C}\right]\frac{\partial u_m}{\partial \eta} \\ = \; & \frac{C}{\gamma}\frac{\partial u_b}{\partial \xi} + \epsilon\left[-\frac{1}{\gamma}u_b\frac{\partial u_b}{\partial \xi} + u_m\frac{\partial u_m}{\partial \xi} - \frac{1}{C}\left(\frac{\partial u_m}{\partial \eta}\right)^2\right], \end{aligned} \tag{3.23}$$

with the boundary conditions:

$$u_m = 0, \quad \eta = -d; \qquad \frac{\partial u_m}{\partial \eta} = 0, \quad \eta = 0. \tag{3.24}$$

The approximate nonlinear mud layer equation (3.23) together with the boundary conditions (3.24) is solved numerically by an iterative scheme similar to the one outlined in §2.2.3, in which the nonlinear terms are calculated based on the results from the previous iteration, while the linear operator is discretized by the Crank–Nicolson method. Using the linear solution (3.13) as an initial guess, the iteration continues until the maximum relative error between the respective results from the current and the previous iterations is smaller than 10^{-6}. The resulting finite difference equation is similar in fashion to (2.30), and it is not repeated here.

3.2.4 Effects of the nonlinearity

To investigate the role of the nonlinear terms, a solitary wave with $\epsilon = \mu^2 = 0.6$ is selected as an example while keeping $d = 1$ and $\gamma = 1.05$. The integrals in the analytical solution (3.13) are evaluated using recursive adaptive Simpson quadrature within a relative error of 10^{-6}. Twenty terms in the series are used, although the solution has already converged when ten terms are used. As shown in figure 3.1, the nonlinear effects are not apparent even with the substantial nonlinearity in the solitary water wave, and solutions converged after only four iterations. The insignificant effect of the nonlinearity results from the essentially uniform horizontal velocity along the x-direction which is again attributed to the flat geometry of the problem and the long horizontal length scale of the solitary wave. It is remarked that similar observations have also been

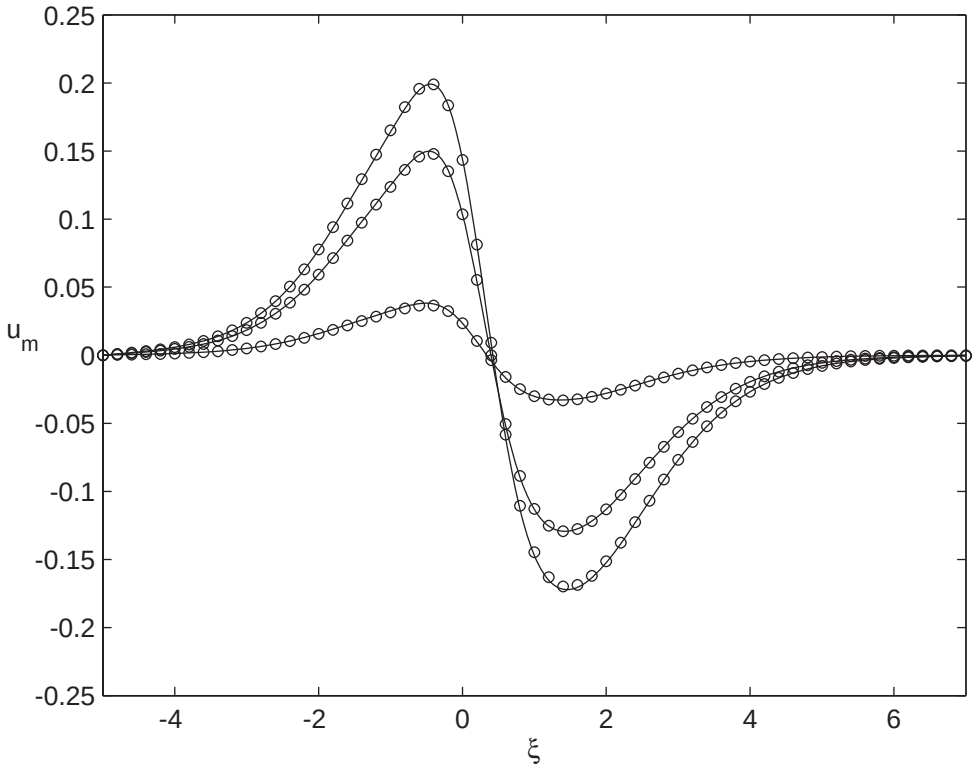

Figure 3.1: Linear and nonlinear solutions for dimensionless horizontal velocity at $\eta = 0$, $-0.5d$, and $-0.9d$ (from top to bottom) for $\epsilon = \mu^2 = 0.6$: ——, the linear solutions (3.13); ∘, the numerical solutions of the approximate nonlinear equation (3.23).

discussed in the previous chapter. For the problems discussed in this chapter, therefore, the linearized form of the governing equation is almost exact and it will be used hereafter. However, with increased level of turbulence or with more sophisticated geometry such as a rippled bottom or a sloping beach, the nonlinear terms could become very important.

3.2.5 Effects of the mud layer thickness

In figure 3.1 one may have noticed that no obvious phase difference is seen among horizontal velocities at different elevations for the case considered, in which $d = 1$. That is because the inertia force in the momentum equation is less important then the viscous shear force. In that case, the governing equation (3.8) can be simplified to read

$$\frac{\partial^2 u_m}{\partial \eta^2} = -\frac{1}{\gamma}\frac{\partial u_b}{\partial t}. \tag{3.25}$$

By integrating twice, while invoking the boundary conditions (3.24), (3.25) yields the parabolic form of the vertical profile of the horizontal mud velocity:

$$u_m \approx \frac{1}{2\gamma}\frac{\partial u_b}{\partial t}\left(d^2 - \eta^2\right). \tag{3.26}$$

Note that u_m is essentially proportional to the acceleration of the free-stream velocity, which results in the reversed flows during the deceleration phase of u_b in figure 3.1, though u_b is always positive.

If the depth of the mud bed is large enough, however, there may exist a well-defined boundary layer inside the mud. Outside the boundary layer the flow becomes practically inviscid in which the inertia force prevails over the viscous force, resulting in the phase difference between the horizontal velocities inside and outside the boundary layer. It is reiterated here that the horizontal pressure gradient can still be approximated by the water particle acceleration (3.11) as long as the thickness of the mud layer is small compared to the horizontal length-scale of the flow. Also note that the theoretical solution (3.13) is valid for not only the solitary wave but also other kinds of long waves in shallow water.

To illustrate, consider now a cnoidal wave with the amplitude a' propagating in a water depth h'. The cnoidal wave can be defined by two dimensionless

parameters: the nonlinearity ϵ and the modulus of the elliptic integral m ($0 < m < 1$). Denoting the complete elliptic integrals of the first and the second kinds with modulus m as K and E, respectively, the dimensionless horizontal water particle velocity at the water–mud interface u_b can be expressed as (see e.g. Mei, 1983)

$$u_b = \frac{K}{K-E}\left[\left(1 - m - \frac{E}{K}\right) + m\ \mathrm{Cn}^2(2K\xi)\right], \tag{3.27}$$

and the dimensionless phase speed is

$$C = \left[1 + \frac{\epsilon\ K}{K-E}\left(-m + 2 - \frac{3E}{K}\right)\right]^{1/2}. \tag{3.28}$$

Note that the wavelength l' has been used as the characteristic length scale, which is given by

$$\frac{l'}{h'} = 4K\left(\frac{K-E}{3\epsilon\ K}\right)^{1/2}. \tag{3.29}$$

To evaluate (3.13), one needs to differentiate (3.27) with respect to t:

$$\frac{\partial u_b}{\partial t} = \frac{4mCK^2}{K-E}\ \mathrm{Cn}(2K\xi)\ \mathrm{Sn}(2K\xi)\ \mathrm{Dn}(2K\xi), \tag{3.30}$$

where Cn, Sn, and Dn are Jacobi elliptic functions.

As an example, a cnoidal wave with $\epsilon = 0.19$ and $m = 0.9$ is plotted in figure 3.2. Vertical profiles of dimensionless horizontal velocity inside the mud bed at four different phases indicated in figure 3.2 are shown in figure 3.3. From figure 3.3 it is clearly observed that there are three different flow regimes according to different values of d. Velocities at different elevations have the same direction when $d < 1$ and the velocity profile can be fitted by a parabola (3.26) with some phase lag (figures 3.3*a–d*). However, when the thickness of the mud layer is much larger than the bottom boundary layer thickness, the velocity profile appears to be a plug flow above a thin viscous layer (figures 3.3*i–l* & *m–p*). Note

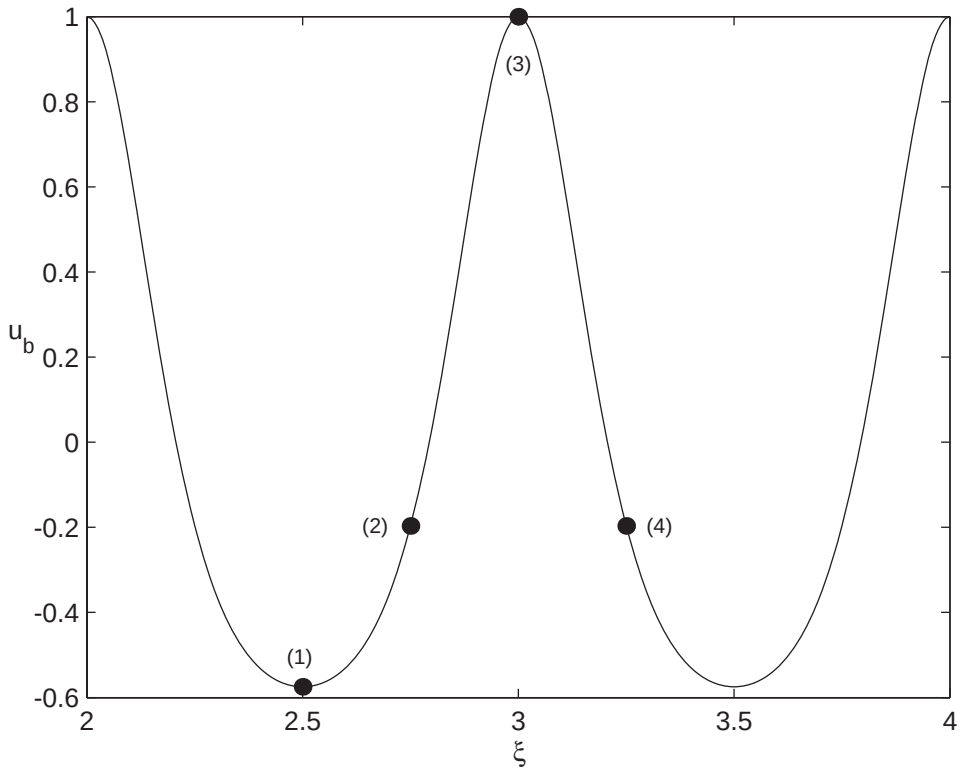

Figure 3.2: u_b under the cnoidal wave with $\epsilon = 0.19$ and $m = 0.9$ during the third period. The numbers in brackets indicate the phases at which the vertical profiles are plotted in figure 3.3.

that the plug flow velocity u_p can be determined as

$$u_p = \frac{1}{\gamma} u_b. \tag{3.31}$$

More complex flows occur for $d \sim O(1)$ (figures 3.3*e–h*).

In the following two sections, the theoretical developments given so far will be validated by means of laboratory experiments. Two kinds of experiments are presented. First, cases with $d < 1$ that were carried out in a wave tank will be shown in §3.3. Then, to overcome the difficulties met in the wave tank which limited the depth of the mud layer, a new experimental apparatus *U-tube* has been built and cases with $d > 1$ were realized. Those results will be discussed in

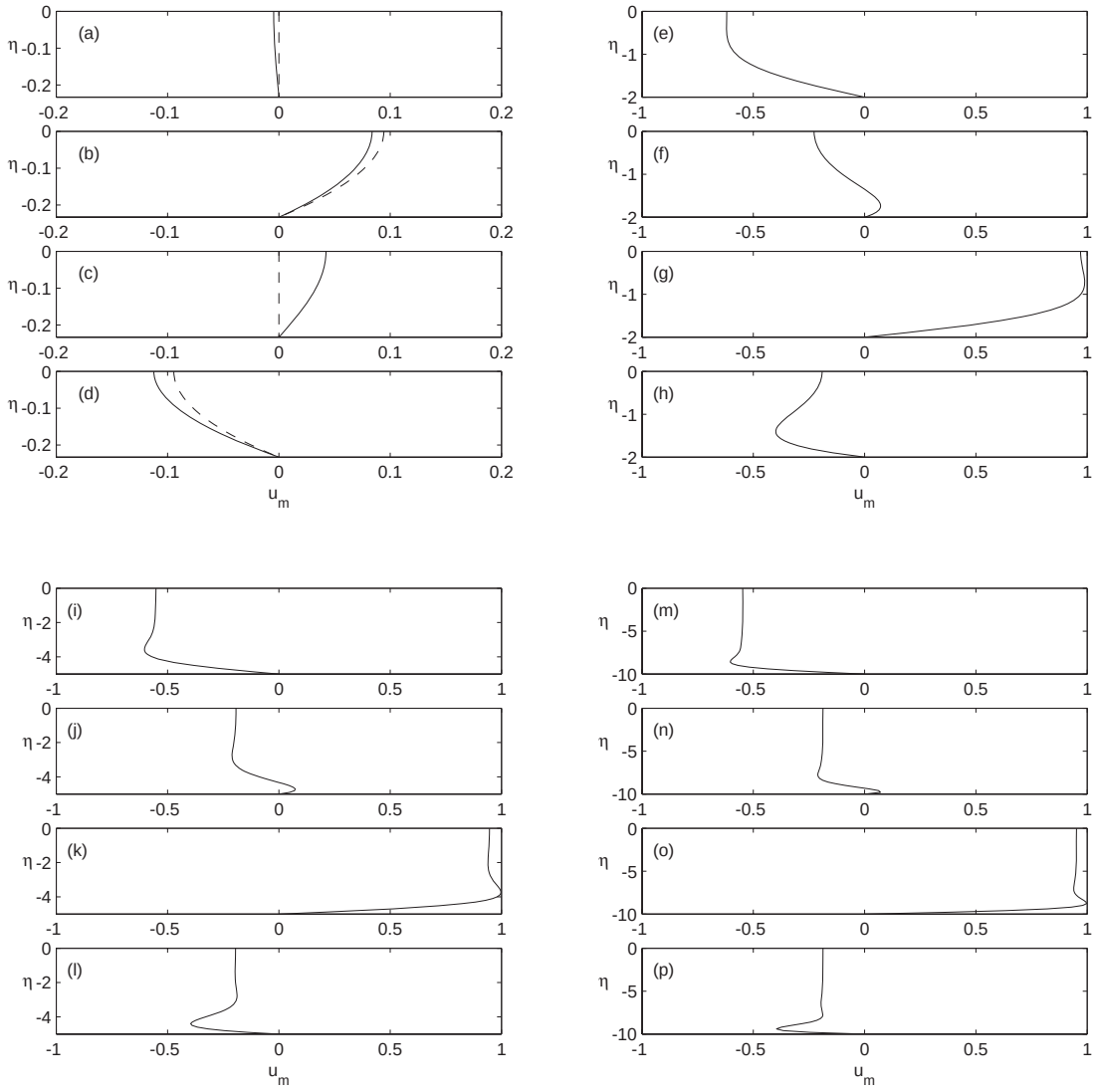

Figure 3.3: Vertical profiles of the dimensionless horizontal velocity under a cnoidal wave at different phases for $\epsilon = 0.19$ and $m = 0.9$ for $d = 0.223$ (*a*–*d*), $d = 2$ (*e*–*h*), $d = 5$ (*i*–*l*) and $d = 10$ (*m*–*p*): ——, the analytical solution (3.13); − − − − −, the parabolic approximation (3.26). (*a*, *e*, *i*, *m*) $\xi = 2.5$; (*b*, *f*, *j*, *n*) $\xi = 2.75$; (*c*, *g*, *k*, *o*) $\xi = 3.0$; (*d*, *h*, *l*, *p*) $\xi = 3.25$.

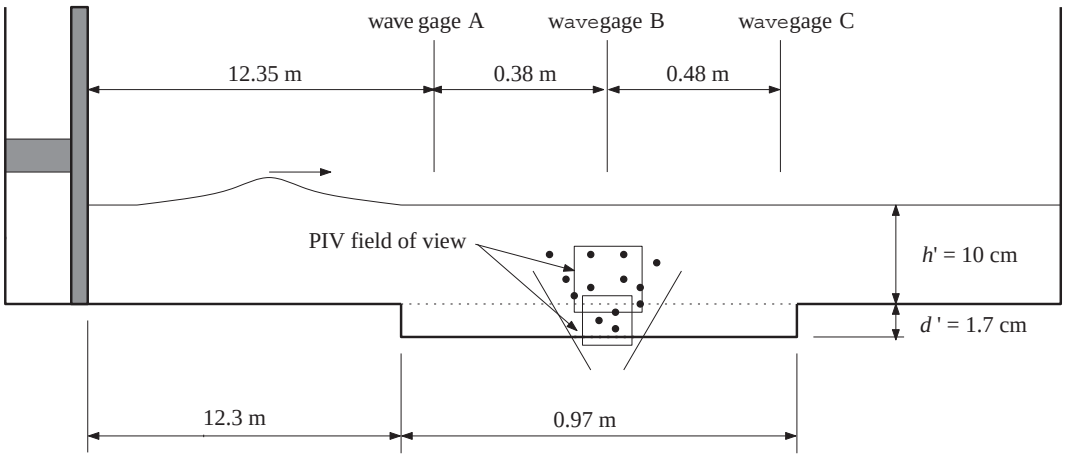

Figure 3.4: Experimental set-up (not to scale).

§3.4.

3.3 Experiments for $d < 1$

The first sets of experiments were conducted in the same wave tank used in Chapter 2 (see §2.3.2). About 1-m-long section of the tank was replaced with a clear acrylic basin which was filled with 1.7 cm deep, clear, highly-viscous silicone fluid. Solitary water surface waves were sent over the basin and the velocity field in the silicone fluid was measured by particle image velocimetry (PIV) technique.

3.3.1 Experimental set-up

Three acoustic wave gauges (Banner Engineering S18U) were used along with the PIV system. The measurement locations are shown in figure 3.4. The effects due to the finite length of the mud basin were insignificant since the interfacial

Table 3.1: Characteristics of solitary waves used in the experiments

Case No.	H' (cm)	l' (m)	T' (s)	ϵ	μ	α	d	Re
V1	0.75	2.62	2.55	0.075	0.038	0.045	0.144	0.45
V2	1.90	1.72	1.59	0.190	0.058	0.056	0.178	1.81
V3	2.90	1.44	1.28	0.290	0.069	0.061	0.195	3.41

displacements were negligible and the maximum particle displacement in the silicone fluid was less than 1 cm, that is, two orders-of-magnitude smaller than the length of the basin.

Three different solitary waves have been studied by changing the wave heights (0.75, 1.90 and 2.90 cm), while the water depth was kept constant, $h' = 10$ cm. The characteristics of the waves generated in the experiments are summarized in table 3.1, where the wavelength l' (2.40) and the wave period T' (2.41) have been defined by the width under the wave crest with both ends where the surface displacement is 1.0% of the wave height. The dimensionless parameters in the table have been previously defined in §2.2 and §3.2.

Figure 3.5 shows the water surface profiles measured at wave gage B (above the center of the PIV measurement region) sampled at 100 Hz for each of the cases in table 3.1. Grimshaw's higher-order solution (2.32) is also plotted in the same figure. The agreement between the theoretical results and experimental data is excellent.

A clear silicone fluid (Dow Corning SYLGARD 184 base fluid; $\gamma = 1.05$; $\nu'_m = 5.24\times10^{-3}$ m^2 s^{-1} at 25 °C) was chosen as the viscous mud. Gade (1958) reported

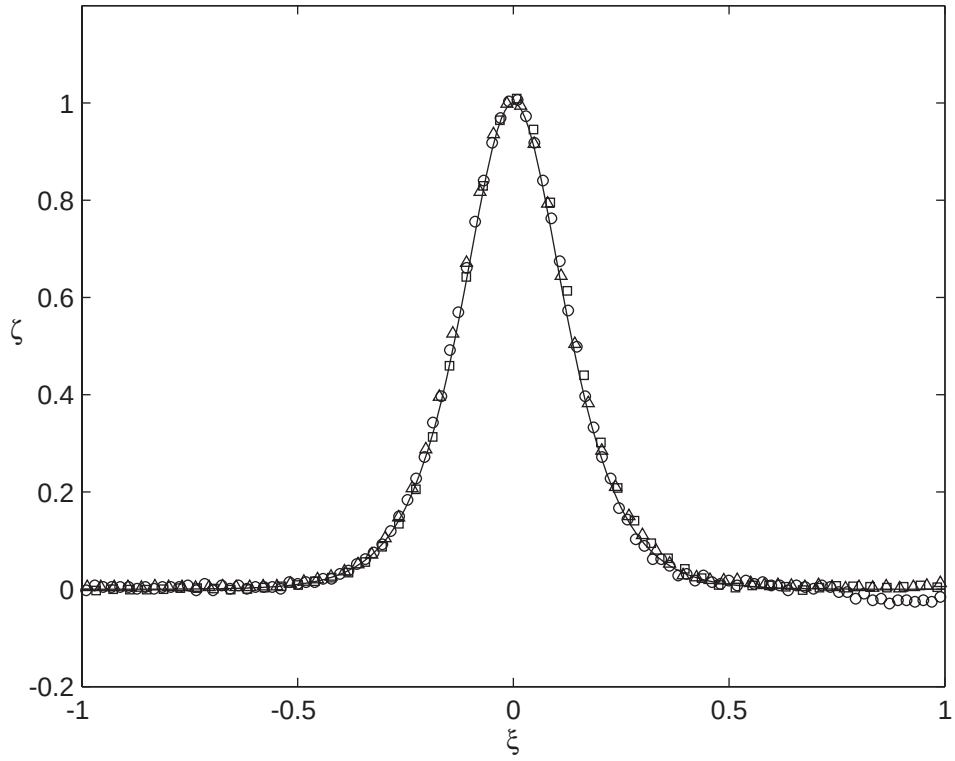

Figure 3.5: Theoretical and experimental dimensionless water surface profiles: ——, Grimshaw's solution (2.32); ∘, wave gage data for the case V1; △, V2; □, V3.

the values of viscosity and density of top-layer sediments in the Mississippi Delta to be $0.1 < \nu'_m < 1$ $\mathrm{m^2\,s^{-1}}$ and $1.6 < \gamma < 2.0$, respectively. Consider the case V2, for which the Reynolds number defined in (2.42) is about 1.81 as shown in table 3.1. The corresponding field condition, using water depth $h' = 10$m, requires $\nu'_m = 5.24$ $\mathrm{m^2\,s^{-1}}$ which is close to the reported values by Gade (1958).

3.3.2 PIV analysis procedure

The PIV technique used here is the same as that employed in Chapter 2 which has been shown to be effective in measuring the velocity field inside the laminar bottom boundary layer under a solitary wave. Therefore, detailed description of the PIV technique will not be repeated here, except a brief explanation with numerical values of parameters that are unique to the present experiments.

Two field-of-views (FOV), which were illuminated with a Spectra Physics PIV400-30 Nd:YAG laser system (300 mJ pulse^{-1}, 60 Hz dual head system), were used to capture images inside as well as above the mud layer (see figure 3.4). By passing the laser beam through a cylindrical lens, a light sheet was formed, which was delivered from below the mud basin to avoid disturbances from the free surface. Since the refractive index of the silicone fluid is different from that of the water, the two square FOVs required separate calibrations, which resulted in different side lengths: 24.6 mm in the mud and 29 mm in the water, respectively. The FOV was set parallel to the sidewalls and slightly off the tank centerline to increase image magnification. The distance between the FOV and the nearest sidewall was about 20 cm, which is larger than the boundary layer thickness of the mud associated with the solitary waves used in the experiments, and the effects of the sidewall are not significant. For each experiment measured inside the mud layer, 105 images were collected with an SMD 1M60-20 camera (12 bits pixel^{-1}, 60 Hz, 1024 $\times$ 1024 pixels) at 15 Hz, yielding 104 velocity field data at the same rate from the successive cross-correlation analyses of two neighboring images. A rectangular interrogation subwindow with long dimension in the horizontal was utilized (256 $\times$ 16 pixel with 75% overlap), which yielded 13 subwindows in the horizontal, and 178 in the vertical (1.5 mm

horizontal and 0.1 mm vertical resolution inside the mud layer). Spurious vectors were flagged using the adaptive Gaussian window filter. The filter rejected less than 10% of the returned data and no attempt was made to smooth or interpolate the original data at this point. On the other hand, exactly the same values of parameters as used in Chapter 2 were applied to acquire and analyze the images of the water region.

Typical PIV results are shown in figure 3.6, in which the velocity vectors at the instants of the positive maxima for the cases V1 & V3, respectively, are plotted. For both cases, the velocities increase almost linearly away from the bottom and they appear to be homongeneous in the horizontal direction. As in the previous chapter, therefore, the PIV data are averaged along the horizontal direction within the FOV.

3.3.3 Water particle velocity in the water region

Some of the laser light was scattered as it passed through the water–mud interface, which caused saturation near the interface in the images taken from the upper FOV (see figure 3.7). Thus, the velocity data inside the interfacial boundary layer could not be extracted. However, the saturation did not occur far above the interface, where the measurements of the free-stream velocity were made. The data is sufficient for the present purpose, as the water is essentially inviscid and the focus here is on the velocity field inside the mud layer.

Figure 3.8 shows the measured water particle velocity components in the horizontal direction compared with Grimshaw's solution (2.37) for each of the cases in table 3.1 . Good agreement is observed and this, together with the water

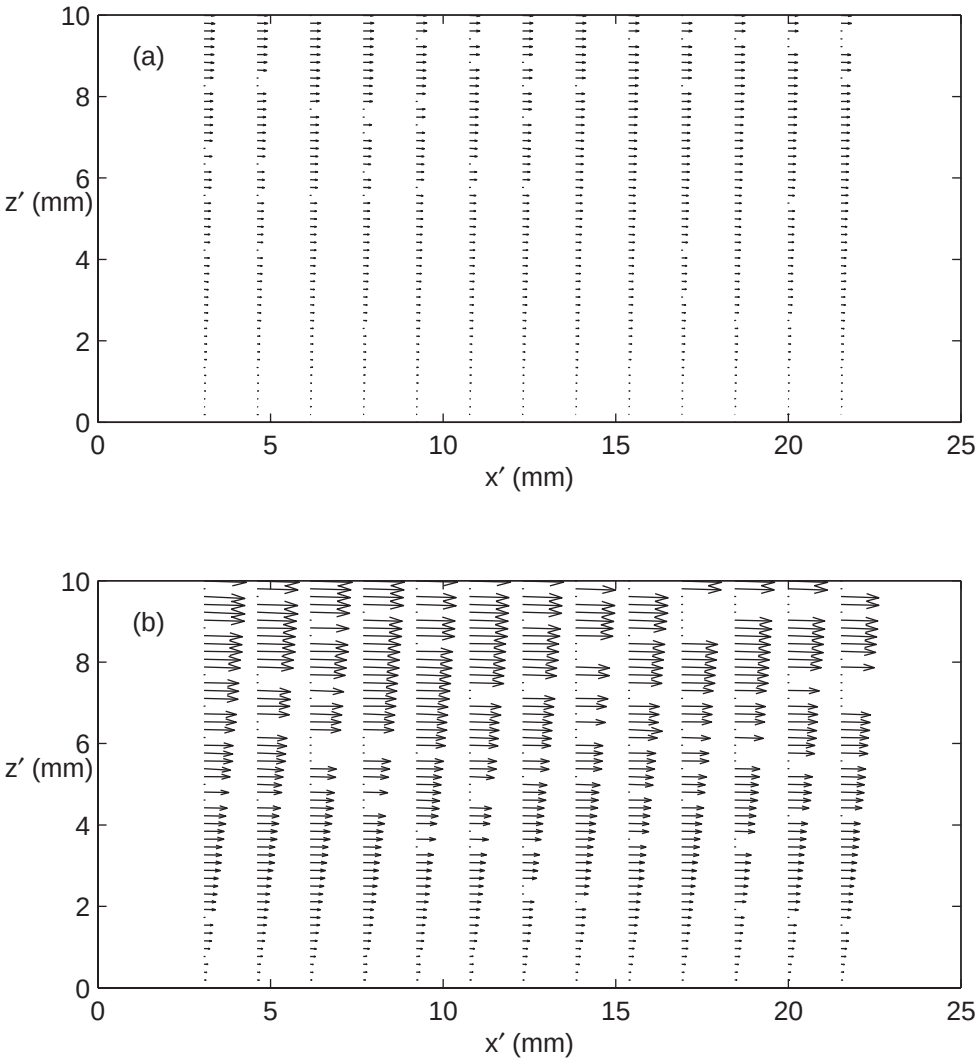

Figure 3.6: Typical results of the PIV analysis inside the viscous mud. (*a*) $\xi = -0.12$ for the case V1; (*b*) $\xi = -0.12$ for the case V3. The largest velocity shown in (*b*) is about 1 $\mathrm{cm\,sec^{-1}}$. Note that only a quater of the total velocity vectors are shown.

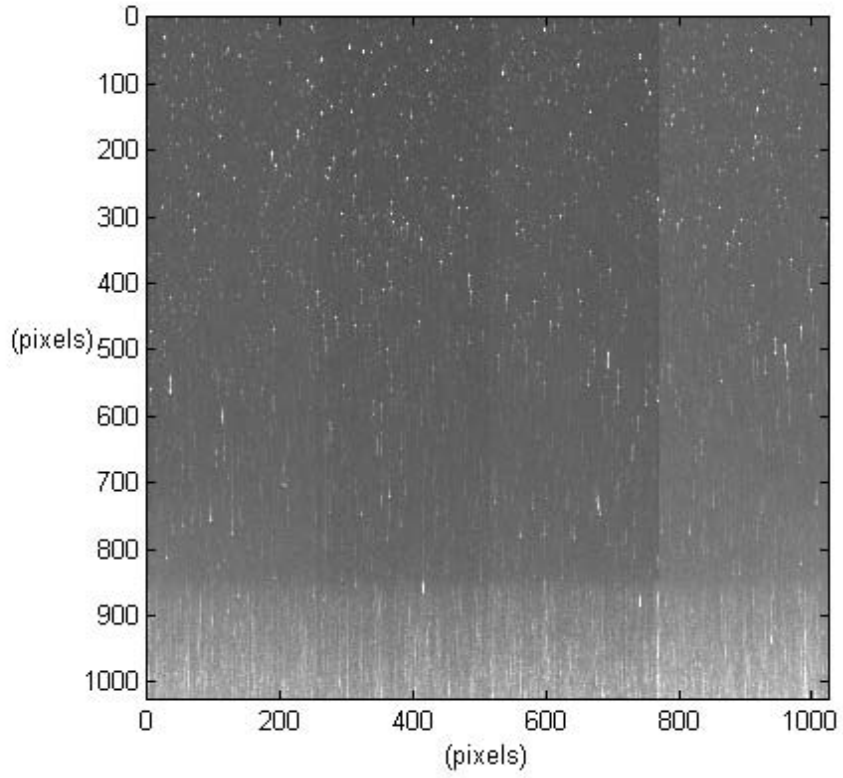

Figure 3.7: An example of the raw PIV image captured in the water side for the case V2. Near the bottom, the image is saturated and blurred due to the refraction of the laser light at the water–mud interface.

surface profile measurements (figure 3.5), demonstrates the high quality of the experimentally generated solitary waves.

3.3.4 The displacement of the water–mud interface

In the development of the theory, the water–mud interface displacment ζ_m' is assumed to be negligible, which must be confirmed.

Experimentally, the interfacial displacements are obtained by the following

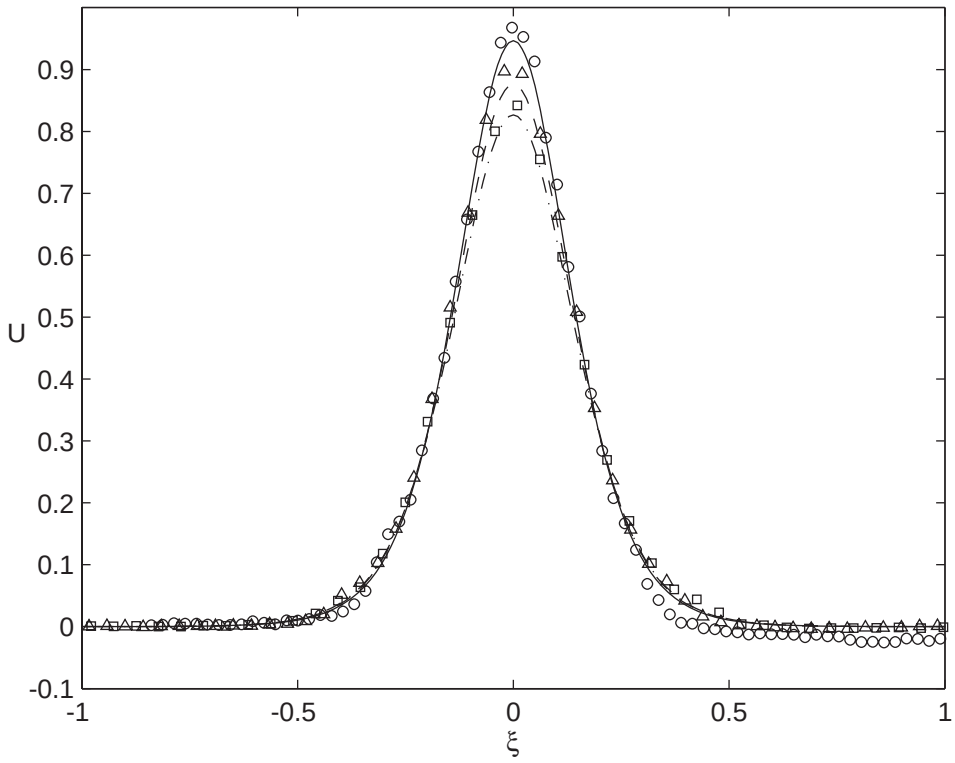

Figure 3.8: Theoretical and experimental dimensionless horizontal water particle velocities: ——, Grimshaw's solution (2.37) for the case V1; – – – – –, V2; — · —, V3; ∘, the experimental data for the case V1; △, V2; □, V3.

procedure. In view of the raw PIV images such as the one in figure 3.9, the locations of the interface are indeed uniform in each image (1024 × 1024 pixels). A Gaussian curve is fitted to each of 1024 columns of an image near the interface (40 pixels per column). For each column, the location of the interface is identified where the fitted curve has the maximum intensity and it is averaged over the 1024 samples. A typical value of the standard deviation is about 3 pixels (0.07 mm), and is just a little larger than the limit of the measurement error (1 pixel).

On the other hand, the theoretical interfacial displacement can be obtained

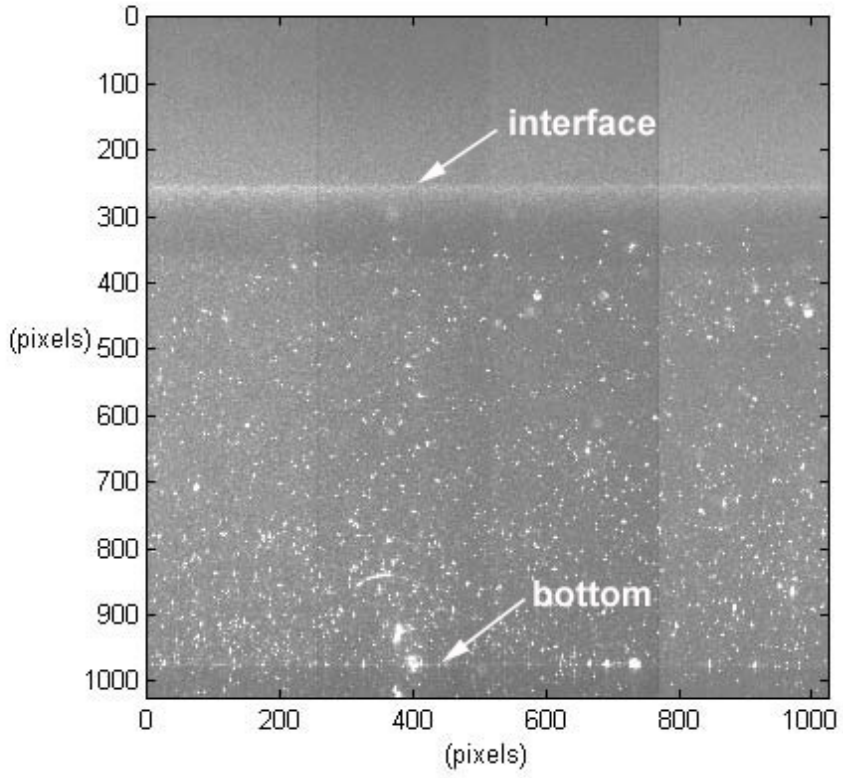

Figure 3.9: An example of the raw PIV image captured in the mud side for the case V2 at the moment of the nearly maximum velocity. A thin bright line, about 250 pixels below the top, is the water–mud interface. A thinner line near the bottom of the image is the bottom of the mud layer, below which is the reflection.

from the kinematic condition. Using the dimensionless variable $\zeta_m = \zeta'_m/H'$, the linearized kinematic condition reads

$$\frac{\partial \zeta_m}{\partial t} = w_m, \quad z = 0. \tag{3.32}$$

Then upon integration,

$$\zeta_m(\xi) = \frac{1}{C}\int_{-\infty}^{\xi} w_m(\xi^*, z = 0)\ \mathrm{d}\xi^*, \tag{3.33}$$

in which the analytical expression for w_m at $z = 0$ is given in (3.15). In figure 3.10, both theoretical estimations and experimental measurements for each of

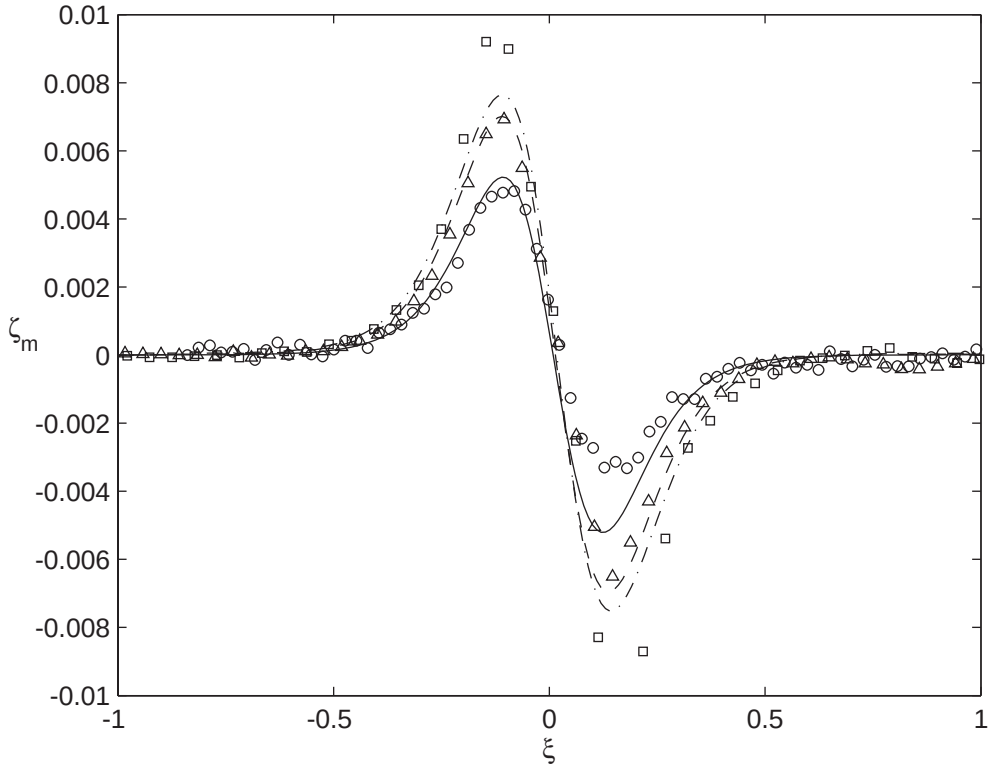

Figure 3.10: Time histories of the dimensionless interfacial displacement: ——, the analytical solution (3.33) for the case V1; − − − − −, V2; —·—, V3; ∘, the experimental data for the case V1; △, V2; □, V3.

the cases are plotted. Generally good agreements between the measurements and the theoretical predictions are seen. The maximum discrepancy between them is about 0.05 mm for the case V3, which is about twice the size of a pixel and well within the uncertainty of the measurement. Note that the displacements of the interface are two to three orders-of-magnitude smaller than those of the free surface. Thus, the effect of the interface displacements can be safely neglected when the viscosity ratio is much greater than 1.

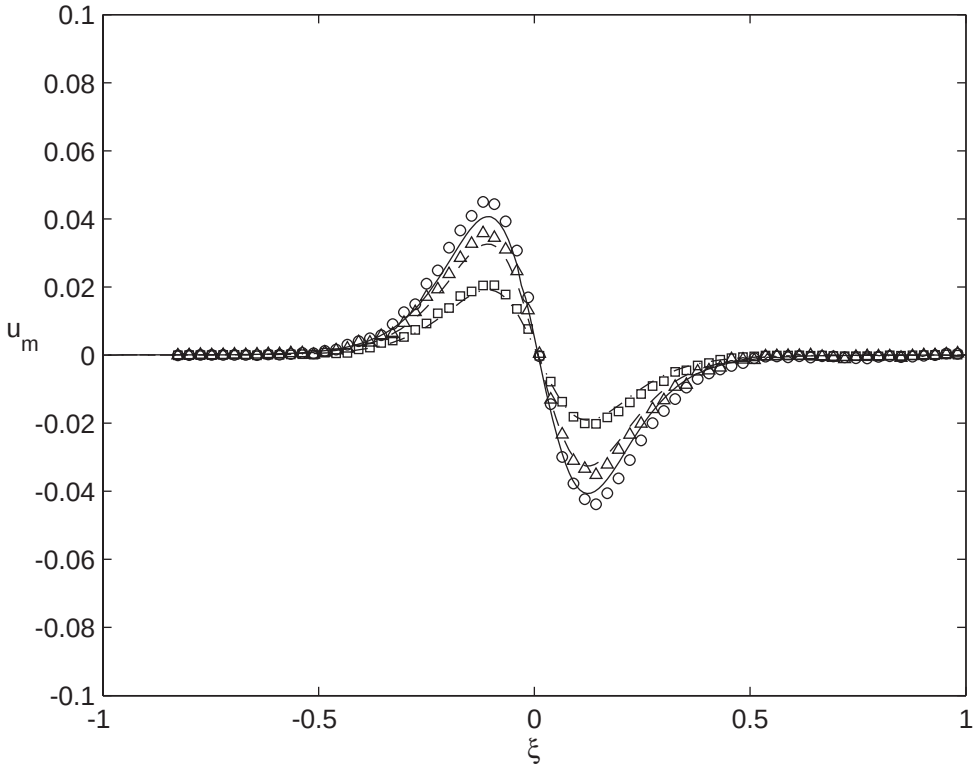

Figure 3.11: Time histories of the dimensionless horizontal velocity for the case V1: ——, the analytical solution (3.13) at $\eta = -0.25d$; – – – – –, $\eta = -0.50d$; —·—, $\eta = -0.75d$; ∘, the experimental data at $\eta = -0.25d$; △, at $\eta = -0.50d$; □, at $\eta = -0.75d$.

3.3.5 Experimental measurements and theoretical results in the mud region

Time histories of the horizontal velocity at three different elevations, namely $\eta = -0.25d$, $-0.50d$ and $-0.75d$, for each of the experimental cases are plotted in figures 3.11–3.13. One can see that the linearized solution predicts the experimental results very well. Some discrepancies, especially those at the positive and negative peaks, are mainly due to the imperfections in generation of the solitary waves shown in figure 3.8.

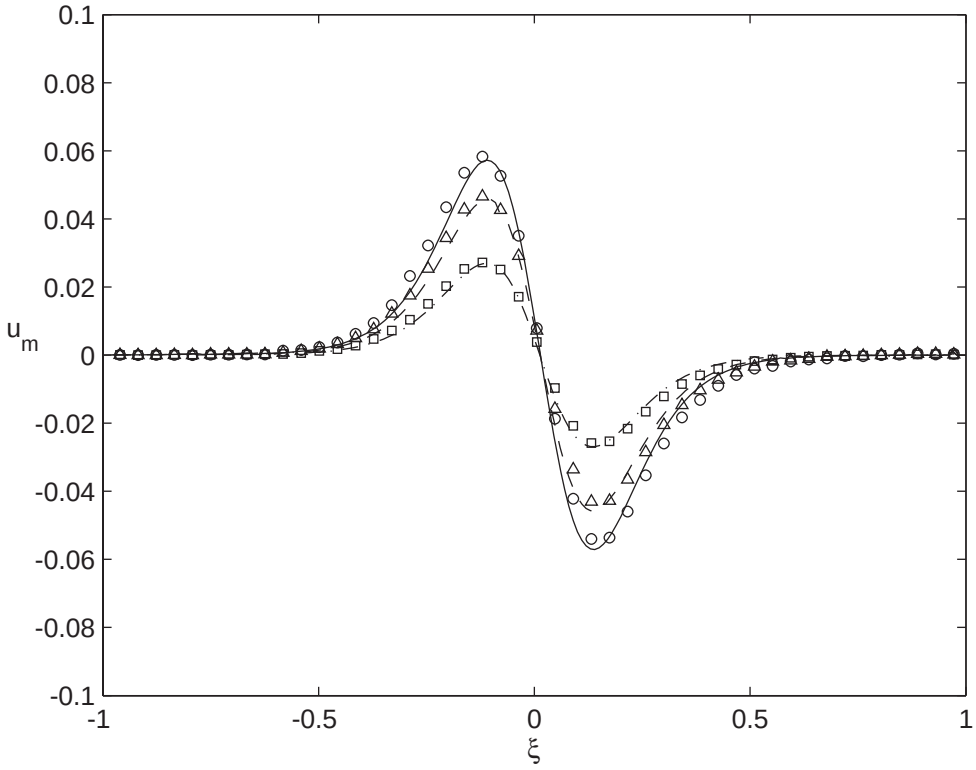

Figure 3.12: Time histories of the dimensionless horizontal velocity for the case V2: ——, the analytical solution (3.13) at $\eta = -0.25d$; – – – – –, $\eta = -0.50d$; —·—, $\eta = -0.75d$; ∘, the experimental data at $\eta = -0.25d$; △, at $\eta = -0.50d$; □, at $\eta = -0.75d$.

The vertical profiles of horizontal velocity components at four different phases for each of the experimental cases are compared with the theoretical solution (3.13) in figures 3.14–3.16, respectively. In all of the experiments conducted, d is less than 0.2 (see table 3.1), i.e., the mud bed thickness is less than 20% of the wave-induced boundary layer thickness. As mentioned before, the velocity profiles can be approximately fitted as a parabolic function (3.26) as shown in the figures 3.14–3.16. Indeed the parabolic approximation satisfactorily matches the experimental data as well as the theoretical solutions.

However, if d is greater than the unity, the parabolic approximation is no

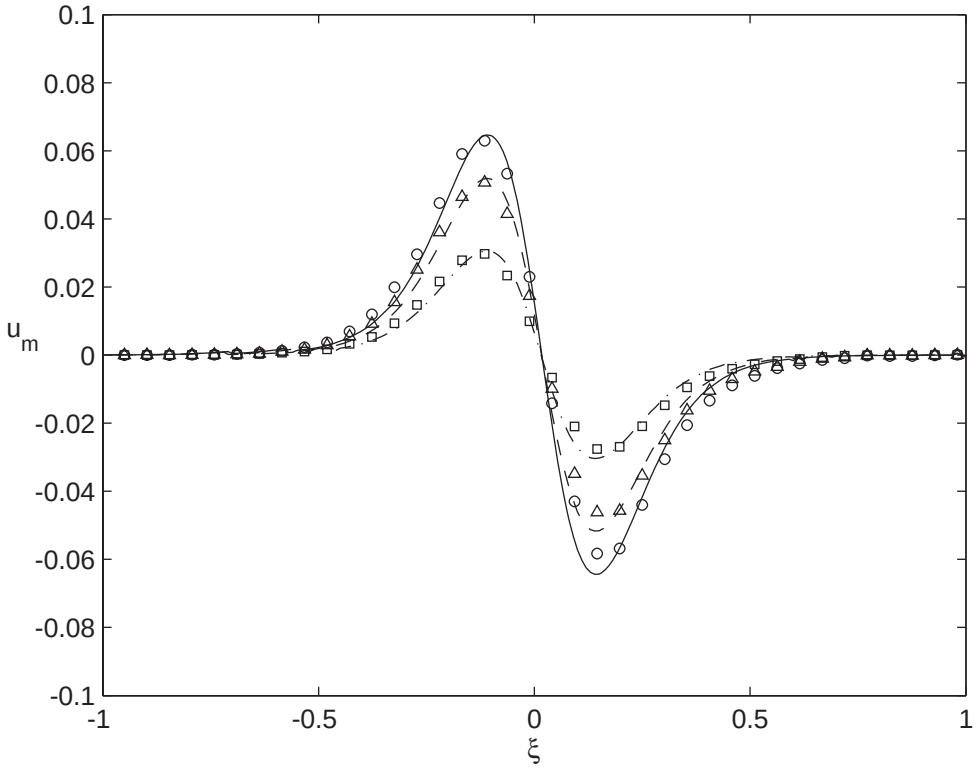

Figure 3.13: Time histories of the dimensionless horizontal velocity for the case V3: ——, the analytical solution (3.13) at $\eta = -0.25d$; – – – – –, $\eta = -0.50d$; —·—, $\eta = -0.75d$; ∘, the experimental data at $\eta = -0.25d$; △, at $\eta = -0.50d$; □, at $\eta = -0.75d$.

longer valid and flow reversal near the bottom as seen in the boundary layer flow in the previous chapter will occur during the deceleration phase ($\xi > 0$). For example, in figure 3.15 (*e*–*h*) the analytical solutions are shown for the same conditions as those used in figure 3.15 (*a*–*d*) except that d is increased to 2. When the thickness of the mud bed is further increased such that it is much greater than the boundary layer thickness, a well-defined boundary layer flow region is developed under the plug flow region where the velocity is essentially uniform (shear-free). This feature can be seen in figure 3.15(*i*–*p*), i.e. for $d = 5$ and 10. In the plug flow region, the inertia force is balanced by the pressure gradient force.

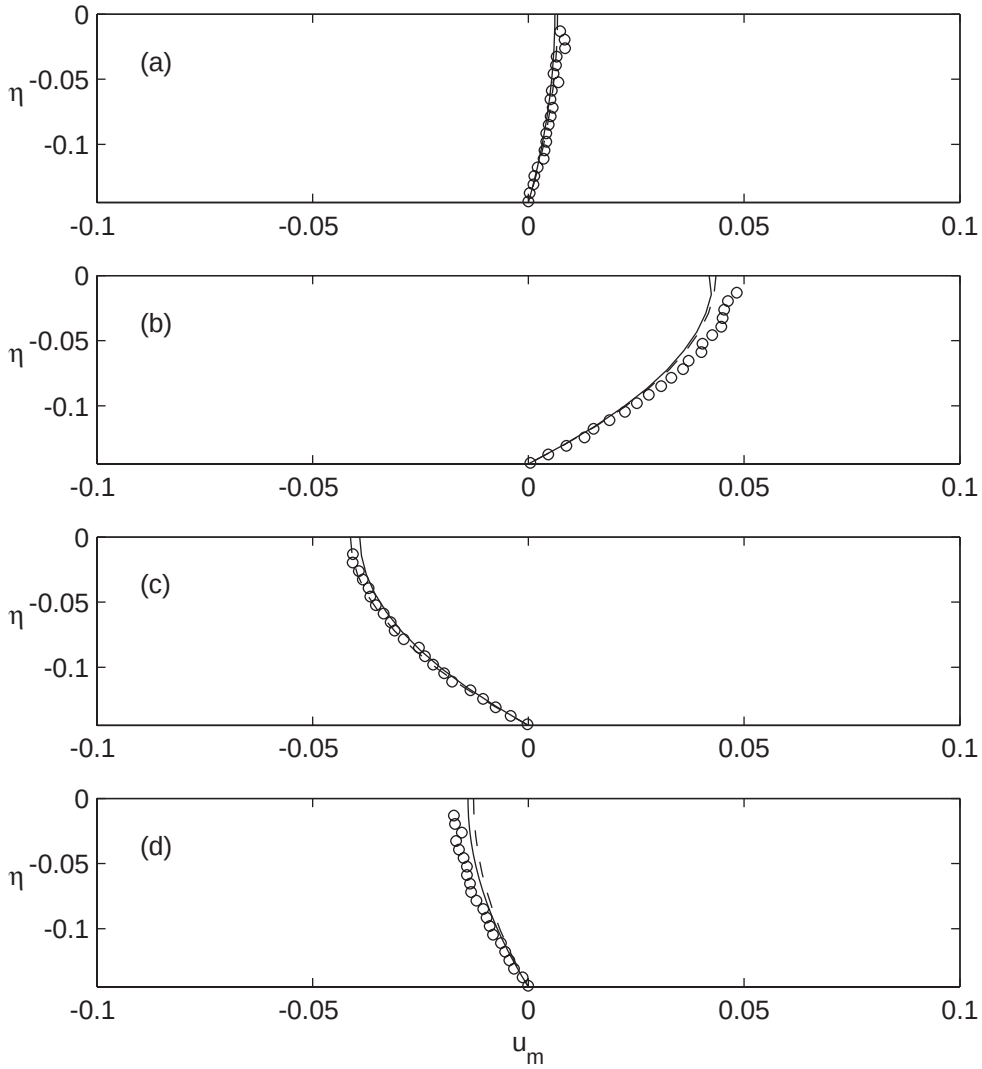

Figure 3.14: Vertical profiles of the dimensionless horizontal velocity at different phases for the case V1: ——, the analytical solution (3.13); −−−−−, the parabolic approximation (3.26); ∘, the experimental data. (*a*) $\xi = -0.36$; (*b*) $\xi = -0.12$; (*c*) $\xi = 0.09$; (*d*) $\xi = 0.30$.

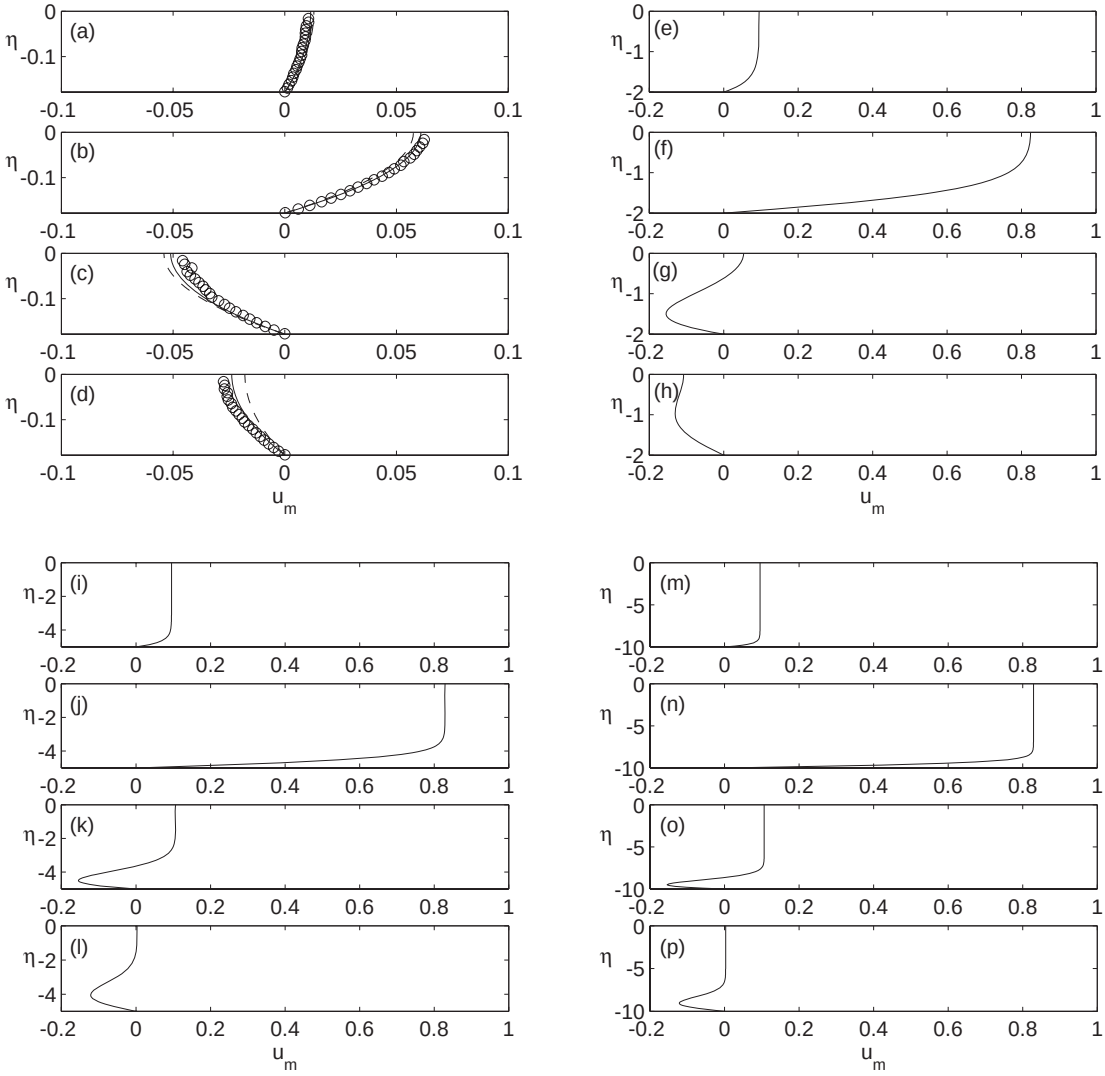

Figure 3.15: Vertical profiles of the dimensionless horizontal velocity at different phases for the case V2 with $d = 0.178$ (*a–d*), $d = 2$ (*e–h*), $d = 5$ (*i–l*) and $d = 10$ (*m–p*): ——, the analytical solution (3.13); − − − − −, the parabolic approximation (3.26); ∘, the experimental data. (*a*) $\xi = -0.33$; (*b*) $\xi = -0.12$; (*c*) $\xi = 0.09$; (*d*) $\xi = 0.33$; (*e*, *i*, *m*) $\xi = -0.3$; (*f*, *j*, *n*) $\xi = 0.0$; (*g*, *k*, *o*) $\xi = 0.3$; (*h*, *l*, *p*) $\xi = 0.6$.

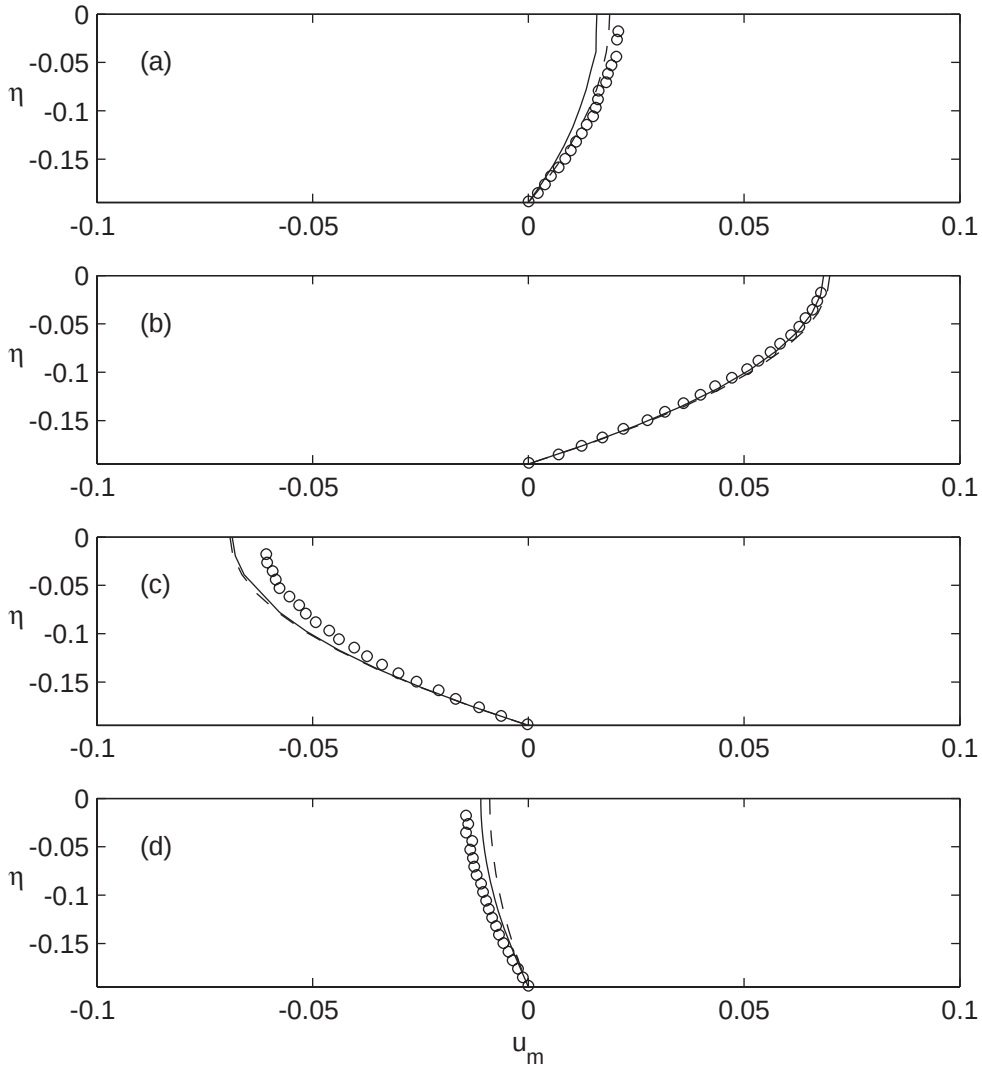

Figure 3.16: Vertical profiles of the dimensionless horizontal velocity at different phases for the case V3: ——, the analytical solution (3.13); − − − − −, the parabolic approximation (3.26); ∘, the experimental data. (*a*) $\xi = -0.33$; (*b*) $\xi = -0.12$; (*c*) $\xi = 0.14$; (*d*) $\xi = 0.40$.

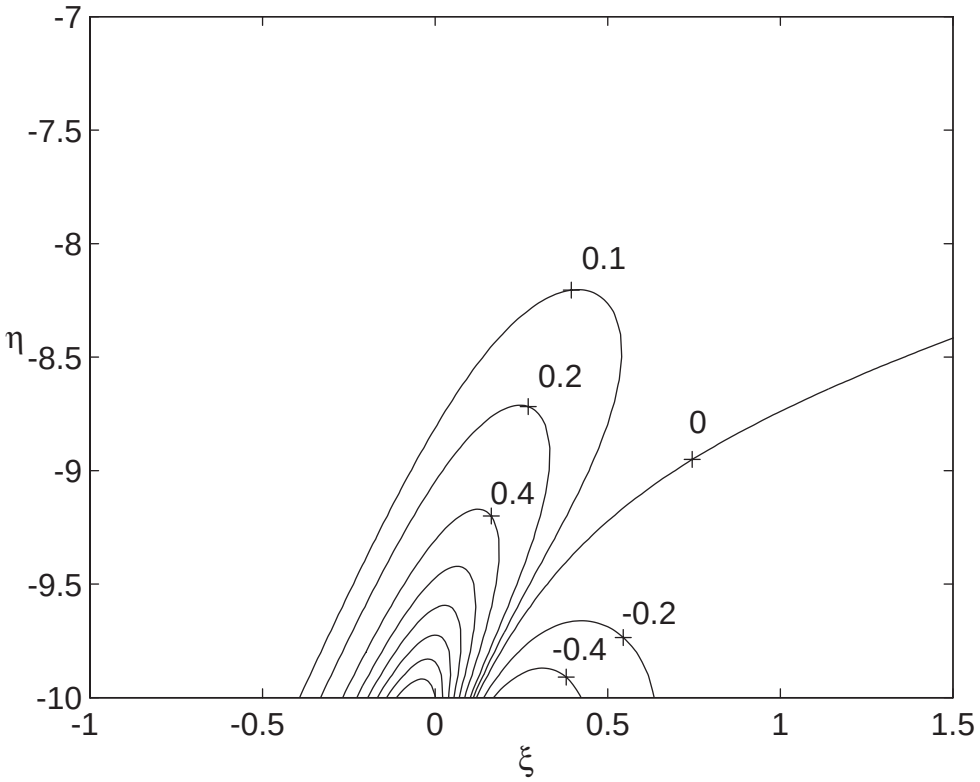

Figure 3.17: A contour plot of $\partial u_m/\partial\eta$ when $d = 10$ for the case V2.

Therefore, the plug flow velocity is given by (3.31).

A contour plot of $\partial u_m/\partial\eta$ is shown in figure 3.17 for $d = 10$ and $\epsilon = 0.190$. In the plug flow region, the value of the derivative should be very close to zero. If we define the bottom of the plug flow as the location where $\partial u_m/\partial\eta = \pm 0.2$, figure 3.17 provides the evolution of the plug flow thickness as the solitary wave passes by.

The dimensionless bottom shear stress for each of the cases is shown in figures 3.18–3.20, respectively. The experimental results are obtained by least-square fitting a straight line through 10 data points (within 1 mm) above the bottom of mud bed. As can be seen in figure 3.6, the velocity profiles are almost

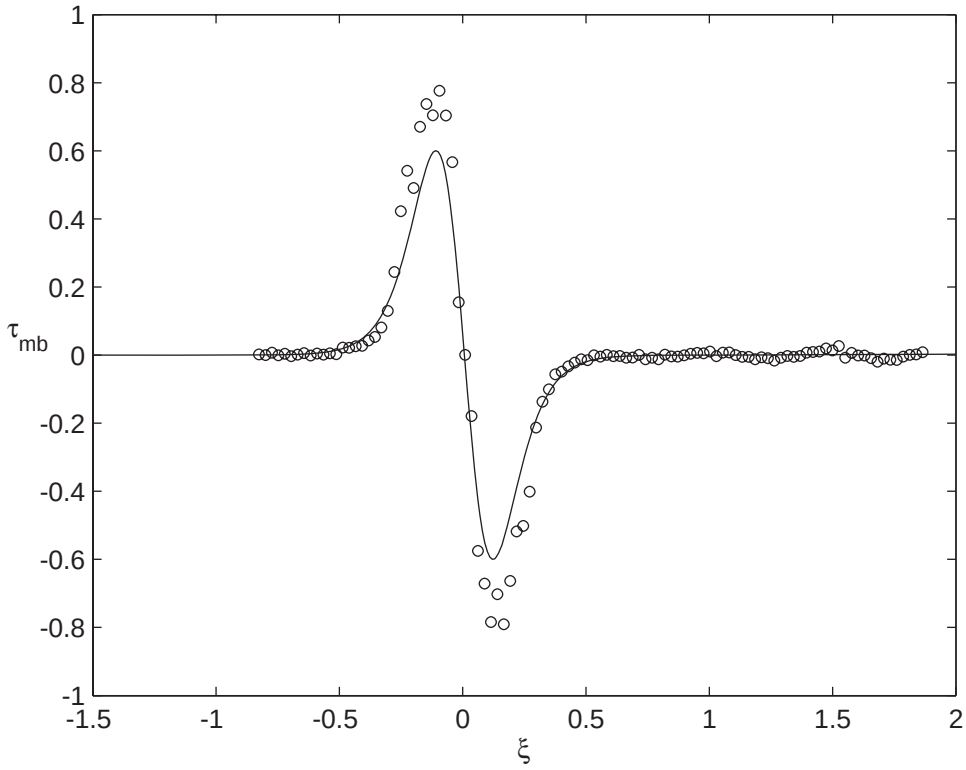

Figure 3.18: Time histories of the dimensionless bottom shear stresses for the case V1: ∘, the experimental data; ——, the analytical solution (3.16).

linear within such a small distance from the bottom. On the other hand, the theoretical values are calculated from (3.16).

Overall good agreement is observed. For the case V1 (figure 3.18), however, the maximum shear stress estimated from the measured velocity is higher than the analytical solution by 30%, though the theory predicts the expected trend very well. Imperfections in wave generation as well as the finite length of the mud basin may be responsible for the discrepancy. On the other hand, much better agreement is achived for the other two cases (figures 3.19 & 3.20). It is interesting to note that the time history of the bottom shear stress is almost

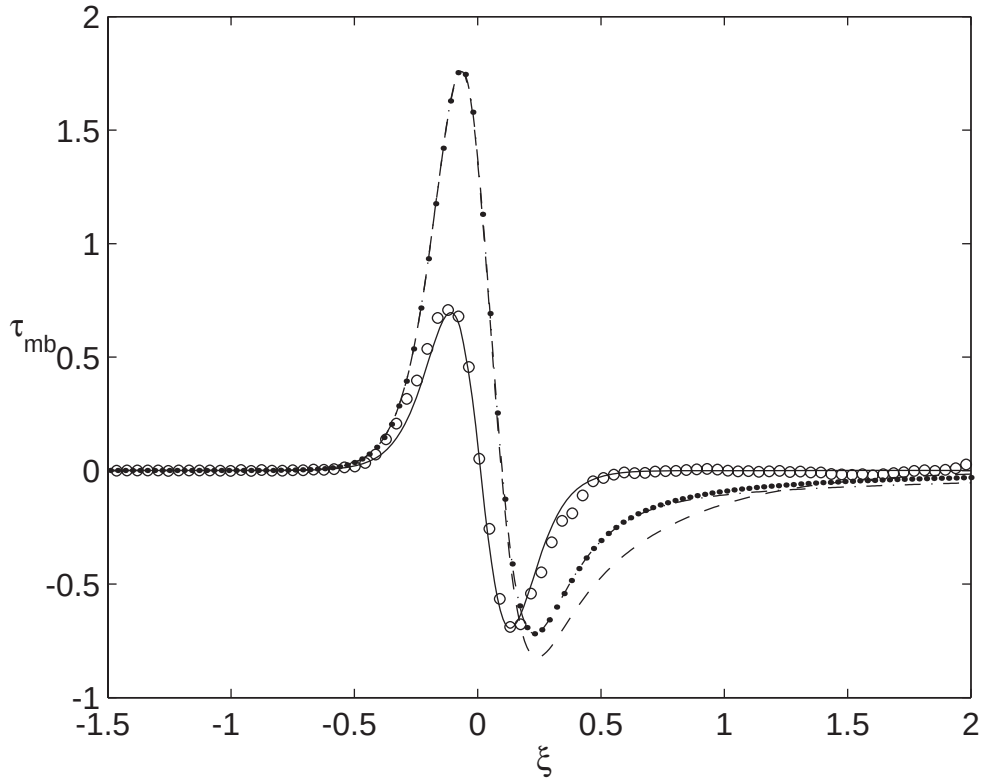

Figure 3.19: Time histories of the dimensionless bottom shear stresses for the case V2: ∘, the experimental data for $d = 0.178$; ——, the analytical solution (3.16) for $d = 0.178$; – – – – –, the analytical solution for $d = 1$; — · —, for $d = 2$; •, for $d = 5$.

symmetric with respect to zero stress for the experimental cases.

Also plotted in figure 3.19 are bottom shear stresses for different values of d with otherwise identical conditions. They are no longer symmetric with respect to zero stress as a distinct shear layer is developed inside the mud bed and the phase difference from that of the forcing wave is apparent. It is also clear that the bottom shear stress becomes independent of the mud bed thickness when d exceeds a critical value, which can be determined from the analytical solutions. For the case V2 the critical value is roughly $d \approx 1.5$.

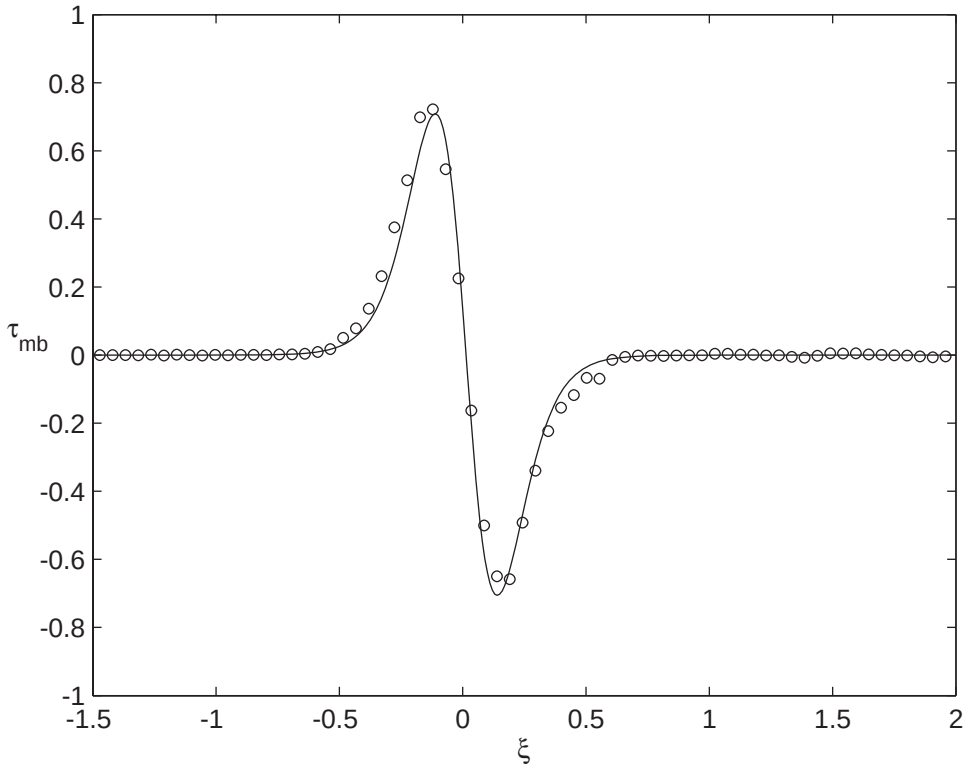

Figure 3.20: Time histories of the dimensionless bottom shear stresses for the case V3: ∘, the experimental data; ——, the analytical solution (3.16).

3.4 Experiments for $d > 1$

So far it has been argued that d, or equivalently $\overline{d}$, is a very important parameter that characterizes the flow in the mud bed. However, only the case with $d < 1$ could be experimentally verified due to limitations in the wave tank experimental set-up. Either increasing the depth of the mud basin or lowering the viscosity of the mud could allow one to achive a larger d value. In fact, experiments with sugar water with otherwise identical conditions were tried, for which $d \approx 2$ because of the much lower viscosity ($\nu'_m = 2.54 \times 10^{-5}$ m^2 s^{-1}) compared to the silicone oil ($\nu'_m = 5.24 \times 10^{-3}$ m^2 s^{-1}). During the experiments, however, signifi-

cant interfacial disturbances and the amplified effects of the finite basin length such as breaking of the interfacial wave around the edge of the basin were observed. Hence, the assumptions made in the theoretical development could not be satisfied.

To overcome the aforementioned difficulties, a new experimental apparatus *U-tube* was constructed. It will be shown that flows in U-tube set-up can truly satisfy all the assumptions of the theory and avoid the difficulties met in the wave tank.

3.4.1 U-tube: an analogy of pressure-gradient-driven mud flow

The mud flow under a long wave and the unsteady Poiseuille flow share the same kind of forcing and boundary conditions. The latter is driven by the pressure gradient that changes in time such that there is only the axial velocity component. From the law of mass conservation, the flow must be uniform in the axial direction which makes the convective acceleration term identically zero in the momentum conservation equation. Because of the geometrical symmetry of the flow configuration, the radial gradient of the axial velocity is always zero along the centerline, which satisfies both the no-shear-stress and the no-interfacial-displacement conditions as required in the theoretical formulation for the mud flow (§3.2). In other words, the unsteady Poiseuille flow is an ideal, linearized model for long-wave-induced flow in a fluid-mud. However, it is noted that the effects of the mud flow in the water column cannot be included in the U-tube experiments.

Figure 3.21 shows a picture of the U-tube facility. One end of the U-tube is

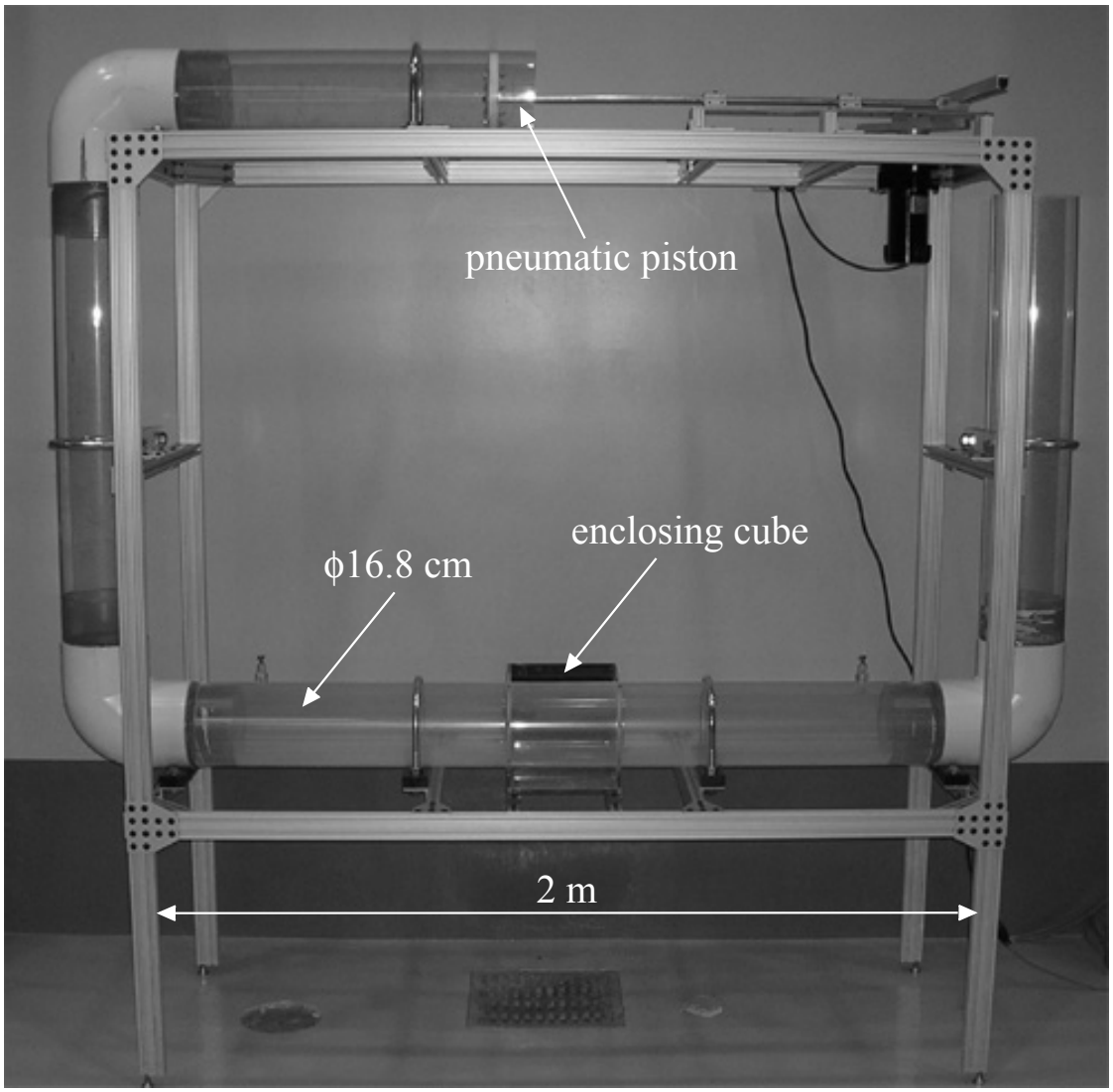

Figure 3.21: The U-tube used in the experiments.

connected to a mechanically-activated pneumatic piston while the other is open to the atmosphere. Typically the fluid is filled up to about half of the vertical columns. The tube is made of acrylic circular pipes with inner diameter $D' = 16.8$ cm, which is about four times larger than a typical thickness of boundary layer of mud of which the viscosity is three orders-of-magnitude larger than that of water. The horizontal section is $l' = 2$ m long and goes through a cube with sidelength 22 cm in the middle. The cube was filled with water and was

used as a prism to minimize the unwelcome refraction when taking PIV images.

3.4.2 Pressure gradient measurement and the natural frequency of the U-tube

Two acoustic wave gages (Banner Engineering S18U) were installed, one at each column, to measure the free surface elevations at the both ends simultaneously and thus to estimate the pressure drop along the U-tube. It is robust because this method can be applied to both Newtonian and non-Newtonian fluids. On the other hand, the attempt to use pressure transducers in the horizontal section of the U-tube was not successful for the non-Newtonian fluid, which will be discussed in the next chapter.

Additionally, free surface measurements reveal that there is the natural frequency determined by the horizontal length of the U-tube. The governing equation in dimensional form is

$$\frac{\partial u'_m}{\partial t'} = -\frac{1}{\rho'_m}\frac{\partial p'}{\partial x'} - \frac{1}{\rho'_m r'}\frac{\partial}{\partial r'}\left(r'\tau'_m\right), \tag{3.34}$$

in which $u'_m(r', t')$ is the axial velocity, r' the radial coordinate, t' the time coordinate, ρ'_m the density of the fluid-mud, p' the pressure, and τ'_m the shear stress. Along the wall the no-slip condition is applied. For laminar flows of a Newtonian fluid, analytical solutions to (3.34) are well-known (e.g. Uchida, 1956). If the radius of the pipe $R'(= D'/2)$ is greater than the Stokes boundary-layer thickness, the shear stress τ'_m is negligible outside the boundary layer. Further, if the axial velocity along the centerline is sinusoidal, that is $u'_m(0, t') = u'_c \cos(\omega' t')$, where u'_c is the maximum centerline velocity and ω' the angular frequency, the

pressure gradient can be approximated as

$$\frac{\partial p'}{\partial x'} = \rho'_m u'_c \omega' \sin(\omega' t') . \tag{3.35}$$

On the other hand, denoting the amplitude of the free surface displacement along the centerline in the columns as Δ', the horizontal length of the U-tube l', and the gravitational acceleration g', the pressure gradient can also be estimated as

$$\frac{\partial p'}{\partial x'} = \frac{\rho'_m g' (2\Delta')}{l'} = \frac{2\rho'_m g' u'_c}{\omega' l'} \sin(\omega' t') . \tag{3.36}$$

Note that the second equality in (3.36) results from that displacement must be uniform along the U-tube. From (3.35) and (3.36), the natural frequency ω'_0 is found:

$$\omega'_0 = \sqrt{\frac{2g'}{l'}}. \tag{3.37}$$

With $l' = 2$ m (see figure 3.21), the natural frequency is roughly $\omega'_0 \approx 3$ rad s^{-1}. While (3.35) and (3.36) are useful in double-checking the pressure gradient measurements, (3.37) suggests that the U-tube system, in general, is limited in terms of the realizable frequencies by the length of the horizontal section. Indeed the system depicted in figure 3.21 operates in regular sinusoidal motion without uncontrolled vibrations only when the forcing frequency is close to the natural frequency.

3.4.3 Velocity field measurement

The PIV system in the DeFrees Hydraulics Laboratory at Cornell University was employed to resolve velocity fields across the whole diameter of the tube at the rate of 10 Hz for 2 minutes. Detailed description about the PIV system and the analysis procedure have been already discussed in §2.3.3 and §3.3.2. Note that

the piston was put in sinusoidal motion with $\omega' \approx \omega'_0$ and each measurement started 5 minutes after the start-up waiting for the quasi-steady state to be esatablished in the system. The vertical resolution of the PIV data was 0.2 mm.

3.4.4 Analytical solution of viscous flow in the U-tube

Rewrite the governing equation (3.34) in terms of dimensionless variables for mud. Denoting

$$-\frac{1}{\rho'_m}\frac{\partial p'}{\partial x'} = P' f(\omega' t'), \tag{3.38}$$

where f is a dimensionless function of order unity, the centerline velocity scales with P'/ω'. Then (3.34) can be normalized to become

$$\frac{\partial u_m}{\partial t} = f(t) + \beta \frac{1}{r}\frac{\partial}{\partial r}\left(r\frac{\partial u_m}{\partial r}\right). \tag{3.39}$$

The radius of the pipe R' was used to scale the raidal coordinate and

$$\beta = \frac{\nu'_m}{\omega' R'^2} \tag{3.40}$$

can be viewed as the inverse of a Reynolds number. Also note that the dimensionless time coordinate has been defined as

$$t = \omega' t'. \tag{3.41}$$

With the Stokes boundary-layer thickness of the mud δ'_m introduced in (3.5), the ratio of the mud bed thickness to the wave-induced boundary-layer thickness d is re-defined as

$$d = \frac{R'}{\sqrt{\pi}\delta'_m} = \frac{1}{\sqrt{2\pi\beta}}, \tag{3.42}$$

The analytical solution for u_m can be obtained by solving (3.39) with the no-slip condition along the wall (e.g. Carslaw & Jaeger, 1986):

$$u_m(r,t) = \int_0^t f(\tau) \sum_{n=1}^{\infty} \frac{2}{\lambda_n \mathrm{J}_1(\lambda_n)} \mathrm{J}_0(\lambda_n r) \exp\left[-\beta\lambda_n^2 (t-\tau)\right] \mathrm{d}\tau, \tag{3.43}$$

Table 3.2: Cases of the U-tube experiments with sugar water.

Case No.	P'	ω'	d	β	Re
	$(\mathrm{m\ s^{-2}})$	$(\mathrm{rad\ s^{-1}})$			
U1	0.167	2.927	20.4	3.81×10^{-4}	1.4×10^2
U2	0.246	3.123	21.1	3.57×10^{-4}	2.5×10^2

where, J_0 and J_1 are the Bessel functions of the first kind of order 0 and 1, respectively, and λ_n ($n = 1, 2, 3, \ldots$) are positive zeros of J_0.

3.4.5 Experimental cases and results

As a model for viscous fluid-mud, sugar water of 35% weight concentration ($\rho'_m = 1156\ \mathrm{kg\ m^{-3}}$, $\nu'_m = 7.876 \times 10^{-6}\ \mathrm{m^2\ s^{-1}}$) was used to ensure $d > 1$ within the U-tube. Two cases with different pressure gradients were tested by adjusting the stroke of the piston and the experimental cases are summarized in table 3.2, in which a Reynolds number Re is defined as

$$Re = \frac{P'^2/\omega'^3}{\nu'}. \tag{3.44}$$

Note that (3.44) is equivalent to (2.42) since here the centerline velocity scales with P'/ω'. Lodahl, Sumer & Fredsøe (1998) reported the critical Reynolds number for the oscillatory flow in a circular pipe to be $Re = 1.5 \times 10^5$ when $d > 10$. As can be seen in table 3.2, the flows were well within the laminar range in both cases.

To be consistent with the previous section, here the stretched coordinate η

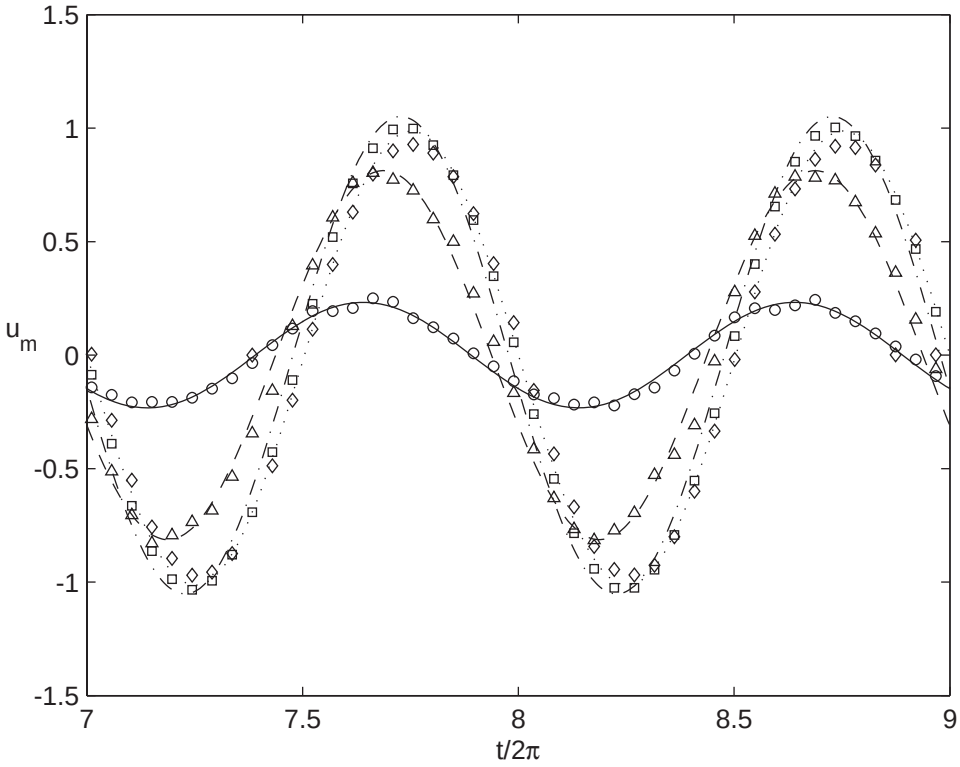

Figure 3.22: Time histories of the dimensionless axial velocity at four different radial positions for the case U1: ∘, PIV data at $\eta = 0.1$; △, PIV data at $\eta = 0.5$; □, PIV data at $\eta = 1.0$; ⋄, PIV data at $\eta = 10.0$; ——, analytical solution at $\eta = 0.1$; − − − − −, analytical solution at $\eta = 0.5$; —·—, analytical solution at $\eta = 1.0$; · · · · ·, analytical solution at $\eta = 10.0$.

has been re-defined as

$$\eta = \frac{R' - r'}{\sqrt{\pi}\delta'_m}. \tag{3.45}$$

Then the domain of η takes $0 \leq \eta \leq d$, and the boundary layer lies in $0 \leq \eta \leq 1$. The dimensionless axial velocity at four different radial positions ($\eta = 0.1$, 0.5, 1.0, and 10) for the cases U1 and U2 are shown in figures 3.22 and 3.23, respectively. Very good agreement between the measured data and the analytical solution is observed in both cases. Clearly there is a phase lag between the velocity inside the boundary layer and that outside as predicted by the theory.

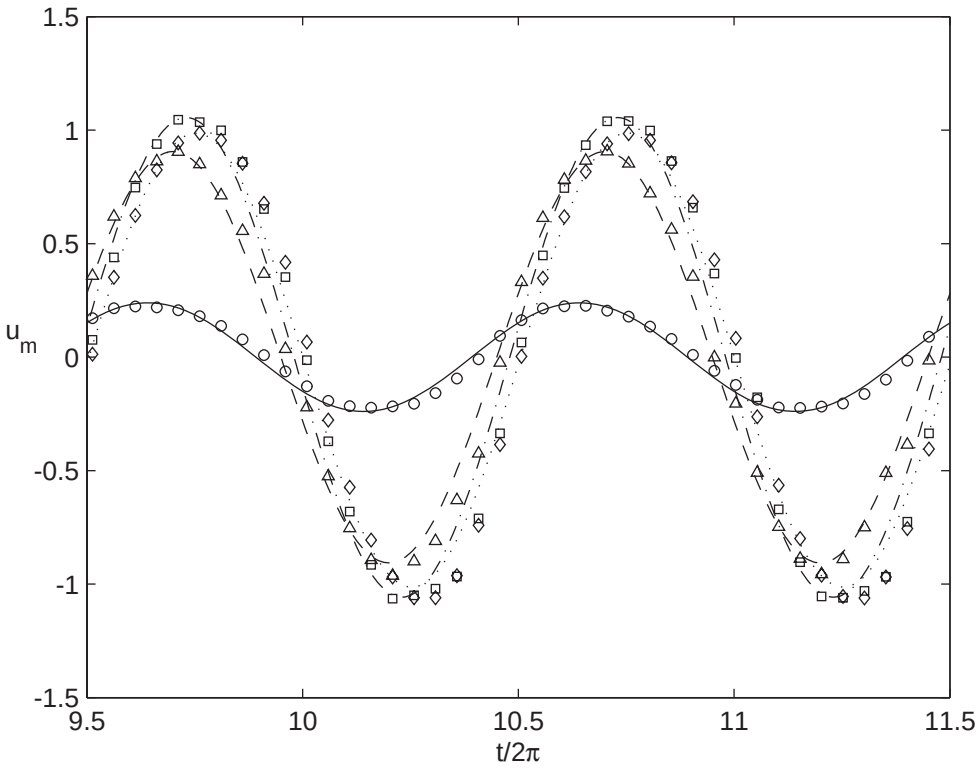

Figure 3.23: Time histories of the dimensionless axial velocity at four different radial positions for the case U2: ∘, PIV data at $\eta = 0.1$; △, PIV data at $\eta = 0.5$; □, PIV data at $\eta = 1.0$; ⋄, PIV data at $\eta = 10.0$; ——, analytical solution at $\eta = 0.1$; − − − − −, analytical solution at $\eta = 0.5$; — · —, analytical solution at $\eta = 1.0$; · · · · ·, analytical solution at $\eta = 10.0$.

The phase lag is more evident in the radial profiles of the axial velocity in figures 3.24 & 3.25. Note that only the region near the wall ($0 \leq \eta \leq 5$) is shown in the figure. While the flow outside the boundary layer is more or less uniform, a dramatic velocity gradient is seen in the boundary layer. The boundary layer flow reacts to the pressure gradient almost instantly, and the flow reversal is seen whenever the pressure gradient becomes unfavorable.

It should be noted that oscillatory pipe flow of a viscous fluid has been ex-

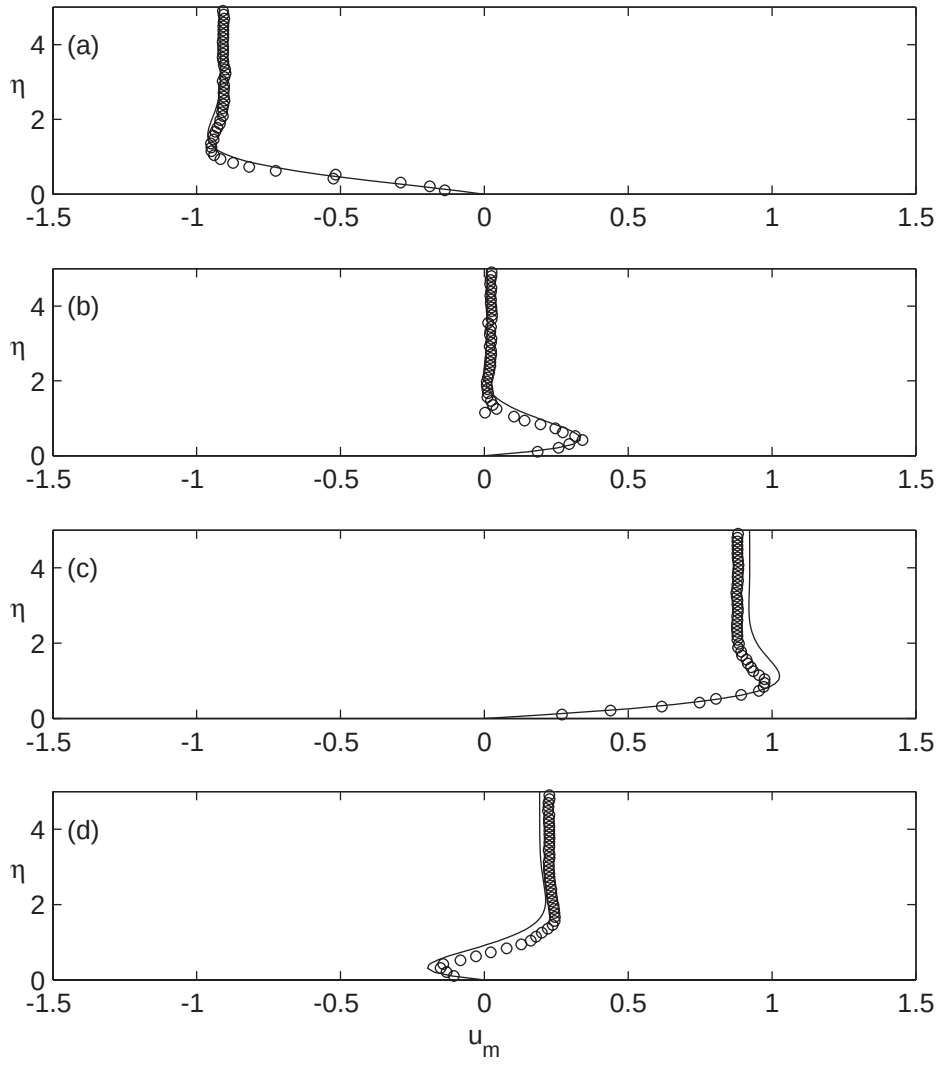

Figure 3.24: Radial profiles of the dimensionless axial velocity for the case U1 at four different phases during the 10th period: ∘, PIV data; ——, analytical solution. (*a*) $t/2\pi = 10.32$; (*b*) $t/2\pi = 10.50$; (*c*) $t/2\pi = 10.69$; (*d*) $t/2\pi = 10.97$.

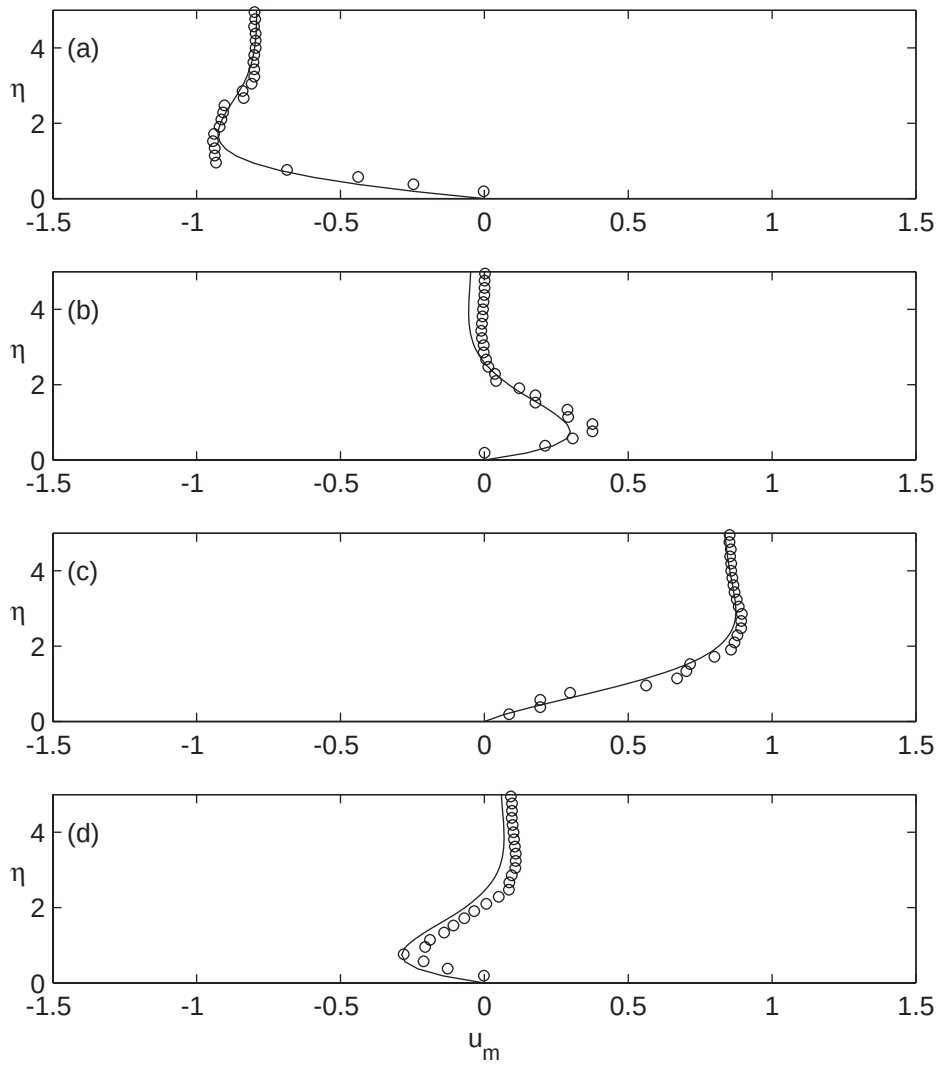

Figure 3.25: Radial profiles of the dimensionless axial velocity for the case U2 at four different phases during the 10th period: ∘, PIV data; ——, analytical solution. (*a*) $t/2\pi = 10.16$; (*b*) $t/2\pi = 10.51$; (*c*) $t/2\pi = 10.85$; (*d*) $t/2\pi = 11.00$.

haustively studied (e.g. Uchida, 1956; Lodahl *et al.*, 1998), and that the novelty in this research lies in its interpretation rather than the result itself. Indeed, the idea of using the U-tube in experiments on mud flows allows one to study more realistic, thus difficult problems. For example, mud often exhibits non-Newtonian behaviors and sophisticated hysteresis (e.g. Balmforth & Craster, 2001), which will be discussed in the next chapter.

3.5 Concluding remarks

In this chapter, theoretical and experimental analyses on the viscous flows inside a muddy seabed driven by the horizontal pressure gradient induced by a long wave have been presented. Especially, the analytical solution of the linearized governing equation by Liu & Chan (2007) has been experimentally verified and the numerical solution of the nonlinear equation has been calculated.

Two sets of experiments, one in the wave tank and the other in the U-tube, revealed the important role of the mud-layer thickness compared to its own boundary-layer thickness in characterizing the mud flow regimes. Time histories of the horizontal velocity showed that velocities at different elevations have the same direction when $d < 1$ and the velocity profile can be fitted by a parabola. However, when the thickness of the mud layer is much larger than the bottom boundary layer thickness, the velocity profile appears to be a plug flow above a thin viscous layer. The plug flow velocity and thickness can be determined theoretically. More complex flows occur for $d \sim O(1)$. Finally, measured and estimated time histories of the bottom shear stress showed that it becomes almost independent of d, when $d > 1.5$.

Additionally, the present work provides a new experimental framework regarding long-wave-induced mud flows using the U-tube. This method eliminates the difficulties that originate from the water–mud interface. Notice that the effects of the interfacial boundary as well as those of the non-uniformities of the flow in the horizontal direction cannot be studied with this methodology. Nevertheless, this method provides a means to experimentally simulate wave-induced flows, or more precisely pressure-gradient-driven flows, of muds with complex rheological characteristics, as will be shown in Chapter 4.

CHAPTER 4

OSCILLATORY FLOWS OF YIELD-STRESS FLUIDS

4.1 Introduction

It is well-known that high-concentration mud suspensions are usually non-Newtonian in the sense that the internal microscopic structure of the material, in addition to the other forces common to Newtonian fluids, balances the external forces exerted to the material (see e.g. Balmforth & Craster, 2001; Winterwerp & van Kesteren, 2004). The same matter may also be called non-Hookean if the focus is on the resistence of the intact but deformable microscopic strucuture. Apparently, viscosity and elasticity are the two important parameters that characterize the macroscopic mechanical properties of the mud, justifying the use of viscoelastic models in many cases (e.g. MacPherson, 1980; Foda, 1989; Jain & Mehta, 2009). Notice that both the viscosity and the elasticity, in general, are not constants but functions of flow and its history as well as the material properties.

For the high-concentration mud suspensions, the elasticity is often neglected and the non-Newtonian character of the mud is manifested by the decrease of the viscosity with the increasing rate of shear strain, so-called shear-thinning behavior (Mei & Liu, 1987; Ng & Mei, 1994). Among many shear-thinning, non-Newtonian models (see, e.g. Bird, 1976), the simplest is the Bingham model (Bingham, 1922). This material remains as a rigid solid as long as the applied shear stress is less than a threshold (yield stress), while it can flow like a viscous fluid otherwise. The Bingham model and other general yield-stress-fluid models such as the Herschel–Bulkley model (for a review, see Nguyen & Boger, 1992) have been successfully applied to many fluid problems both in nature

(Balmforth & Craster, 2001) and in industry (Bird, Dai & Yarusso, 1983).

Mei & Liu (1987) and more recently Chan & Liu (2009) studied flows inside a seabed made of a Bingham mud driven by the pressure-gradient force which again is induced by water surface waves. In particular, Chan & Liu (2009) argued that the multiple alternating layers of rigid-solid-like plug flow region and of fluid-like shear flow region can develop within the muddy seabed. While considering the Stokes's second problem of a yield-stress fluid described by the Herschel–Bulkley model, Balmforth, Forterre & Pouliquen (2009) also predicted the presence of the alternating layers of plug flow and of shear flow. However their experiment, using a kaolin slurry partially filling an oscillating rectangular box, showed characteristically different result from that of the numerical simulation. Balmforth *et al.* (2009) speculated that the hysteresis, specifically thixotropy which is defined as a gradual decrease of the viscosity under shear stress followed by a gradual recovery of structure when the shear stress is removed (Barnes & Walters, 1985), may be responsible for the discrepancy. It is remarked here that their experiment was not consistent with the Stokes's problem. Since the entire box was in oscillatory motion, not just the bottom plate, the problem is equivalent to the oscillatory pipe flow in a reference frame moving with the box as long as the vertical displacement of the free surface is negligible.

The initial motivation of the present research was to experimentally demonstrate the aforementioned alternating rigid-solid-like and fluid-like layers in a muddy seabed made of a yield-stress fluid. Particulary, aqueous solutions of Carbopol were used as they are known to follow typical yield-stress-fluid models without any significant thixotropy (Piau, 2007). Moreover, they are optically clear so that quantitative flow visualization technique, e.g. particle image ve-

locimetry (PIV), can be readily applied. However, the experimental results were again very different from the numerical simulations and the alternating layers structure was not apparent. It is argued here that this discrepancy results from applying the constitutive model based on steady-shear measurements to the unsteady flow. Therefore, in this study, a new procedure to deduce the underlying constitutive equations directly from the flow measurements is suggested. It is found that the deformability and the eventual dismantlement of the microscopic structure play important roles in the unsteady flow. Analytical solutions are then found which show much improved agreement with the experimental data.

In the following section, the rheological characteristics of the Carbopol solutions in relation to the Bingham model will be reviewed. The experiments were carried out using the U-tube (see §3.4.1) and the results will be compared with the numerical simulations based on the Bingham-like constitutive relation in §4.3. Poor agreement was observed and more pertinent rheological properties of the Carbopol solutions under the oscillatory motions were deduced from the PIV data, which will be shown in §4.4. After summarizing the chapter, in §4.5, the possibility of developing an *in-situ* rheometer will be discussed.

4.2 Carbopol: a physical model for the non-thixotropic yield-stress-fluid mud

The objective of the present research is to experimentally investigate long-wave-induced flows inside seabed made of a yield-stress fluid, namely the one described by the Bingham model. In this section, first we review the constitu-

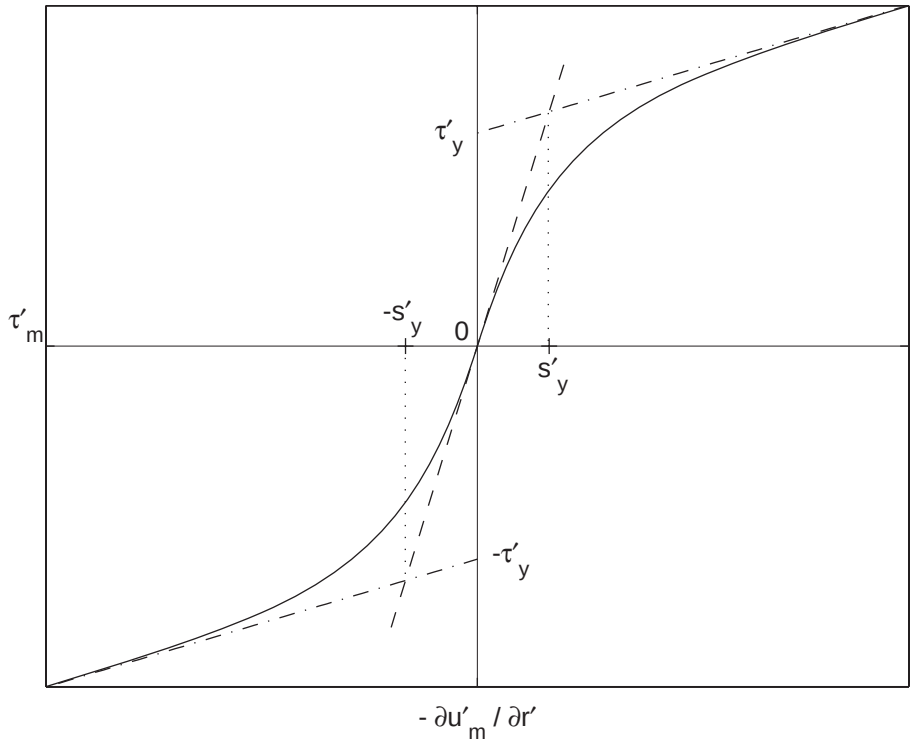

Figure 4.1: Constitutive relations for yield-stress fluids; —·—, the Bingham model (4.2); ——, the Papanastasiou model (4.3); −−−−−, the initial Newtonian state (4.4).

tive equations, followed by flow-curve measurements of a yield-stress fluid, the aqueous solution of Carbopol.

4.2.1 Bingham model and its regularized variation

In simple shear the Bingham model in terms of the cylindrical coordinate reads as follows (see figure 4.1):

$$\frac{\partial u'_m}{\partial r'} = 0, \qquad \left|\tau'_m\right| \le \tau'_y; \tag{4.1}$$

$$\tau'_m = -\rho'_m \nu'_m \frac{\partial u'_m}{\partial r'} - \tau'_y \operatorname{sgn}\left(\frac{\partial u'_m}{\partial r'}\right), \qquad \left|\tau'_m\right| \ge \tau'_y, \tag{4.2}$$

in which τ'_y denotes the yield stress and the other variables have been defined in §3.4.2. This constitutive model has been extensively used in many applications and analytical solutions are available for some simple flows (see Bird *et al.*, 1983). However, it is often hard to track the yield surface and the solutions can exhibit singularities in more complex flows especially when the strain rate vanishes (Balmforth & Craster, 2001).

To avoid difficulties arising from the discontinuous constitutive relation, Papanastasiou (1987) suggested a modified version of the Bingham model (see figure 4.1):

$$\tau'_m = -\rho'_m \nu'_m \frac{\partial u'_m}{\partial r'} - \tau'_y \operatorname{sgn}\left(\frac{\partial u'_m}{\partial r'}\right)\left[1 - \exp\left(-\frac{1}{s'_y}\left|\frac{\partial u'_m}{\partial r'}\right|\right)\right], \tag{4.3}$$

where s'_y is the characteristic strain rate at which the flow is *yielded* as depicted in figure 4.1. As the strain rate increases (4.3) converges to (4.2), whereas with a vanishing strain rate the model approximates a highly viscous Newtonian fluid, i.e.

$$\tau'_m \to -\left(\rho'_m \nu'_m + \tau'_y / s'_y\right)\frac{\partial u'_m}{\partial r'} = -\rho'_m \nu'_0 \frac{\partial u'_m}{\partial r'}, \quad \frac{\partial u'_m}{\partial r'} \to 0, \tag{4.4}$$

where

$$\nu'_0 \equiv \nu'_m + \tau'_y / \left(\rho'_m s'_y\right) \tag{4.5}$$

is the zero-strain-rate viscosity. That is to say, the modified model (4.3) is not singular even when the rate of strain becomes zero, while it can be arbitrarily close to the Bingham model (4.1 & 4.2) with a sufficiently small value of s'_y. Consequently, this model has been successfully utilized for numerical simulations of yield-stress-fluid flows and known as computationally economic and robust compared to other kinds of regularized models such as the bi-viscosity model (see e.g. Fan, Phan-Thien & Tanner, 2001). Finally the yield surface can be readily tracked if appropriately defined, for example, as $\partial u'_m / \partial r' = \pm s'_y$.

4.2.2 Rheological properties of aqueous solutions of Carbopol

Carbopol is well-known for its thickening property in aqueous system (Barnes & Walters, 1985). Individual particles take the form of roughly spherical blobs that tend to swell in water and beyond certain concentration they squeeze each other (Coussot *et al.*, 2009). Under large enough shear stress, the squeezed blobs can jump from one place to another hence the aqueous solution of Carbopol appears to have a yield stress (Piau, 2007). Once the applied stress is removed, the repulsive forces of the blobs quickly restores the overall strucutre, thus there is no inherent mechanism responsible for siginificant thixotropy. Note that this property is common to other yield-stress fluids that are formed by microscopic repulisve forces (Coussot *et al.*, 2009), while materials formed by the attractive interactions such as kaolin slurry exhibit substantial hysteresis (Balmforth & Craster, 2001). In addition, the Carbopol solution is optically clear, non-toxic and stable (Peixinho *et al.*, 2005).

For the experiments, Carbopol 940 polymer (Lubrizol Advanced Materials, Inc.) with two different concentrations (0.075% and 0.1% by weight) was used. Each time, the desired amount of the polymer powder was carefully added to 1 liter of distilled water on a magnetic stirrer, then mixed for 2 hours. After it was completely dissolved into water, sodium hydroxide was added to neutralize the solution. This procedure was repeated to make 50 liters of the solution for each concentration.

Rheological properties of the Carbopol solutions were measured using a rheometer (Anton-Paar Physica MCR 300) with a cone geometry (CP25-4.5sn478) and a plate in Professor Lynden Archer's laboratory at Cornell University. Flow curves shown in figure 4.2 were obtained by measuring the rate

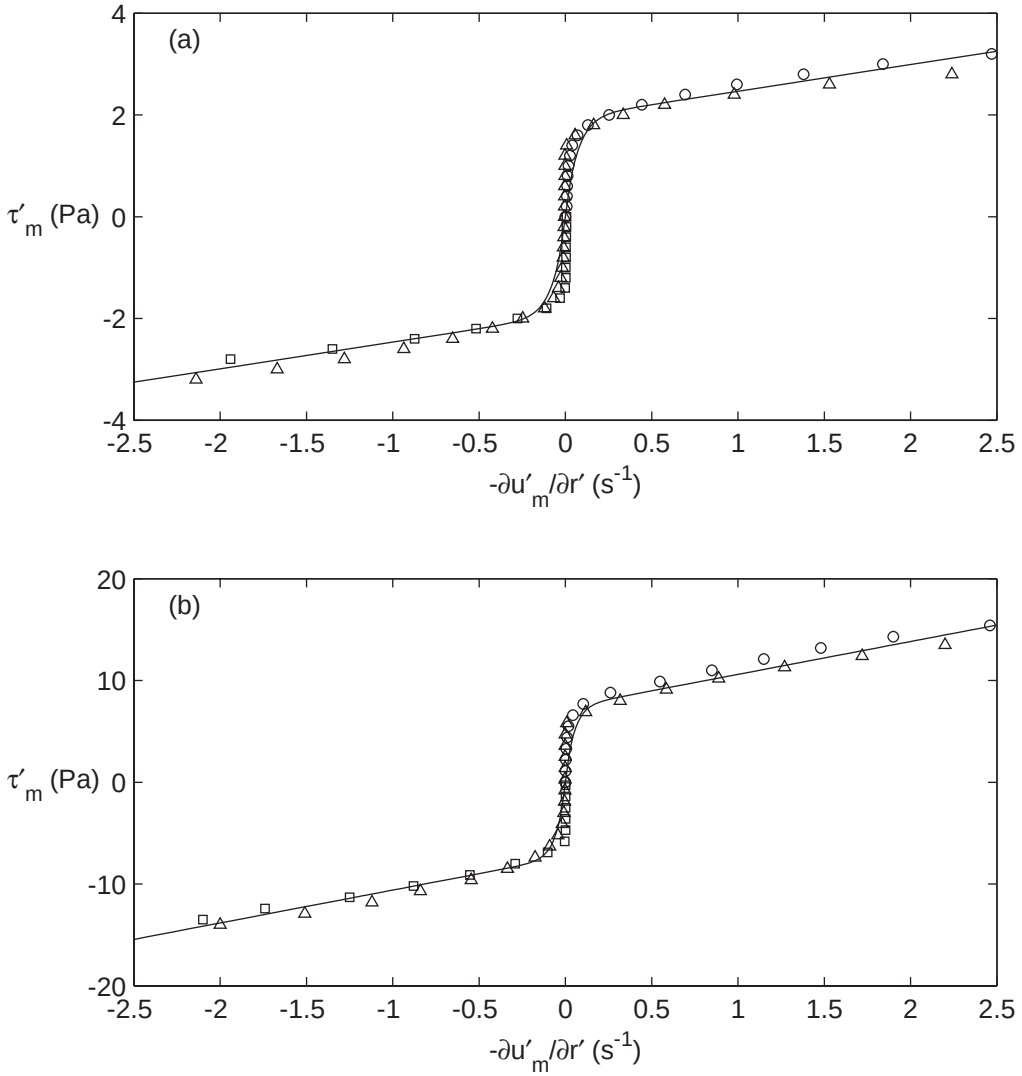

Figure 4.2: Rheological measurements of 0.075% Carbopol solution (*a*) and of 0.1% (*b*): ○, from zero shear stress to the maximum shear stress (τ'_{max}); △, from τ'_{max} to $-\tau'_{max}$; □, from $-\tau'_{max}$ to 0; ——, fitted Papanastasiou model (4.3).

Table 4.1: Fitted parameters of the Papanastasiou model (4.3) for the Carbopol solutions.

Concentration by weight (%)	ν'_m ($m^2\,s^{-1}$)	τ'_y (Pa)	s'_y (s^{-1})	γ
0.075	5.005×10^{-4}	1.939	0.039	1.05
0.1	3.076×10^{-3}	7.366	0.021	1.05

of strain while controlling the shear stress. For each measurement, the shear stress was maintained constant for 10 seconds to assure the steady state in the flow field before measuring the rate of strain. To estimate hysteretic effects, the shear stress was first increased to a certain level, say $\tau'_{\max}$, then decreased to $-\tau'_{\max}$, and finally increased back to zero. As can be seen in figure 4.2, hysteresis is not significant at least for the steady-shear measurements. Parameters of the Papanastasiou model (4.3) were then found from least-square curve fitting and are summarized in table 4.1.

Note that the values of the yield stresses and the viscosities agree very well with the independent measurements by Piau (2007). More specifically, from figure 29 of Piau (2007), the yield stress for the 0.075% concentration is about 2 Pa and that for the 0.1% concentration is 8 Pa. Also, figure 5 of Piau (2007) indicates that the viscosity values in table 4.1 are within the range of his measurements.

Though measured values of the rheological quantities for fluid mud under field conditions are scarce, Mei & Liu (1987) summarized some of the earlier measurements. Among them, typical values for the mud in Provins Estuary, France (Migniot, 1968) are listed in table 4.2 (see also Liu & Mei, 1990) to be compared with those of the Carbopol solutions in table 4.1.

Table 4.2: Typical values of the rheological properties of the fluid mud in Provins Estuary, France (Migniot, 1968).

Concentration by volume (%)	ν'_m ($m^2\,s^{-1}$)	τ'_y (Pa)	γ
5	3.3×10^{-4}	0.03	1.03
10	2.5×10^{-3}	0.79	1.06
20	1.8×10^{-2}	122	1.13

Clearly, rheological properties vary widely with the concentration of the sediment. The values for the 5–10% concentration in table 4.2 are comparable to those of the Carbopol solutions used in the experiments. It is noted that the yield stresses of the Carbopol solutions are considerably higher. Considering that the yield stress is the very material property of interest, the high values of the yield stress suit the purpose of the present research. However the one with the higer concentration (0.1%) of Carbopol turned out to be too thick to generate appreciable flow with the current experimental set-up, thus results using only the lower-concentration (0.075%) solution will be presented in the subsequent discussion. Nevertheless, rheological properties of the 0.1% Carbopol solution have been reported in table 4.1 to illustrate the sensitivity of those quantities to the concentration as well as the quality of steady-shear measurements.

4.3 The paradox of oscillatory pipe flows of the aqueous solutions of Carbopol

The experiments were carried out using the U-tube that has already been introduced in §3.4.1. Measurement techniques used for the experiments are described in §3.4.2 and §3.4.3. In this section, the experimental results are compared with the numerical simulations using the Papanastasiou model (4.3). Unexpectedly, they are characteristically different from each other, posing a paradox.

4.3.1 Numerical simulations

To solve the governing equation (3.34) with the regularized Bingham model (4.3) as the constitutive equation, an iterative scheme was employed in which the nonlinear viscosity is calculated based on the results from the previous iteration, while the linear operators are discretized by Crank–Nicolson method. In view of the initial Newtonian behavior as shown in figure 4.1 and in (4.4), the results of Newtonian fluid with the viscosity ν_0' were used as an initial guess. The iteration continued until the maximum relative error between the respective results from the current and the previous iterations was smaller than 10^{-6}. The finite difference equation, which is similar to (2.30), is not repeated here.

Table 4.3: Experimental cases with the 0.075% Carbopol solution.

Case No.	P'	ω'	d	He	Re_H
	$(\mathrm{m\,s^{-2}})$	$(\mathrm{rad\,s^{-1}})$	(cm)		
Y1	0.103	3.786	2.92	210	9
Y2	0.191	3.109	2.64	210	21
Y3	0.304	3.364	2.75	210	30
Y4	0.467	2.994	2.59	210	52

4.3.2 Experimental cases

Different cases were measured by varing the pressure gradient of the U-tube for the 0.075% Carbopol solution. Experimental cases are summarized in table 4.3, in which the Hedström number He and the associated Reynolds number Re_H are defined as follows (see Mei & Liu, 1987):

$$He = \frac{\tau_y' D'^2}{\nu_m'^2}, \tag{4.6}$$

$$Re_H = \frac{(P'/\omega')\, D'}{\nu_m'}. \tag{4.7}$$

While the critical Reynolds number at which an oscillatory pipe flow of a yield-stress fluid becomes turbulent, to the author's knowledge, has not been reported, the transition for a steady uni-directional flow occurs when $Re_H \approx 2100$ if $He < 10^4$ (Mei & Liu, 1987). The Reynolds numbers in table 4.3 are at least two orders-of-magnitude smaller than the critical value, and the flows appeared to be within laminar regime during the experiments.

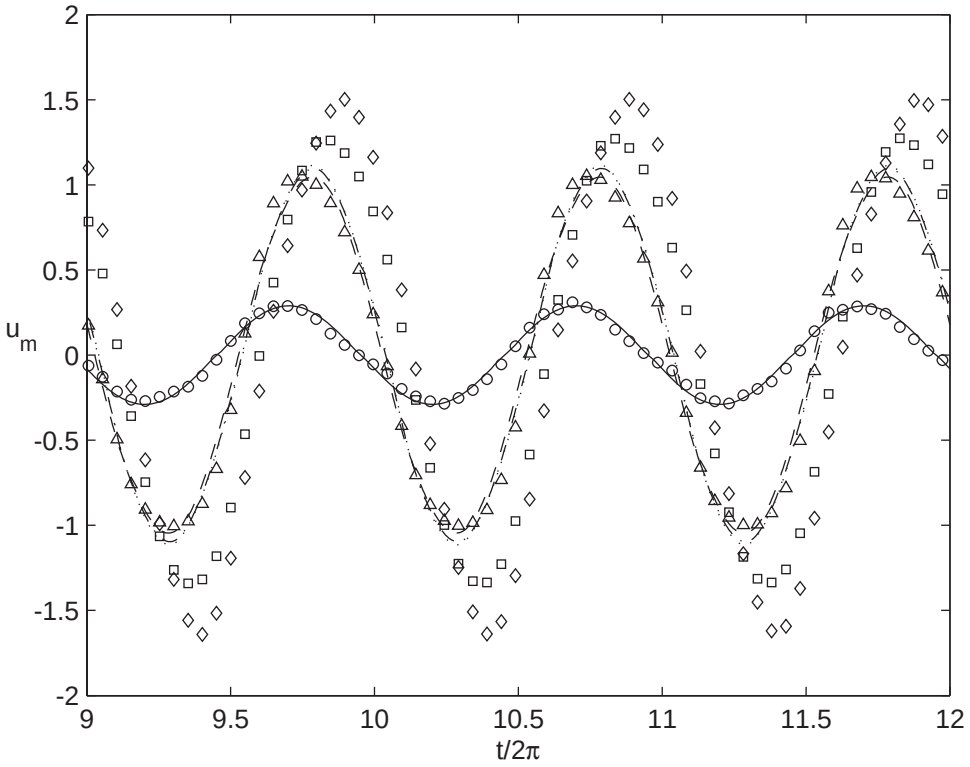

Figure 4.3: Time histories of the dimensionless axial velocity at four different radial positions for the case Y2: ∘, PIV data at $\eta = 0.1$; △, PIV data at $\eta = 1.0$; □, PIV data at $\eta = 1.8$; ⋄, PIV data at $\eta = d$; ——, numerical solution using the regularized Bingham model (4.3) at $\eta = 0.1$; −−−−−, numerical solution at $\eta = 1.0$; —·—, numerical solution at $\eta = 1.8$; · · · · ·, numerical solution at $\eta = d$.

4.3.3 Experimental results and discussions

Typical experimental results as well as those from the numerical simulations are shown in figures 4.3 & 4.4, in which the radial coordinate has been normalized by the length scale δ'_m (see 3.5) as in (3.45). Also plotted in figure 4.4 is the analytical solution for a Newtonian fluid with the same viscosity. Only the results for the case Y2 are shown here, because the purpose of this section is to demonstrate the significant difference between the numerical simulation and the experimen-

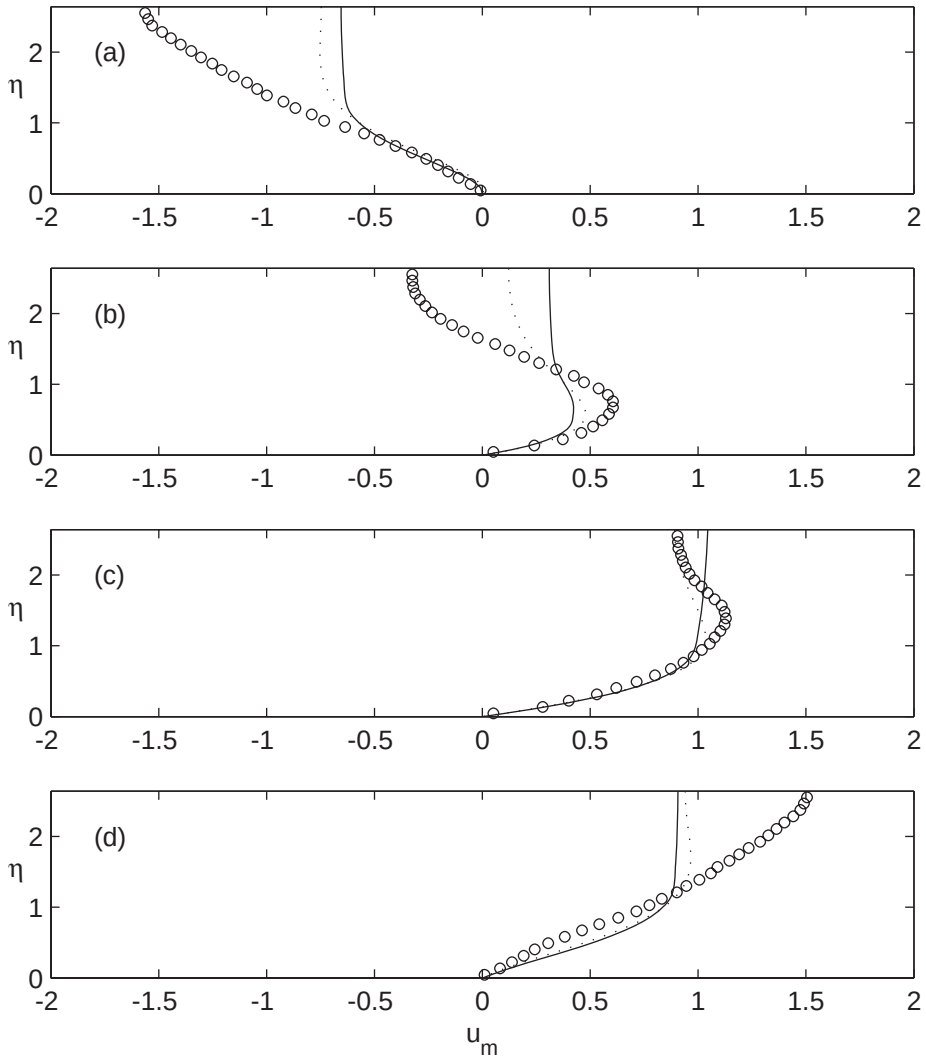

Figure 4.4: Radial profiles of the dimensionless axial velocity for the case Y2 at four different phases during the 10th period: ∘, PIV data; ——, the numerical solution using the regularized Bingham model (4.3); · · · · ·, the analytical solution for a Newtonian fluid with the same viscosity (3.43). (*a*) $t/2\pi = 10.44$; (*b*) $t/2\pi = 10.59$; (*c*) $t/2\pi = 10.74$; (*d*) $t/2\pi = 10.89$.

tal measurement. Rest of the experimental results will be discussed in the next section.

Dynamic developments of the unyielded plug flow and the sheared viscous zones have been considered as the key feature of the Bingham fluid as pointed out by Balmforth *et al.* (2009) and Chan & Liu (2009). Due to the no-shear-stress condition imposed along the water–mud interface, or the centerline of the pipe in this case, the numerical solution has the plug flow near the interface all the time. This behavior tends to smoothen the velocity profile as abrupt changes in forcing must be delayed and damped by the presence of the unyielded plug flow while Newtonian fluid would respond rather quickly. More interestingly, two disconnected plug flow regions are observed in the numerical solution whenever free-stream flow decelerates, one of which is near the bottom as in figure 4.4(b), consistent with the semi-analytical solution of Chan & Liu (2009). It is remarked here that the theoretical solution of Chan & Liu (2009) is only for a solitary wave, and the extension to the periodic forcing such as the one considered in this chapter is not straightforward.

One may observe that, at least near the wall ($\eta \leq 1$), agreement between the experiment and the numerical simulations (both the regularized Bingham and the Newtonian models) is generally good. However, the additional plug flow near the bottom under the unfavorable pressure gradient, which the regularized Bingham model predicts as in figure 4.4(b), are not observed.

Interestingly, or perhaps discouragingly, neither the regularized Bingham model nor the Newtonian model succeeds in predicting the experimental measurements, especially outside the boundary layer of the corresponding Newtonian fluid ($\eta > 1$). When compared to the cases with the viscous mud flow (see

Chapter 3), this result is indeed puzzling. While one can see the hook in the profile (figures 4.4*b* & 4.4*c*), which only occurs for $d > 1$, the sheared layer extends all the way up to the centerline (figures 4.4*a* & 4.4*d*), which corresponds to the case with $d < 1$. No plug-flow was ever observed and, therefore, the alternating layer structures predicted by Chan & Liu (2009) could not be seen.

Moreover, the maximum velocity along the centerline is about 50% higher than what would have been for an inviscid fluid. It is worth noting that Balmforth *et al.* (2009) also observed a similar overshooting, as large as nearly 100% for some cases, but failed to explain the reason. This issue will be addressed in the next section when an alternative dynamic rheological model is developed. Note that, despite the complex behavior of the Carbopol solution, the measured data clearly show periodicity (see figure 4.3), thus only the periodic motions will be considered in the following discussion.

4.4 The U-tube as a new kind of rheometer

The significant discrepancy between the experimental results and the numerical simulations suggests that the constitutive equation such as (4.3) does not reflect the dynamic behavior of the material. This might as well have been expected because typical rheological models for yield-stress fluids are based on the flow-curve measurement such as those in figure 4.2, which consists of a series of steay-state measurements. To explain the physics of the unsteady flows of the yield-stress fluids, therefore, one would need a new constitutive equation that reflects the dynamic mechanical properties of the material. In this section, some rheological information is deduced directly from the flow field measurements.

4.4.1 Estimation of the shear stress, the shear strain and the rate of shear strain from the velocity field data

First, it is noted that the substantial overshooting in the velocity measurements (see figure 4.4) cannot be fully explained by the viscous effects alone. By adding the elastic effects, on the other hand, the overshooting may be accounted for. To obtain the constitutive relations that are more appropriate for the oscillatory pipe flow of the Carbopol solutions, rheological quantities such as the shear stress, the shear strain and the rate of shear strain have been calculated directly from the experimental data.

Given the velocity and the pressure gradient, the shear stress τ'_m can be calculated as

$$\tau'_m(r', t') = -\frac{1}{r'} \int_0^{r'} r^* \left(\rho'_m \frac{\partial u'_m}{\partial t'} + \frac{\partial p'}{\partial x'} \right) \mathrm{d}r^*, \tag{4.8}$$

where it has been assumed that the shear stress vanishes along the centerline. To estimate the particle acceleration in (4.8), the velocity data at each radial position were first least-square fitted by a truncated Fourier series with first three terms with coefficients of determination (R-square) greater than 0.99. Typical results are shown in figure 4.5 for the case Y2. Then the fitted curves were analytically differentiated with respect to time. The integral in (4.8) was also analytically evaluated upon interpolating the integrand using the cubic spline for each time t' (for example, see figure 4.6). Finally, $\tau'_m(r', t')$ for all of the experimental cases are plotted in figures 4.7–4.10, respectively, along with the measured pressure gradient as well as the estimated inertial force at the center of the pipe.

As expected, the particle acceleration along the centerline shows about 180° phase difference compared to the forcing pressure gradient for all the experi-

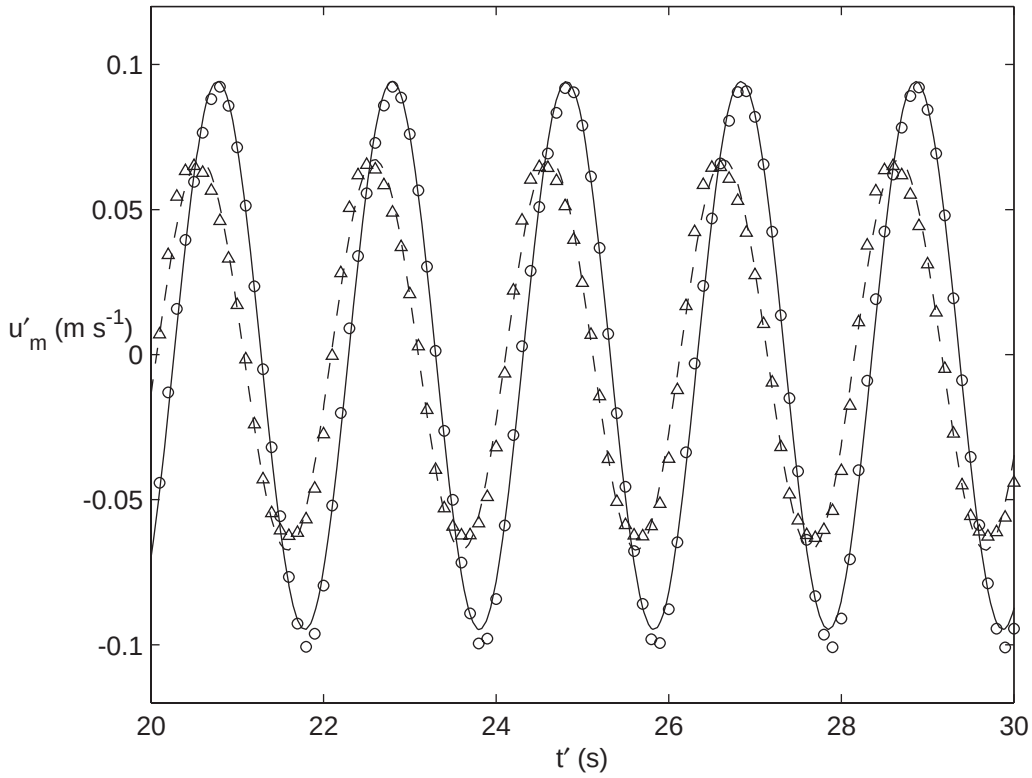

Figure 4.5: Curve fitting of time histories of the axial velocity with a truncated Fourier series at two different radial positions for the case Y2: ∘, PIV data at $r' = 0$ cm; △, PIV data at $r' = 5.0$ cm; ——, fitted curve at $r' = 0$ cm; −−−−−, fitted curve at $r' = 5.0$ cm.

mental cases. The shear stress also appears to be periodic in time with the same frequency as that of the forcing. By definition, the shear stress vanishes at the center of the pipe and it monotonously increases in magnitude with increasing r'. Also the experimental cases with the higher Re_H show the larger maximum shear stresses.

In figure 4.11, the dimensionless amplitude of the shear stress is plotted against the radial coordinate, in which the shear stress is normalized by the

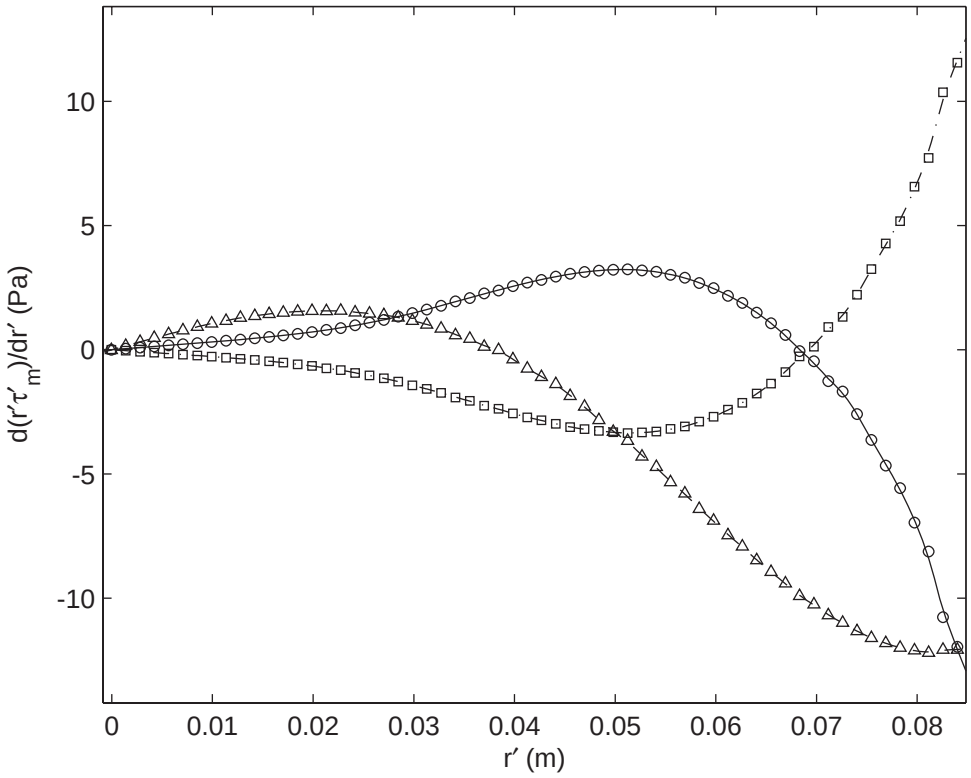

Figure 4.6: Interpolation of the radial profiles of the integrand in (4.8), that is $\mathrm{d}(r'\tau'_m)/\mathrm{d}r'$, at three different instants for the case Y2: ∘, experimental data at $t' = 24$ s; △, experimental data at $t' = 24.5$ s; □, experimental data at $t' = 25$ s; ——, interpolation at $t' = 24$ s; − − − − −, interpolation at $t' = 24.5$ s; —·—, interpolation at $t' = 25$ s.

yield stress:

$$\tau_m = \frac{\tau'_m}{\tau'_y}. \tag{4.9}$$

The experimental cases with the lower Reynolds numbers (Y1 & Y2) are characterized by the inflection points in the profiles and their amplitudes remain close to the yield stress. The profiles for the other cases resemble that of a typical Newtonian fluid, of which the shear stress amplitude varies more or less linearly within the boundary layer ($\eta < 1$). Based on the observations, it is conjectured that the material properties change from solid-like state under lower

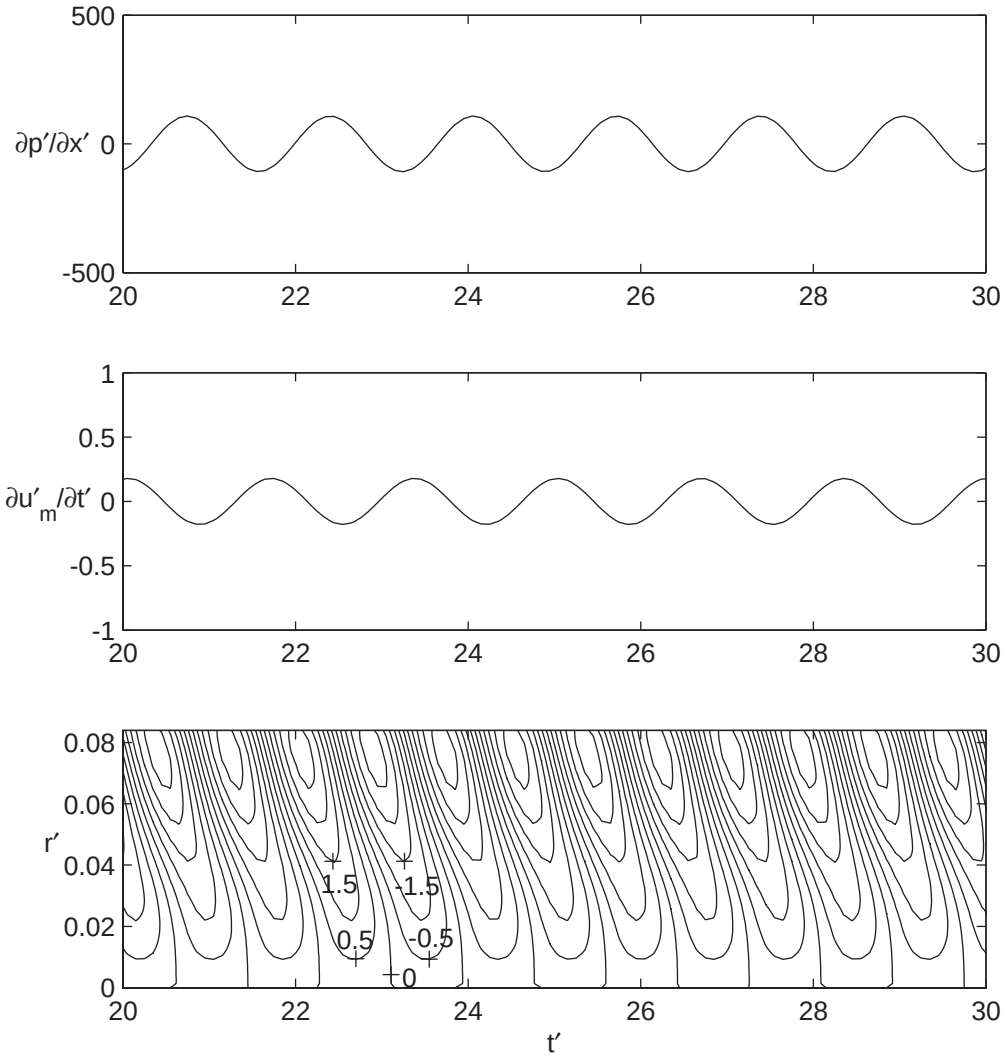

Figure 4.7: Time histories of the measured pressure gradient in Pa m^{-1} (top panel) and the estimated acceleration along the centerline in m s^{-2} (mid panel) and the contour plot of the estimated shear stress in Pa as a function or r' (m) and t' (s) (bottom panel) for the case Y1.

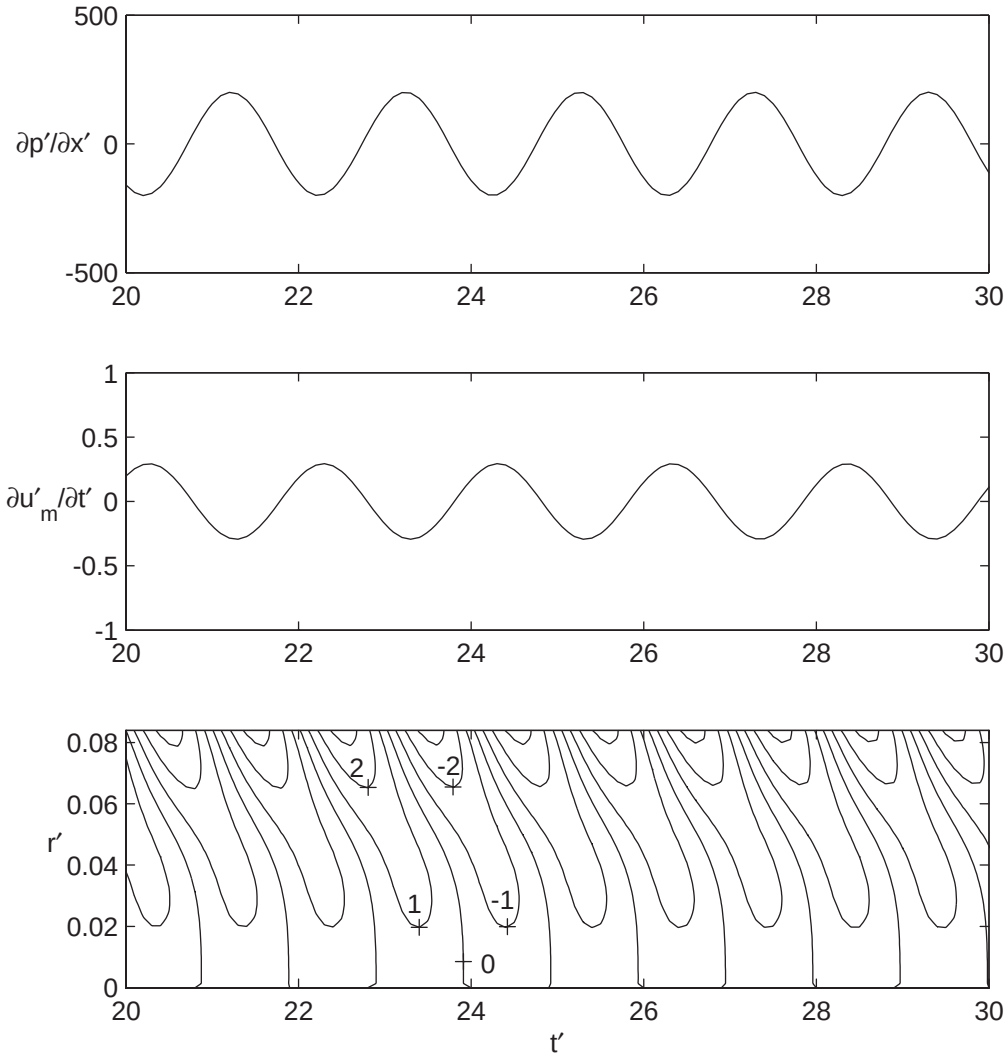

Figure 4.8: Time histories of the measured pressure gradient in Pa m^{-1} (top panel) and the estimated acceleration along the centerline in m s^{-2} (mid panel) and the contour plot of the estimated shear stress in Pa as a function or r' (m) and t' (s) (bottom panel) for the case Y2.

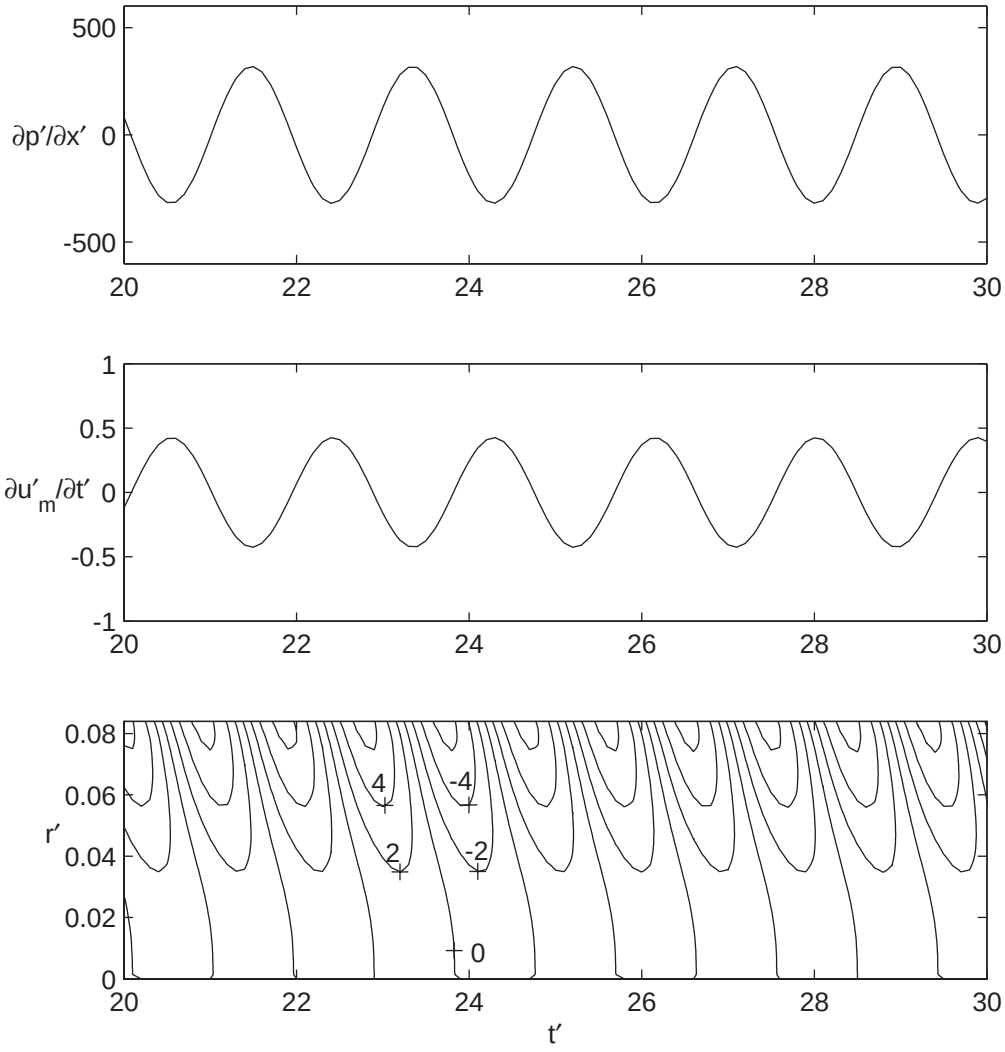

Figure 4.9: Time histories of the measured pressure gradient in Pa m^{-1} (top panel) and the estimated acceleration along the centerline in m s^{-2} (mid panel) and the contour plot of the estimated shear stress in Pa as a function or r' (m) and t' (s) (bottom panel) for the case Y3.

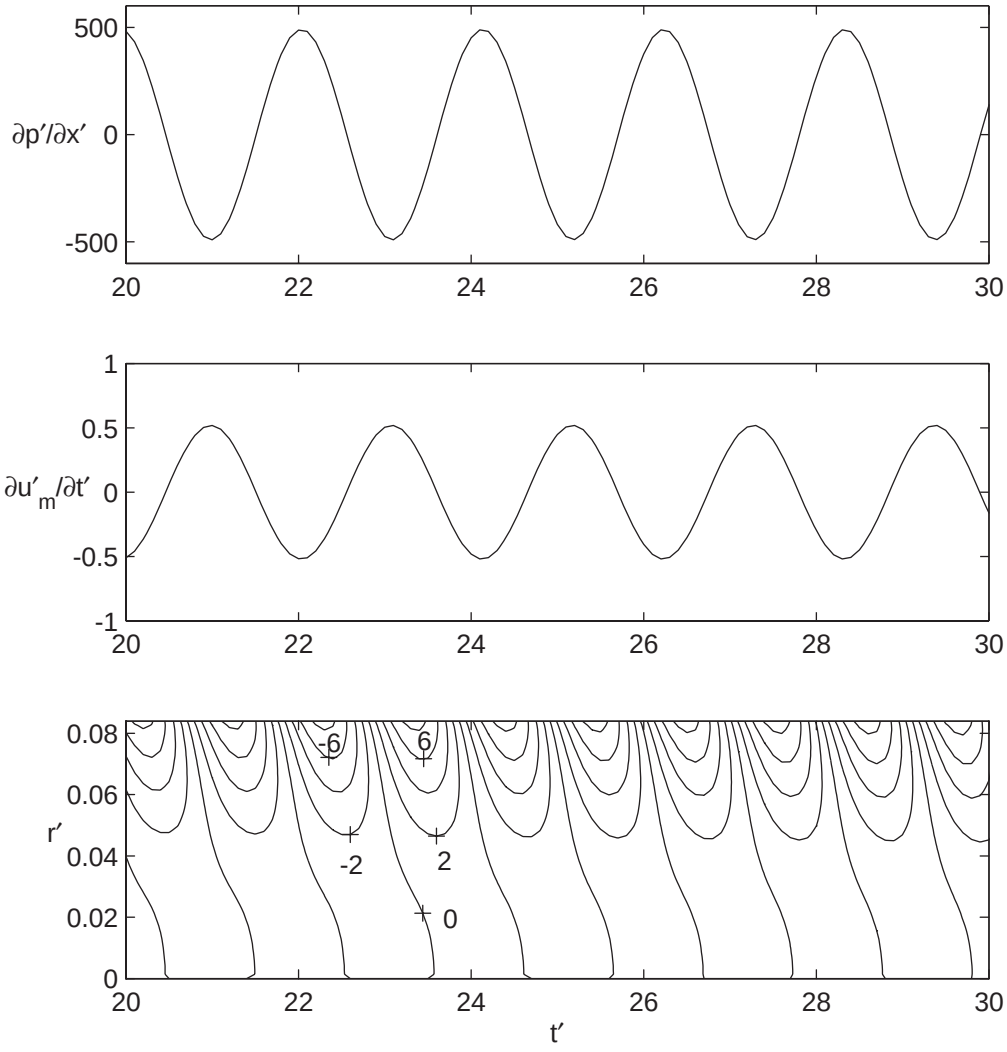

Figure 4.10: Time histories of the measured pressure gradient in Pa m^{-1} (top panel) and the estimated acceleration along the centerline in m s^{-2} (mid panel) and the contour plot of the estimated shear stress in Pa as a function or r' (m) and t' (s) (bottom panel) for the case Y4.

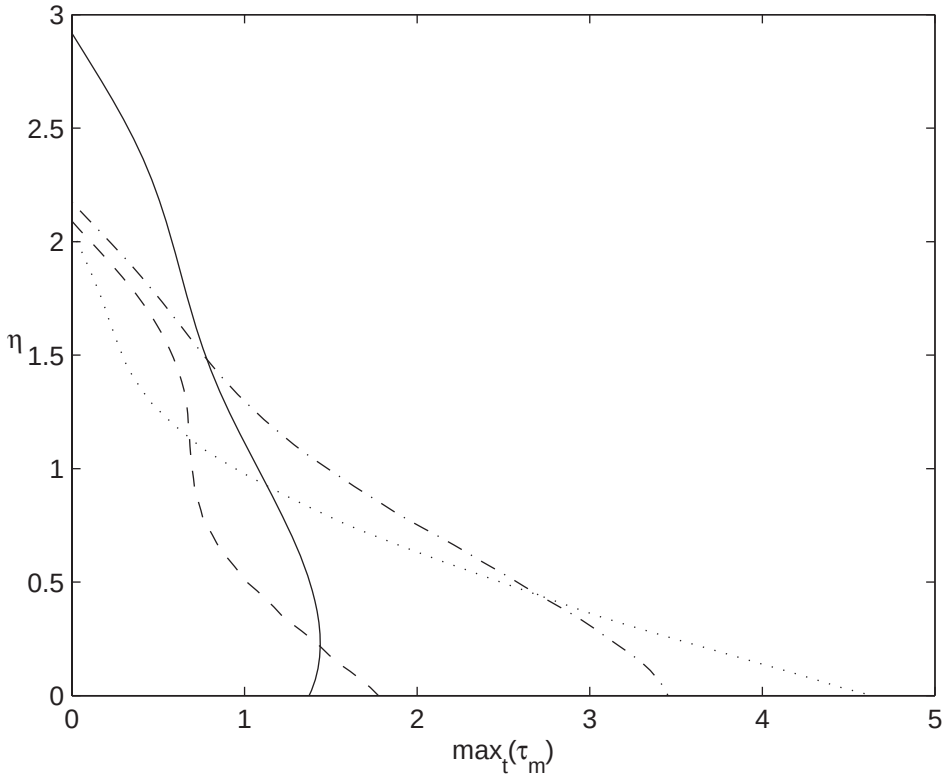

Figure 4.11: Radial profiles of the dimensionless amplitude of the estimated shear stress: ——, case Y1; − − − − −, Y2; — · —, Y3; · · · · ·, Y4.

pressure loading to fluid-like state under higher pressure loading. This point will be further investigated in the next section.

The particle displacements $X'(r', t')$ were obtained by analytically integrating the fitted curves of the velocity data (e.g. figure 4.5). To obtain the analytical expressions of the radial profiles of the displacement, the data were least-square fitted with a fourth-order polynomial which efficiently avoided the adverse effects of the noise, while maintaining satisfactory goodness-of-fit with R-square values typically greater than 0.99 (see figure 4.12). On the other hand, the velocity data are almost free of noise but its radial profiles have more pronounced

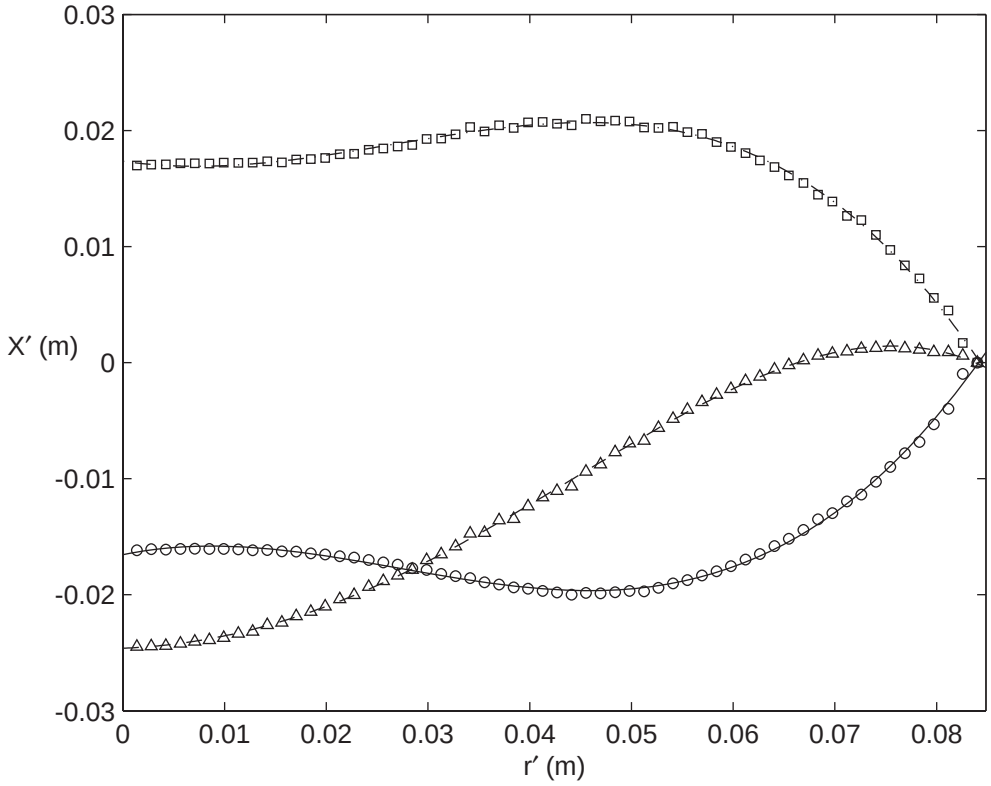

Figure 4.12: Curve fitting of the radial profiles of the horizontal displacement with a fourth-order polynomial at three different instants for the case Y2: ∘, experimental data at $t' = 24$ s; △, experimental data at $t' = 24.5$ s; □, experimental data at $t' = 25$ s; ——, fitted curve at $t' = 24$ s; − − − − −, fitted curve at $t' = 24.5$ s; — · —, fitted curve at $t' = 25$ s.

curvature. So the cubic spline was used to interpolate the radial profiles of the velocity as shown in figure 4.13. Finally, the radial gradients of the displacement (shear strain) and of the velocity (rate of shear strain) were estimated by differentiating the respective quantities with respect to the radial position r'.

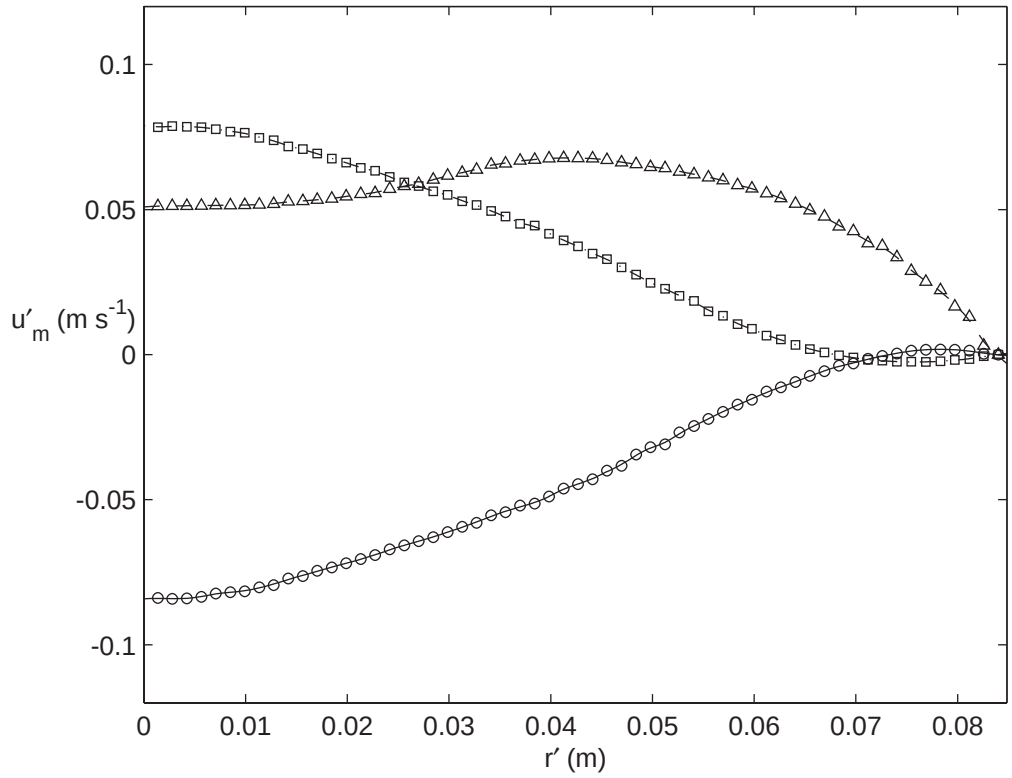

Figure 4.13: Interpolation of the radial profiles of the horizontal velocity with cubic spline at three different instants for the case Y2: ∘, experimental data at $t' = 24$ s; △, experimental data at $t' = 24.5$ s; □, experimental data at $t' = 25$ s; ——, interpolation at $t' = 24$ s; − − − − −, interpolation at $t' = 24.5$ s; — · —, interpolation at $t' = 25$ s.

4.4.2 Experimental construction of the constitutive relations

If the material is purely elastic, a straight line that goes through the origin would be obtained in the stress–strain plot. On the other hand, the shear stress–rate of shear strain plot would be composed of concentric ellipses with the center at the origin and the axes coincident with the coordinate axes, which results from the fact that the phase difference between the shear stress and the rate of shear strain is 90° under a sinusoidal motion. For a purely viscous fluid, the opposite

is the case: (i) a linear relationship between the shear stress and the rate of shear strain; and (ii) the concentric ellipses in the stress–strain plot. Note that the correlation coefficient for the linear line is 1, whilst those of the ellipses vanish, if the axes are parallel to the respective coordinate axes.

In figures 4.14–4.17, the shear stress is plotted against the rate of shear strain and the shear strain at four different radial positions for each of the cases, respectively. Again the periodicity and the monotonous increase of the shear stress toward the wall are evident. Apparently both the rate of shear strain and the shear strain have sophisticated and nonlinear functional relatioships with the shear stress, that change from one location to another and vary across the experimental cases. In other words, the same material appears to have distinctive rheological characteristics according to the flow history. Similar observations can also be made from figure 4.18, in which the entire data is plotted collectively.

To detect any linear dependence, the correlation coefficients between the shear stress and the rate of shear strain and those between the shear stress and the shear strain for each of the cases have been computed (see table 4.4). In general, the correlation between the rate of shear strain and the shear stress tends to increase as the forcing pressure gradient becomes larger, and the opposite trend is observed between the shear strain and the shear stress. Note that the negative correlation between the shear stress and the shear strain for the case Y4 is seen. Considering that the absolute value is very small, it is understood that there exists negligible correlation between them.

Neglecting the nonlinearity and the non-uniformity, the viscosity and the shear modulus for each of the experimental cases were estimated by fitting a

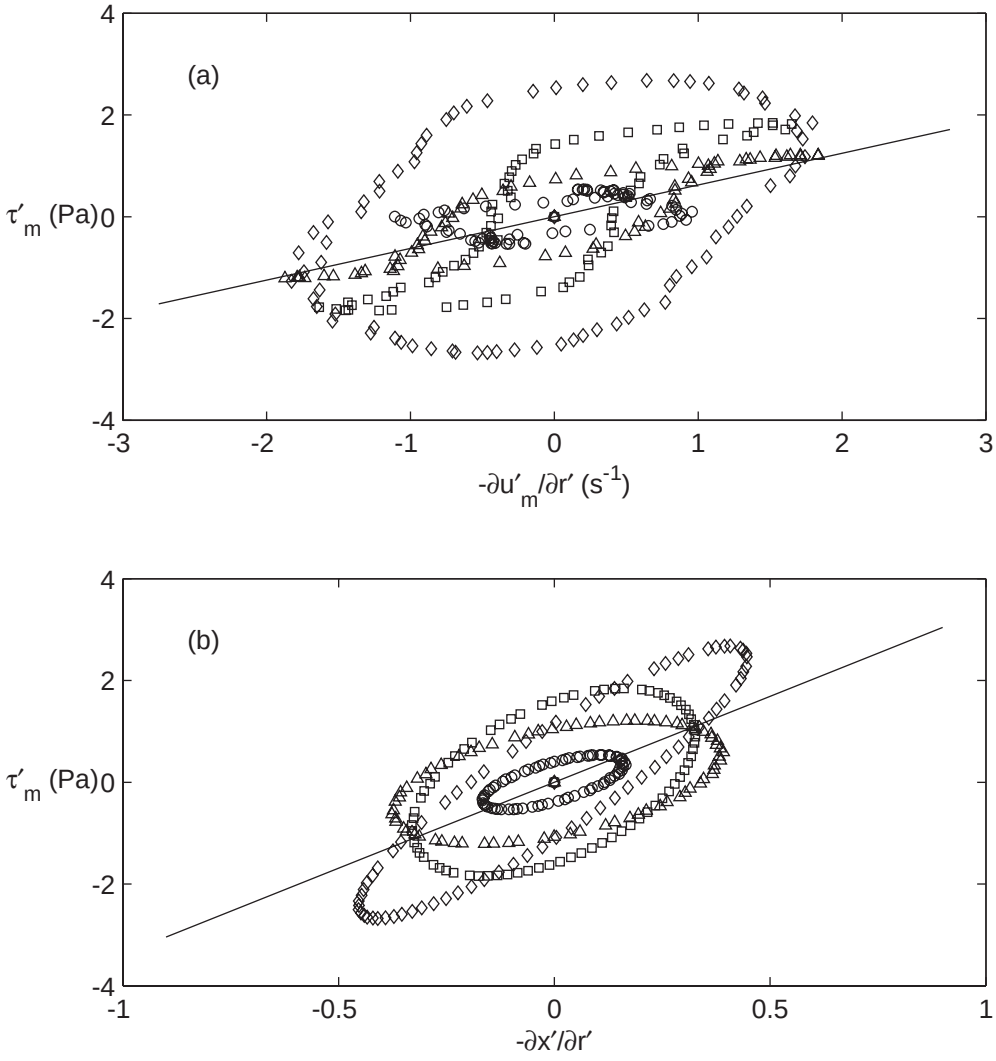

Figure 4.14: (*a*) Shear stress–rate of shear strain relations and (*b*) shear stress–shear strain relations at four different radial positions for the case Y1: ○, r' = 1 cm; △, r' = 3 cm; □, r' = 5 cm; ◇, r' = 7 cm; ——, linear regression.

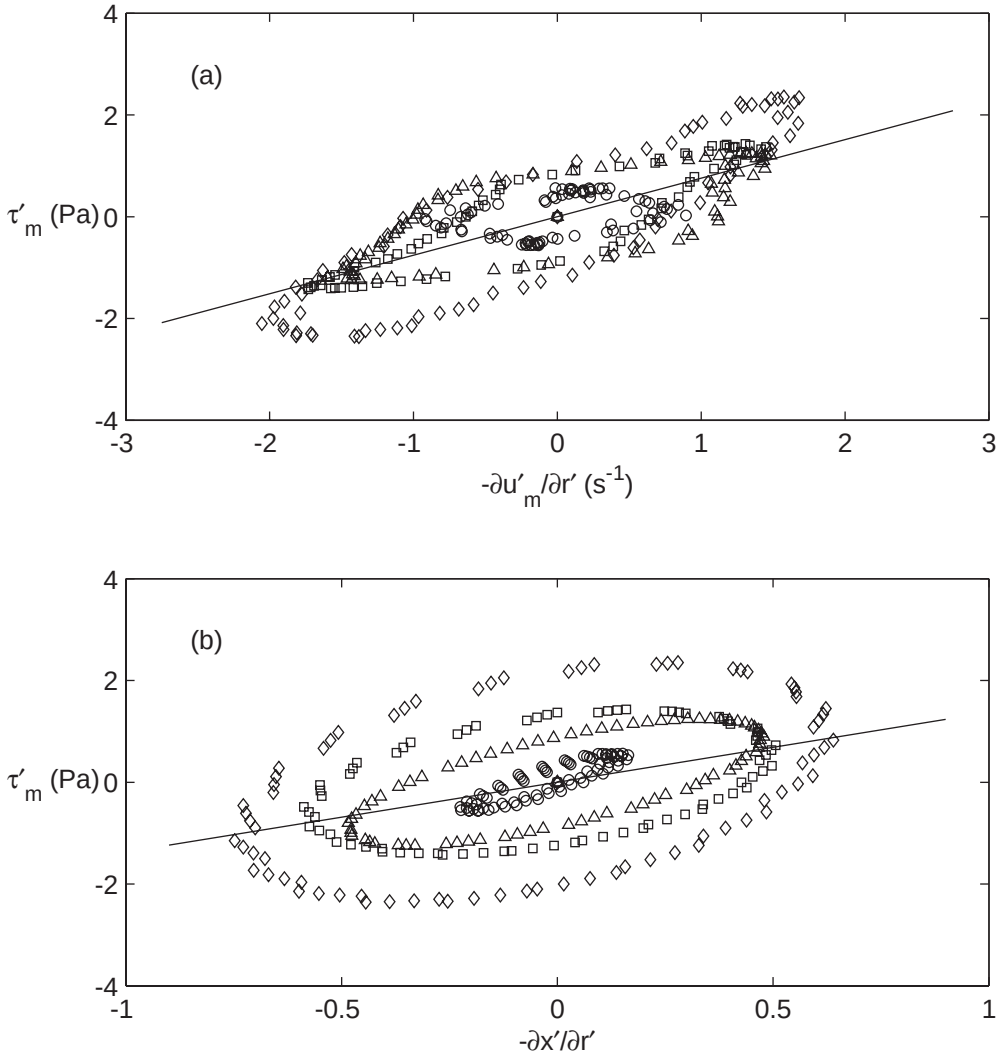

Figure 4.15: (*a*) Shear stress–rate of shear strain relations and (*b*) shear stress–shear strain relations at four different radial positions for the case Y2: ○, r' = 1 cm; △, r' = 3 cm; □, r' = 5 cm; ◇, r' = 7 cm; ——, linear regression.

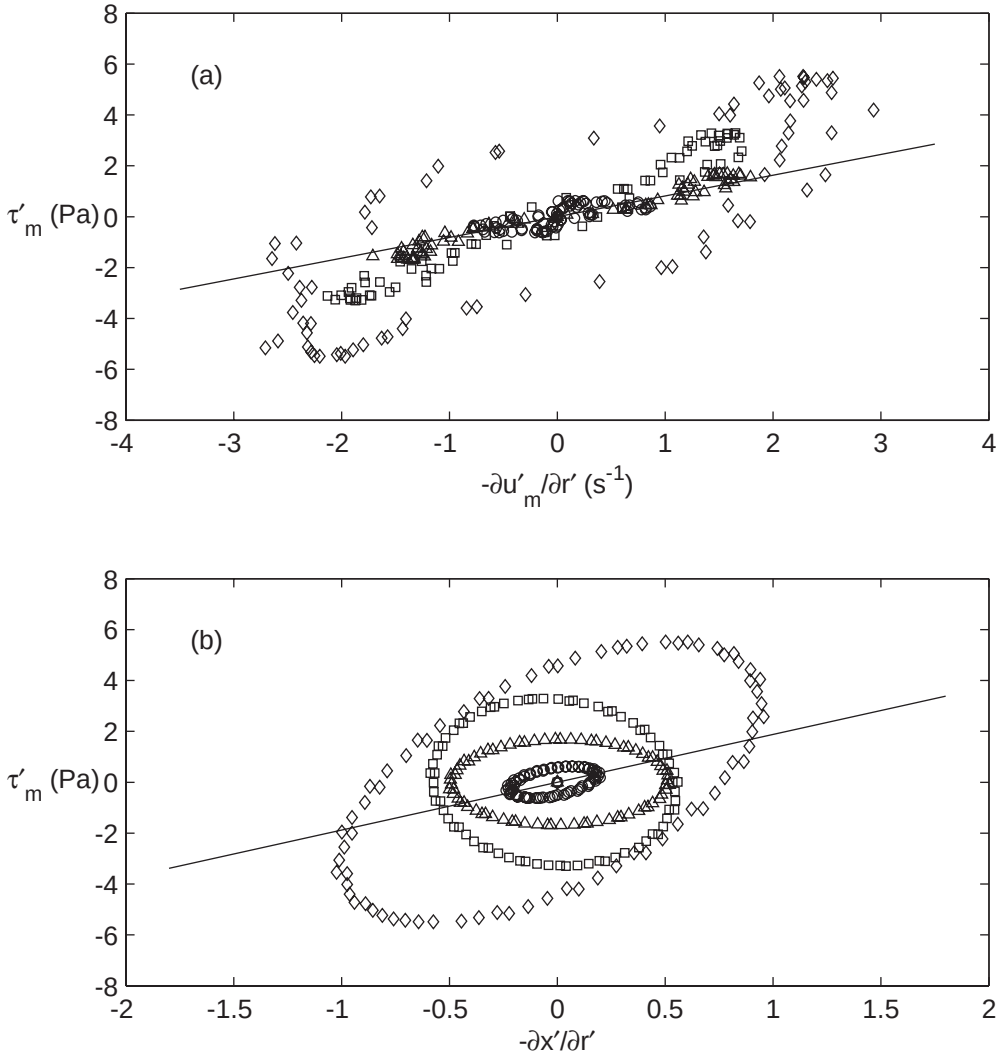

Figure 4.16: (*a*) Shear stress–rate of shear strain relations and (*b*) shear stress–shear strain relations at four different radial positions for the case Y3: ○, r' = 1 cm; △, r' = 3 cm; □, r' = 5 cm; ◇, r' = 7 cm; ——, linear regression.

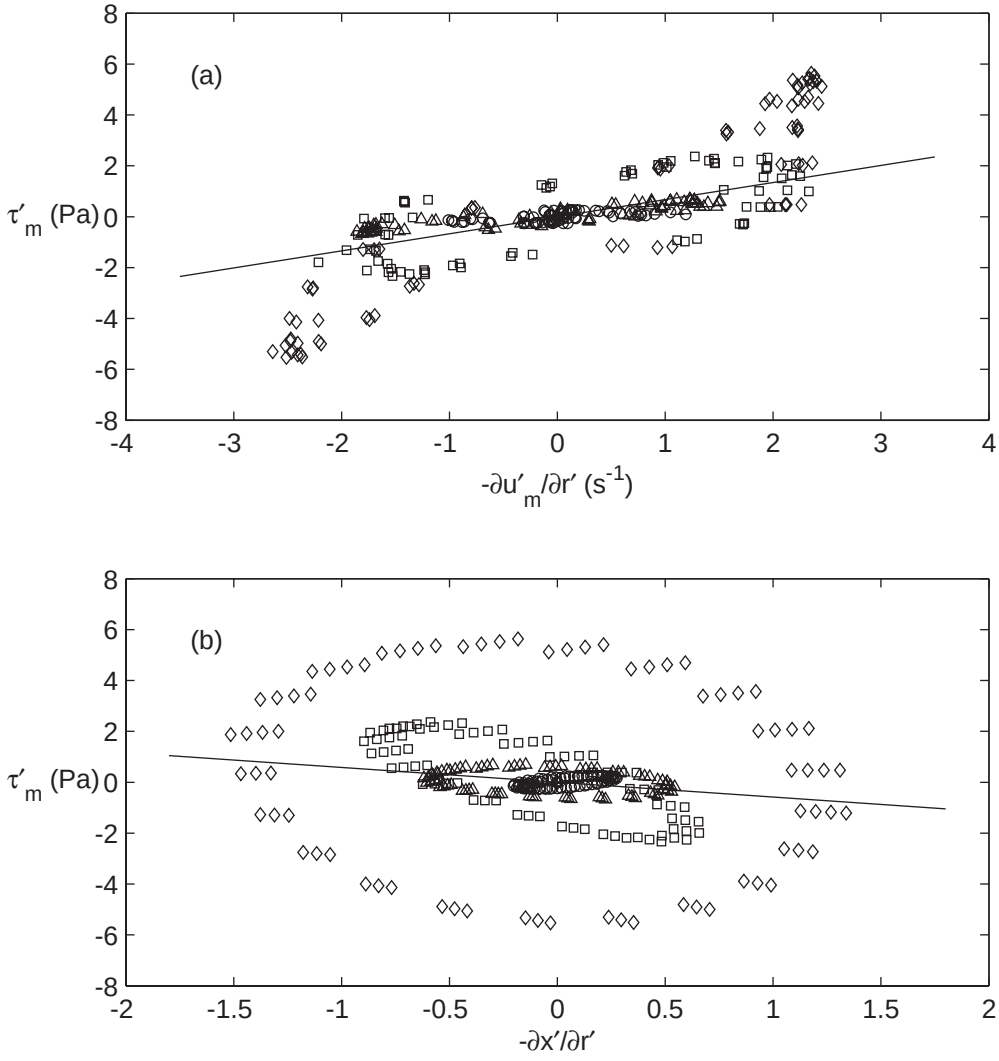

Figure 4.17: (*a*) Shear stress–rate of shear strain relations and (*b*) shear stress–shear strain relations at four different radial positions for the case Y4: ○, r' = 1 cm; △, r' = 3 cm; □, r' = 5 cm; ◇, r' = 7 cm; ——, linear regression.

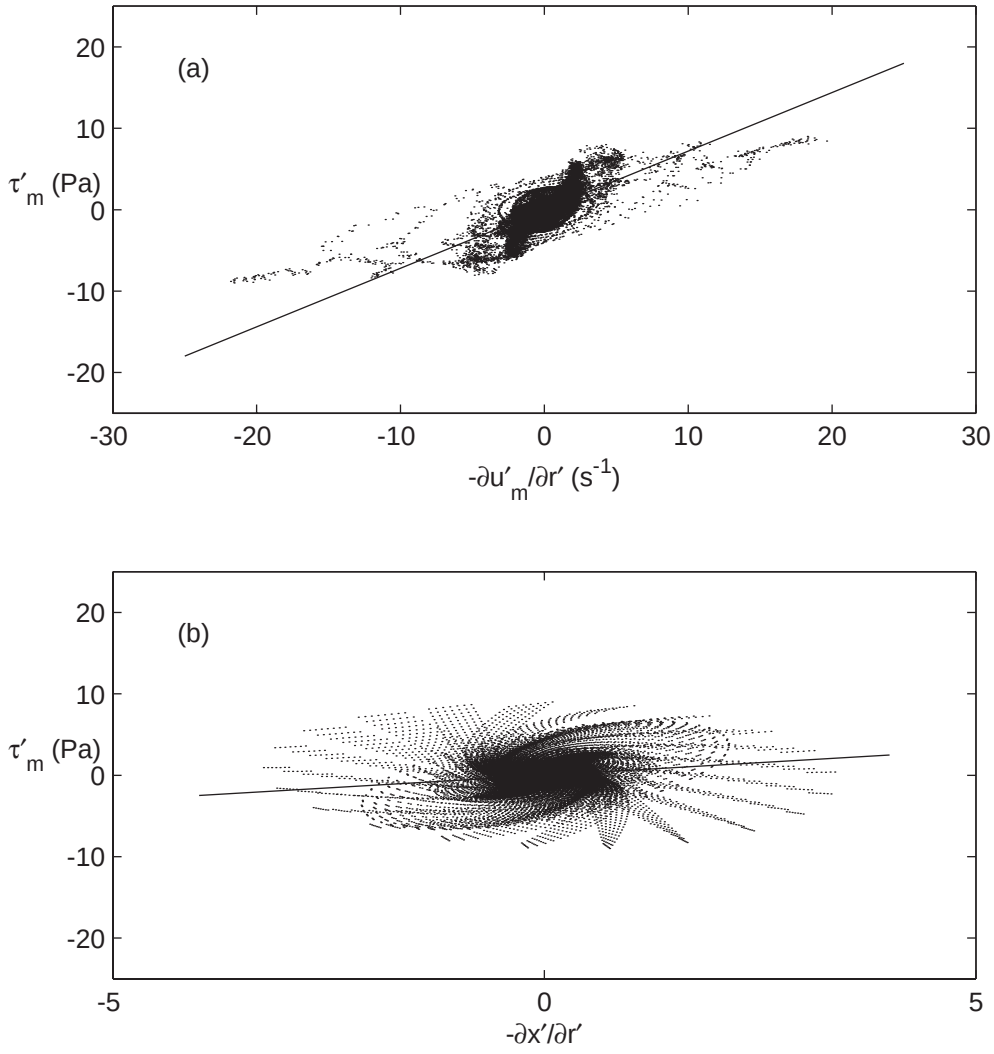

Figure 4.18: (*a*) Shear stress–rate of shear strain relation and (*b*) shear stress–shear strain relation using the entire data from all of the experimental cases: ·, experimental data; ——, linear regression.

Table 4.4: Correlation coefficients between the shear stress versus the rate of shear strain and versus the shear strain

Case No.	vs. $-\partial u'_m/\partial r'$	vs. $-\partial X'/\partial r'$
Y1	0.5166	0.7320
Y2	0.8381	0.4751
Y3	0.7424	0.4160
Y4	0.8238	-0.1759
All	0.7637	0.1667

Table 4.5: Estimation of the viscosity and the shear modulus by linear regression

Case No.	ν'_m ($m^2\,s^{-1}$)	G' (Pa)	β	κ	k
Y1	5.978×10^{-4}	3.3788	0.0225	0.0318	4.8293 – 1.5324 i
Y2	7.205×10^{-4}	1.3715	0.0330	0.0191	4.4368 – 2.5562 i
Y3	7.765×10^{-4}	1.8819	0.0329	0.0224	4.4306 – 2.3421 i
Y4	6.404×10^{-4}	-0.5815	0.0302	0.0000	4.0686 – 4.0686 i
All	6.851×10^{-4}	0.6194	-	-	-

straight line to the data (see figures 4.14–4.17 and figure 4.18). The results are listed in table 4.5. The goodness-of-fit for each case can be estimated by the correlation coefficients in table 4.4 because the coefficients of determination are equal to the squares of the correlation coefficients. It is remarkable that slopes of the shear stress–rate of shear strain curves do not change significantly for different cases in contrast to the shear stress–shear strain curves. Notice that the estimated viscosities are close to the one obtained from the flow-curve mea-

surement in table 4.1. Also the estimated shear moduli are in the same order of magnitude with the measured yield stress.

Now the individual contributions of the viscosity and of the elasticity of the material are combined using one of the simplest viscoelastic model, namely Kelvin-Voigt model, which may be figuratively described as a spring and a dashpot connected in parallel. In simple shear, the Kelvin-Voigt model in the cylindrical coordinate system is given as follows:

$$\tau' = -\rho'_m \nu'_m \frac{\partial u'_m}{\partial r'} - G' \frac{\partial X'}{\partial r'}. \tag{4.10}$$

For the sinusoidal pressure loading, the dimensionless function f defined in (3.38) can be written in complex notation as

$$f(t) = \mathrm{e}^{\mathrm{i}t}, \tag{4.11}$$

and the normalized governing equation is written as

$$\frac{\partial u_m}{\partial t} = \mathrm{e}^{\mathrm{i}t} + (\beta - \mathrm{i}\kappa)\left(\frac{\partial^2 u_m}{\partial r^2} + \frac{1}{r}\frac{\partial u_m}{\partial r}\right), \tag{4.12}$$

in which β has been defined in (3.40) and

$$\kappa = \frac{G'}{\rho'_m \omega'^2 R'^2}, \tag{4.13}$$

is a dimensionless parameter representing the ratio of elastic to inertial force. Note that u_m in the above equation is a complex-valued function and only the real part of the resulting complex expression is of interest. The analytical solution of (4.12) with the no-slip condition along the wall can be easily found as

$$u_m(r,t) = \mathrm{Re}\left\{ \mathrm{i}\,\mathrm{e}^{\mathrm{i}t}\left(\frac{\mathrm{J}_0(kr)}{\mathrm{J}_0(k)} - 1\right)\right\}, \tag{4.14}$$

where, J_0 is the Bessel function of the first kind of order 0 and k is given as

$$k^2 = \frac{-\mathrm{i}}{\beta - \mathrm{i}\kappa}. \tag{4.15}$$

The dimensionless parameters β, κ and k have been calculated based on the values in table 4.5 and are summarized in the same table. Note that the shear modulus for the case Y4 has been assumed to be 0.

Then the analytical solutions are compared with the experimental data (see figures 4.19–4.22). Also plotted in the figures are the analytical solutions using the values estimated from the collection of the entire data (figure 4.18). Overall, the agreement seems far better than those using the regularized Bingham model (e.g. figures 4.3 & 4.4). In particular, the overshooting in the centreline velocities and the ostensible curvatures in the radial profiles are well captured by the simple viscoelastic model. The analytical solutions using the case-specific parameters seem to agree better compared to the one using the parameters from the collection of the entire data. In other words, the solution is sensitive to the values of the material properties, which evidently change according to the flow history.

4.4.3 Further discussion

Indeed, yield-stress fluid is known to have some (linear or nonlinear) viscoelastic properties especially in the solid regime (Nguyen & Boger, 1992; Coussot, 2005) and the yield stress corresponds to the minimum stress needed to break or to rearrange the internal structure. For the case of the aqueous solutions of Carbopol, the macroscopic rheological parameters such as viscosity, shear modulus of elasticity and yield stress result from deformations and rearrangements of the swollen micro-gel blobs, which themselves are viscoelastic (Piau, 2007). Since the time scale corresponding to the elastic effects are typically very small,

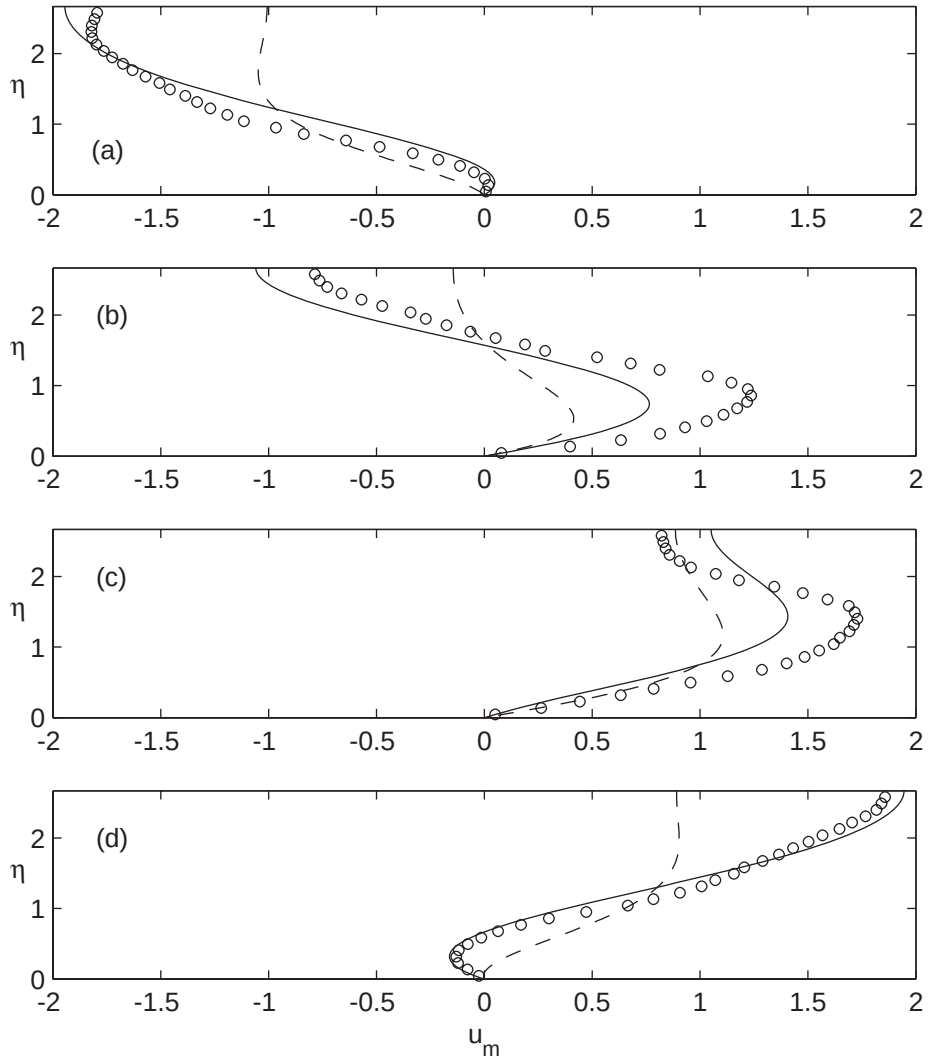

Figure 4.19: Radial profiles of the dimensionless axial velocity for the case Y1 at four different phases during the 10th period: ∘, PIV data; ——, the analytical solution using the rheological values estimated from the case Y1 only; – – – – –, the analytical solution using the rheological values estimated from the collection of the entire data. (*a*) $t/2\pi = 10.43$; (*b*) $t/2\pi = 10.61$; (*c*) $t/2\pi = 10.79$; (*d*) $t/2\pi = 10.97$.

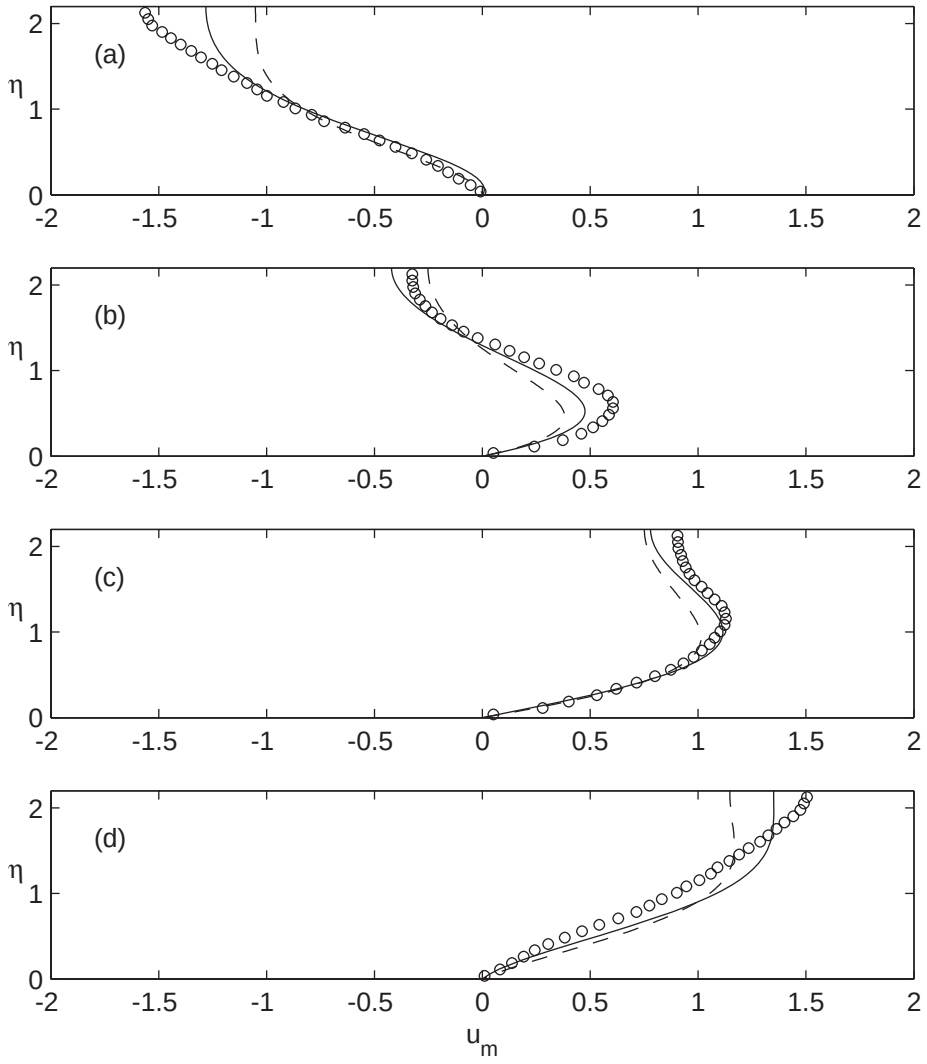

Figure 4.20: Radial profiles of the dimensionless axial velocity for the case Y2 at four different phases during the 10th period: ∘, PIV data; ——, the analytical solution using the rheological values estimated from the case Y2 only; – – – – –, the analytical solution using the rheological values estimated from the collection of the entire data. (*a*) $t/2\pi = 10.44$; (*b*) $t/2\pi = 10.59$; (*c*) $t/2\pi = 10.74$; (*d*) $t/2\pi = 10.89$.

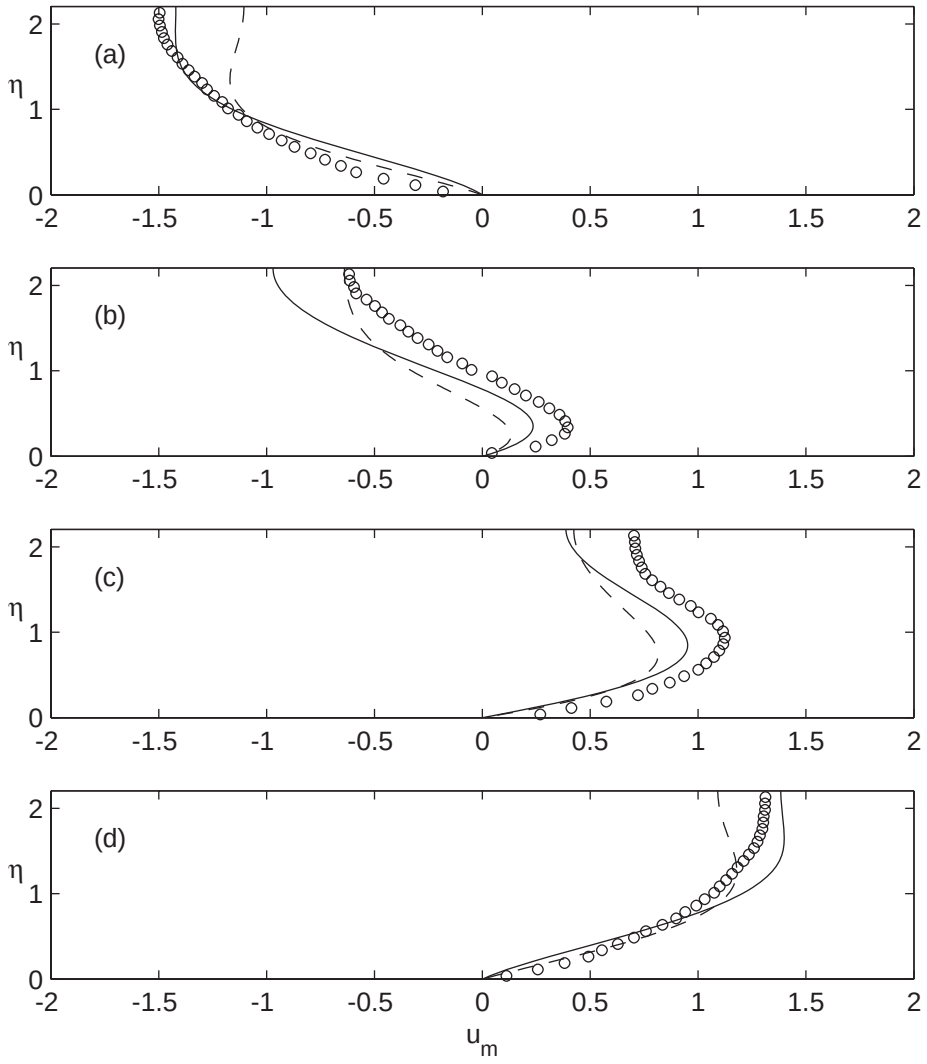

Figure 4.21: Radial profiles of the dimensionless axial velocity for the case Y3 at four different phases during the 10th period: ∘, PIV data; ——, the analytical solution using the rheological values estimated from the case Y3 only; − − − − −, the analytical solution using the rheological values estimated from the collection of the entire data. (*a*) $t/2\pi = 10.37$; (*b*) $t/2\pi = 10.53$; (*c*) $t/2\pi = 10.69$; (*d*) $t/2\pi = 10.85$.

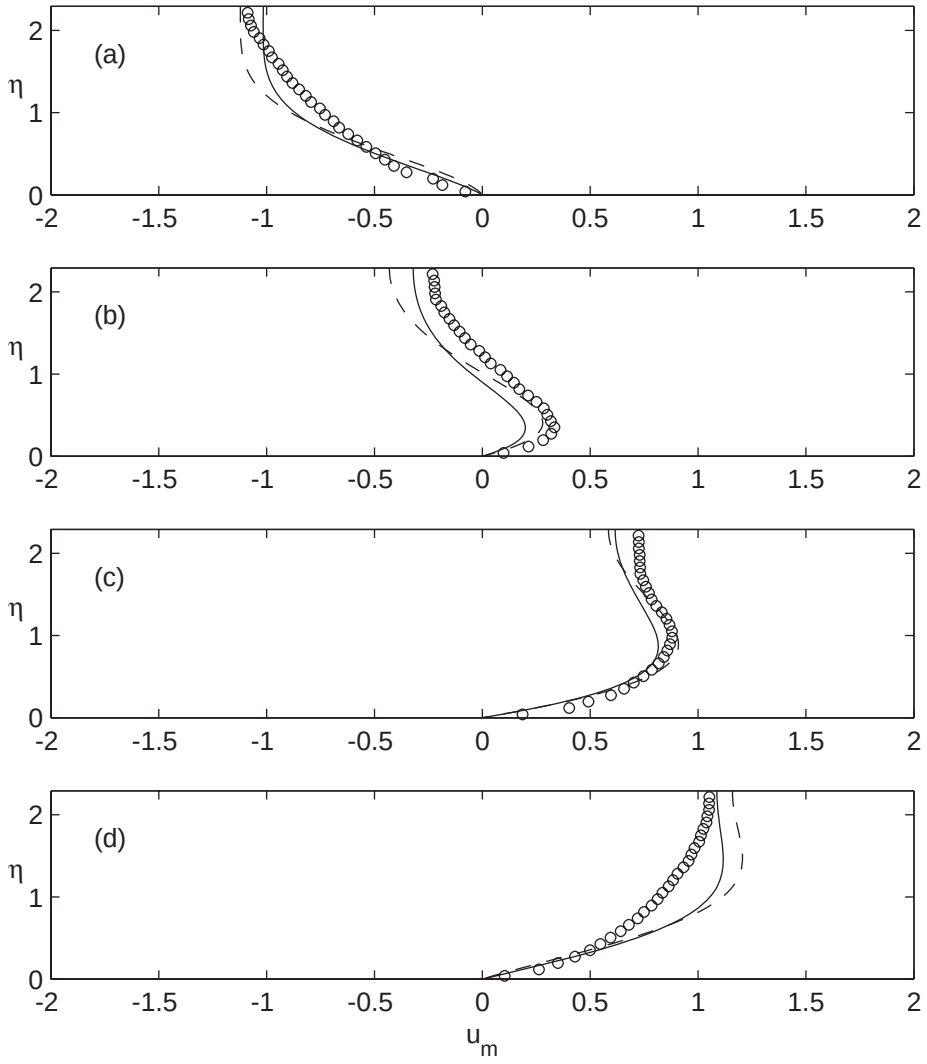

Figure 4.22: Radial profiles of the dimensionless axial velocity for the case Y4 at four different phases during the 10th period: ∘, PIV data; ——, the analytical solution using the rheological values estimated from the case Y4 only; − − − − −, the analytical solution using the rheological values estimated from the collection of the entire data. (*a*) $t/2\pi = 10.43$; (*b*) $t/2\pi = 10.57$; (*c*) $t/2\pi = 10.71$; (*d*) $t/2\pi = 10.86$.

the material can be modeled nicely by Bingham-type constitutive equations under steady flow condition. However if one tries to apply the steady-state models to unsteady flows, then the dynamic characteristics of the material would not be well reflected. For example, what is implied by (4.1) is that the material is strictly rigid in its solid regime and it recovers the rigidity as soon as the stress becomes less than the threshold. On the other hand, Coussot (2005) argued that the transition from solid regime to fluid regime is virtually irreversible, and the yield-stress fluid will never return to its solid state as long as the steady or unsteady flow which caused the transition remains imposed even if the the rate of shear strain vanishes at some moments. Therefore it is argued here that the qualitative difference between the experimental results and the numerical simulation using the Bingham model shown in figure 4.4 results from neglecting the deformability of the unyielded part of the material.

While the agreement between the experimental data and the analytical solutions using the Kelvin–Voigt model is encouraging, some discrepancies still remain between them. The neglected effects of the nonlinearity and the non-uniformity may be responsible for the discrepancies. If the rheological data shown in figures 4.14–4.17 are replotted in the $(\partial u'_m/\partial r',\ \partial X'/\partial r',\ \tau'_m)$ space (e.g. see figure 4.23), the Kelvin–Voigt model (4.10) would be represented as a flat plane. Therefore the success of the model depends on how close the distribution of the rheological data are to the plane.

Clearly the rheology data in the $(\partial u'_m/\partial r',\ \partial X'/\partial r',\ \tau'_m)$ space are much more sophisticated than the flat plane. More accurate representation of the manifold would be required for better description of the material behavior. It is worth noting that the U-tube experiment can provide more complete rheological infor-

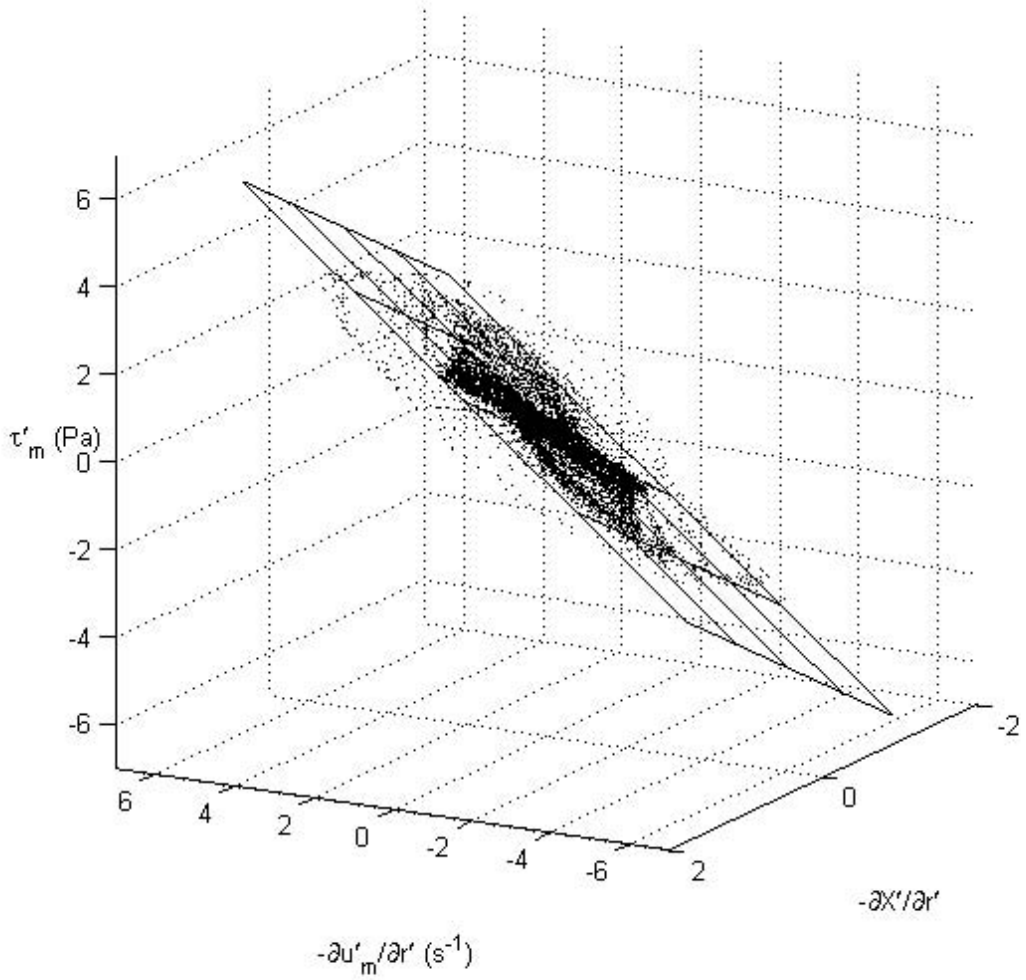

Figure 4.23: Three dimensional plot of the shear stress as a function of the strain and the rate of shear strain for the case Y2: ·, the experimental data; ——, the Kelvin-Voigt model (4.10) using the parameters in table 4.5.

mation in comparison to the traditional rheological measurements. In terms of the three-dimensional representation of the data, the traditional measurement corresponds to only a slice of the manifold. Moreover the U-tube provides the important information on the material properties under dynamic condition. A completely new kind of rheometer can be considered based on the U-tube experiment as well as other canonical unsteady flows.

4.5 Concluding remarks

Motivated by the need to understand non-Newtonian mud flows in the coastal environment, oscillatory pipe flows of a yield-stress fluid (an aqueous solution of Carbopol) in the U-tube have been experimentally investigated in this chapter. Most importantly, we have shown that the rheology of the material under the unsteady motion cannot be adequately described by the widely used Bingham model. Indeed any generalized Newtonian model, in which the shear stress is a function of the rate of shear strain only (Bird, 1976), fails to explain the overshooting of the measured velociy. At this point, it seems obvious that the elastic effects play an important role in the unsteady flow of the yield-stress fluid.

From the measured velocity field, $u'_m(r', t')$, as well as the known pressure loading, rheological information such as the shear stress, the shear strain and the rate of shear strain could be directly calculated. In fact, this approach provides more complete information compared to traditional measurements using rheometers in the sense that a wide range in the $(\partial u'_m/\partial r',\ \partial X'/\partial r',\ \tau'_m)$ space could be covered by a single experiment under dynamic conditions. As the

simplest model, the shear stress was assumed to be a linear combination of the viscous and the elastic contributions. The analytical solution for the velocity field using the simple constitutive relation was found, which agreed with the experimental data remarkably well.

A number of future researches can be suggested. First of all, a more complete constitutive relation can be developed by accurately describing the shear stress–shear strain–strain rate surface. Also, to extend the results to the real muds, various types of materials need to be examined. While both Carbopol solutions and muds are classified into yield-stress fluids, their microscopic structures that are responsible for the yield stress are very different from each other. In particular, Carbopol solutions are formed by microscopic repulisve forces, as opposed to muds which are constituted by the attractive internal interactions. Furthermore, the optical measurements used for the Carbopol solutions cannot be applied to muds, hence alternative measurement techniques such as ones using acoustic signals need to be developed. It is also reminded that the flows generated in the U-tube is only two-dimensional while the material properties are likely to be three-dimensional, which needs to be addressed by exploring other types of flows. The new framework developed in this chapter will guide all these future endeavors.

CHAPTER 5

A TRAIN OF SOLITARY WAVES BREAKING ON A PLANE BEACH

5.1 Introduction

As ocean waves propagate onto a beach, decrease in water depth causes the wave fronts to steepen, which often leads into breaking (e.g. Peregrine, 1983). There are several types of breakers depending on the wave steepness in deep water and the beach slope. In this chapter, only the plunging breaker is considered, which is distinguished by an overturning jet plunging into the water ahead of the wave, followed by large splash-up. For other types of breakers, one can refer to reviews by Peregrine (1983) and Battjes (1988).

The surf zone, the region demarcated by the breaker line and the shoreline, is characterized by the intense level of turbulence near the water surface as well as the bubbles and foams due to wave breaking. A substantial amount of wave energy is dissipated through the process and the wave momentum is transferred to the water body, resulting in near-shore currents and transport of sediments (e.g. Mei, 1983). Breaking waves can also result in significant hydrodynamic loads on coastal structures.

Despite the dominating presence of the breaking waves in the surf zone, full understanding of their physics has been impeded for a number of reasons. Even for two-dimensional plane waves, the initially two-dimensional vortical structures on the vertical plane, developed in the early stage of the initial plunging, quickly evolve into three-dimensional turbulence (Watanabe, Saeki & Hosking, 2005). Furthermore, the flow associated with breaking waves is strongly tran-

sient and transitional from an essentially laminar and irrotational state before breaking to an established turbulent flow. Meanwhile, a large amount of air is entrapped, resulting in a multi-phase flow. Consequently, there is no established theory that can fully explain the wave breaking mechanism and breaking-induced flows.

Time-averaged and depth-integrated flow fields of regular periodic waves are relatively well-understood. Especially the concept of the radiation stresses, which represent the time averages (over a wave period) of the local horizontal wave momentum flux, has provided the fundamental framework for theoretical as well as experimental investigations (see Longuet-Higgins & Stewart, 1962). In the cross-shore direction of a uniform beach, if the bottom shear stress is neglected, the gradient of the radiation stresses is balanced by the mean pressure gradient. Consequently, water surface elevation outside the surf zone decreases (set-down), while that within the surf zone increases (set-up). The mean momentum balance in the longshore direction results in mean currents, which have very important implications in the sediment transport. In practice, the bottom topography as well as the angle of wave incidence causes more complex mean flow structure in the surf zone (Battjes, 1988). In addition, it is well-known that the time-averaged wave-induced mass flux is directed to the shore above the trough line, while it is balanced by a seaward directed return flow underneath, so-called undertow (e.g. Putrevu & Svendsen, 1993). Due to the viscous effects, there also exists a steady shoreward streaming near the bottom boundary, known as Stokes drift (Longuet-Higgins, 1953).

Substantial efforts have been made to measure and model the turbulence in the surf zone. For example, Svendsen (1987) compiled several earlier laboratory

turbulence measurements associated with periodic breaking waves. He maintained that the temporal variation of the turbulent kinetic energy at a fixed position is relatively small and that the vertical variation of the time-averaged turbulent kinetic energy is also small. Note that most of the experimental data that Svendsen (1987) used were only for the region below the trough line. Using a particle image velocimetry (PIV), Cowen *et al.* (2003) observed that the breaking-generated turbulence dominates the uprush phase, while the turbulence is essentially generated from the bottom boundary during the backwash until the flow meets the next oncoming wave. More recently, Sou (2006) and Kimmoun & Branger (2007) carried out very detailed PIV measurements of breaking waves on a sloping beach for a periodic wave train. Both reported time-averaged and phase-averaged flow fields as well as the respective fluctuating components in the vertical plane.

Three-dimensional coherent structures of the turbulence in the laboratory surf zone were first reported by Nadaoka, Hino & Koyano (1989). The horizontal eddies develop during the plunging–splash-up process and the obliquely decending eddies follow. Using both flow visualization techniques and a laser Doppler velocimeter (LDV), they found that both types of the coherent structures are significant in their contribution to Reynolds stresses. Watanabe *et al.* (2005) carried out a three-dimensional large eddy simulation to study the large-scale vortex structures under breaking waves. Though the effects of aeration and surface tension were not considered in their simulation, it appears that the originally two-dimensional horizontal eddies due to plunging are strained during the splash-up, which triggers the spanwise undulations of the horizontal eddies. The undulations are further amplified and develop into counter rotating vortex loops, which are again strained through the splash-up cycles and

finally take the form of the obliquely descending eddies observed by Nadaoka *et al.* (1989).

The large amount of air bubbles entrapped throughout breaking and splash-up cycles poses an inherent difficulty both in measuring and modeling breaking waves. Kimmoun & Branger (2007) estimated that the volume fraction of the bubbles can be as high as 0.88 near the first splash-up point and then slowly decreases to 0.2–0.3 near the shore. Also the time-averaged mass transport was estimated to be 25% lower when the void fraction is considered than the estimation without considering the void fraction. Direct measurements of the void fraction in the surf zone are scarce compared to those for the breaking waves in deep water (e.g. Melville, 1996; Deane & Stokes, 2002). Cox & Shin (2003) utilized an impedance void fraction meter in their laboratory experiments and their maximum phase-averaged void fractions were between 15 and 20%. The dicrepancy between the two experiments can be attributed to the different methods employed. Generally speaking, the intrusive point measurement such as that of Cox & Shin (2003) is believed to be more accurate especially for the flows with high void fraction (Lim *et al.*, 2008), though it cannot cover the entire flow field at the same time. On the other hand, Deen, Westerweel & Delnoij (2002) reviewed some PIV techniques for bubbly flows, which are mostly restricted to simple steady flows or those with low void fraction up to 4%.

So far, time-averaged and phased-averaged flow fields of periodic incident waves have been discussed. From the viewpoint of disaster mitigation, however, important events often occur during time scales that are too short to justify the averaging. Tsunamis are an important example. During the 2004 Indian Ocean Tsunami, for instance, eyewitnesses described only one to three waves

depending on the locations (Liu *et al.*, 2005). Notice that, based on pictures and videos taken during the tsunami, most of the waves broke before reaching the shore.

Traditionally, many theoretical and experimental researches on tsunamis have been based on the assumption that each wave can be modeled as a solitary wave (Synolakis & Bernard, 2006). Important characteristics such as breaking criteria (Grilli, Svendsen & Subramanya, 1997) and run-up height that is defined as the vertical distance above the still water level that the wave reaches on a slope (e.g. Synolakis, 1987; Li & Raichlen, 2003) are found to be dependent on the relative height of the solitary wave compared to the deep water depth and the beach slope. In addition, more detailed information on the velocity fields during run-up and run-down of solitary waves have been studied numerically (e.g. Lin, Chang & Liu, 1997). On the other hand, flow field measurements under a breaking solitary wave are scarce and challenging. As Svendsen (1987) and Cox & Shin (2003) already pointed out, the only way to reliably estimate turbulence under a transient flow is through the ensemble average, which requires a number of repeated experiments with a very high degree of repeatability of each realization. However, the arrival times of the broken solitary waves almost always fluctuate across experiments in an ensemble as in recent PIV measurements by Ting (2006, 2008) and the turbulence is not well-defined for this intermittent experimental data.

To summarize, researches on breaking waves in the near-shore region have focused on (i) mean (time-averaged over a wave period or phase-averaged) flow fields of periodic incident waves or (ii) ensemble-averaged run-up–run-down process of a solitary wave. While much useful knowledge and insight have

been obtained by each of the approaches, respectively, many challenges still remain. In particular, it is noted that interactions between successively breaking waves have been obscure or absent in those frameworks. Therefore, in this chapter, laboratory experiments on a train of almost identical solitary waves breaking on a 1:20 sloping beach are disscussed for the first time. The objectives of this study are twofold. First, the interactions between waves are of great interest since tsunami usually comes as a group of a few waves rather than a single wave pulse. Second, the identification of the origins and the development paths of the mean quasi-steady flow characteristics can provide deeper understanding of surf-zone hydrodynamics. However, the experimental results are by no means claimed to be complete due in part to lack of guiding theory and to the limitations in the experimental set-up. Rather, it is hoped that fundamental questions can be identified and a new direction of the research can be established by making careful observations of the available data.

In the following section, experimental conditions will be described. Up to two solitary waves were used in the experiments and different cases were considered by varying the time separation between the crests. Detailed measurements on water surface profiles, instantaneous velocity fields and depth-averaged velocities under breaking waves will be discussed in §5.3. Finally this chapter will be concluded by suggesting outstanding questions and the future research direction in §5.4.

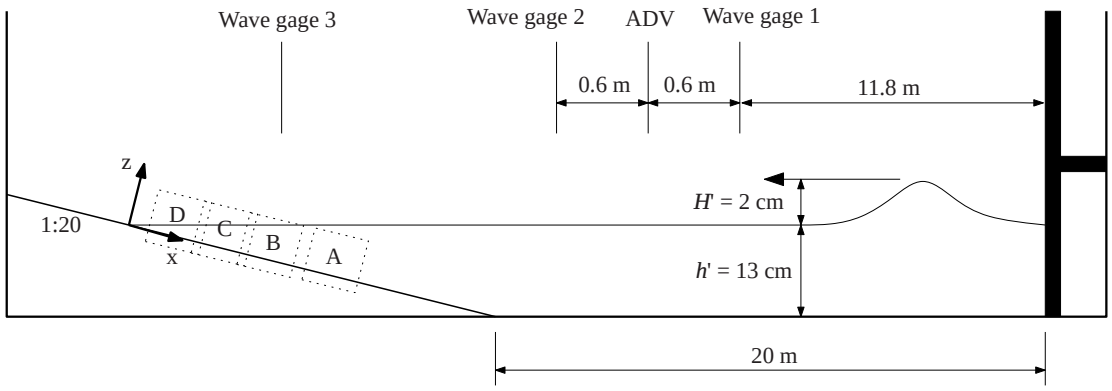

Figure 5.1: Experimental set-up (not to scale).

5.2 Experimental set-up and cases

5.2.1 Overview of the experimental set-up

The experiments were conducted in the same wave tank described in Chapters 2 & 3, which is 32 m long, 0.6 m wide and 0.9 m deep. The wave tank is equipped with a hydraulically-driven piston-type wavemaker with 25 cm stroke. At the opposite end, a 1:20 sloping beach is installed, where two-dimensional velocity fields were measured using a PIV technique. Three Banner Engineering S18U acoustic wave gages (two in the constant depth and one in the middle of each PIV field-of-view) and an acoustic Doppler velocimeter (ADV, Nortek Vectrino with Plus Firmware) were also used. The locations of measurements as well as the coordinate system are shown in figure 5.1. Note that the x-axis is aligned with the beach and the origin is located at the intersection of the still water level and the beach.

Table 5.1: Sizes and locations of the four FOV's in figure 5.1.

FOV	Side length (mm)	x-coordinate of the left side (cm)
A	67	30.0
B	68	21.7
C	70	16.4
D	70	10.0

5.2.2 Velocity field measurements using PIV

The four squares enclosed by dotted lines in figure 5.1 (labeled A, B, C and D, respectively) indicate locations of PIV field-of-view (FOV) covering much of the area between the breaker line and the shore line (see table 5.1). We remark here that the locations and the sizes of the FOVs in table 5.1 were chosen to capture the entire water column of the breaking waves with the maximum possible resolution. Based on the empirical formulas by Grilli *et al.* (1997), for example, the location x'_b and the wave height H'_b at the point of breaking for the current experimental condition were estimated as $x'_b \approx 34$ cm and $H'_b \approx 5$ cm, respectively. Accordingly, the FOV A is centered around $x' = x'_b$ and it just covers the whole water column during the breaking.

Each FOV was illuminated by a Spectra Physics PIV400-30 Nd:YAG laser system (300 mJ pulse^{-1}, 60 Hz dual head system). By passing the laser beam through a cylindrical lens, a light sheet was formed, which was delivered from below the glass beach to avoid disturbances from the free surface. One disadvantage of using the small FOVs for highly aerated flows is that laser light scatterd by the air bubbles and the irregular free surface can saturate the en-

tire image. Following Cowen *et al.* (2003), fluorescent seeding particles (Dantec Dynamics FPP-RhB-10) were used, which absorbs the green laser light while emitting the red light. By using an optical filter that cuts off the green light, the scattered light can be effectively blocked and only the reflected light from the fluorescent particles is recorded. As a result, however, velocities only in the water phase, i.e. regions where the air bubble density is very low, could be measured.

The image acquisition system was triggered to capture two images of an image pair with 2.00 ms time delay. An SMD 1M60-20 camera (12 bits pixel^{-1}, 60Hz, 1024×1024 pixels) was used with the framing rate 30 Hz, giving a PIV velocity field rate of 15 Hz.

5.2.3 Generation of the solitary waves

Generation methods of a solitary wave and of a series of solitary waves have been discussed earlier in §2.3.2 and §2.4.1, respectively. With the stroke length of 25 cm, only up to two waves with $H' = 2$ cm in the water depth $h' = 13$ cm were used for the current experiments.

A typical surface profile of the case D0 (see table 5.2) measured from the wave gage 1 are compared with the theoretical solution (2.32) in figure 5.2. Note that the variables are normalized following (2.10), with the effective wavelength defined by the both locations where the surface displacement is 1.0% of the wave height (2.40). While generally good agreement is seen in the figure, the second wave is followed by an undulating tail with the maximum amplitude of order $0.1H'$. This did not happen in the earlier experiments (see figure 2.17)

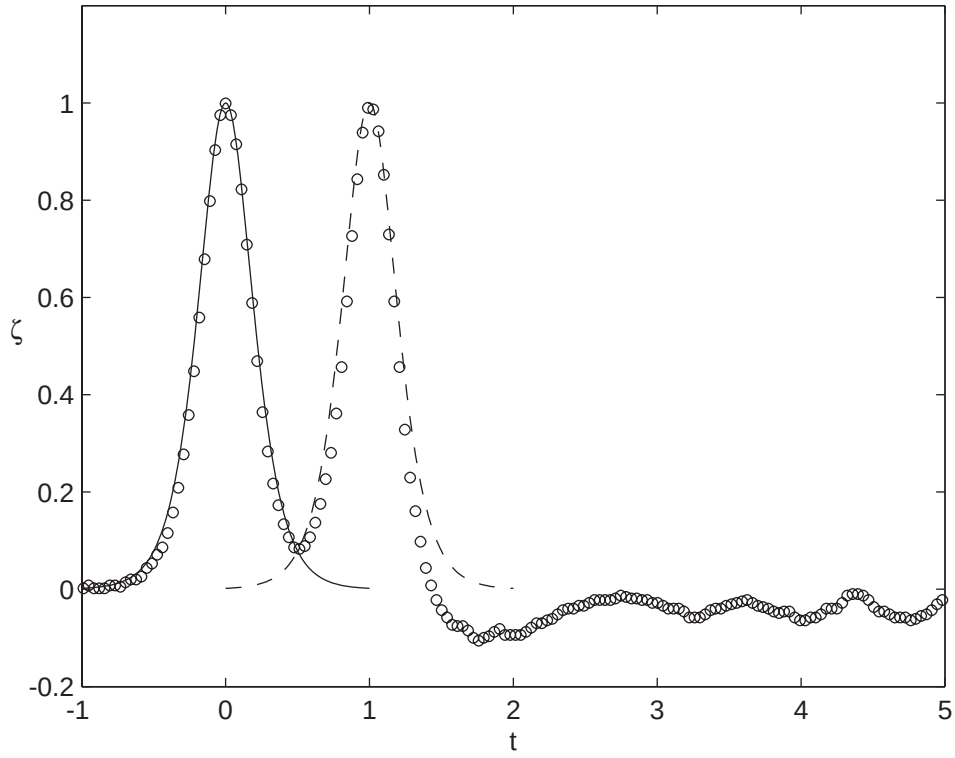

Figure 5.2: Theoretical and experimental dimensionless water surface profiles: ——, Grimshaw's solution (2.32) centered at $t = 0$;– – – –, Grimshaw's solution centered at $t = 1$; ∘, measured data from the wave gage 1.

and the aging of the equipment might have caused the defects. However, the interaction between the two waves in the surf zone is of main interest, and so the adverse effects of the undulating tail are not significant.

5.2.4 Experimental cases

A total of 9 different cases was studied by varying the number of waves and the time separation ($\Delta t'$) between the crests as summarized in table 5.2 in which T' denotes the wave period. While all the four PIV FOVs (A, B, C and D) were

Table 5.2: Experimental cases.

Case No.	No. of waves	$\Delta t'$ (s)	measured FOV
S	1	-	A, B, C, D
D0	2	1.30 ($\approx 1T'$)	A, B, C, D
D1	2	1.65	D
D2	2	2.00	D
D3	2	2.35	D
D4	2	2.70 ($\approx 2T'$)	D
D5	2	3.05	D
D6	2	3.40	D
D7	2	3.75	D

covered for the cases S and D0, the measurements for the other cases were only carried out at window D.

Additionally, experiments with two successive solitary waves with $H' = 2$ cm in $h' = 10$ cm were repeated twenty times to investigate the turbulence characteristics by ensemble averaging. However, the arrival times of the first waves at the shoreline, where the PIV measurements were made, varied within the range of ±10 ms. On the other hand, the 15 Hz data rate was not fast enough to adjust the time coordinate according to the arrival time, and the turbulence calculation seemed contaminated. Hence, discussion on the turbulence under successively breaking waves will be delayed until an instrument with sufficient temporal resolution is available.

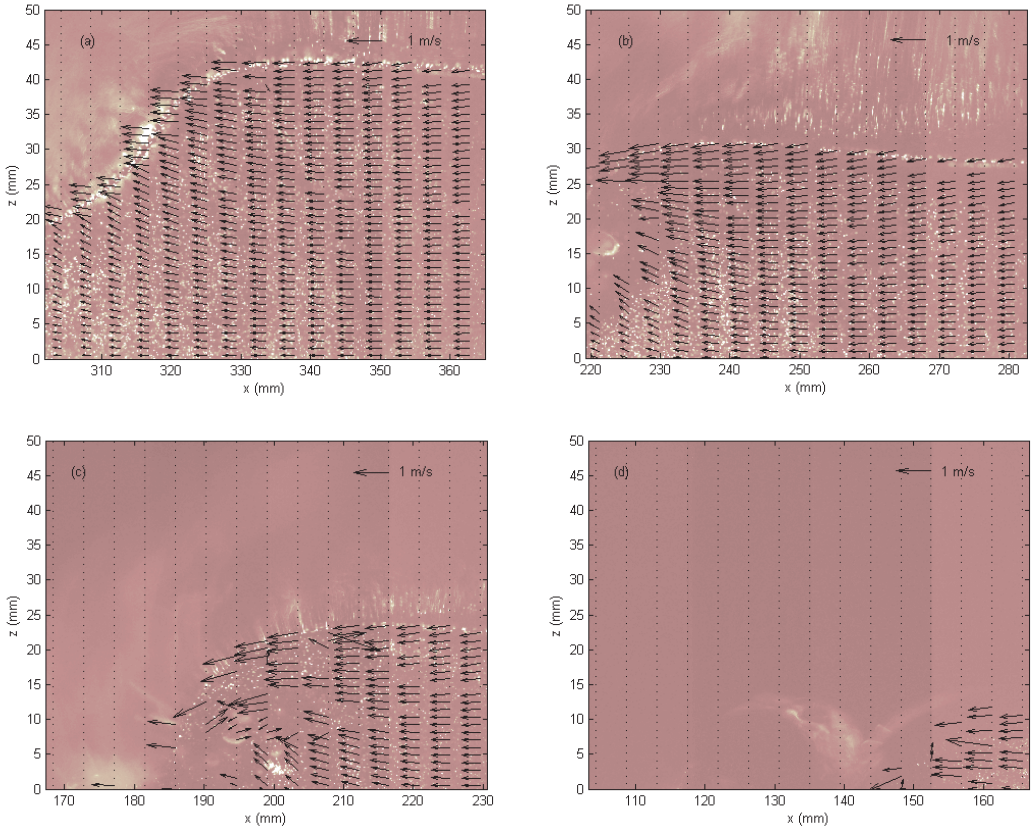

Figure 5.3: PIV images and velocity vectors of a breaking solitary wave taken at each of the FOVs in table 5.1. Wave propagates from right to left. (*a*) window A at $t = 6.43$; (*b*) window B at $t = 6.49$; (*c*) window C at $t = 6.58$; (*d*) window D at $t = 6.73$. Note that $t = 0$ when the wave crest passes the location of wave gage 1.

5.3 Experimental results

5.3.1 The single-wave case

A sequence of raw PIV images with the superimposed velocity vectors during breaking–splah-up for the case S are shown in figure 5.3. Note that the camera was tilted so that FOV of the PIV images is parallel to the beach. As a solitary wave climbs up the beach against gravity toward shallower depth, the part of

the water body behind the crest catches up with the front, and the wave continues to lose its symmetry (figure 5.3*a*). About the instant that the front surface becomes almost vertical, a jet emerges from the upper front corner of the wave as depicted in figure 5.3(*b*). Soon the jet hits the free surface in the front, which in turn initiates the first splash-up event (figure 5.3*c*). When the splashed-up body of water hits the free surface again, it generates a similar, only smaller in size, splash-up (figure 5.3*d*). While no velocity information could be found in highly aerated regions, bright background indicates the second splash-up. It is remarkable that the velocity is fairly uniform in the entire FOV except the frontal region where high level of turbulence and bubbles appear after breaking.

After passage of the wave front during the uprush, the water surface continually decreases at any location in the surf zone, and so does the velocity until the flow reverses its direction. This reversal first occurs close to the bottom boundary, so at least for a moment, a shear flow develops (figure 5.4).

In the later stage of the backwash, the flow away from the bottom boundary eventually changes direction and the wall-jet-like flow is established. The rundown flow continues to accelerate due to the gravity and eventually reaches a supercritical state (see figure 5.6*c*). Then a moving hydraulic jump or the backwash bore is formed near the initial shoreline. A number of researchers have observed the hydraulic jump in studying breaking solitary waves (e.g. Lin *et al.*, 1997; Li & Raichlen, 2002) or bores (e.g. Hibberd & Peregrine, 1979; Zhang & Liu, 2008). The flow structure near the hydraulic jump is complex. Besides the air entrainment and turbulent generation inside the roller of the hydraulic jump, there is a bottom boundary layer separation near the toe of the hydraulic jump due to the unfavorable pressure gradient (see figure 5.5). It is believed that the

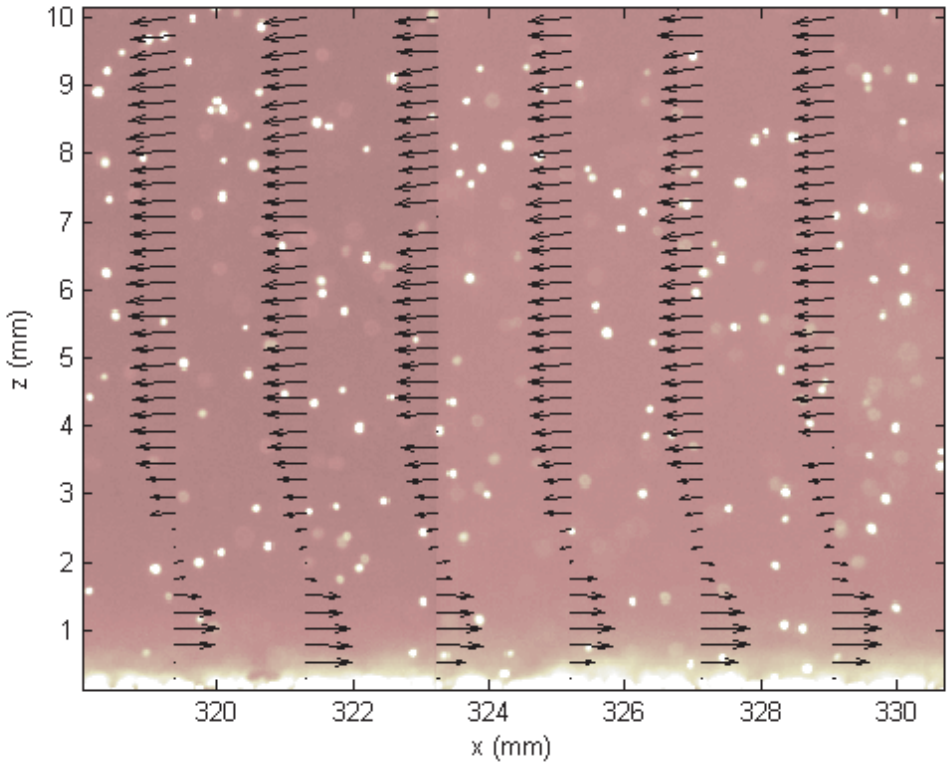

Figure 5.4: Initiation of the backwash phase at window A at $t = 7.41$. The picture has been zoomed-in to show the boundary layer more clearly. Typical velocity magnitude outside the boundary layer is about 3 cm sec^{-1}.

separated vortical flow at the base of a periodic breaking wave that Matsunaga & Honji (1980, 1983) observed is related to the boundary layer separation of the moving hydraulic jump. To prove the connection, however, experiments with more waves will be needed.

Figures 5.6–5.9 summarize the experimental data. Note that both the surface elevation and the velocity are normalized following (2.10). The depth-averaged velocities and the Froude numbers were calculated at the center of the each FOV. No attempt to reduce the noise in the data was made for these preliminary experiments. Instead, outlier-robust estimators were used to calculate the

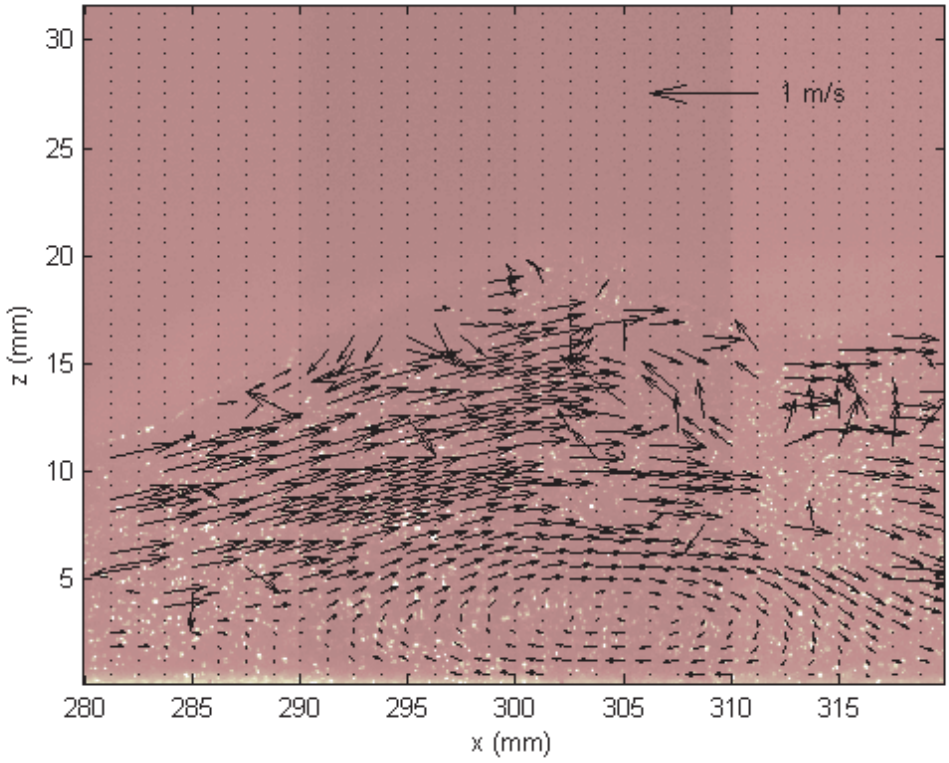

Figure 5.5: The bottom boundary layer separation at the toe of the moving hydraulic jump during the run-down process. The image was captured during a separate set of experiment at a location between windows A and B at $t = 8.97$.

statistics. In particular, the median was used to estimate the depth-averaged velocities and the inter-quatile range (IQR) was used to estimate the spread of the data. The wave passes the wave gage 1 at $t = 0$.

In the panels (*a*), notice that the acoustic wave gages are less accurate when gradient of surface profile is very steep. This happens when the wave front passes wave gage 3 during the uprush. In that situation, the surface elevation estimated from the raw PIV images are available. For each of the raw PIV images, the location of the free surface at center is visually identified, since automatic surface detection, such as the one used in §3.3.4, performed poorly when

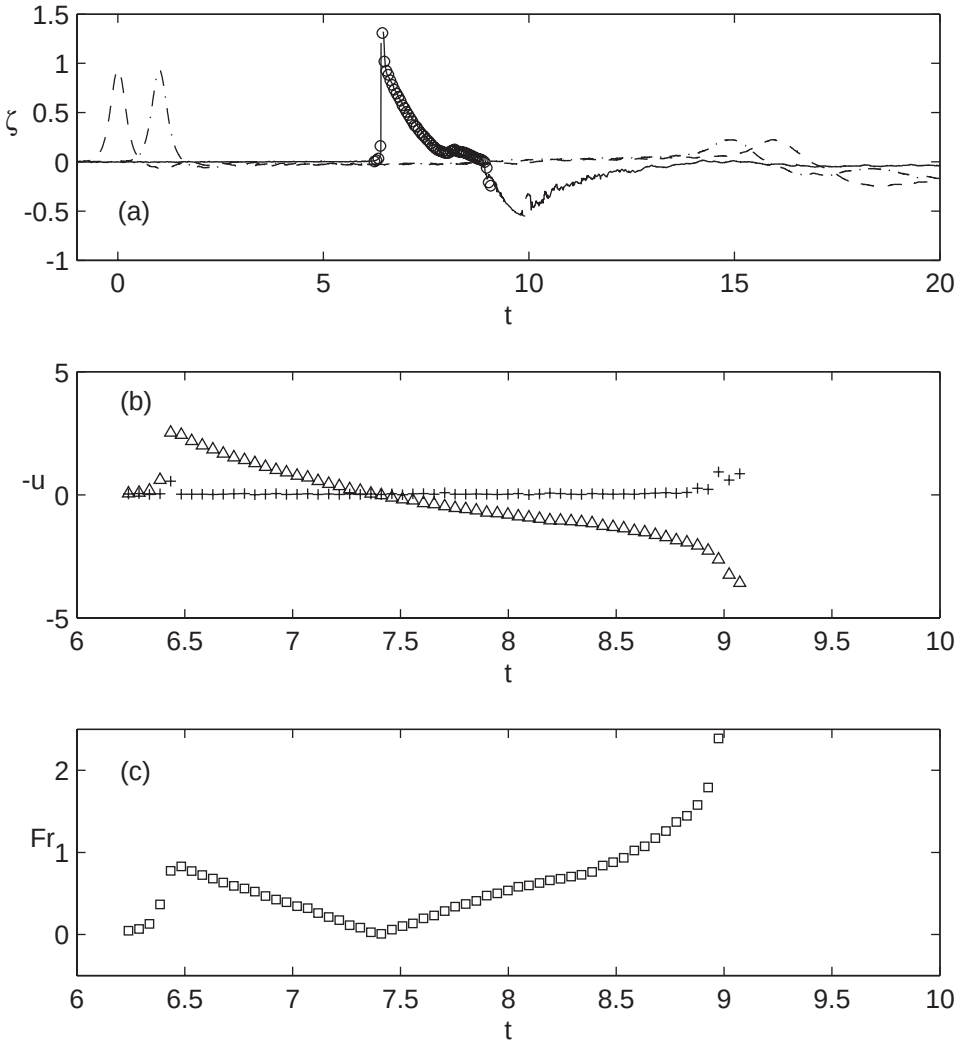

Figure 5.6: Time evolution of the surface elevation (*a*), the depth-averaged velocity (*b*) and the Froude number (*c*) for the case S at window A: −−−−−, water surface profile measured at wave gage 1; —·—, wave gage 2; ——, wave gage 3; ∘, water surface profile estimated from the PIV images; △, depth-averaged velocity; +, IQR around the depth-averaged velocity; □, Froude number based on the depth-averaged velocity and the total water depth.

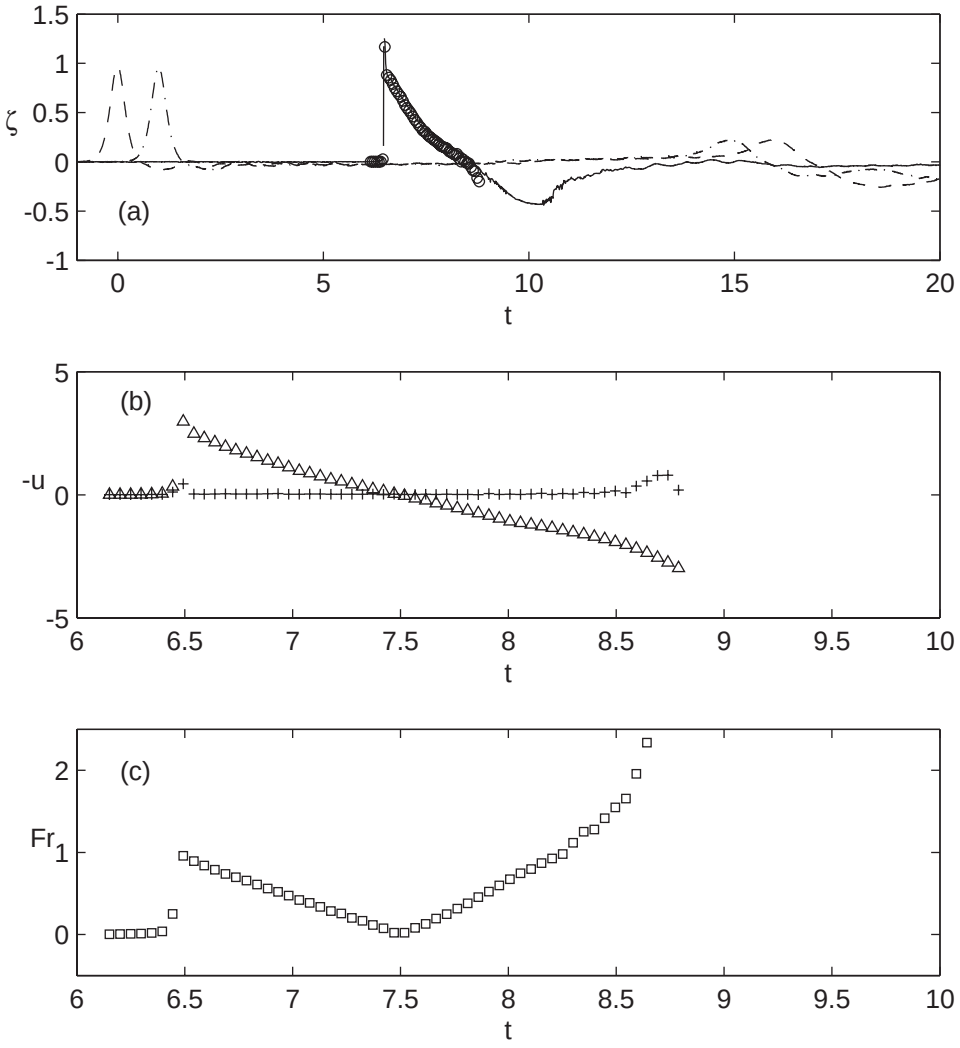

Figure 5.7: Time evolution of the surface elevation (*a*), the depth-averaged velocity (*b*) and the Froude number (*c*) for the case S at window B: −−−−−, water surface profile measured at wave gage 1; —·—, wave gage 2; ——, wave gage 3; ∘, water surface profile estimated from the PIV images; △, depth-averaged velocity; +, IQR around the depth-averaged velocity; □, Froude number based on the depth-averaged velocity and the total water depth.

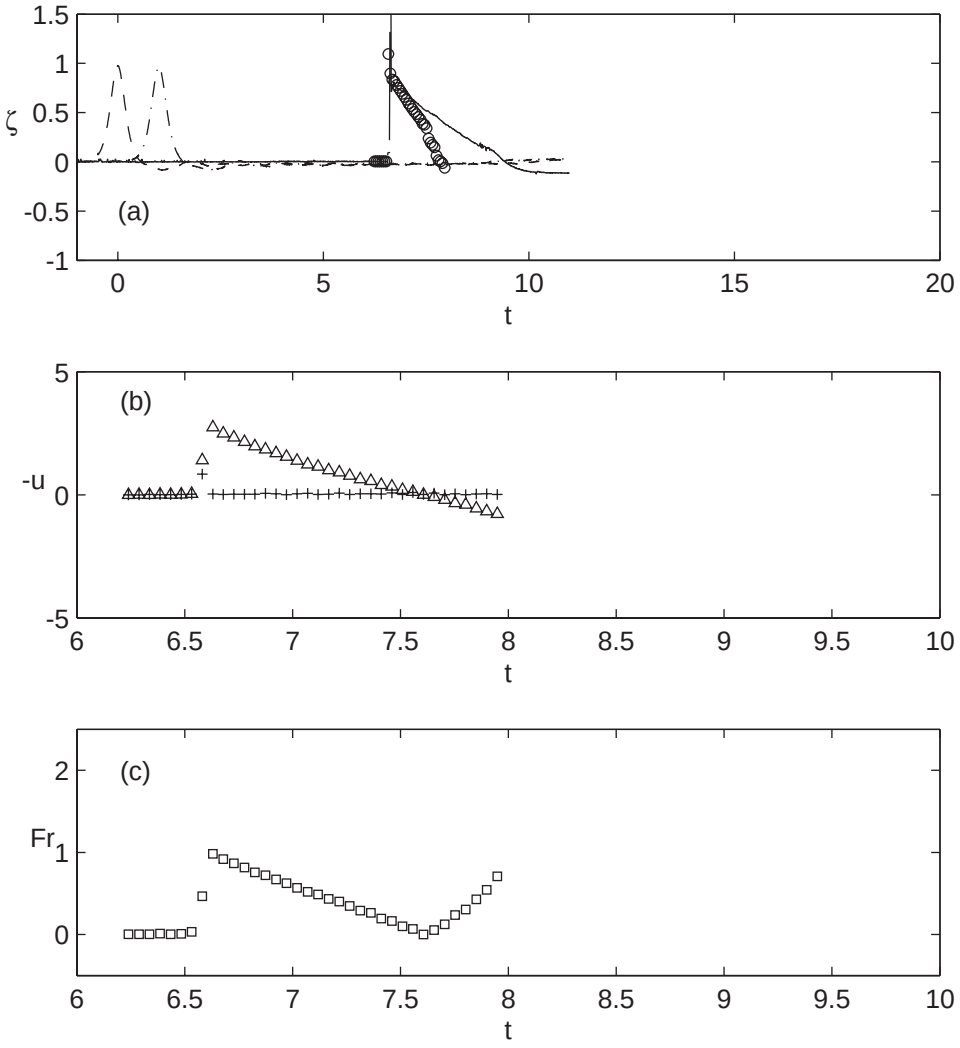

Figure 5.8: Time evolution of the surface elevation (*a*), the depth-averaged velocity (*b*) and the Froude number (*c*) for the case S at window C: −−−−−, water surface profile measured at wave gage 1; —·—, wave gage 2; ——, wave gage 3; ∘, water surface profile estimated from the PIV images; △, depth-averaged velocity; +, IQR around the depth-averaged velocity; □, Froude number based on the depth-averaged velocity and the total water depth.

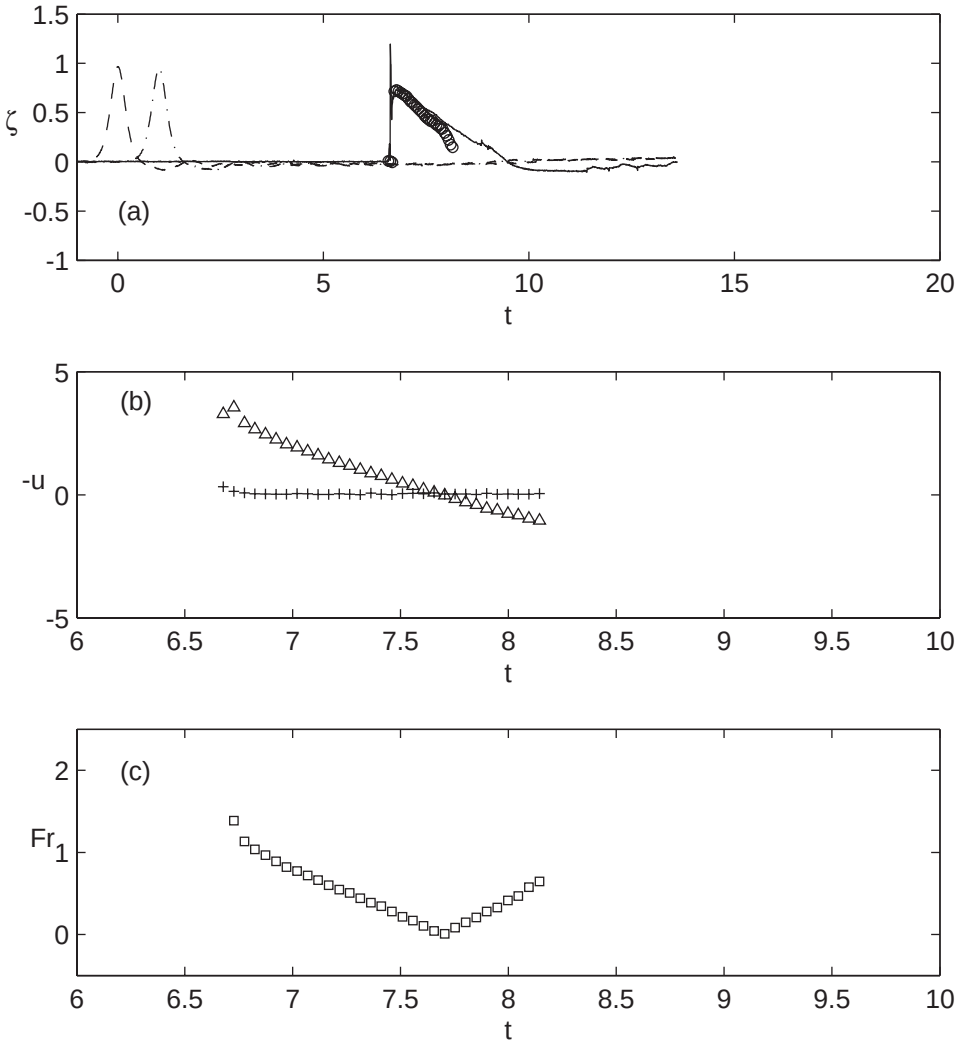

Figure 5.9: Time evolution of the surface elevation (*a*), the depth-averaged velocity (*b*) and the Froude number (*c*) for the case S at window D: −−−−−, water surface profile measured at wave gage 1; —·—, wave gage 2; ——, wave gage 3; ∘, water surface profile estimated from the PIV images; △, depth-averaged velocity; +, IQR around the depth-averaged velocity; □, Froude number based on the depth-averaged velocity and the total water depth.

a large amount of air bubbles is present in the flow. The free surface is less apparent in the PIV images during the backwash phases because fewer number of seeding particles remain in the flow field. Since the surface profile is much smoother, however, the acoustic wave gage can operate properly.

It is observed that the uprush duration is roughly one wave period, while the backwash process lasts slightly longer. Both the water surface elevation and the depth-averaged velocities decrease monotonously after the passage of the wave front.

In the offshore windows A & B, a sudden decrease of water surface elevation is observed for $t > 8.5$, which is accompanied by the increase in the depth-averaged velocity. In view of the Froude number (Fr) based on the depth-averaged velocity and the total water depth, it seems that the moving hydraulic jump occurs ($Fr > 1$) close to window B around this time. It has been shown in figure 5.5 that a clockwise vortex is found at the toe of the hydraulic jump. It is noted that at this location the overturning jet emerges during the uprush (see figure 5.3*b*), resulting in the counterclockwise vortex. These alternating vortices may play important roles in the cross-shore sediment transport, but more experiments with different conditions such as the wave nonlinearity and the slope of the beach will be needed before reaching any conclusion. It is also interesting to note that the wave front maintains critical state ($Fr \sim 1$) during the run-up process.

Finally, the IQR in the vertical profile of the velocity are close to zero except when the wave breaks during the uprush and when the hydraulic jump is formed during the backwash.

5.3.2 The double-wave case with the minimum time separation

For the case with two successive solitary waves, the run-up process of the first wave is very similar to that of the single-wave case (compare figure 5.10*a* with figure 5.3*b*). The interaction between the two successive waves can be immediately recognized by the delay in backwash of the first wave due to the increased positive pressure gradient as the second wave arrives at the beach (figure 5.10*b*). For the case D0, the second wave arrives at the moment the first starts to retreat. The second wave maintains symmetry in the surface profile as the front face is augmented by the water that belonged to the first wave. The water depth of the second wave is deeper while the velocity is slower. As a result, the second wave breaks at a location further onshore and the breaker is much weaker (see figure 5.11).

Again the experimental data taken at the four windows (A, B, C & D) are summarized in figures 5.12–5.15. As was observed in the PIV images and velocity field data, the second wave has the deeper depth and the slower velocity at least during the run-up process.

The run-down process of the first wave is completely stopped by the incoming second wave, during which no significant increase in the IQR in the vertical profile of the velocity is seen. The two waves then merge into one lump of water body and only one reflected wave is found in the constant depth region. Comparing figure 5.13(*a*) with figure5.7(*a*), the arrival time of the reflected wave for the case D0 at the wave gage stations in the constant depth is very close to that of the case S. Though the merged reflected wave of the case D0 depart the beach more than one wave period later the one of the case S did, the much faster phase speed associated with the increased wave height compensates the delay.

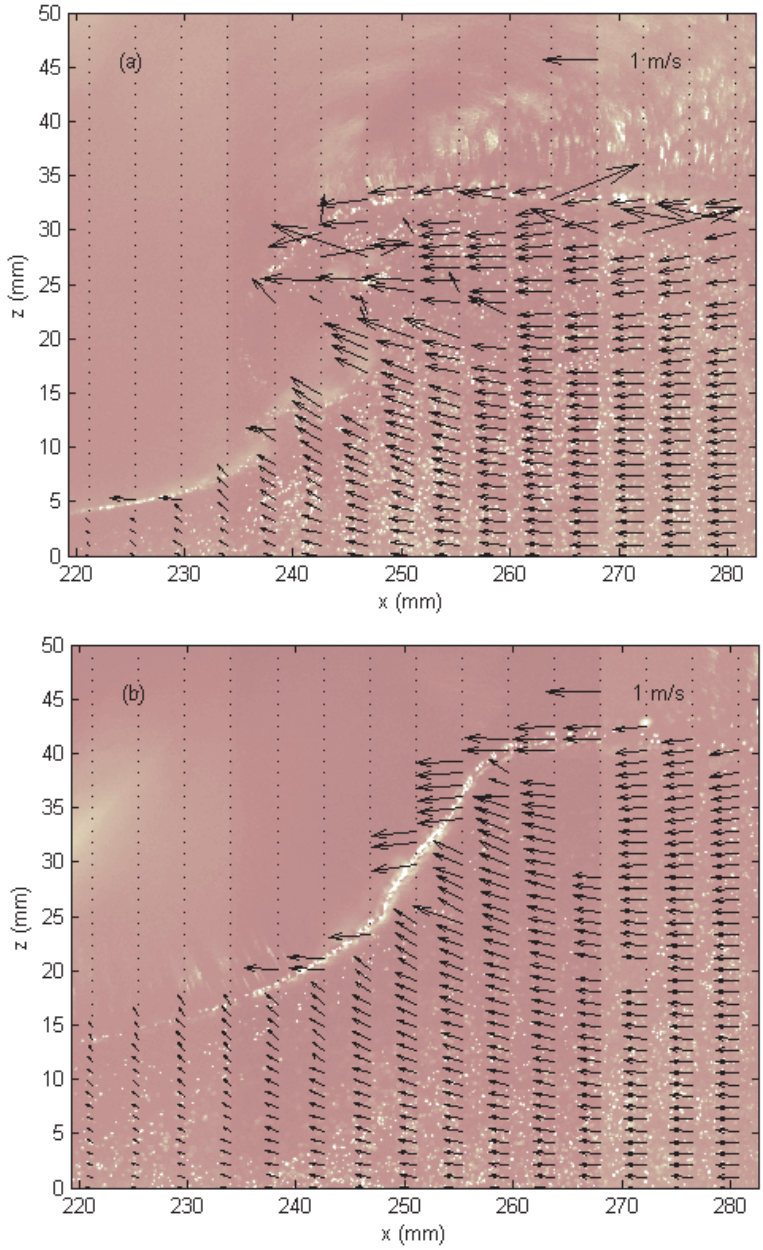

Figure 5.10: The first wave (*a*) and the second wave (*b*) taken at window B for the case D0 at $t = 6.51$ and $t = 7.53$, respectively. While the formation of the overturning jet is apparent in (*a*), the breaking has not occurred in (*b*) due to much milder surface slope.

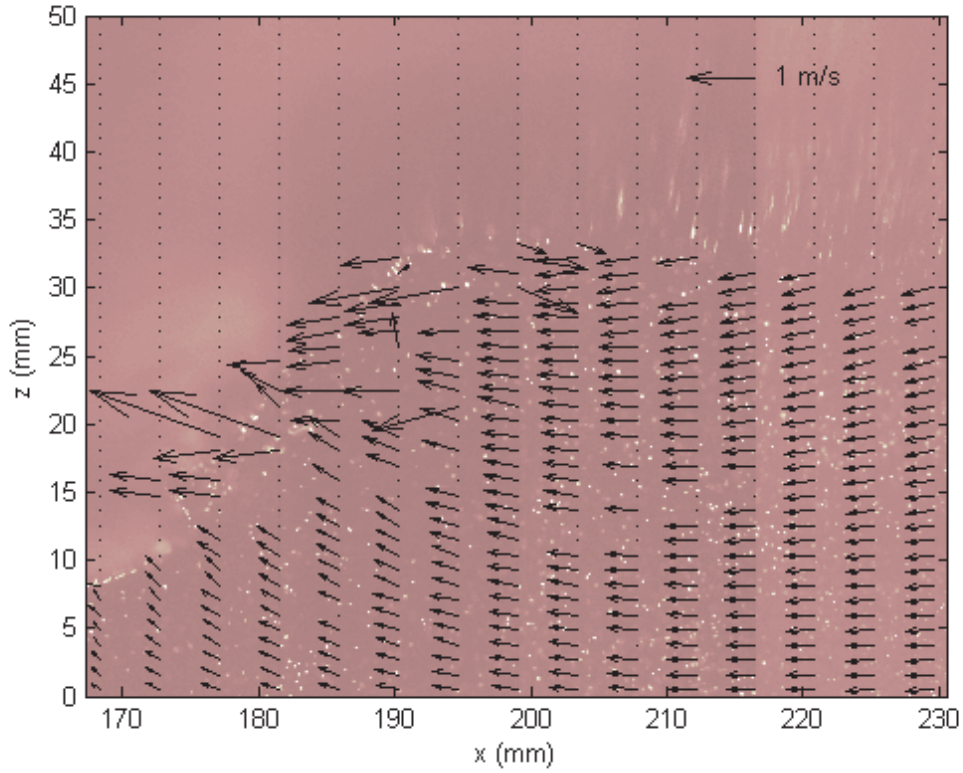

Figure 5.11: Breaking of the second wave taken at window C for the case D0 at $t = 7.74$. Compared to the first wave in figure 5.10(*a*), this occurs further onshore and the breaker is much weaker.

The moving hydraulic jump during the run-down of the merged wave also occurs and appears as the rapid change of slope in the surface profile as well as velocity profile for $t > 9.5$ at windows A & B.

5.3.3 Effects of the time separation

As regular periodic waves approach the beach, nonlinear effects become more important resulting in higher and narrower crests and shallower and wider troughs. Then a series of solitary waves can be thought of as an extreme case

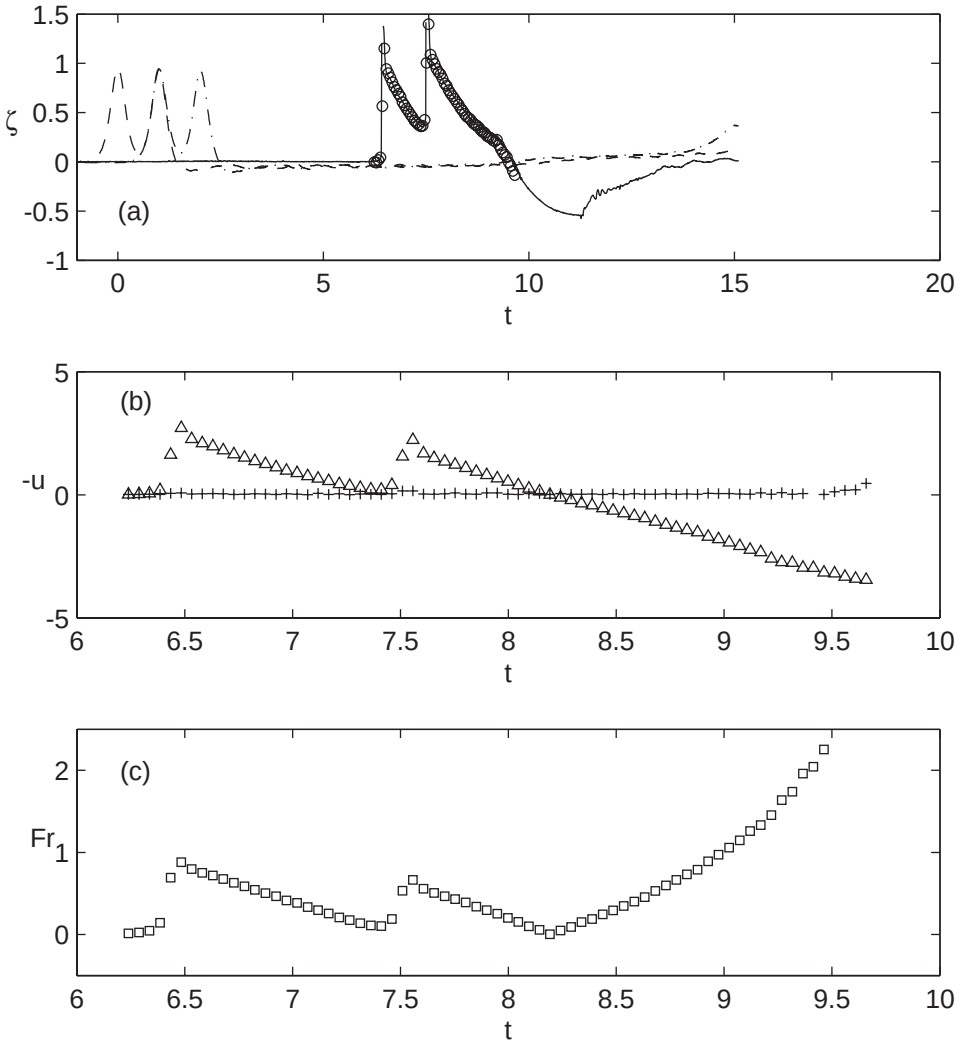

Figure 5.12: Time evolution of the surface elevation (*a*), the depth-averaged velocity (*b*) and the Froude number (*c*) for the case D0 at window A: −−−−−, water surface profile measured at wave gage 1; —·—, wave gage 2; ——, wave gage 3; ∘, water surface profile estimated from the PIV images; △, depth-averaged velocity; +, IQR around the depth-averaged velocity; □, Froude number based on the depth-averaged velocity and the total water depth.

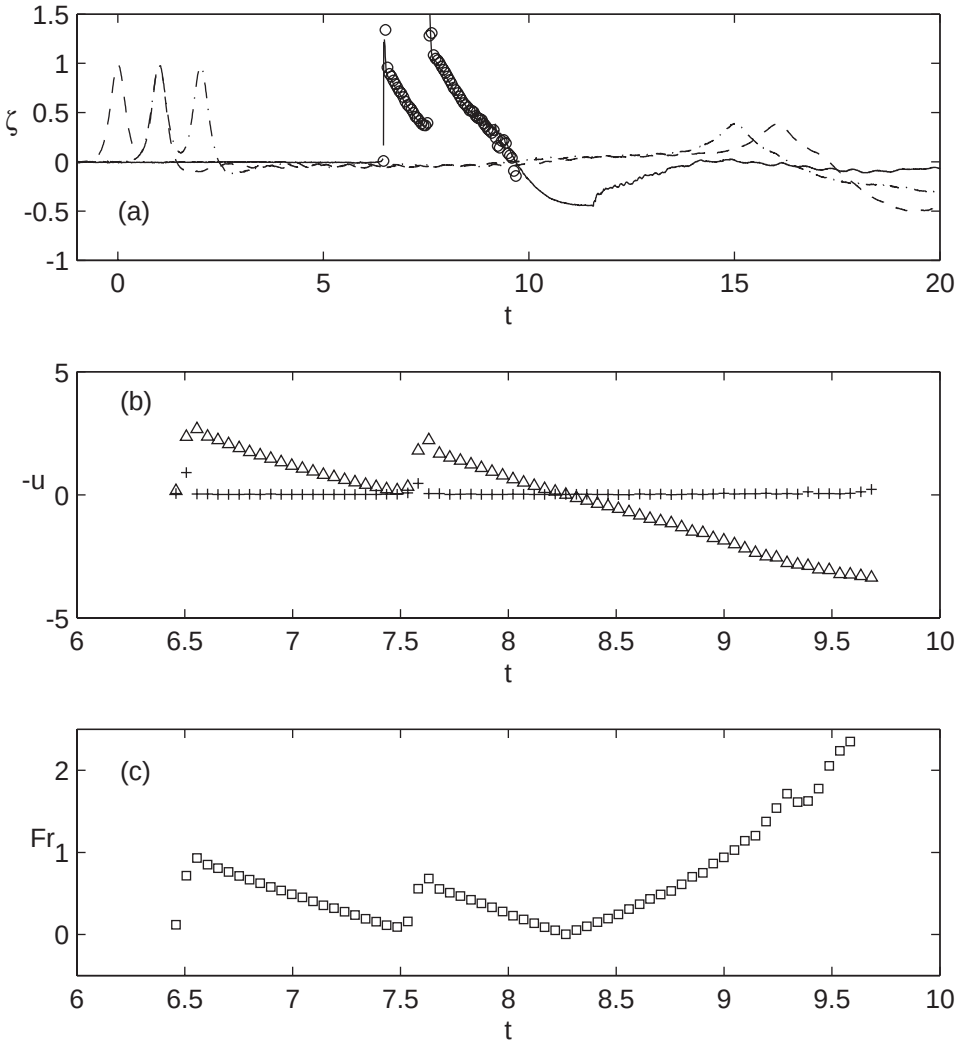

Figure 5.13: Time evolution of the surface elevation (*a*), the depth-averaged velocity (*b*) and the Froude number (*c*) for the case D0 at window B: −−−−−, water surface profile measured at wave gage 1; —·—, wave gage 2; ——, wave gage 3; ∘, water surface profile estimated from the PIV images; △, depth-averaged velocity; +, IQR around the depth-averaged velocity; □, Froude number based on the depth-averaged velocity and the total water depth.

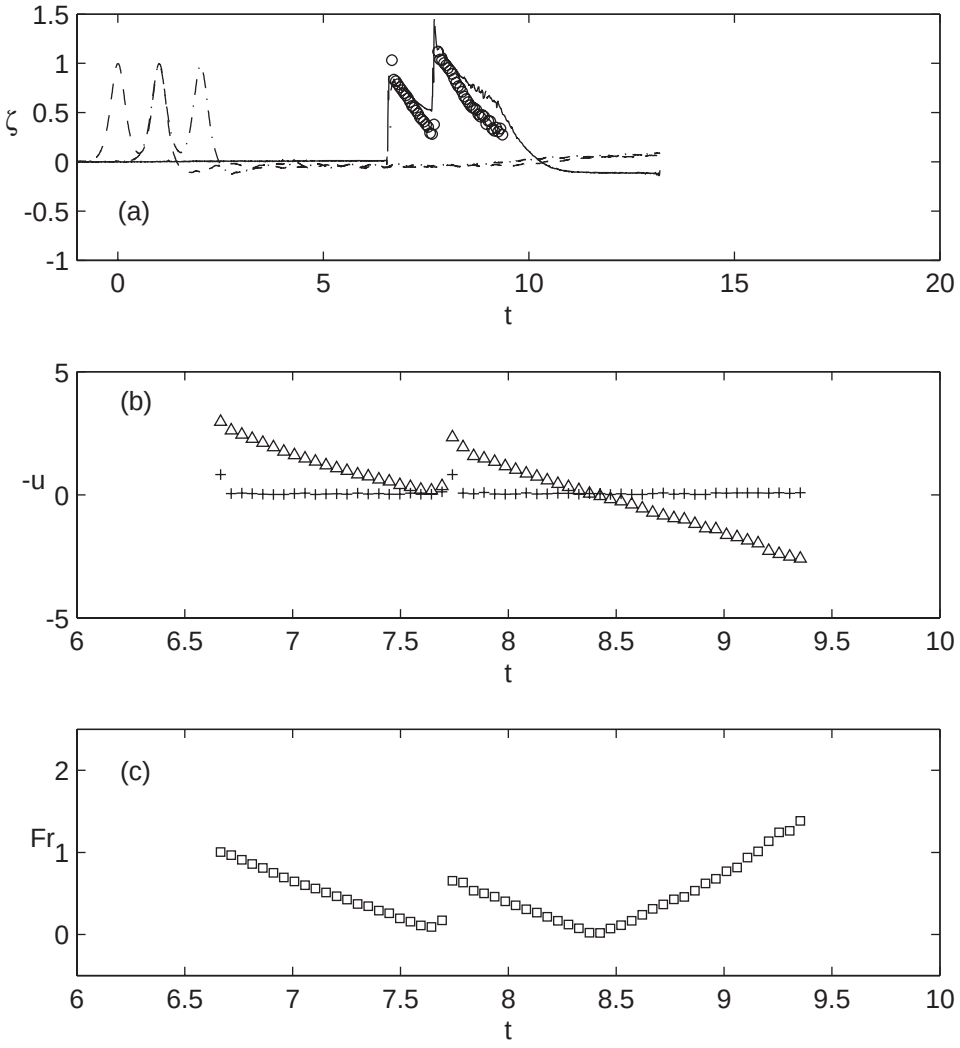

Figure 5.14: Time evolution of the surface elevation (*a*), the depth-averaged velocity (*b*) and the Froude number (*c*) for the case D0 at window C: −−−−−, water surface profile measured at wave gage 1; —·—, wave gage 2; ——, wave gage 3; ∘, water surface profile estimated from the PIV images; △, depth-averaged velocity; +, IQR around the depth-averaged velocity; □, Froude number based on the depth-averaged velocity and the total water depth.

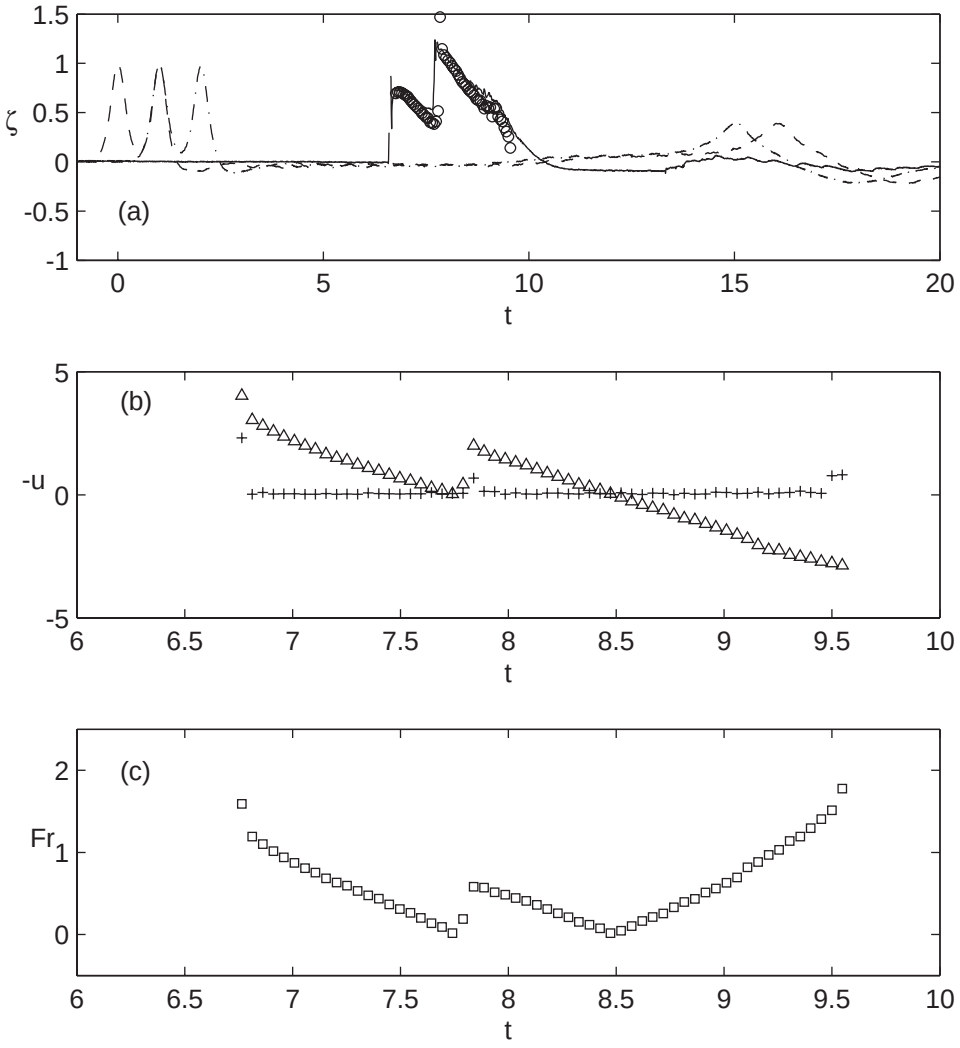

Figure 5.15: Time evolution of the surface elevation (*a*), the depth-averaged velocity (*b*) and the Froude number (*c*) for the case D0 at window D: −−−−−, water surface profile measured at wave gage 1; —·—, wave gage 2; ——, wave gage 3; ∘, water surface profile estimated from the PIV images; △, depth-averaged velocity; +, IQR around the depth-averaged velocity; □, Froude number based on the depth-averaged velocity and the total water depth.

consisting of elevation waves only (Stiassnie & Peregrine, 1980). If troughs are not negligible, however, a surf zone induced by the successively breaking solitary waves may be too skewed towards the uprush phases, especially near the breaker line. To estimate the role of troughs in the surf zone hydrodynamics, a few different time separations between the two crests have been studied. The rationale is that the second wave meets the first wave at different stages of the backwash depending on the time separation.

The experimental results for the cases D1 throught D7 are shown in figures 5.16–5.22.

With the larger time separation between the two waves, the run-down process of the first wave develops further before the incoming of the second wave. Generally, the wave heights of the second waves arriving at window D are smaller for the cases with the larger separation, which may be explained by less supply of water from the first waves.

For the depth-averaged velocity, there seems to exist some optimum value of the time separation that minimizes the velocity of the second wave. As can be seen in the Froude number plots, for some cases, the backwash flow of the first wave can reach supercritical state before meeting with the second wave. Considering flow behind the wave front during the run-up process must be subcritical, the collision of the waves should result in a hydraulic jump. If that is combined with the breaking of the second wave, a large amount of energy dissipation as well as canceling of momentum with opposite signs might happen. If the time separation is beyond the optimum value, then the first wave can already finish the run-down process before the second wave arrives. Thus the run-up process of the second wave resembles that of the first as can be seen

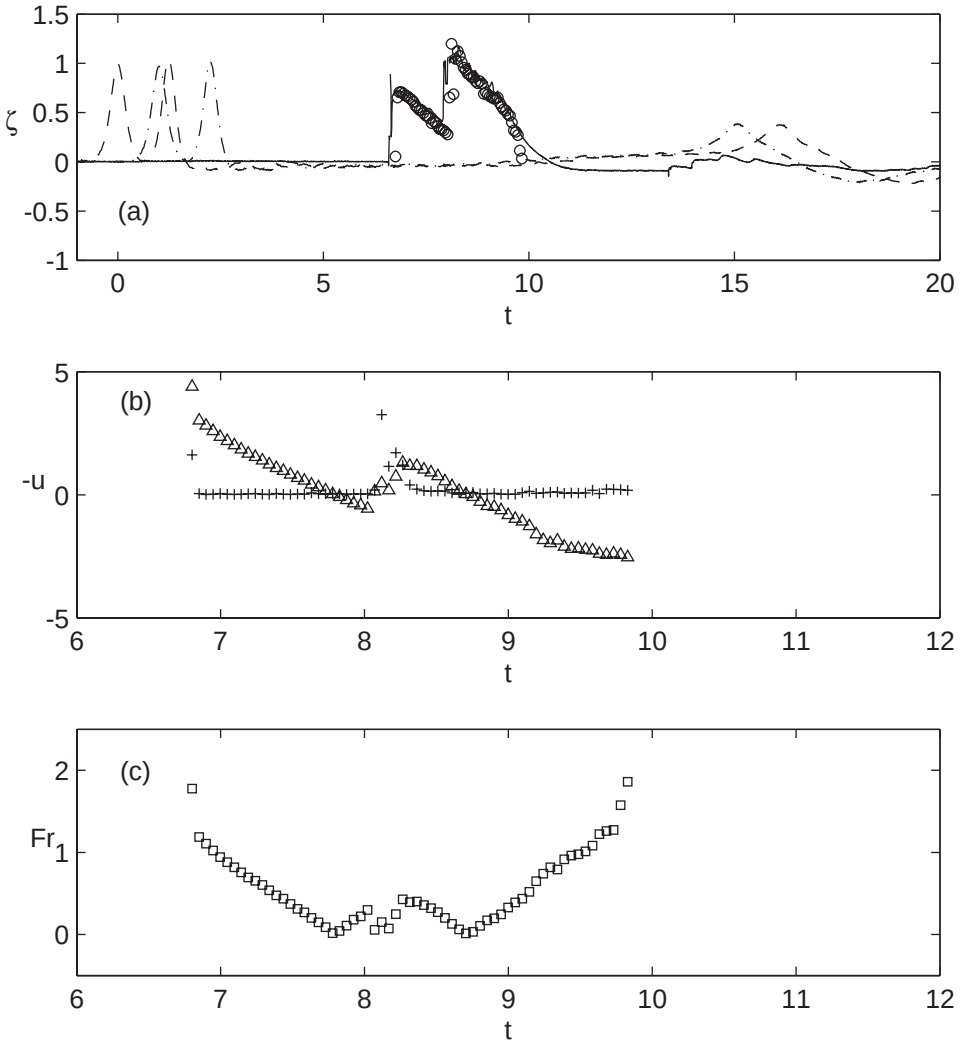

Figure 5.16: Time evolution of the surface elevation (*a*), the depth-averaged velocity (*b*) and the Froude number (*c*) for the case D1 at window D: −−−−−, water surface profile measured at wave gage 1; —·—, wave gage 2; ——, wave gage 3; ∘, water surface profile estimated from the PIV images; △, depth-averaged velocity; +, IQR around the depth-averaged velocity; □, Froude number based on the depth-averaged velocity and the total water depth.

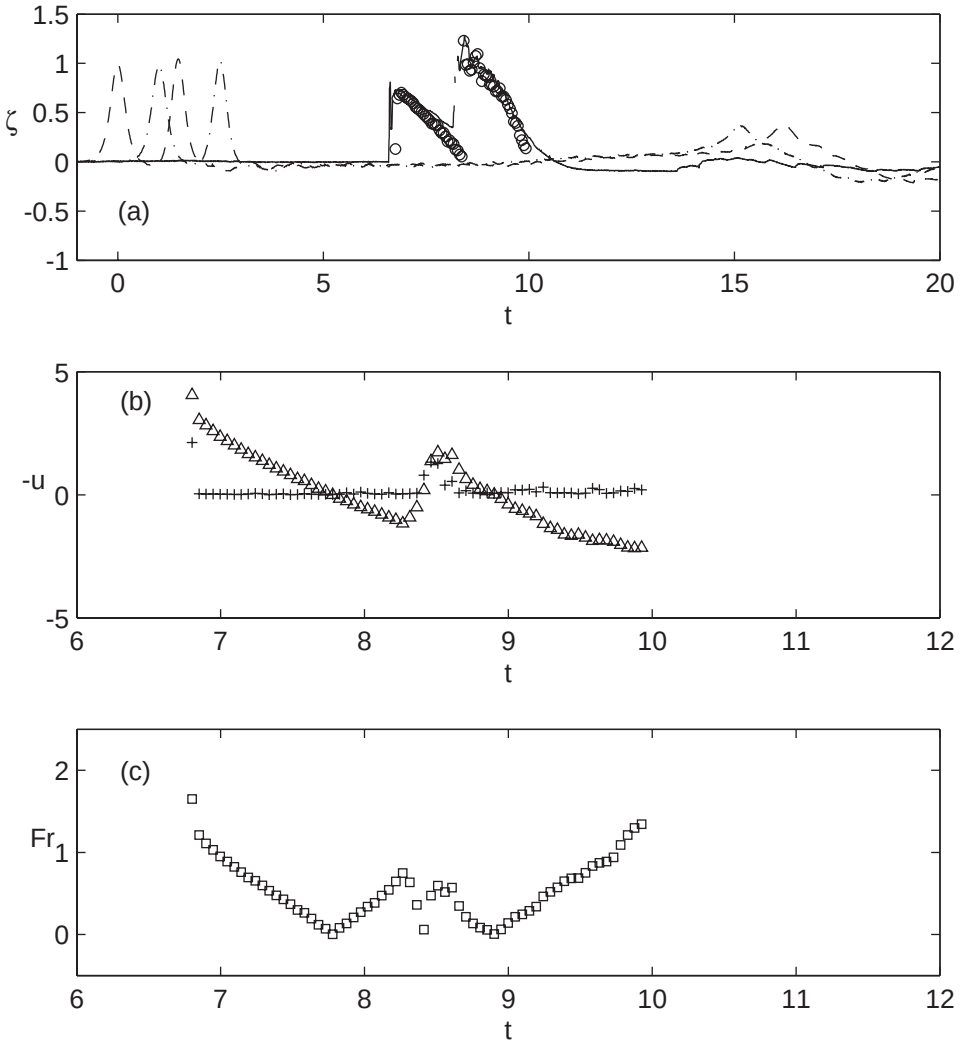

Figure 5.17: Time evolution of the surface elevation (*a*), the depth-averaged velocity (*b*) and the Froude number (*c*) for the case D2 at window D: −−−−−, water surface profile measured at wave gage 1; —·—, wave gage 2; ——, wave gage 3; ∘, water surface profile estimated from the PIV images; △, depth-averaged velocity; +, IQR around the depth-averaged velocity; □, Froude number based on the depth-averaged velocity and the total water depth.

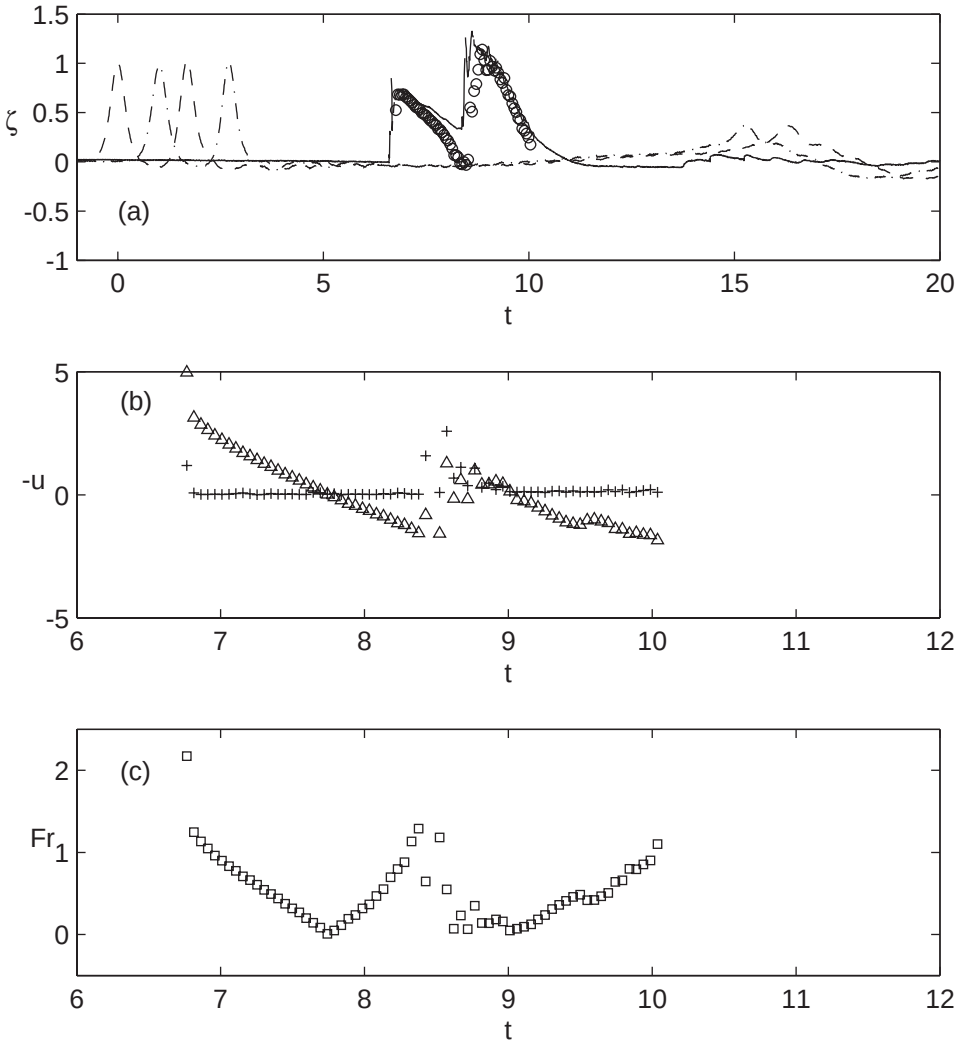

Figure 5.18: Time evolution of the surface elevation (*a*), the depth-averaged velocity (*b*) and the Froude number (*c*) for the case D3 at window D: −−−−−, water surface profile measured at wave gage 1; —·—, wave gage 2; ——, wave gage 3; ∘, water surface profile estimated from the PIV images; △, depth-averaged velocity; +, IQR around the depth-averaged velocity; □, Froude number based on the depth-averaged velocity and the total water depth.

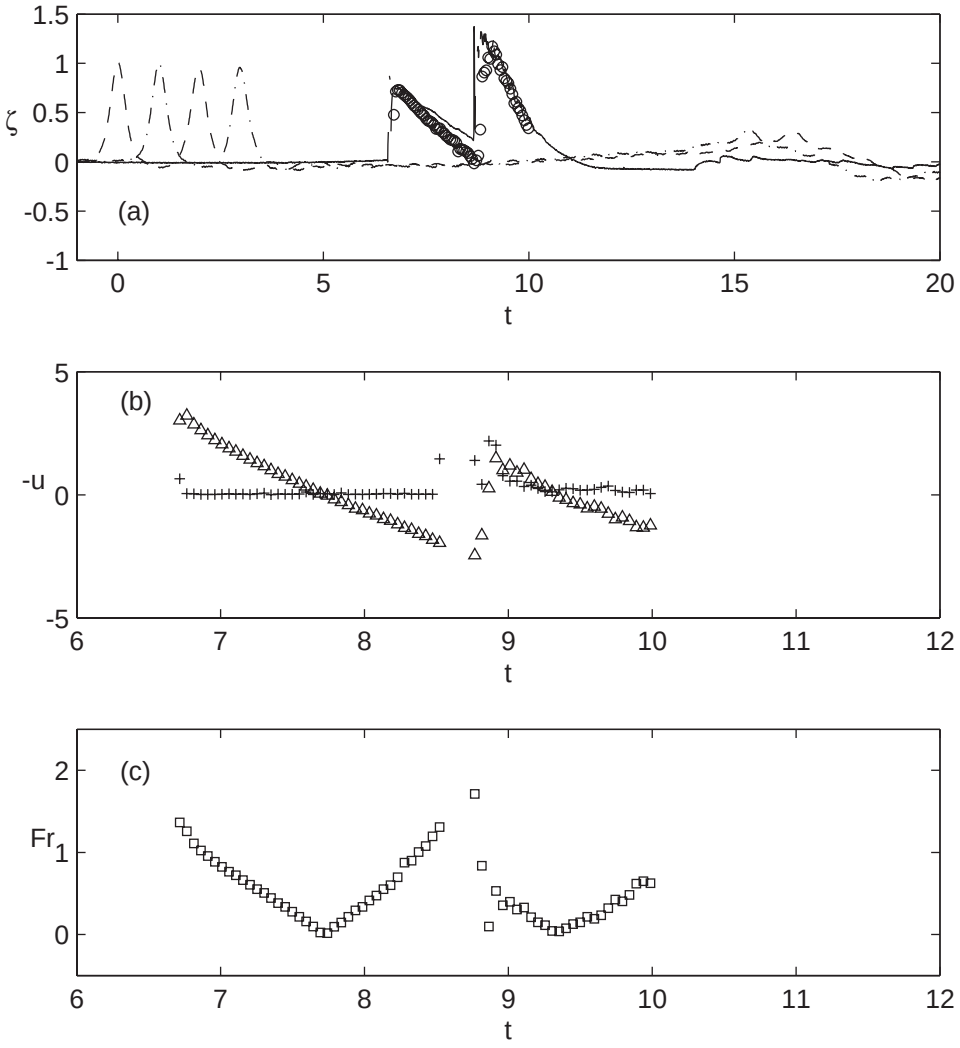

Figure 5.19: Time evolution of the surface elevation (*a*), the depth-averaged velocity (*b*) and the Froude number (*c*) for the case D4 at window D: −−−−−, water surface profile measured at wave gage 1; —·—, wave gage 2; ——, wave gage 3; ∘, water surface profile estimated from the PIV images; △, depth-averaged velocity; +, IQR around the depth-averaged velocity; □, Froude number based on the depth-averaged velocity and the total water depth.

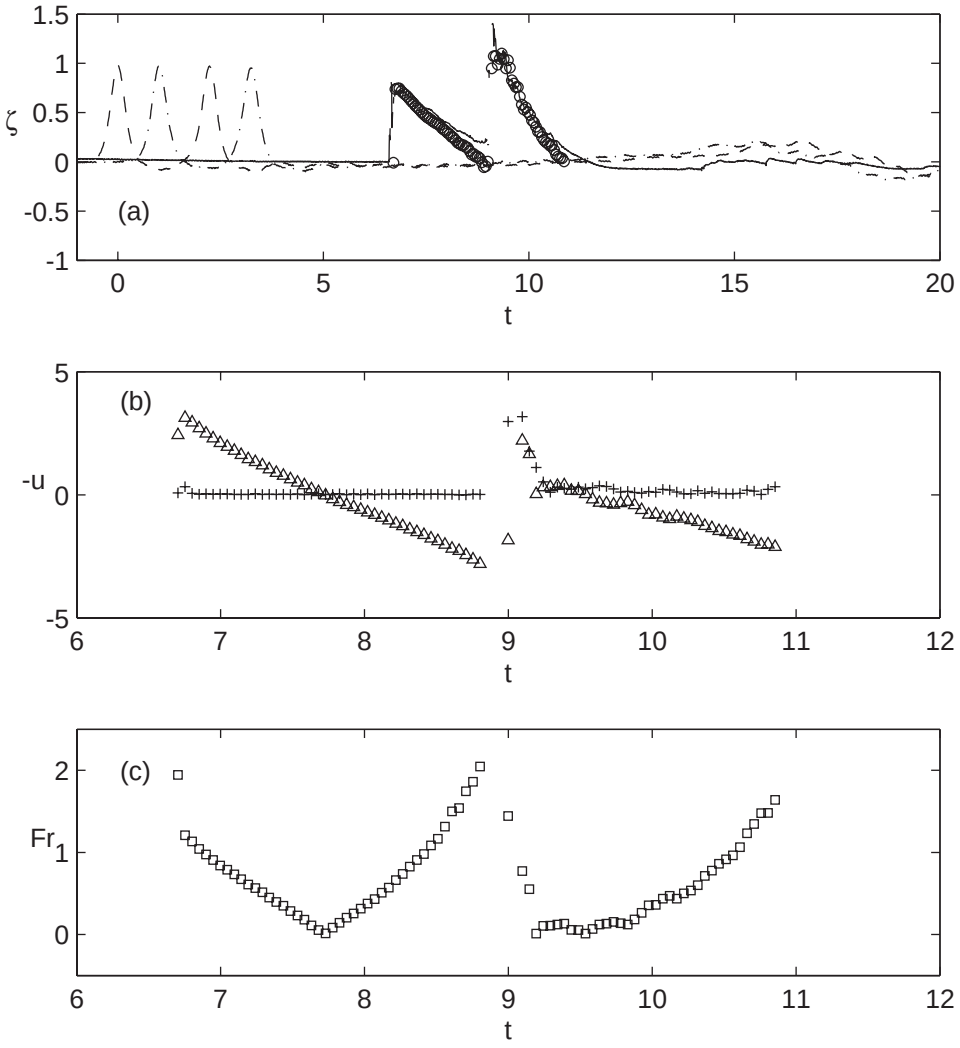

Figure 5.20: Time evolution of the surface elevation (*a*), the depth-averaged velocity (*b*) and the Froude number (*c*) for the case D5 at window D: −−−−−, water surface profile measured at wave gage 1; —·—, wave gage 2; ——, wave gage 3; ∘, water surface profile estimated from the PIV images; △, depth-averaged velocity; +, IQR around the depth-averaged velocity; □, Froude number based on the depth-averaged velocity and the total water depth.

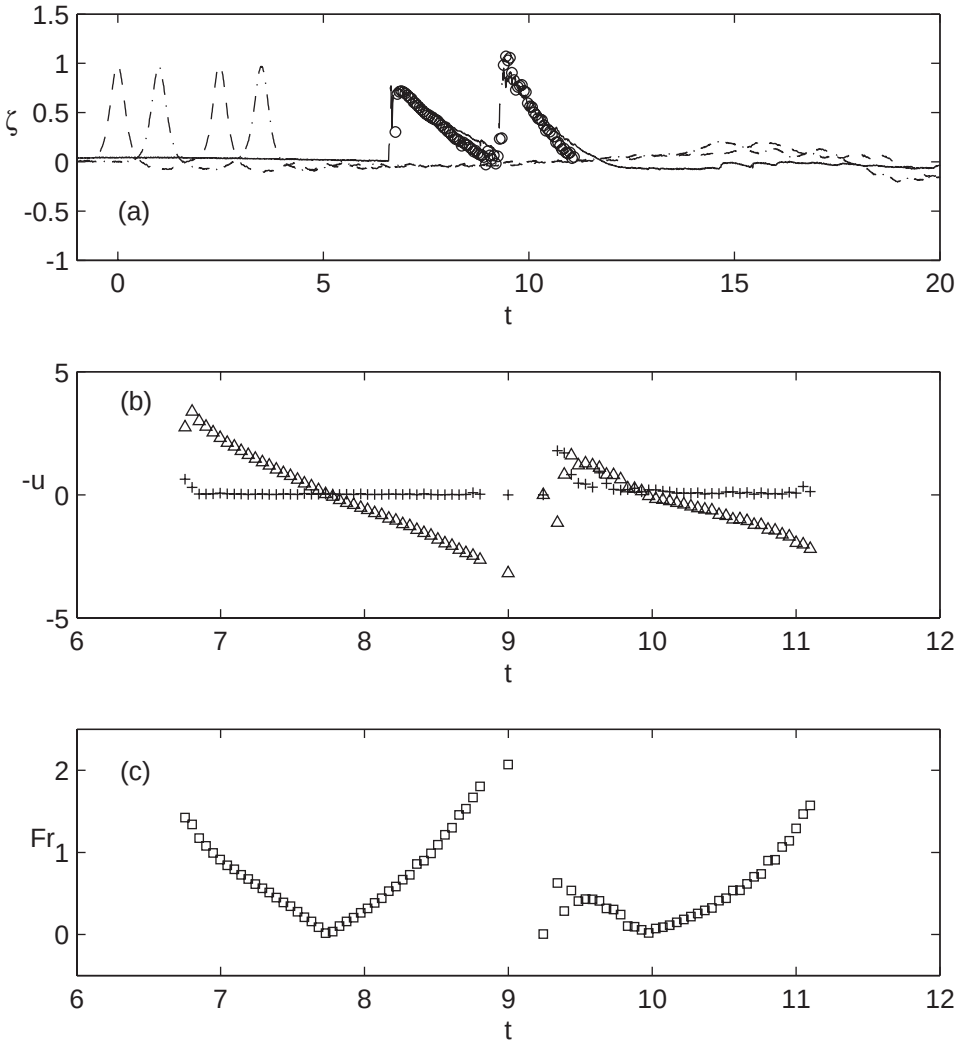

Figure 5.21: Time evolution of the surface elevation (*a*), the depth-averaged velocity (*b*) and the Froude number (*c*) for the case D6 at window D: −−−−−, water surface profile measured at wave gage 1; —·—, wave gage 2; ——, wave gage 3; ∘, water surface profile estimated from the PIV images; △, depth-averaged velocity; +, IQR around the depth-averaged velocity; □, Froude number based on the depth-averaged velocity and the total water depth.

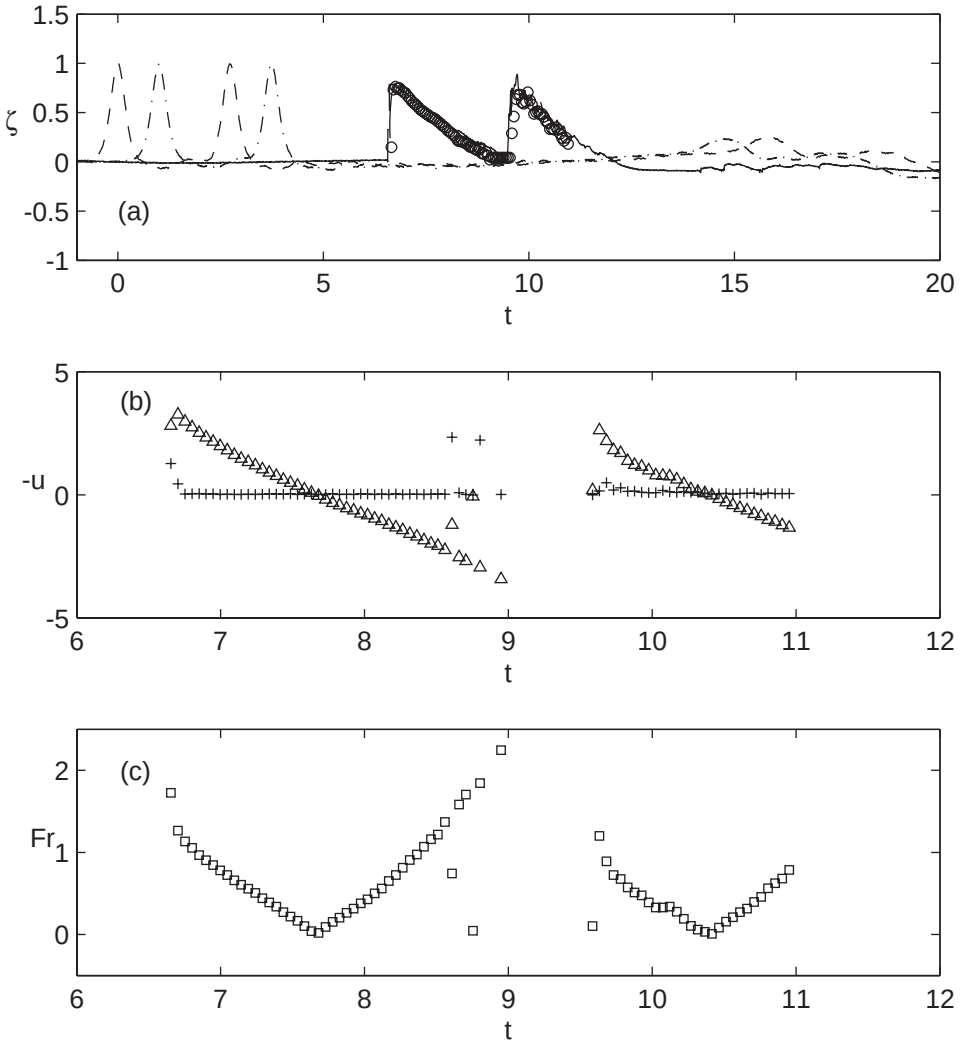

Figure 5.22: Time evolution of the surface elevation (*a*), the depth-averaged velocity (*b*) and the Froude number (*c*) for the case D7 at window D: −−−−−, water surface profile measured at wave gage 1; —·—, wave gage 2; ——, wave gage 3; ∘, water surface profile estimated from the PIV images; △, depth-averaged velocity; +, IQR around the depth-averaged velocity; □, Froude number based on the depth-averaged velocity and the total water depth.

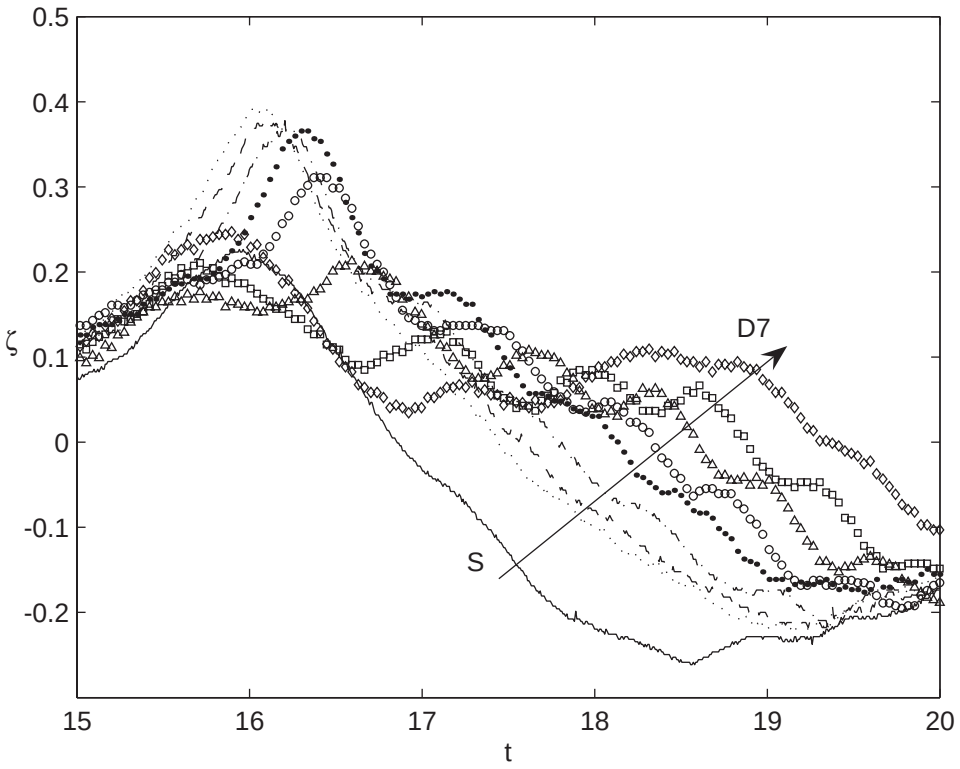

Figure 5.23: Reflected waves from all of the experimental cases: —·—, case S; · · · · ·, D0; − − − − −, D1; —·—, D2; •, D3; ◦, D4; △, D5; □, D6; ⋄, D7.

in figure 5.22(*b*).

As mentioned before, reflected waves can play a role as an indicator of the wave–wave interaction in the surf zone. In figure 5.23, reflected waves from all of the experimental cases are plotted together. Overall, it is first noted that all the surface profiles can be covered by an envelop. When the two wave crests are very close to each other (cases D0 to D3), only one relected wave is observed, though the arrival time of the peak shows a positive correlation with the time separation. From the case D4, secondary peaks start to emerge on both sides of the main peaks. The secondary peaks ahead of the main peaks keep growing

with the increasing time separation and approach toward the reflected wave of the experimental case with a single wave.

5.4 Concluding remarks

Wave breaking is a highly transient and nonlinear phenomenon, which results in a multi-phase, three-dimensional, turbulent flow. Hence, studying breaking waves and breaking-induced flow fields is challenging, while it is critically important in protecting and managing coastal environments. Over the last few decades, researchers have painstakingly built up a considerable amount of knowledge and, as a result, mean (time-averaged over a wave period or phase-averaged) flow fields are relatively well understood. Still, it is noted that interactions between successively breaking waves have not received much attention. Aiming to identify the origins and the development paths of the mean quasi-steady flow characteristics in surf zone, laboratory experiments on a train of almost identical solitary waves breaking on a 1:20 sloping beach were carried out and reported for the first time.

By generating up to two solitary waves with varied time separations between the crests, the effects of the earlier breaking waves on the next were investigated by measuring water surface profiles and detailed velocity fields. The vast amount of data could be effectively summarized in terms of the time-varying Froude number (Fr) based on the depth-averaged velocity and the total water depth. From the experiments with a single wave, it was observed that the front of the wave maintains critical state ($Fr \sim 1$) during the uprush. A moving hydraulic jump was also observed during the backwash near the initial shore

line when the flow reaches the critical state again. In the double-wave cases, the run-up of the first wave was almost identical to the single-wave case until the moment the second wave arrives. When the time separation between the crests are small, the run-down of the first wave is delayed and the breaking of the second wave occurs further onshore in a much weaker form, with the Froude number less than 1. With the increasing time separation, the water surface elevation and the depth-averaged velocity under the front of the second wave become close to those of the first wave. Still, the level of turbulence, which is indirectly estimated by the IQR of the velocity around the depth-averaged velocity, is higher for the second wave. Reflected waves measured in the constant depth region turned out to be a good indicator of the interactions between the two waves. Especially, when the two waves were close to each other, only one reflected wave could be observed.

Still, many important questions have been left unanswered mainly due to the limitations in the experimental equipment. First of all, cases with three or more waves need to be studied to connect this research to the existing knowledge on the mean flow fields. However only up to two waves could be generated with 25 cm stroke length of the wavemaker. Void fraction and turbulence were not measured, which are crtical in understanding surf-zone dynamics. In that sense, the current research cannot be claimed to be complete, but it is intended to invite and guide future research. For example, a new wavemaker with 4 m stroke has been installed in the DeFrees Hydrualics Laboratory, which will enable the generation of many solitary waves with increased wave heights. More insightful results are expected in the coming years.

CHAPTER 6

CONCLUSIONS

The coastal regions are the intersection of ocean, atmosphere, land and human activities. The focus of this disseration has been the dynamics of the sea bottom boundary and the free surface breaking in the coastal areas. Naturally, the disseration is divided into two parts.

In the first part, the dynamics of the bottom boundary with various rheological properties has been examined within the framework of the boundary layer theory. Experimental measurements on the laminar boundary layer flows under a long wave clearly proved the validity of the theory. In particular, a flow reversal was observed during the deceleration phase of the long wave, which agreed with the theoretical prediction very well. Then the theory was extended to describe wave-induced flows inside a viscous mud. Two sets of experiments were conducted, one in the wave tank and the other in the U-tube to investigate the role of the mud-layer thickness compared to the boundary-layer thickness of the mud. Again excellent agreement between the theory and the experiment was achieved. Then the U-tube, which was specially built for the current research, enabled the study of the oscillatory flows of a non-Newtonian fluid. Experimental results showed that the generalized Newtonian constitutive relations, in which the shear stress is assumed to be some function of the rate of shear strain only, are not appropriate in describing unsteady flows of the yield-stress material. More relevant rheological properties were directly calculated from the velocity data and the resulting analytical solutions matched the experimental data very well.

Many questions still remain. Particularly, turbulent boundary layer needs to be studied as well as its effects on muddy seabeds of various rheological properties. Throughout the dissertation, efforts have been made to provide theoretical and experimental frameworks to pursue this unanswered questions. For example, though the experiments on the non-Newtonian seabed were carried out with a physcial model for muds, characteristics of real mud flows can be studied in the same way.

This attention to the future research was also maintained in the second part of the disseration. Up to now, the research on breaking waves in the near-shore area has focused on time-averaged or phase-averaged mean flow fields. However, many important natural events (disasters) are indeed transient. To bridge the gap between our knowledge and the need of deeper understanding on surf-zone dynamics, it is proposed here to study the interactions of successively breaking waves. With the absence of the guiding theory and the limitations in the experimental set-up, the objective from the beginning was to provide a framework for the future research. Especially, it was found that the vast amount of data are effectively summarized in terms of the Froude number and the reflected waves can be used as a convenient indicator of the wave–wave interactions. Further experiments with more waves are needed before reaching any conclusion. In response to this research, a new wavemaker has been installed in the DeFrees Hydraulics Laboratory at Cornell University. More results will follow in the near future.

REFERENCES

ADGER, W. N., HUGHES, T. P., FOLKE, C., CARPENTER, S. R. & ROCKSTRÖM. J. 2005 Social-ecological resilience to coastal disasters. *Science* **309**, 1036–1039.

BALMFORTH, N. J. & CRASTER, R. V. 2001 Geophysical aspects of non-Newtonian fluid mechanics. In *Geomorphological Fluid Mechanics* (ed. P. A. Tyvand & A. Provenzale), pp. 34–51. Springer.

BALMFORTH, N. J., FORTERRE, Y. & POULIQUEN, O. 2009 The viscoplastic Stokes layer. *J. Non-Newtonian Fluid Mech.* **158**, 46–53.

BARNES, H. A. & WALTERS, K. 1985 The yield stress myth? *Rheol. Acta* **24**, 323–326.

BARNES, M. P., O'DONOGHUE, T., ALSINA, J. M. & BALDOCK, T. E. 2009 Direct bed shear stress measurements in bore-driven swash. *Coastal Engng* **56**, 853–867.

BARSTOW, S., MØRK, G., MOLLISON, D. & CRUZ, J. 2008 The wave energy resource. In *Ocean Wave Energy* (ed. Cruz, J.), 93–132. Springer.

BATTJES, J. A. 1988 Surf-zone dynamics. *Annu. Rev. Fluid Mech.* **20**, 257–293.

BINGHAM, E. C. 1922 *Fluidity and Plasticity.* McGraw-Hill.

BIRD, R. B. 1976 Useful non-Newtonian models. *Annu. Rev. Fluid Mech.* **8**, 13–34.

BIRD, R. B., DAI, G. C. & YARUSSO, B. J. 1983 The rheology and flow of viscoplastic materials. *Rev. Chem. Engng* **1**, 1–70.

CARSLAW, H. S. & JAEGER, J. C. 1986 *Conduction of Heat in Solids.* The Clarendon.

CHAN, I.-C. & LIU, P. L.-F. 2009 Responses of Bingham-plastic muddy seabed to a surface solitary wave. *J. Fluid Mech.* **618**, 155-180.

COUSSOT, P. 2005 *Rheometry of Pastes, Suspensions and Granular Materials: Applications in Industry and Environment.* John Wiley & Sons.

COUSSOT, P., TOCQUER, L., LANOS, C. & OVARLEZ, G. 2009 Macroscopic vs. local rheology of yield stress fluids. *J. Non-Newtonian Fluid Mech.* **158**, 85–90.

COWEN, E. A. 1996 An experimental investigation of the near-surface effects of waves traveling on a turbulent current. PhD dissertation, Stanford University.

COWEN, E. A. & MONISMITH, S. G. 1997 A hybrid digital particle tracking velocimetry technique. *Exps. Fluids* **22**, 199–211.

COWEN, E. A., SOU, I. M., LIU, P. L.-F. & RAUBENHEIMER, B. 2003 Particle image velocimetry measurements within a laboratory-generated swash zone. *J. Engng Mech.* **129**, 1119–1129.

COX, D. T., KOBAYASHI, N. & OKAYASU, A. 1996 Bottom shear stress in the surf zone. *J. Geophys. Res.* **101**, 14337–14348.

COX, D. T. & SHIN, S. 2003 Laboratory measurements of void fraction and turbulence in the bore region of surf zone waves. *J. Engng Mech.* **129**, 1197–1205.

CROSSETT, K. M., CULLITON, T. J., WILEY, P. C. & GOODSPEED, T. R. 2004 *Population Trends Along the Coastal United States: 1980-2008*. National Oceanic and Atmospheric Administration.

DALRYMPLE, R. A. & LIU, P. L.-F. 1978 Waves over soft muds: a two-layer model. *J. Phys. Oceanogr.* **8**, 1121–1131.

DEANE, G. B. & STOKES, M. D. 2002 Scale dependence of bubble creation mechanisms in breaking waves. *Nature* **418**, 839–844.

DEEN, N. G., WESTERWEEL, J. & DELNOIJ, E. 2002 Two-phase PIV in bubbly flows: status and trends. *Chem. Engng Technol.* **25**, 97–101.

EFRON, B. & TIBSHIRANI, R. 1993 *An Introduction to the Bootstrap.* Chapman & Hall.

FAN, Y., PHAN-THIEN, N. & TANNER, R. I. 2001 Tangential flow and advective mixing of viscoplastic fluids between eccentric cylinders. *J. Fluid Mech.* **431**, 65–89.

FODA, M. A. 1989 Sideband damping of water waves over a soft bed. *J. Fluid Mech.* **201**, 189–201.

GADE, H. G. 1958 Effects of a nonrigid, impermeable bottom on plane surface waves in shallow water. *J. Mar. Res.* **16**, 61–82.

GORING, D. K. 1979 Tsunamis–the propagation of long waves onto a shelf. PhD dissertation, California Institute of Technology.

GRILLI, S. T., SVENDSEN, I. A. & SUBRAMANYA, R. 1997 Breaking criterion and characteristics for solitary waves on slopes. *J. Wtrwy, Port, Coastal and Oc. Engng* **123**, 102–112.

GRIMSHAW, R. 1971 The solitary wave in water of variable depth. Part 2. *J. Fluid Mech.* **46**, 611–622.

HIBBERD, S. & PEREGRINE, D. H. 1979 Surf and run-up on a beach: a uniform bore. *J. Fluid Mech.* **95**, 323–345.

IPPEN, A. T. & MITCHELL, M. M. 1957 The damping of the solitary wave from boundary shear measurements. *Tech. Rep., Hydrodynamics Laboaratory* **23**. Massachusetts Institute of Technology.

JAIN, M. & MEHTA A. J. 2009 Role of basic rheological models in determination of wave attenuation over muddy seabeds. *Cont. Shelf Res.* **29**, 642–651.

JENSEN, B. L., SUMER, B. M. & FREDSØE, J. 1989 Turbulent oscillatory boundary layers at high Reynolds numbers. *J. Fluid Mech.* **206**, 265–297.

KEULEGAN, G. H. 1948 Gradual damping of solitary waves. *J. Res. Natl Bur. Stand.* **40**, 487–498.

KIMMOUN, O. & BRANGER, H. 2007 A particle image velocimetry investigation on laboratory surf-zone breaking wave over a sloping beach. *J. Fluid Mech.* **588**, 353–397.

KNABB, R. D., RHOME, J. R. & BROWN, D. P. 2005 Hurricane Katrina 23-30 August 2005. Tropical Cyclone Report, National Hurricane Center.

LI, Y. & RAICHLEN, F. 2002 Non-breaking and breaking solitary wave run-up. *J. Fluid Mech.* **456**, 295–318.

LI, Y. & RAICHLEN, F. 2003 Energy balance model for breaking solitary wave run-up. *J. Wtrwy, Port, Coastal and Oc. Engng* **129**, 47–59.

LIM, H.-J., CHANG, K.-A., SU, C. B. & CHEN, C.-Y. 2008 Bubble velocity, diameter and void fraction measurements in a multiphase flow using fiber optic reflectometer. *Rev. Sci. Instrum.* **79**, 125105.

LIU, K.-F. & MEI, C. C. 1990 Approximate equations for the slow spreading of a thin sheet of Bingham plastic fluid. *Phys. Fluids A* **2**, 30–36.

LIN, P., CHANG, K.-A. & LIU, P. L.-F. 1999 Runup and rundown of solitary waves on sloping beaches. *J. Wtrwy, Port, Coastal and Oc. Engng* **125**, 247–255.

LIU, P. L.-F. 2006 Turbulent boundary-layer effects on transient wave propagation in shallow water. *Proc. R. Soc. A* **462**, 3481–3491.

LIU, P. L.-F. & CHAN, I.-C. 2007 On long wave propagation over a fluid-mud seabed. *J. Fluid Mech.* **579**, 467–480.

LIU, P. L.-F., LYNETT, P., FERNANDO, H., JAFFE, B. E., FRITZ, H., HIGMAN, B., MORTON, R.,GOFF, J. & SYNOLAKIS, C. 2005 Observations by the international tsunami survey team in Sri Lanka. *Science* **308**, 1595.

LIU, P. L.-F. & ORFILA, A. 2004 Viscous effects on transient long-wave propagation. *J. Fluid Mech.* **520**, 83–92.

LIU, P. L.-F. & PARK, Y. S. 2008 Recent advancement in modeling seafloor dissipative mechanism in shallow water. *China Ocean Engng*, **22**, 1–10.

LIU, P. L.-F., PARK, Y. S. & COWEN, E. A. 2007 Boundary layer flow and bed shear stress under a solitary wave. *J. Fluid Mech.* **574**, 449–463.

LIU, P. L.-F., PARK, Y. S. & LARA, J. L. 2007 Long-wave-induced flows in an unsaturated permeable seabed. *J. Fluid Mech.* **586**, 323–345.

LODAHL, C. R., SUMER, B. M. & FREDSØE, J. 1998 Turbulent combined oscillatory flow and current in a pipe. *J. Fluid Mech.* **373**, 313–348.

LONGUET-HIGGINS, M. S. 1953 Mass transport in water waves. *Philos. Trans. R. Soc.* **345**, 535–581.

LONGUET-HIGGINS, M. S. & STEWART, R. W. 1962 Radiation stress and mass transport in gravity waves, with application to 'surf beats'. *J. Fluid Mech.* **13**, 481–504.

MACPHERSON, H. 1980 The attenuation of water waves over a non-rigid bed. *J. Fluid Mech.* **97**, 721–742.

MATSUNAGA, N. & HONJI, H. 1980 The backwash vortex. *J. Fluid Mech.* **99**, 813–815.

MATSUNAGA, N. & HONJI, H. 1983 The steady and unsteady backwash vortex. *J. Fluid Mech.* **135**, 189–197.

MCANALLY, W. H., FRIEDRICHS, C., HAMILTON, D., HAYTER, E., SHRESTHA, P., RODRIGUEZ, H., SHEREMET, A. & TEETER, A. 2007*a* Management of fluid mud in estuaries, bays and lakes. Part 1. Present state of understanding on character and behavior. ASCE Task Committee on Management of Fluid Mud. *J. Hydraul. Engng* **133**, 9–22.

MCANALLY, W. H., FRIEDRICHS, C., HAMILTON, D., HAYTER, E., SHRESTHA, P., RODRIGUEZ, H., SHEREMET, A. & TEETER, A. 2007*b* Management of fluid mud in estuaries, bays and lakes. Part 2. Measurement, modeling and management. ASCE Task Committee on Management of Fluid Mud. *J. Hydraul. Engng* **133**, 23–38.

MEI, C. C. 1983 *The Applied Dynamics of Ocean Surface Waves*. John Wiley & Sons.

MEI, C. C. & LIU, K.-F. 1987 A Bingham-plastic model for a muddy seabed under long waves. *J. Geophys. Res.* **92**, 14581–14594.

MEI, C. C. & LIU, P. L.-F. 1973 The damping of surface gravity waves in a bounded liquid. *J. Fluid Mech.* **59**, 239–256.

MELVILLE, W. K. 1996 The role of surface-wave breaking in air-sea interaction. *Annu. Rev. Fluid Mech.* **28**, 279–323.

MIGNIOT, P. C. 1968 Etude des proprietes physiques de differents sediments tres fins et leur comportement sous des actions hydrodynamiques. *Houille Blanche* **7**, 591–620.

MILES, W. M. 1981 The Korteweg–de Vries equation: a historical essay. *J. Fluid Mech.* **106**, 131–147.

MINIRANI, S. & KURUP, P. G. 2007 Energy attenuation of sea surface wves through generation of interface waves on visco-elastic bottom as in the mud banks, SW coast of India. *J. Ind. Geophys. Union* **11**, 143–146.

NADAOKA, K., HINO, M. & KOYANO, Y. 1989 Structure of the turbulent flow field under breaking waves in the surf zone. J. FLUID MECH. **204**, 359–387.

NG, C.-O. & MEI, C. C. 1994 Roll waves on a shallow layer of mud modelled as a power-law fluid. *J. Fluid Mech.* **263**, 151–183.

NGUYEN, Q. D. & BOGER, D. V. 1992 Measuring the flow properties of yield stress fluids. *Annu. Rev. Fluid Mech.* **24**, 47–88.

NICHOLLS, R. J., WONG, P. P., BURKETT, V. R., CODIGNOTTO, J. O., HAY, J. E., MCLEAN, R. F., RAGOONADEN, S. & WOODROFFE, C. D. 2007 Coastal systems and low-lying areas. In *Climate Change 2007: Impacts, Adaptation and Vulnerability. Contribution of Working Group II to the Fourth Assessment Report of the Intergovernmental Panel on Climate Change* (ed. Parry, M. L., Canziani, O. F., Palutikof, J. P., van der Linden, P. J. & Hanson, C. E.), 315–356. Cambridge University Press.

PAPANASTASIOU, T. C. 1987 Flows of materials with yield. *J. Rheol.* **31**, 385–404.

PARK, Y. S., LIU, P. L.-F. & CLARK, S. J. 2008 Viscous flows in a muddy seabed induced by a solitary wave. *J. Fluid Mech.* **598**, 383–392.

PATEL, M. H. 1977 On turbulent boundary layers in oscillatory flow. *Proc. R. Soc. Lond. A* **353**, 121–144.

PEIXINHO, J., NOUAR, C., DESAUBRY, C. & THÉRON, B. 2005 Laminar transitional and turbulent flow of yield stress fluid in a pipe. *J. Non-Newtonian Fluid Mech.* **128**, 172–184.

PEREGRINE, D. H. 1983 Breaking waves on beaches. *Annu. Rev. Fluid Mech.* **15**, 149–178.

PIAU, J. M. 2007 Carbopol gels: elastoviscoplastic and slippery glasses made of individual swollen sponges. Mese- and macroscopic properties, constitutive equations and scaling laws. *J. Non-Newtonian Fluid Mech.* **144**, 1–29.

PRANDTL, L. 1952 *Essentials of Fluid Dynamics*. Blackie, London.

PUTREVU, U. & SVENDSEN, I. A. 1993 Vertical structure of the undertow outside the surf zone. *J. Geophys. Res.* **98**, 22707–22716.

SANA, A., TANAKA, H., YAMAJI, H. & KAWAMURA, I. 2006 Hydrodynamic behavior of asymmetric oscillatory boundary layers at low Reynolds numbers. *J. Hydraul. Engng* **132**, 1086–1096.

SMALL, C. & NICHOLLS, R. J. 2003 A global analysis of human settlement in coastal zones. *J. Coastal Res.* **19**, 584–599.

SOU, I. M. 2006 An experimental investigation of the turbulence structure within the surf and swash zones. PhD dissertation, Cornell University.

STIASSNIE, M. & PEREGRINE, D. H. 1980 Shoaling of finite-amplitude surface waves on water of slowly-varying depth. *J. Fluid Mech.* **97**, 783–805.

SUMER, B. M., JENSEN, P. M., SØRENSEN, L. B., FREDSØE, J. & LIU, P. L.-F. 2008 Turbulent solitary wave boundary layer. *Proc. 8th Intl Offshore and Polar Engng Conference*, Vancouver, Canada, July 6–11, 2008, 775–781.

SVENDSEN, I. 1987 Analysis of surf zone turbulence. *J. Geophys. Res.* **92**, 5115–5124.

SYNOLAKIS, C. E. 1987 The runup of solitary waves. *J. Fluid Mech.* **185**, 523–545.

SYNOLAKIS, C. E. & BERNARD, E. N. 2006 Tsunami science before and beyond Boxing Day 2004. *Phil. Trans. R. Soc.* A **364**, 2231–2265.

TING, F. C. K. 2006 Large-scale turbulence under a solitary wave. *Coastal Engng.* **53**, 441–462.

TING, F. C. K. 2008 Large-scale turbulence under a solitary wave. Part 2. Forms and evolution of coherent structures. *Coastal Engng* **55**, 522–536.

UCHIDA, S. 1956 The pulsating viscous flow superposed on the steady laminar motion of incompressible fluid in a circular pipe. *Z. Angew. Math. Phys.* **7**, 403–422.

WATANABE, Y., SAEKI, H. & HOSKING, R. J. 2005 Three-dimensional vortex structures under breaking waves. *J. Fluid Mech.* **545**, 291–328.

WINTERWERP, J. C. & VAN KESTEREN, W. G. M. 2004 *Introduction to the physics of cohesive sediment in the marine environment*. Elsevier.

WEN, J. & LIU, P. L.-F. 1995 Mass transport in water waves over an elastic bed. *Proc. R. Soc. Lond.* A **450**, 371–390.

ZHANG, Q. & LIU, P. L.-F. 2008 A numerical study of swash flows generated by bores. *Coastal Engng* **55**, 1113–1134.